Developing Whole-Cell Biosensors for Microbiome Engineering Applications

Jack William Rutter

A thesis submitted in partial fulfilment

of the requirements for the degree of

Doctor of Philosophy

of

University College London

Computational Systems & Synthetic Biology Group

University College London

2021

I, Jack William Rutter, confirm that the work presented in this thesis is my own. Where information has been derived from other sources, I confirm that this has been indicated in the work.

Abstract

It is becoming increasingly apparent that the microbiota has a profound effect on human health and disease. Modern synthetic biology provides tools that can be used to engineer new diagnostic and therapeutic circuits- facilitating microbiome engineering and the creation of engineered biotherapeutics. These engineered biotherapeutics have the potential to expand our knowledge of microbial communities, host-microbe interactions and human health. However, to achieve these ambitious goals several challenges remain to be solved. These involve the creation of novel model systems and design strategies that can be used to characterise and improve these engineered strains.

The primary focus of this thesis are whole-cell biosensors, that can be used to monitor molecules relevant to human health. Within this work I develop a novel model system, based on the *Caenorhabditis elegans* nematode that can be used to characterise biosensor strains *in vivo*. Through the developed protocols I use the nematode model to show that ratiometric biosensors can detect and report on changes within the *C. elegans* digestive tract. This model could be used to improve engineered biosensor strains, while also expanding our understanding of nematode biology and host-microbe interactions. In addition, I engineer a range of new ratio-

metric plasmids that can be used in conjunction with the *C. elegans* model system in future. Finally, I develop a range of acetoacetate-inducible biosensors; while also exploring methods of rationally improving two-component system biosensors. Two component systems are a common sensing mechanism that can be used to create a range of biosensors, therefore methods of rationally improving these biosensors would be an invaluable tool.

Overall, it is hoped that the tools developed within this thesis can be used to further engineer whole-cell biosensors, which may help expand our knowledge of host-microbe interactions and human health.

Impact Statement

The work presented throughout this thesis has the potential to impact research both within and outside of academia. A range of biosensor plasmids, characterised within *Escherichia coli* Nissle 1917, are reported. These may be used in other experimental research to help explore the microbiota, allowing researchers to expand our knowledge of microbial communities and host-microbe interactions. They may also be incorporated into microbiome engineering studies, outside of academia. This research could help contribute towards the creation of clinically relevant strains that can be used to help treat patients and combat pathologies of the digestive tract, including conditions such as inflammatory bowel disease. Eventually these strains could be incorporated into engineered biotherapeutics, helping to contribute towards this newly emerging branch of therapies that will become increasingly available to patients and doctors.

Furthermore, although *C. elegans* is commonly used within many academic fields it has not yet been used extensively within the synthetic biology field. Currently, the mouse is the most frequently used model; however, the work presented here serves to emphasise the potential *C. elegans* offers as a viable model system. By highlighting the relatively quick, simple and inexpensive *C. elegans* model, it is

hoped that other researchers will be encouraged to incorporate it within their synthetic biology studies. This will help to cut down on the time and cost required to perform complex microbiome engineering studies, while also reducing the amount of vertebrate animals that need to be involved and sacrificed within these fields.

Acknowledgements

Firstly, I would like to offer my sincere thanks to Professors Chris Barnes and Geraint Thomas. I can not thank them enough for their support and guidance throughout my PhD studies.

I have also been fortunate enough to be part of two extremely welcoming labs, so I would like to thank both the Barnes and Thomas lab groups. In particular, Dr Tanel Ozdemir, Dr Linda Dekker, Dr Alex Fedorec and Lewis Tanner for the advice that they were always more than willing to share, and to Lewis for all of the cheesy jokes and music recommendations that helped to keep me entertained in the lab. Also, I would like to give a special thanks to Dr Leonor Quintaneiro for supporting me during my time with the Cabreiro lab group.

Thank you to the BBSRC for funding my studies. Thank you to LIDo and its organisers (especially Nadine Mogford, Dr QueeLim Ch'ng and Prof. Geraint Thomas) for the opportunity to carry out my PhD as part of their amazing DTP and the events they provided to support my professional development. Thank you to the Bogue Fellowship for awarding me the funds to attend the synthetic biology summer school at Cold Spring Harbor Laboratories. Also, a huge thank you to the Open Innovation Team, at the Cabinet Office, for allowing me to carry out my PIPS

as part of their awesome team, and for giving me a taste of what it is like to work within Whitehall.

In addition, I would like to thank all of the friends, both within and outside UCL, that have been there for me throughout my PhD. Although there are too many to mention all by name, I would like to give a special thank you to Bobby for listening to my grumbles after a long day spent in the lab. Luca R, Luca P, Bez, Jon, Mike, Ben and Jordan were all beside me when we decided to begin our journey into academic research and I am grateful to them for the welcome distractions, laughs and well-earned pints we shared during the more stressful times of our PhDs; I have no doubt we will continue to share many more in the future.

Most importantly, I would like to thank my parents for all the love, endless patience and support they have given me. I appreciate it more than I could ever put into words.

Contents

List of Figures

List of Tables

Abbreviations

AcAc Acetoacetate

AHL Acyl homoserine lactone

AT Axe-Txe

aTc Anhydrotetracycline

AU Arbitrary units

CFP Cyan fluorescent protein

DNA Deoxyribonucleic acid

DoE Design of experiments

EcN *Escherichia coli* Nissle 1917

FCS Flow cytometry standard

FUdR Fluorodeoxyuridine

GFP Green fluorescent protein

HIV Human immunodeficiency virus

HK Histidine kinase

hMSC Human mesenchymal stem cell

IBD Inflammatory bowel disease

IBS Irritable bowel syndrome

IPTG Isopropyl β-D-1-thiogalactopyranoside

LB Lysogeny broth

LD_{50} Lethal dose for 50% of animals

MCS Multiple cloning site

MEF Molecules of equivalent fluorophore

MM Master mix

M9 Minimal M9 media

NGM Nematode growth medium

OAT One-at-a-time

ODE Ordinary differential equation

PBS Phosphate buffered saline

PCCA Propionyl-CoA carboxylase subunit α

PCCB Propionyl-CoA carboxylase subunit β

PCR Polymerase chain reaction

PHB Poly-(R)-3-hydroxybutyrate

qPCR Quantitative real-time PCR

RBS Ribosome binding site

RR Response regulator

SA Sensitivity analysis

SCFA Short chain fatty acids

SE Standard error

SEVA Standard European vector architecture

SOC Super Optimal broth with Catabolite repression

TCS Two-component system

TF Transcription factor

WCB Whole-cell biosensor

WT Wild-type

YFP Yellow fluorescent protein

2-MC 2-methylcitrate

3HB 3-β-hydroxybutyrate

Chapter 1

Introduction

Science is but a perversion of itself, unless it has as its ultimate goal the betterment of humanity.

Nikola Tesla

Contents

1.1 Project Overview

In the future, it may be possible to engineer bacterial strains that are able to reside as a small part of an individual's microbiome. These engineered strains may be able to monitor changes in their environment, indicative of disease; and subsequently, take action on these signals. These actions could involve producing therapeutic molecules to combat these changes in a controlled and predictable manner, producing reporters to aid in diagnosis, or even preventing colonisation of the host by pathogenic strains. In recent years, increasing efforts have gone towards developing these strains; which may be referred to as 'engineered biotherapeutics'. Figure 1.1 provides a schematic of how these engineered biotherapeutics may operate within the digestive tract; however, it should be noted that this concept could also be extrapolated to other areas of the body.

This thesis explores some of the major aspects that may be involved in the creation of whole-cell biosensors for engineered biotherapeutics. Mainly, this work focuses on how the principles of synthetic biology may be employed to produce bacterial strains that can operate as diagnostics to monitor disease and improve our knowledge of host-microbe interactions.

1.2 Thesis Aims

As discussed above, this project set out to explore some of the major aspects involved in the design of whole-cell biosensors. The major aims of this thesis were therefore:

1. Develop circuits that can be used as the 'sensing' portion of engineered bio-

therapeutics. In theory, these could be used as straight diagnostics or to control expression of therapeutic molecules.

2. Design a model system that can be used to begin characterising the behaviour of these strains. This model should be amenable to the design paradigm of synthetic biology (i.e. rapid completion of multiple iterations).

More specific aims for each portion of this project can be found within their respective chapters.

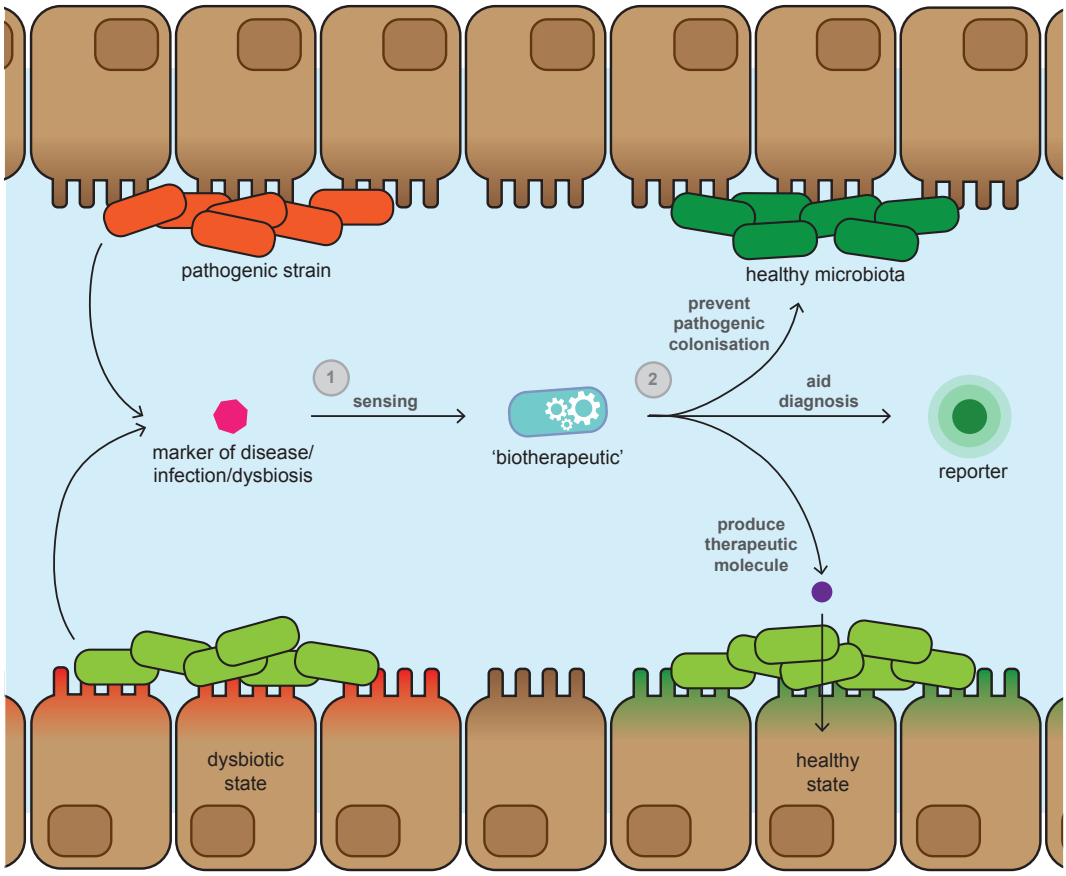

Figure 1.1: How 'engineered biotherapeutics' of the the future may operate in the digestive tract. Bacterial strains will be engineered to sense certain markers within their environment (part 1) and subsequently, report on, or try to influence the environment (part 2).

1.3 Thesis Outline

In the broadest sense, this thesis explores how synthetic biology may be used to develop whole-cell biosensors that can further our understanding of the microbiome and in time, how this knowledge may be leveraged for therapeutic or diagnostic applications. The thesis layout is as follows:

- **Chapter 2** contains a literature review in which I expand on the topics of the microbiota and synthetic biology, giving the general background and motivation for my project.

- **Chapter 3** details the materials and methods used to conduct and analyse the experiments performed throughout this thesis.

- **Chapter 4** covers the development of a *C. elegans* based host-microbe model for characterising engineered bacterial strains. This covers the creation of an automated image pipeline for quantifying biosensor induction *in vivo*. Finally, I use the developed protocols to show that engineered bacterial biosensors can be used to monitor changes in the *C. elegans* intestinal environment.

- **Chapter 5** details the design and construction of an improved ratiometric biosensor plasmid, which can be used as the backbone for a range of bacterial biosensors. These ratiometric plasmids may be used in conjunction with the *C. elegans* model described in chapter 4.

- **Chapter 6** in which I develop a range of acetoacetate-inducible biosensors and explore methods of engineering two-component system biosensors. This

includes attempts to model the Ato system and explores the effects of host strains and plasmid copy numbers on acetoacetate biosensor behaviour.

- **Chapter 7**, within this chapter I summarise the key findings of this work and offer some thoughts on the future directions of the field.

Experimental chapters 4, 5 and 6 contain their own background sections, the relevant materials and methods are contained within the corresponding sections of chapter 3.

1.4 Work Contributed by Other Individuals

Throughout my PhD, I have been fortunate enough to receive help from numerous people. Alex Fedorec and Tanel Ozdemir (Barnes Lab, UCL) cloned the original plasmid stability mechanism that was later incorporated into the pRB_AT backbone. The scripts used for conversion of flow cytometry data, from arbitrary units to MEF, were initially developed by Luca Rosa, Clare Robinson and Alex Fedorec (Barnes Lab, UCL). The initial work presented in chapter 4 was carried out with supervision from Tanel Ozdemir, who also performed the original cloning of the dual-plasmid biosensors, and Leonor Quintaneiro (Cabreiro Lab, UCL). Linda Dekker (Barnes Lab, UCL) helped carry out cloning of the ASAH2J06 plasmid used within chapter 6 and Emma Donovan (Barnes Lab, UCL) developed the initial AtoSC ODE equations and model.

1.5 Publications

The work carried out during my PhD candidature has contributed towards the following publications.

Research papers:

- A. Fedorec, T. Ozdemir, A. Doshi, Y. Ho, L. Rosa, J. Rutter, O. Velazquez, V. Pinheiro, T. Danino, C. Barnes. Two new plasmid post-segregational killing mechanisms for the implementation of synthetic gene networks in *E. coli*. *iScience* (2019). DOI: 10.1016/j.isci.2019.03.019.

- J. Rutter, T. Ozdemir, E. Galimov, L. Quintaneiro, L. Rosa, G. Thomas, F. Cabreiro, C. Barnes. Detecting changes in the *Caenorhabditis elegans* intestinal environment using an engineered bacterial biosensor. *ACS Synthetic Biology* (2019). DOI: 10.1021/acssynbio.9b00166.

- Acetoacetate-inducible whole-cell biosensors based on the AtoSC two-component system. *(under preparation)*

Book chapters:

- KY. Wen, J. Rutter, C. Barnes, L. Dekker. Fundamental building blocks of whole-cell biosensor design. *Handbook of Cell Biosensors* (2020). DOI: 10.1007/978-3-319-47405-2_181-1.

Chapter 2

Background

Contents

2.1 The Microbiota and the Microbiome

The human microbiota and microbiome are research areas that have garnered much interest in recent years. Primarily due to the development of new sequencing and analysis tools that allow a greater insight into the microbes present within the human body [1, 2]. Although original estimates suggested that microbial cells may outnumber human host cells by 10:1, more recent studies have suggested that this ratio may be overestimated [2–4]. However, there is no doubt that the human body plays host to a huge microbial community. The cells of this community come from thousands of species; spanning across bacteria, archaea and eukaryotes (although this project will focus on bacteria) [5–8]. These are distributed across various regions of the body in microbial communities, examples of these locations can be seen in Figure 2.1.

Although the terms are sometimes used interchangeably, the microbiota refers to the microbial organisms associated with the host; whereas the microbiome refers more specifically to the genetic material contained within these communities [1]. Previously, it has been shown that the composition of the microbiome can have a huge effect on the host organism, promoting health and preventing disease through host-microbe symbiosis [9]. The huge influence that the microbiome exerts on the host is true for a range of eukaryotic organisms [10]. This has even led to the suggestion that the microbiota should be thought of as an additional 'microbial organ' within, or on, the host [11].

Alongside their impact on human heath, it is also important to remember that these diverse communities are not isolated and are subject to the same dynamics

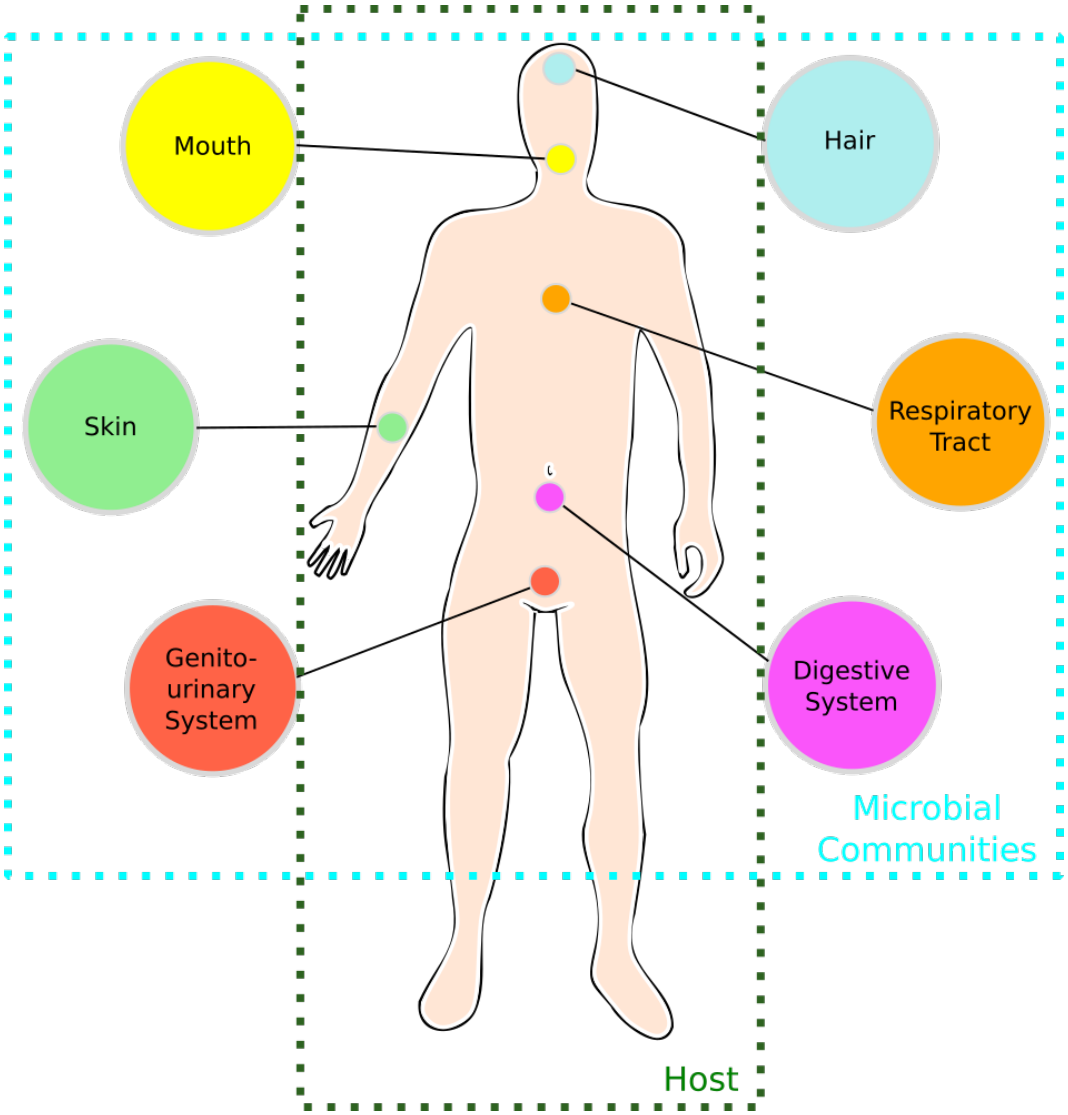

Figure 2.1: A host's overall microbiota encompasses numerous microbial communities. The composition of these communities can vary across bodily locations and also between individuals. For humans the largest community may be found within the digestive tract.

that can be observed in other bacterial communities [12]. These include (but are not limited to) cross-feeding, competition for resources and cell-to-cell communication, through mechanisms such as quorum sensing [13]. Some of these interactions are described in Figure 2.2. All of these factors result in an extremely complex and dynamic environment; much of which still remains to be unravelled [13]. However, this complexity also provides many exciting opportunities for improving our knowledge of bacterial communities, host-microbe interactions and human health.

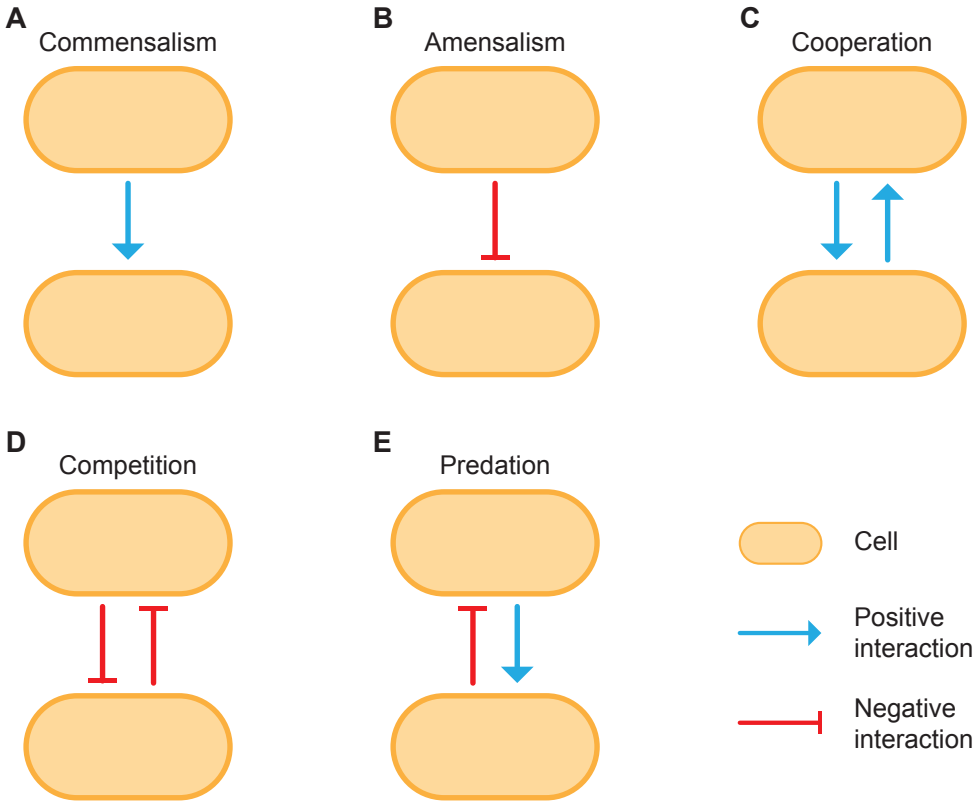

Figure 2.2: A subset of the interactions that can occur between members of a microbial community: (**A**) commensalism, (**B**) amensalism, (**C**) cooperation, (**D**) competition and (**E**) predation. Other interactions also exist, illustrating the complex networks that can develop within microbial communities.

2.1.1 The Gut Microbiota

The human gut hosts one of the largest and most complex microbial communities within humans and is thought to be one of the most densely populated microbial habitats on Earth [13–15]. The most prominent bacterial groups within the digestive tract belong to the Bacteroidetes (including genera such as *Bacteroides*) and Firmicutes (including genera such as *Lactobacillus* and *Enterococcus*) phyla [16]; which are thought to account for over 90% of the distal gut microbiota [5]. However, it should be noted that variation in this composition can be found across different areas of the digestive tract, both temporally and spatially, and between individuals [15]. Other prominent groups include Actinobacteria (mainly *bifidobacteria*, which have found widespread use as probiotics) [17] and Proteobacteria (which contain members of the *Escherichia* genus) [15, 18].

2.1.2 Healthy Function

The gut microbiota serves many roles within the host. Primarily the gut microbiota aids in the digestion and extraction of nutrients [19]. However, as with other communities of the microbiota, it also helps to develop the immune system, prevent colonisation by pathogens [20] and plays a role in energy metabolism and stimulating other host activities [16, 21].

Within the anaerobic gut environment undigested carbohydrates are fermented by bacteria to produce gases, such as methane and CO_2 and short chain fatty acids (SCFAs), such as acetate, butyrate and propionate [21]. SCFAs serve a number of roles within the human body [22]. Estimates state that SCFAs may account

for up to 15% of the calorific requirements of humans; with butyrate acting as the primary energy source for the colonic epithelium and acetate becoming available systemically [23, 24]. In addition, SCFAs exhibit numerous anti-inflammatory and anti-carcinogenic effects and links have been drawn to several diseases [25].

The gut microbiota is also now thought to play a role in the health of organs outside the digestive tract. This includes the liver, through the gut-liver axis [26] and the brain, through the gut-brain axis [27, 28]. As such, it is increasingly clear that the gut microbiota is intricately linked to the health of the host through an array of bidirectional interactions.

The composition of a host's microbiota may vary greatly throughout their lifetime. These changes in composition can be brought about by a wide range of factors. These include: age, diet, geographical location and lifestyle (e.g. exercise and hygiene) [29–32]. Another factor is the use of antibiotics to treat infection. When broad-spectrum antibiotics are used they may indiscriminately target commensal strains of the native microbiota. This provides opportunistic bacteria with a chance to establish themselves within the gut. The changes introduced by antibiotic administration can also be exacerbated by the community interactions discussed within section 2.1. Zhang and Chen (2019) provide an example of where a cross-feeding relationship coupled with antibiotic use can adversely disrupt the gut microbiota [33]. *Bifidobacterium adolescentis* breakdown starch and produce lactate and acetate; in turn these act as a growth substrate for some butyrate-producing species that are not able to breakdown starches directly. Therefore, if an antibiotic was to kill *B. adolescentis* this would go on to impact a number of other species within the

gut microbiota. Through examples such as this, it is evident that many factors can affect the gut microbiota and in turn disrupt a healthy host-microbe balance.

2.1.3 Dysbiosis and Disease

Disruptions in the gut microbiota composition can affect its ability to carry out healthy functions and lead to a condition known as 'dysbiosis'. Gut dysbiosis has been closely related to a range of harmful conditions [34]. To date gut dysbiosis has been implicated in both intra- and inter-intestinal diseases, including: diabetes [35], obesity [36, 37], allergies [38], irritable bowel syndrome (IBS) [39], inflammatory bowel disease (IBD) [40] and certain forms of cancer [41], amongst others.

However, despite recent progress, the causal relationships between dysbiosis and certain conditions still remain relatively poorly-defined and it is not yet clear the full range of conditions that dysbiosis may be involved in [15, 42]. As such, there is constant demand for new systems and models that may potentially be used to elucidate the causal relationships between the microbiota and disease.

The close link between the gut microbiota and this wide range of pathologies opens up the possibility of combating these diseases through influencing the function of the microbiota [43]. This has led to huge interest in developing methods capable of manipulating the microbiota. Not only to prevent gut dysbiosis, but also to fight diseases and monitor health across the whole body. One approach to provide these methods is through the application of synthetic biology techniques [42–44]. In theory, using synthetic biology, coupled with novel model systems, should aid greatly in improving our understanding of the microbiome and its involvement in

disease. In turn allowing the design of more effective therapeutic strategies.

2.2 Synthetic Biology

Synthetic biology as a field is found at the intersection of biology and engineering. It can be thought of as an ongoing effort to establish and formalise an engineering discipline in the context of biology and biological systems [45]. One of the primary aims of synthetic biology is to apply engineering paradigms to the study of biology [46]. Engineering principles are adopted from fields such as computer science, electrical and chemical engineering. In turn, these principles allow for the rational design and investigation of biology; thereby allowing us to increase our understanding of complex, natural biological systems and to create novel synthetic systems tailored towards a predictable purpose. Specifically, synthetic biology employs a forward engineering, or 'bottom-up' approach [47]. This relies on creating standardised 'parts' that can be combined to create more complex systems.

In particular, synthetic biology holds huge potential in: farming and agriculture [48, 49], sustainable energy [50] and personalised medicine [51, 52]. Early achievements of synthetic biology included the creation of genetic oscillators [53] and toggle switches [54]; subsequently, these have been built upon in more recent years [55]. Prominent examples include Cello, a computer aided design program for the construction of genetic circuits based on Boolean logic [56], the synthesis of minimal bacterial genomes [57], and the engineering of *Escherichia coli* for CO_2 fixation [58].

2.2.1 The Engineering of Biology

Perhaps the most often quoted engineering principle adopted by synthetic biology is the 'design-build-test-learn' cycle presented in Figure 2.3A [59, 60]. Within this cycle a system is conceptualised and then constructed using DNA assembly techniques. The system is then tested to see if it exhibits the desired behaviour, subsequently informing future designs. Due to the complexity of many biological systems it is often necessary to build on this simple design cycle through the completion of multiple iterations or the addition of more complex steps such as directed evolution or mathematical modelling. However, each iteration aims to provide a greater understanding of how the system works and may behave in future.

Other prominent engineering principles used by synthetic biology include ab-

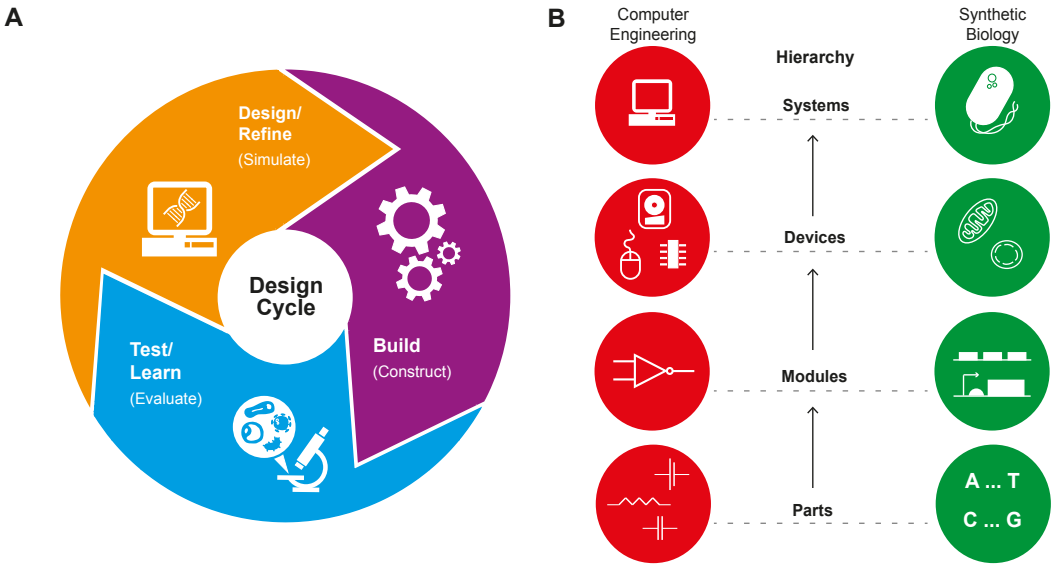

Figure 2.3: The 'design cycle' and 'abstraction hierarchy' of synthetic biology. (**A**) The design cycle adopted from numerous engineering disciplines. (**B**) The synthetic biology design hierarchy alongside the hierarchy of an established engineering discipline- computer engineering. Within synthetic biology, DNA is used to build functional modules, such as biochemical reactions or gene expression. These can then be combined to perform increasingly complex tasks.

straction, standardisation and decoupling [61]. As discussed by Heinemann and Panke (2006), abstraction in some form is found in nearly every established engineering discipline [62]. The abstraction process of breaking down a system into different design 'tiers' can be used to help simplify and manage the complexity of the design process [62]. Within synthetic biology, simple DNA sequences encoding a specific genetic component (e.g. a promoter or protein sequence) can be thought of as a 'part'. These parts may then be combined to create a module that is capable of expressing a desired protein (this would involve promoter, RBS, protein and terminator parts), or performing a specific biochemical reaction. Subsequently, multiple modules can be combined to make whole systems that perform novel functions (this hierarchy is shown in Figure 2.3B). This abstraction allows us to discuss synthetic biology projects at the most convenient level, without the need for constantly referring to every individual DNA sequence or part that is present in the final design [63]. Standardisation builds on this and is another widely-adopted concept in more traditional engineering fields [62]. Standardisation ensures the compatibility of modules and devices across designs, through defining the connections that are made between parts. In theory, the standardisation of synthetic biology aims to facilitate a 'plug and play' approach for designing novel systems [64]. Attempts to introduce synthetic biology standards include the Biobricks Foundation and the Registry of Standard Biological Parts [64–66]. Finally, decoupling is the notion of separating the design and fabrication processes, which often require different expertise [67]. In reality, this requires a sound understanding of the underlying science, in order to ensure that systems are designed in a way in which it is physically possible

to construct them [62].

Overall, these principles aim to create a range of characterised biological parts, which may be combined to fulfil novel purposes; similar to the way electronic components can be combined within multiple designs in electronic engineering. Although it is desirable to adopt the above concepts from other engineering disciplines, it should be noted that working with biological systems can be extremely complex and will continuously uncover numerous challenges that have not been encountered in other engineering disciplines [68]. Therefore, it is essential that these concepts continuously evolve and adapt to allow synthetic biology to grow as a true engineering discipline.

To date these principles have helped improve the sustainable production of high value chemicals, through the design of metabolically engineered microorganisms [69, 70]. They have also provided technologies that can be used to monitor and breakdown environmental pollutants [71, 72]. Furthermore, they are helping to combat disease through the creation of probiotic bacterial strains or cancer therapeutics that exploit the natural ability of some bacteria to accumulate within the hypoxic environment of tumours [73, 74]. Despite this success, it should be noted that there are still a number of problems that face the field of synthetic biology. The performance of systems is often context-dependent and many synthetic systems suffer from cross-talk with natural systems, while also undergoing mutation or loss of function over prolonged periods [75–77]. These problems have limited our ability to successfully design large, complex systems and will need to be addressed in future.

2.3 Engineering the Microbiome

As can be seen from Figure 2.4, over the last 20 years much research has gone into both the field of synthetic biology and, in particular, understanding the microbiota. More recently, in conjunction with our growing knowledge of the microbiota, increased interest has emerged in combining these fields; leading to a rapid increase in microbiome engineering publications (Figure 2.4D). As mentioned in section 2.1.3, the ability to engineer the microbiota of a host offers the potential to open up a whole new branch of therapeutic strategies, while also allowing us to improve our knowledge of host-microbe interactions and biology. In recent years there have been numerous attempts to engineer the microbiota for novel functions [78]. One important aspect in attempting to engineer the microbiome is the choice of cell chassis [79]. For microbiome engineering applications the chassis must be chosen both on their ease of manipulation within the lab and also their suitability to survive within the desired host environment. Published examples for intestinal microbiome engineering include genera such as *Escherichia*, *Lactobacillus* and *Bacteroides* [80]. However, the selection of cell chassis available for microbiome engineering applications is continuously expanding with the development of techniques to culture new species [79].

One of the most commonly used bacterial chassis for microbiome engineering applications is *E. coli* Nissle 1917 (EcN). EcN is a strain that was isolated from the microbiota of a First World War soldier who was found to be resistant to bacterial dysentery [81]. Subsequently, it has been shown that EcN can be beneficial in treating infectious GI diseases, maintaining remission of ulcerative colitis [82] and also

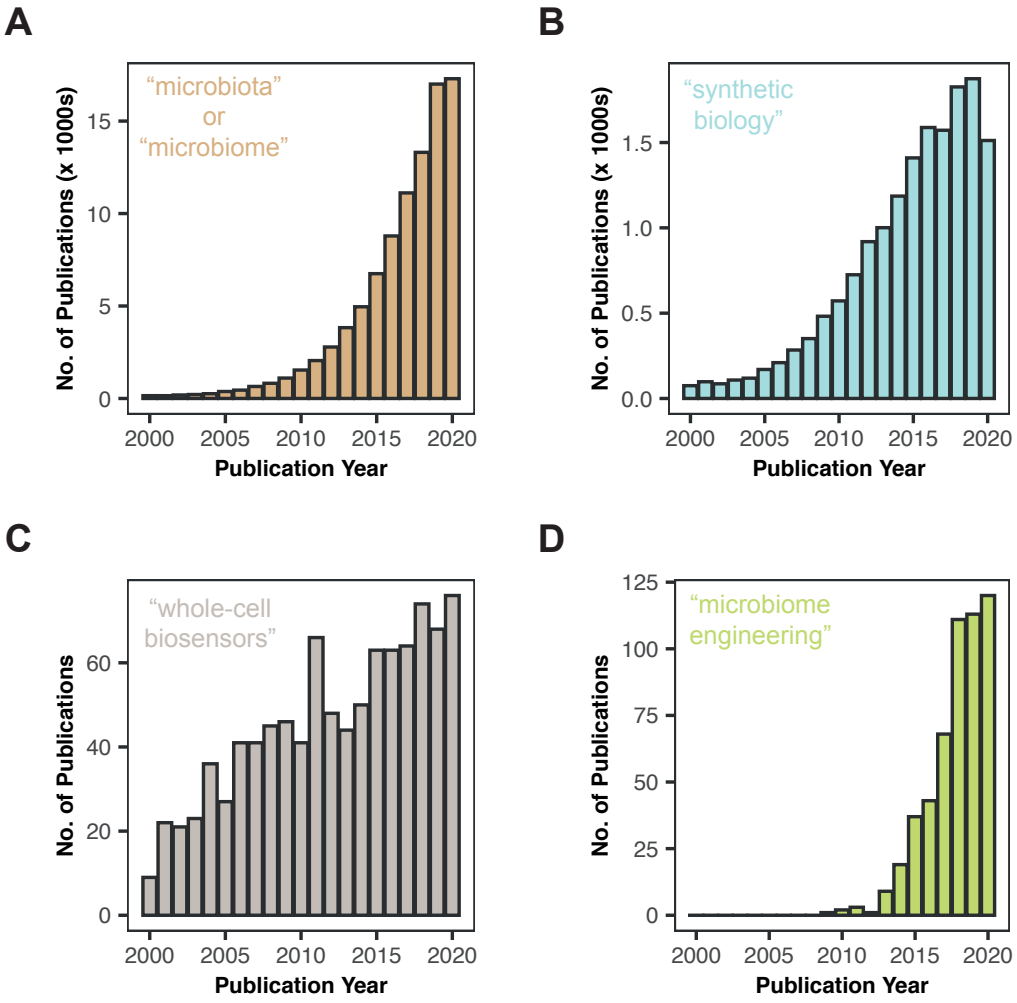

Figure 2.4: The number of publications per year, related to each of the specified fields: (**A**) microbiota or microbiome, (**B**) synthetic biology, (**C**) whole-cell biosensors and (**D**) microbiome engineering. These literature searches were performed through Web of Science, using the entire core collections database.

in preventing colonisation by pathogenic bacteria [81]. In addition, EcN currently has generally recognised as safe status [83]. Alongside this, *E. coli* strains have been studied extensively for biotechnological applications, resulting in a wide range of microbiology tools and parts that are compatible with this species. This coupled with the fact that the full genome sequence of EcN is now available [83], means that EcN is an ideal candidate for attempts to engineer the microbiota [84–86]. As such, EcN is used as one of the primary host chassis within this thesis.

2.3.1 Engineered Biotherapeutics

Engineered biotherapeutics are strains that are engineered to help treat, prevent or diagnose a disease. There are numerous examples of studies that have tried to engineer bacterial strains for diagnostic or therapeutic purposes [87]. These include attempts to target HIV infection [88], allergies [89], pathogenic infection [90, 91], cancer [74] and diabetes [92]. To date, these applications range from novel activation of a host's immune system and targeted delivery of drugs broken down by the stomach, to recording the presence of specific metabolites associated with disease [51]. Approaches such as these would be particularly useful in environments that do not have ready access to modern healthcare services. This could include future manned-space missions [93], where astronauts will be required to monitor and maintain their health within a hostile environment [94].

2.4 Whole-Cell Biosensors

One popular area of synthetic biology is the creation of biosensors. These aim to incorporate the components of a traditional sensor, detector-actuator-output, into a (at least partially) biological system. Biosensors may be used in a range of fields, such as environmental/industrial process monitoring or, as mentioned previously, for diagnosing disease [95, 96]. Over millennia cells have evolved the ability to detect and respond to various elements in their immediate surroundings. This allows bacteria to regulate their gene expression, in turn providing the capacity for bacteria to adapt to their environment [96]. From these systems, genetic parts can be repurposed for the creation of detection circuits and sensors. These can be used to build whole-cell biosensors (WCBs), which contain the sensing circuit within a single living cell. In order to produce a working WCB, suitable parts must be found that are responsive to the target of interest. These parts can be identified through a variety of methods, for example bioinformatic techniques or searching through protein databases [97, 98]. WCBs offer a number of benefits over more conventional sensing technologies. These can include low cost, portability, lack of specialised equipment for readout and, in some cases, information on the bioavailability of environmental pollutants [99–101].

2.4.1 Applications

Some of the earliest biosensors relied on using microorganisms (both natural and engineered) to report on the presence of toxic molecules through the expression of a reporter protein [102, 103]. Since these first examples the application of more mod-

ern microbiology and synthetic biology techniques has caused a surge of interest in developing WCBs that can be used in a range of fields. One area is the design of biosensors that are able to monitor environmental pollutants. One early attempt by King et al. (1990) detailed the construction of a luminescent biosensor that could report on levels of naphthelene [104]. Another study used *Pseudomonas fluorescens* to report on the toxicity of a range of heavy metals, including zinc, copper and cadmium, in environmental samples [105]. Since then, many more WCBs have been developed for environmental monitoring. Stocker et al. (2003) constructed *E. coli* WCBs based on components of the *ars* operon, that could be used to detect the presence of arsenite and arsenate in potable water [106]; these have subsequently been developed further through a mechanistic modelling approach [107]. Wan et al. (2019) also reported the creation of metal-inducible WCBs, sensitive to arsenic and mercury [108]. Within this study, genetic amplifiers were used to improve the behaviour of the WCB constructs, with the authors showing that multiple amplifiers can be placed in a cascade to further improve WCB performance. Subsequently, a sensor array was developed using agarose gel entrapment of the arsenic WCB; that could be used to give readouts of arsenic concentration based on a simple bar-like pattern similar to that used for signal strength on mobile phones [108]. A more recent study developed a WCB for the detection of pathogenic strains in drinking water, based on the QscR quorum sensing system [109]. Other biosensors have been designed for the detection of metals such as gold [110], lead [111] and mercury [112], explosive materials [113], and potentially harmful pesticides [114].

Outside of environmental detection, WCBs can also be used to monitor con-

ditions during bioproduction. This includes WCBs that have been developed to monitor metabolite availability and production in real-time [115]. Another example is the lactate WCB reported by Goers et al. (2017) [95]. Within this study the authors developed a lactate-responsive WCB based on the *lldPRD* operon found within *E. coli*. They went on to suggest that the WCB could be used to monitor the status of mammalian cell cultures during biopharmaceutical production [95].

Another rapidly growing area of WCB research, is their use in the medical field. WCBs are particularly exciting for diagnostic applications as they can reach areas of the body that are inaccessible to more traditional technologies and be used for the targeted delivery of therapeutics directly at the disease site (as illustrated in Figure 1.1) [51]. Danino et al. (2015) designed an engineered EcN strain that was able to selectively colonise liver metastases. This strain was used for the detection of tumours, through monitoring of a luciferin signal in the urine of a colonised mouse cancer model [116]. WCBs have also been applied for the measurement of pathological markers in human clinical samples [117]. Courbet et al. (2015) designed a range of WCBs (which they termed 'bactosensors') based on both *E. coli* and *Bacillus subtilis*, showing that they were able to survive in a range of human urine and serum samples. Subsequently, these WCBs were developed so that they could report on the presence of nitric oxides (involved in inflammation of the gut) and glucose in these samples, through the pYear and pCpxP promoters [117]. Riglar et al. developed a WCB for the detection of tetrathionate, using the *ttrRS* system [118]. These WCBs integrated a previously published *cro/cI* memory circuit [119] and were able to detect tetrathionate within both induced and genetic mouse models

of inflammation [118]. Mao et al. (2018) engineered an *L. lactis* strain to detect CAI-1, a quorum-sensing molecule secreted by *Vibrio cholerae*; showing that the WCB was able to report on cholera infection through an mCherry reporter in a mouse model [120]. WCBs have also been developed for the detection of a range of other medically-relevant biomarkers [51, 96, 121]. As such, it is clear that WCBs may find use in an array of diverse applications.

2.4.2 Common Architectures

In general, WCBs couple a 'sensing' promoter element with a readily detectable and quantifiable output signal. This output signal usually takes the form of a fluorescent protein, however, other forms that do not require specialist equipment for read-out may be used. A schematic of this process is included in Figure 2.5.

Biosensor circuits make use of the many natural bacterial sensing mechanisms

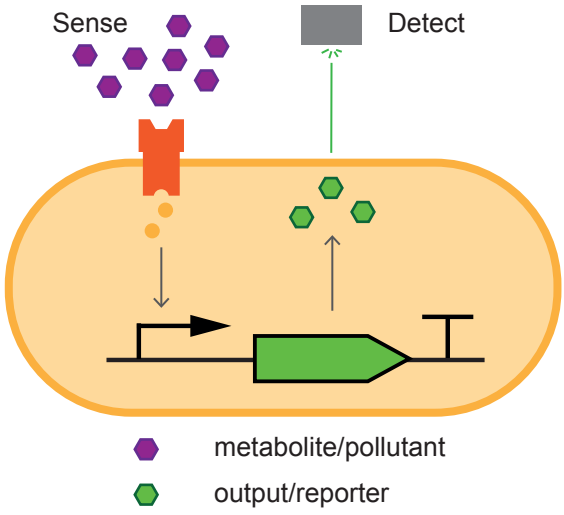

Figure 2.5: A typical layout of a whole-cell biosensor, with a measurable output. The cell is able to detect a specific input signal and produces a reporter in response. Many different sensing mechanisms can be incorporated into the design to create biosensors sensitive to a wide range of inputs.

that exist. The most common architectures of these signalling mechanisms are included within Figure 2.6A. The transcription factor (TF) mechanism is used extensively for metabolite-responsive sensors; within *E. coli* alone it is estimated that around one third of the total transcription factors have evolved to be metabolite-responsive [122]. This provides a huge range of targets from which biosensor circuits may be developed. Within the TF mechanism the TF interacts with the metabolite of interest and subsequently controls the expression of a target gene. These TF mechanisms can be found in four major layouts, which are shown in Figure 2.6B, repressed-repressor, repressed-activator, activated-repressor or activated-activator [122]. An example of the repressed-repressor architecture is the IPTG-inducible pLac system, which is discussed further within chapters 4 and 5.

Another common bacterial sensing mechanism is the two-component system (TCS). TCSs are found across most bacterial species and are involved in cell-to-cell communication, signalling events and pathogenesis [123, 124]. These systems consist of a histidine kinase (HK) and response regulator (RR) [125]. A more detailed explanation of how this architecture functions is given in chapter 6. TCSs are of particular interest as they do not occur within mammalian cells, therefore they have been proposed as potential targets for antibiotic therapies [123, 126]. Other sensing mechanisms include extracytoplasmic function sigma-factors.

2.4.3 Design Considerations

Chapters 4, 5 and 6 of this thesis all incorporate biosensors in some way. Therefore, it is important to define some of the major characteristics that are considered when

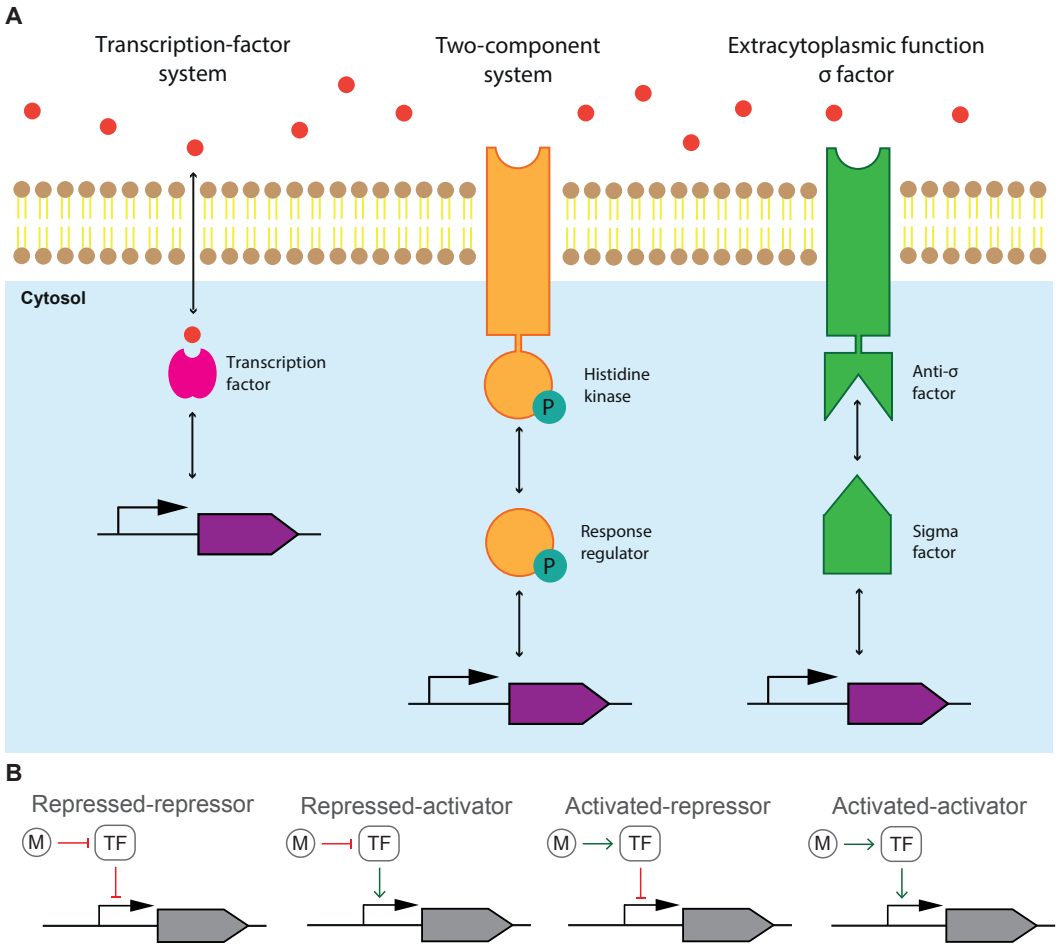

Figure 2.6: (**A**) The major sensing mechanisms found within bacteria. (**B**) Possible architectures for metabolite-responsive transcription factors, M = input metabolite, TF = transcription factor [122].

measuring biosensor performance. There are many aspects of performance that gain relative levels of importance depending on the intended use and context of the biosensor. One of the most commonly reported measures of biosensor performance is the 'dose-response curve' (Figure 2.7A) [127]. These curves are used to map the relationship between input and output for a given biosensor. Explanations of the various components of this curve are given in Table 2.1.

Decisions on the desired performance of a WCB need to be made within a specific context and will likely need to be tailored across different applications. One

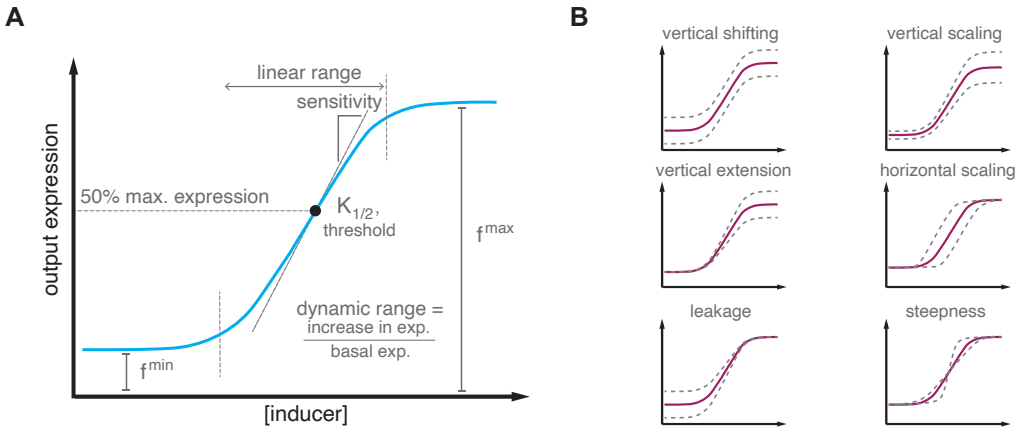

Figure 2.7: (**A**) A common biosensor response curve, annotated with general parameters of interest. (**B**) Common transformations that may be applied to the biosensor response curve.

illustration of this is within protein engineering studies. Imagine a study where a range of enzymes are tested for their ability to produce a certain molecule, for which we have a responsive WCB. The investigators may wish to carry out an initial screen to identify promising protein variants for further study. In order to do this a biosensor with a sharp digital on/off response (small linear range) and low $K_{1/2}$ would be desirable. This would allow us to discount enzymes from the study that do not produce the target molecule. Subsequently, it may be useful to rank the remaining enzyme variants based on the amount of target molecule they produce; thereby allowing us to isolate the most promising candidates. This subsequent screening would require a WCB that has a larger linear range, allowing us to determine between the different levels of our target molecule produced by each enzyme. These two scenarios are shown in Figure 2.8. Although this is a relatively simple scenario, it serves to illustrate how the desired application often dictates the most suitable behaviour of a WCB.

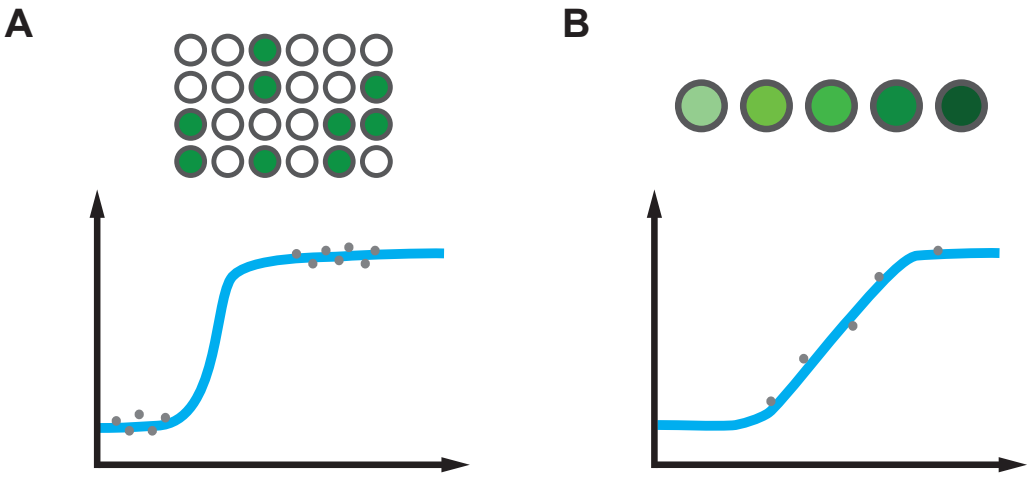

Figure 2.8: An example of how different WCB responses can be employed within different scenarios. In this case an initial screen is carried out to identify promising enzymes that produce the target molecule (this would require WCB behaviour similar to that shown in **A**). Subsequently, the candidates identified in **A** can be carried forward and ranked in order of their production capabilities (for this WCB behaviour similar to **B** would preferable). Through combining WCBs with different responses in this way we could readily carry out a simple enzyme screening experiment.

Table 2.1: Definitions of parameters on a biosensor response curve.

Parameter	Definition
f^{min}	minimum recorded output ('leakiness' in the uninduced state).
f^{max}	maximum recorded output.
$K_{1/2}$	inducer concentration which gives 50% of the max. output.
Linear range	inducer range over which output is concentration dependent.
Dynamic range	increase in output compared to the output in the uninduced state.
Sensitivity	the gradient of the response curve at $K_{1/2}$.
LOD	inducer which gives an output distinguishable from background.

The response curve of a biosensor may be tuned in a number of different ways. These changes can affect a range of parameters, including the $K_{1/2}$ and f^{min}. Some of the major ways that biosensor behaviour can be modified are shown in Figure 2.7B. A more detailed summary of these transformations is given in Ang et al. (2013) [45]. Initially, many attempts were made to design WCBs through a trial

and error approach [101]. However, more recent studies have reported methods that can be used to engineer specific biosensor performance. Xiaoqiang et al. (2018) created an improved lead biosensor using two strategies. Firstly, they changed the orientation of the regulatory elements and then incorporated positive feedback loops into the biosensor design [128]; based on a previous modified LuxR genetic amplifier [129]. Using this method they were able to improve both the sensitivity ($K_{1/2}$ in this case) and maximal output of their lead sensor. Other genetic amplification circuits have since been developed that can also be used to improve the final dynamic range of biosensor circuits [130]. Alternatively, some studies have shown methods of directed evolution that can be used to alter biosensor performance. Within directed evolution a library of mutants are created and then screened for desirable behaviour. This cycle is continued until the desired response is obtained [101]. One example of directed evolution in practice is the creation of the 'Marionette' *E. coli* strain that incorporated biosensors for 12 small molecules [131]. However, it is not always easy to isolate which of the specific mutations resulted in improved biosensor behaviour if the directed evolution method is employed. Therefore, directed evolution approaches may make it difficult to pick out specific design rules, and rational design strategies may be preferable and more widely applicable to different constructs [99, 101].

Chapter 3

Materials & Methods

Contents

3.1 General Methods

3.1.1 Bacterial Transformations

3.1.1.1 Electro-competent Cells

For electroporation 1 μl of plasmid DNA was added to 50 μl of competent cells. This mixture was then placed in an electroporation cuvette and shocked using a Bio-Rad micropulser. The mixture was then suspended in 500 μl of SOC media and recovered for 1 hour at 37°C. 50 μl of this mixture was then streaked onto an agar plate, with relevant antibiotics and incubated overnight.

Electrocompetent cells were prepared via a glycerol-mannitol density step protocol. The desired cells were grown in 400 ml of LB medium to an OD of 0.4-0.6. These cells were then chilled on ice for 5 minutes, before centrifuging at 2000g for 15 minutes, at 4°C. Cell pellets were resuspended in 10 ml of ice-cold milliQ H_2O. A density step was then prepared by adding 10 ml of 20% (w/v) glycerol and 1.5% (w/v) mannitol (autoclaved before use), below the resuspended cells. Care was taken to avoid displacing the interface between each solution. The mixture was then centrifuged for 15 minutes at 2000g and 4°C, with a slow acceleration cycle (to force cells through the density step). Following centrifugation, the aqueous layer was removed, followed by the glycerol-mannitol layer. Finally, the cell pellet was resuspended in 200 μl of ice-cold glycerol-mannitol solution and stored in aliquots, at -80°C, until needed.

3.1.1.2 Chemically-competent Cells

Chemically-competent *E. coli* NEB5α (New England Biolabs) cells were purchased and transformed according to the manufacturer's protocol. In brief, 1 μl of plasmid was added to 25 μl of cells on ice. This mix was left for 30 minutes on ice and then heat-shocked at 42°C for 30 seconds. The mix was then returned to ice for a further 2 minutes. 100 μl of SOC medium was then added and the cells recovered at 37°C for 1 hour. 50 μl of the transformation mix was then streaked onto an agar plate, with relevant antibiotics and incubated overnight.

3.1.2 Media

Where used Lysogeny Broth (LB) media was prepared through the addition of 2 g LB broth (Sigma Aldrich) in 100 ml MilliQ H_2O. This was then autoclaved before use. Minimal M9 (M9) media was prepared using the recipe shown in Table 3.1, all components were sterilised before use. For streaking and recovery of strains after transformation, LB agar was used. For LB agar, 2 g LB Broth (Sigma Aldrich) and 1.5 g Agar (Sigma Aldrich) was added to 100 ml MilliQ H_2O before autoclaving.

When required, antibiotic selection was used for plasmid maintenance. Antibi-

Table 3.1: The base recipe used to create minimal M9 medium (this was supplemented with the relevant antibiotics/inducers as required).

Media Component	**Volume / per 100 ml**
5x M9 salts	20 ml
80% glycerol	500 μl
10% casamino acids	2 ml
1 M $MgSO_4$	200 μl
1 M $CaCl_2$	10 μl
H_2O	up to 100 ml

otic stocks were prepared to the following concentrations; kanamycin - 50 mg/ml, ampicillin - 100 mg/ml and streptomycin - 50 mg/ml. These were then added at a 1 in 1000 dilution to bacterial media.

3.1.3 Colony PCRs

Colony PCRs where performed based on standard protocols. PCR reactions were based on the recipe given in table 3.2 and run in a T100 Thermal Cycler (BioRad) based on the program given in table 3.3. The T_M of DNA primers was calculated using the NEB T_M calculator.

3.1.4 Gel Electrophoresis

Final PCR products were visualised via gel electrophoresis. 1% (w/v) gels were prepared by dissolving agarose in tris-acetate EDTA (TAE) buffer, supplemented

Table 3.2: Mixture used for 25 μl colony PCR reaction.

Component	**Volume / μl**
OneTaq quick-load MM	12.5
Forward primer (10 μM)	0.5
Reverse primer (10 μM)	0.5
Template DNA	single colony
H_2O	11.5

Table 3.3: PCR program used for colony PCRs.

Process	**Temperature / °C**	**Time / s**	
Initial Denaturation	94°	180	
Cycle x 30	94°	30	(denature)
	T_M (45-72°)	15	(anneal)
	68°	20-30 /kb	(extend)
Final Extension	68°	300	
Hold	10°	∞	

with 1 µl GelGreen stain per 10 ml buffer. The gels were allowed to set and then the desired DNA ladder and sample volumes added. Gels were then run in TAE buffer, at 100V for 60 minutes (the time and voltage was adjusted depending on fragment size). Final images of gels were collected using a Chemidoc imager.

3.1.5 Gel and PCR Purification

Gel and PCR products were purified using either a Wizard SV Gel and PCR Clean-Up System (Promega) or a Monarch® PCR & DNA Cleanup Kit (New England Biolabs), following the manufacturer's protocols.

3.1.6 Plate Reader Assays

Timecourse assays were performed to collect growth curves for a variety of the constructs within this thesis (chapters 5 and 6). Overnight bacterial cultures were diluted to an approximate OD_{700} of 0.05, within fresh media. 120 µl of each culture was then added to the well of a 96-well clear bottom microplate (Greiner Bio-One) with a magnetic removable lid. The cultures were incubated in a Tecan Spark plate reader for 2 hours at 37°C with shaking at 150 rpm (2 mm amplitude, double orbital) with a reading taken every 30 minutes. Cultures were then induced with the relevant inducer concentration and sealed with a breath-easy permeable membrane (Diversified Biotech). The plates were then left to grow for a further 16 hours, with measurements taken every 20 minutes (the same temperature and shaking conditions were maintained). Measurements for OD_{600}, OD_{700} (to avoid overlap with fluorescent protein absorption/emission spectra), GFP and mCherry intensity were taken. Inducers were added to the 96-well plates with the aid of an I-Dot liquid han-

dler (Dispendix). Inducers were diluted to the desired stock concentrations and then custom protocols set up within the I-Dot, using the I-Dot assay studio software, to automate addition of the correct inducer volumes. Taking the total volume in each well to 125 µl.

3.1.7 Deep-well Concentration Assays

Bacterial cultures, grown overnight in LB media, were diluted to an OD_{700} of approximately 0.05 in fresh media, and incubated for 2 hours at 37°C, with 350 rpm shaking. Inducers were then added to the desired concentration and 200 µl of culture added to each well of a polypropylene deep-well plate (Brand, Sigma Aldrich), sealed with an autoclaved system Duetz lid. The induced cultures were then incubated at 37°C, with 350 rpm shaking for 16 hours. One µl samples were taken as required for flow cytometry analysis.

3.1.8 Flow Cytometry Assays

Flow cytometry was performed on an Attune NxT acoustic focusing cytometer with an Attune NxT autosampler (Thermo Fisher Scientific). One µl of the appropriate strain culture was transferred into 200 µl of sterile phosphate-buffered saline (PBS) in a shallow U-bottom 96-well plate (Thermo Fisher Scientific). The Attune NxT autosampler was used to record 10,000 events (for each individual sample) with 4 mixing and washing cycles between each sample. 10,000 events were recorded for all samples, across all experiments, to keep the total number of events constant. Flow options were set to an acquisition volume of 40 μl, sample volume of 200 μl and flow rate of 200 μl/min. Voltage settings were adjusted based on negative

controls. GFP was excited using a blue laser (488 nm) and detected using a 530/30 nm bandpass filter. mCherry was excited with a yellow laser (561 nm) and detected using a 620/15 nm bandpass filter. Additionally, a 1:300 dilution of rainbow calibration particles (Spherotech) in sterile PBS was recorded, allowing for the conversion of arbitrary units to MEF.

3.1.9 Hill Function Fitting

Curve fitting was performed in R, using the 'nls' fitting function. GFP induction and ratiometric increase data were fit using Hill functions:

$$f = f^{min} + (f^{max} - f^{min})\frac{[x]^n}{{K_{1/2}}^n + [x]^n},$$

where f is the observed value (either fluorescence or ratio), f^{min} is the minimum fitted value, f^{max} is the maximum fitted value, $[x]$ is the inducer concentration, $K_{1/2}$ is the threshold sensitivity and n is the cooperativity. Reported errors are the standard errors returned by the 'nls' function, using a least-squares fit. Dynamic range was calculated using the expression:

$$dynamic\,range = \frac{f^{max} - f^{min}}{f^{min}}.$$

Using the fitted f^{min} and f^{max} values. The operating/linear range, where reported, was calculated by taking the derivative of the Hill function over the length of the Hill fit:

$$f' = \frac{n(\frac{[x]}{K_d})^n}{[x]((\frac{[x]}{K_d})^n + 1)^2},$$

and then defined as the range of concentrations, over which the derivative of the Hill function was above 5% of the max value.

3.1.10 Data Visualisation and Plotting

All data was analysed and plotted using custom scripts created in Matlab, Python or R (based on the 'ggplot2' library). Final figures were arranged with Adobe Illustrator software.

3.2 Methods for *C. elegans* Host-Microbe Model

This section contains the methods used to collect the results given in chapter 4, 'Development of *Caenorhabditis elegans* as a synthetic biology model system'.

3.2.1 Strains and Plasmids

Table 3.5 contains a list of all the strains used within chapter 4, which focuses on the development of a *C. elegans* model for exploring host-microbe interactions. The plasmids reported in Table 3.5 were previously developed within the Barnes lab [132].

Table 3.4: Bacterial strains used within chapter 4.

Strain designation	Host	Plasmids
EcN_OG241	EcN	pOG241_GFP_pUC_KanR, p47_M7_mCherry_SC101_StrpR
EcN_OXB19	EcN	pOXB19_GFP_pUC_KanR, p47_M7_mCherry_SC101_StrpR
EcN_pLac	EcN	pLac_GFP_pUC_KanR, p47_M7_mCherry_SC101_StrpR
EcN_pProE	EcN	pProE_GFP_pUC_KanR, p47_M7_mCherry_SC101_StrpR

Table 3.5: Plasmids used within chapter 4.

Plasmid	Description	Source
pOG241_GFP	Promoterless GFP construct	Oxford Genetics, UK
pOXB19_GFP	Constitutive GFP construct	Barnes Lab, UCL
pLac_GFP	IPTG-inducible GFP construct	Barnes Lab, UCL
pProE_GFP	Propionate-inducible GFP construct	Barnes Lab, UCL
p47_M7_mCherry	Constitutive mCherry construct	Barnes Lab, UCL

3.2.2 Flow Cytometry Data Analysis

Within this chapter flow cytometry standard (FCS) data were collected and analysed using custom python scripts based on the FlowCal package (provided by Luca Rosa, Barnes lab) [133]. This python script performed density gating on forward and side scatter measurements to extract cell data from debris. The rainbow calibration beads were then used to create a standard curve to convert AU to MEF. This curve was then applied across all gated samples to collect the final fluorescent data in MEF.

3.2.3 *C. elegans* Propagation

For all *C. elegans* experiments the wild-type lab strain N2 was used (provided by the *Caenorhabditis* Genetics Centre, USA). *C. elegans* nematodes were maintained using standard laboratory practices. Adults worms were grown on nematode growth medium (NGM) agar plates, seeded with *E. coli* OP50 (an auxotroph strain with limited growth on NGM) and incubated at 20°C unless otherwise stated. For propagation *E. coli* lawns were created by seeding NGM plates with 150 μl of overnight OP50 culture, which was incubated for 48 hours at 20°C. Approximately 5-6 L4 adult nematodes were allowed to mature and lay eggs for 24 hours on each seeded plate. The adults were then removed and the eggs allowed to hatch and incubated for a further 48 hours. Five adult nematodes were then selected at random and the

Table 3.6: The base NGM recipe used to create the agar plates used in all nematode propagation and colonisation experiments (this was supplemented with the relevant inducer when needed).

Media Component	**Volume / per 200ml**	
NaCl	0.6	g
Bactopeptone	0.5	g
Agar	3.4	g
dH_2O	200	ml
Autoclave and cool to 55°C		
KH_2PO_4 (pH = 6)	5	ml
$MgSO_4$ (1M)	0.4	ml
$CaCl_2$ (1M)	0.4	ml
Cholesterol (5mg/ml)	0.4	ml
Shake well and allow bubbles to settle		

process repeated on a new set of NGM plates.

Nematode Growth Medium (NGM) was prepared using the recipe in Table 3.6. This recipe was modified in order to create the relevant inducer plates when testing the biosensor strains within the intestines of the *C. elegans*. For IPTG inducer plates, IPTG was added directly to the NGM medium until the desired final concentration. For the propionate inducer plates the pH was measured and adjusted if necessary. In order to do this propionate was added to the post-autoclave media components, and adjusted to pH 6 using KOH pellets.

3.2.4 'Egg Prep' Collection of Sterile Eggs

When uncolonised nematodes were needed, these were collected using an 'egg prep'. This allowed the harvest of unhatched eggs from pregnant adults. In brief, NGM plates were washed with sterile M9 media and all adult worms collected. The worms were then allowed to settle into a pellet and excess M9 media was removed

by aspiration. The worm pellet was then added to a 2 ml solution of bleach and 1M NaOH, at a ratio of 7:8. This mixture was then vortexed until all adult worm bodies had disintegrated and released fertile eggs, this required approximately 3 minutes. The bleach solution was then immediately diluted in approximately 13 ml of M9 media, to prevent excessive damage to the eggs. This egg solution was then centrifuged at 5000 rpm (Eppendorf 5702/R centrifuge with A-4-38 rotor) for 1 minute to pellet all the worm eggs. The M9 media was then carefully removed, replaced with 10 ml of fresh M9 media and the egg pellet resuspended. This wash process was repeated twice more to remove all remaining bleach, before the egg pellet was finally resuspended in 10 ml of M9. The final solution was transferred to a sterile Petri dish and incubated at 20°C overnight. This allowed time for any viable eggs to hatch and arrested their growth at the L1 stage. The sterile nematodes could then be transferred to the desired bacterial strain for biosensor colonisation or propagation.

3.2.5 *C. elegans* Host Biosensor Assay

The *C. elegans* colonisation protocol can be seen in Figure 4.2. EcN-NGM plates (seeded with the biosensor/control strains) were prepared through adding overnight culture of the desired strain to empty NGM plates and incubating overnight at 37°C, to form a bacterial lawn. It should be noted that antibiotics were not added to the EcN-NGM plates; it was assumed that the majority of the bacterial lawn would retain the dual-plasmid sensor system for the duration of the assay. Approximately 50 sterile nematodes (collected through an 'egg prep') were added to each EcN-NGM plate. The nematodes were then incubated at 20°C for 48 hours. 30 nematodes were

then selected at random and transferred to fresh EcN-NGM plates, seeded with the same strain and further supplemented with 20 μM fluorodeoxyuridine (FUdR), a drug used to prevent the development of fertile eggs. The nematodes were then incubated for a further 5 days (to a total age of 7 days) to allow colonisation of a majority of the nematodes. 25 nematodes were then selected at random and transferred to unseeded NGM plates supplemented with the desired inducer concentration. The nematodes were then incubated at 20°C, for the desired assay period. Induced nematodes were then anaesthetised with 0.02% levamisole prior to imaging.

3.2.6 *C. elegans* Biosensor Imaging

Anaesthetised *C. elegans* nematodes were imaged using a Zeiss Axio Scope. Images were collected using the brightfield, GFP (excitation = 470 nm; emission = 525 nm), mCherry (excitation = 560 nm; emission = 630 nm) and merged channels. The exposure times of each imaging mode were set to 500 ms and laser intensities kept constant throughout all imaging. Images were collected using Zen software.

3.2.7 *C. elegans* Manual Image Processing

Where reported, manual nematode image analysis was carried out with FIJI software based on the method developed by Ozdemir (2017) [132]. In short, background subtractions were applied to the mCherry and GFP images (using a rolling ball, radius 1000 pixels). The fluorescent area of the mCherry image was then manually traced and the resultant region of interest applied to both the mCherry and GFP images. The mean pixel intensity of the mCherry and GFP regions was then calculated and these intensity values were used to calculate the final GFP:mCherry

ratio of each image.

3.2.8 *C. elegans* Automated Image Processing

To replace the manual image analysis an automated Matlab pipeline was developed to process the collected nematode images. A graphical representation of this pipeline can be seen in Figure 4.3. This pipeline was implemented in Matlab version R2016b on a 2015 MacBook Pro (8GB RAM), using the 'imaging processing toolbox' freely available with MatLab. The automated pipeline was able to calculate the GFP:mCherry ratios and greatly reduced the processing time required to carry out analysis. Where reported, statistical significance was calculated by performing a two-sided Mann-Whitney U test, using custom R scripts.

3.3 Methods for Ratiometric Whole-Cell Biosensors

This section contains the methods used to collect the results given in chapter 5, 'Construction of a whole-cell biosensor platform for improved ratiometric reporting and plasmid stability'.

3.3.1 Strains and Primers

The host strains and primers used within this chapter are given in Tables 3.7 and 3.8.

3.3.2 Gibson HiFi DNA Assembly

Within this chapter a Gibson assembly method was employed for plasmid construction. This was based on the NEBuilder HiFi DNA assembly master mix (NEB). Ligation reactions were assembled using the protocol given in Table 3.9. Reaction

mixtures were then incubated for 15 minutes at 50°C and transferred to a freezer for storage or used directly for transformation.

Table 3.7: Host strains used within chapter 5.

Host strain	Description	Source
E. coli NEB 5α	Cloning strain	New England BioLabs
E. coli BW25113	Keio collection parent strain	Keio collection
E. coli Nissle	Commensal *E. coli* strain	Prof. Ian Henderson, University of Birmingham

Table 3.8: Primers used within chapter 5. Lowercase letters indicate the annealing sequence.

Primer	Sequence
DegTag.F	tttatacagttcatccatgccg
DegTag.R	taacgatgcgcgcaataaaa
pJRBB_fragment.F	CCCAataagcgtcatcctttagtaactaac
pJRBB_fragment.R	TTAAATCGTAAtacggcaaaagtgaatccag
pJRBB_vector.F	CTTTTGCCGTattacgatttaaatttgtgtctcaaaatct
pJRBB_vector.R	GGATGACGCttattggggacccctggattct
pJRc_fragment.F	GCATGCAAagtgggtctcaggagttgacg
pJRc_fragment.R	AGCTAAGCgctagcactgtacctaggactgag
pJRc_vector.F	TGCTAGCgcttagctgtcaccggatgt
pJRc_vector.R	GACCCACTttgcatgcctgcaggtcg
pJRLac_fragment.F	CATGCAAGCTgatctcaagaagatcatcttattaatcagataaaatatttctaggatcat
pJRLac_fragment.R	GTGACAGCTAaattgtgagcgctcacaattccac
pJRLac_vector.F	GCTCACAATttagctgtcaccggatgtgctt
pJRLac_vector.R	TCTTGAGATCagctgttgcatgccatgcctgcag
pJRAto_fragment.F	CATGCAAgccgtgcattgatgtataaactccag
pJRAto_fragment.R	CAGCTAAGCgtatgcatacaccgttgtgggt
pJRAto_vector.F	ATGCATACgcttagctgtcaccggatgtgct
pJRAto_vector.R	TGCACGgcttgcatgcctgcagg
pJRPro_fragment.F	AGTCGACCTGCAGGCATGCAcagataaaatatttgctcatgagcccg
pJRPro_fragment.R	CATCCGGTGACAGCTAAGCTtgttatcaacttgttatttgcgt
pJRPro_vector.F	CAAATAACAAGTTGATAAcaagcttagctgtcaccggat
pJRPro_vector.R	ATGAGCAAATATTTTATCTGtgcatgcctgcaggtcgac

Table 3.9: NEBuilder HiFi DNA assembly reaction mix.

Component	Amount
NEBuilder HiFi DNA Assembly MM	10 μL
vector:insert ratio	1:2
Total DNA amount	up to 0.2 pmols
ddH_2O	up to 20 μL

3.4 Methods for AtoSC TCS Biosensor Design

This section contains the methods used to collect the results given in chapter 6, 'Engineering of acetoacetate whole-cell biosensors based on the AtoSC two-component system'.

3.4.1 MoClo DNA Assembly

The majority of new plasmids within this section were built using CIDAR MoClo assembly [134]. Through this method individual 'parts' are combined to make 'transcriptional units', which are then combined into the final circuit design (see Figure 3.1). This method relies on type IIS restriction enzymes (BbsI and BsaI) that allow the interchange of parts based on short recognition sequences found at fusion sites. An overview of this method can be seen in Figure 3.1.

MoClo reactions were set up as given in Table 3.10. All DNA parts added to MoClo reactions were diluted to 20 fmol/μl. MoClo reactions were then carried out in a T100 Thermal Cycler (BioRad), following the programme given in Table 3.11. After construction the final reactions were either frozen for storage or transformed into competent cells ($\sim$5 μl of reaction into 15-50 μl of cells). The correct constructs were selected for through blue/white colony screening. For this, LB agar plates were coated with 40 μl of 20 mg/ml X-gal and 4 μl of 1 M IPTG, and al-

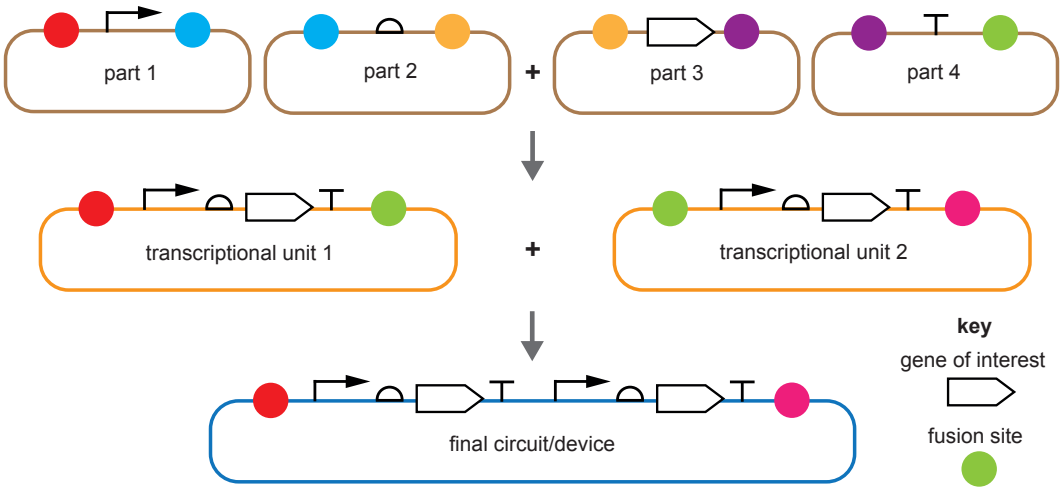

Figure 3.1: MoClo DNA assembly method, relying on type IIS restriction enzymes. These cut the DNA parts at areas known as fusion sites. Parts are then combined within a new vector to produce transcriptional units, using the resultant overhangs. Transcriptional units can then be combined to produce the final desired circuits [134].

Table 3.10: MoClo assembly reaction mix.

Component	**Volume / μl**
each DNA part	1
T4 ligase buffer	1
T4 ligase (HC)	1
BsaI-HF v2/BbsI-HF	1
H_2O	up to 10 μl

lowed to dry before the addition of transformed cells. The cells were then incubated overnight, and white colonies selected for miniprep and sequencing confirmation.

Table 3.11: MoClo assembly thermal cycler program.

	Temperature / °C	**Time / s**
Cycle x 25	37°	90
	16°	180
	50°	300
	80°	600
	12°	∞

3.4.2 Ato Plasmid Construction

A MoClo transcription unit containing the pato promoter and GFP was constructed from the LD1 pato DVA_EB (Linda Dekker, UCL), DVK_EF, B0034m_BC, E0040m_CD and B0015_DF (CIDAR MoClo kit) DNA parts. This unit was designated pAto + GFP. The ASAH0 plasmid was constructed by adding the pAto + GFP transcriptional unit, into the DVA_EF MoClo backbone plasmid. The low-copy ASAL0 plasmid was made by amplifying the SC101 origin from the DVS471_AF plasmid, using the SC101_fragment.F and SC101_fragment.R primers (Table 3.12). ASAH0 was amplified using the SC101_vector.F and SC101_vector.R primers. The SC101 fragment was then inserted through HiFi DNA assembly.

The AtoS/AtoC fragment was amplified from *E. coli* genomic DNA using the LD9 and LD10 primers, by Linda Dekker (UCL) and placed within the DVA_CD MoClo backbone to produce AtoSC_CD. A transcription unit was then created using AtoSC_CD, DVK_FG, J23106_FB, B0034m_BC and B0015_DG. This transcription unit was designated AtoSC unit. The AtoSC02 unit and AtoSC16 unit were created by replacing the J23106_FB part with J23102_FB and J23116_FB, respectively. The ASAH2J06 plasmid was made by combining the AtoSC and pAto + GFP units in the DVA_EG backbone. ASAH2J02 was made by combining the AtoSC02 and pAto + GFP units in the DVA_EG backbone. ASAH2J16 was made by combining the AtoSC16 and pAto + GFP units in the DVA_EG backbone. As with ASAL0, the low-copy ASAL2J06 plasmid was made by amplifying the SC101 origin from the DVS471_AF plasmid, using the SC101_fragment.F and SC101_fragment.R primers (Table 3.12). ASAH2J06 was amplified using the

Table 3.12: Primers used within chapter 6. Lowercase letters indicate the annealing sequence. Underlined letters show addition of restriction enzyme cleavage sites.

Primer	Sequence
SC101_fragment.F	TGGCGTTcttttccgctgcataaccctgc
SC101_fragment.R	AAAGGATCTTCgagttatacacagggctgggatctatt
SC101_vector.F	GTGTATAACTCgaagatcctttgatcttttctacggggt
SC101_vector.R	CGGAAAAGaacgccagcaacgcggc
LD9	GGCGGTCTCAAATGatgcattatatgaagtggatttatccacgcc
LD10	GGCGGTCTCTACCTTCAttatacatccgccggatc
LD89	GGCGGTCTCTACCTcatacagtctgatttccctgcgg

SC101_vector.F and SC101_vector.R primers. The SC101 fragment was then inserted through HiFi DNA assembly.

The AtoS fragment was amplified from ASAH2J06 using the LD9 and LD89 primers (Table 3.12). This was then combined with DVK_FG, J23106_FB, B0034m_BC and B0015_DG, to produce the AtoS unit. The AtoS02 and AtoS16 units were created by replacing the J23106_FB part with J23102_FB and J23116_FB, respectively. The ASAH1J06 plasmid was made by combining the AtoS and pAto + GFP units in the DVA_EG backbone. ASAH1J02 was made by combining the AtoS02 and pAto + GFP units in the DVA_EG backbone. ASAH1J16 was made by combining the AtoS16 and pAto + GFP units in the DVA_EG backbone. Again, the low-copy ASAL1J06 plasmid was made by amplifying the SC101 origin from the DVS471_AF plasmid, using the SC101_fragment.F and SC101_fragment.R primers (Table 3.12). ASAH1J06 was amplified using the SC101_vector.F and SC101_vector.R primers. The SC101 fragment was then inserted through HiFi DNA assembly.

3.4.3 Ato Biosensor Host Strains

A range of host strains were used as chassis for the Ato biosensor plasmids. The BW25113, JW2213 and JW2214 strains were purchased from the Keio collection (*E. coli* Genetic Stock Centre). The BW28878 double-knockout strain was provided by Professor Kyriakidis (University of Thessaloniki) and *E. coli* Nissle by Professor Henderson (University of Birmingham). Competent NEB5α cells were purchased commercially (New England Biolabs). These strains are shown in Table 3.13.

3.4.4 Ato ODE Modelling and Sensitivity Analysis

Within this chapter an ODE model attempting to describe the Ato WCBs was developed. This modelling was performed using custom Python scripts, initially developed by Emma Donovan (Barnes Lab, UCL). The equations and parameters used for this model are given in section 6.3.1. Sensitivity analysis was performed based on the SA.lib python package. Custom scripts were created to perform Morris analysis.

Table 3.13: Host strains used within chapter 6.

Strain	Description	Source
E. coli NEB 5α	Cloning strain	New England BioLabs
E. coli BW25113	Keio collection parent strain	Keio collection
E. coli JW2213	Keio collection AtoS knockout	Keio Collection
E. coli JW2214	Keio collection AtoC knockout	Keio Collection
E. coli BW28878	AtoS and AtoC double-knockout	Prof. Kyriakidis, University of Thessaloniki
E. coli Nissle	Commensal *E. coli* strain	Prof. Ian Henderson, University of Birmingham

3.4.5 FlopR Data Analysis

The FCS and plate reader data collected within this chapter were analysed using the FlopR package [135]. In short, the FlopR package was used to normalise plate reader growth curves against empty media and convert FCS data into MEF. The FlopR method required wells containing an empty media sample and negative control sample to be run with every plate reader assay, for normalisation to be applied.

Chapter 4

Development of *Caenorhabditis elegans* as a Synthetic Biology Model System

Contents

4.1 Background

4.1.1 Current Models for Microbiota and Synthetic Biology Studies

Animal models are vital for the study of biology. For example, models ranging from prokaryotic *E. coli*, to eukaryotic *Saccharomyces cerevisiae*, mice and zebrafish [136, 137], have allowed scientists to ask fundamental questions across biology. In turn, these studies have provided invaluable insights and greatly advanced our knowledge of biological processes and mechanisms.

There are a range of organisms that are currently used as viable models in microbiome studies. These include: mice, zebrafish, *drosophila* and *Caenorhabditis elegans*, amongst others [138, 139]. Of these models, the mouse is the most frequently employed [140]. In addition, nearly every attempt to engineer the microbiome to date has been performed with the mouse model [116, 119, 141–143]. The mouse offers similar taxonomic levels of the microbiota to humans, with a range of custom phenotypes available [144]. However, there are considerable concerns over the reproducibility of any findings caused by differences in vendors, diet and handling techniques [145].

Furthermore, the 'Three Rs' are currently used to guide animal welfare and model use in science. These ethical guidelines refer to 'Replace', 'Reduce' and 'Refine' [146]. As such, there is a drive towards replacing more sentient animals (vertebrates- such as mice) with animals that current science suggests have a lower perception of pain and suffering (invertebrates- such as *C. elegans*) [146]. This has

resulted in a demand for alternative, cheap and robust model systems that will allow us to expand our knowledge of host-microbe interactions and attempts to engineer the microbiome. The development of a suitable *C. elegans* model that can be used to help reduce and replace the use of mice within microbiome and synthetic biology studies would provide a substantial step towards satisfying this goal.

4.1.2 The *C. elegans* nematode

C. elegans is a nematode species, used extensively across biology. In the wild, these nematodes are typically found in soil and plant matter [147] and were the first multicellular-species to have their full genome sequenced [148]. Within lab studies the most common strain is the N2 or 'Bristol' strain [149]. This domesticated strain is widely used as the laboratory wild-type. The nematodes naturally prey on a range of bacteria found within soil [150] and boast a diverse native microbiota. However, in the lab they are often grown on a single strain [151]. This allows researchers complete control over the composition of their intestinal microbiome. In addition, they are small, easy to propagate and have a fast reproduction cycle [149]. These are all traits that make *C. elegans* amenable to research investigations. Consequently, *C. elegans* have been used in studies on aging [152], the microbiome [153], diet [154] and disease [155, 156], amongst others [157].

4.1.3 *C. elegans* in Synthetic Biology

Despite their many attractive traits, *C. elegans* have not yet been widely incorporated into synthetic biology studies. There have been very few published uses of *C. elegans* as a model in synthetic biology studies, outside of this work. One study

engineered nematocidal strains of bacteria to target *C. elegans* [158]. In another study, Hwang et al. (2017) were able to characterise a 'sense-kill' circuit within EcN, capable of suppressing *Pseudomonas aureginosa* infection [159]; building upon a previously engineered bacterial strain [91]. The EcN host was engineered to detect *P. aureginosa* within the digestive tract (through detection of AHLs) and subsequently produce pyocin S5 (a *P. aureginosa* toxin), dispersin B (an anti-biofilm enzyme) and E7 (a lysis protein). The study went on to display that the engineered EcN strain reduced *P. aureginosa* infection in both *C. elegans* and mouse *in vivo* models of infection. These studies serve to highlight the potential of *C. elegans* as a model for characterising, diagnostic and therapeutic, engineered bacterial strains.

Alongside this, the rapid growing time, high level of microbiota control and relatively low upkeep cost of *C. elegans* make it an ideal candidate for further incorporation into synthetic biology studies. In particular, this should complement the 'design-build-test-learn' cycle (shown in Figure 2.3) that is fundamental to the field of synthetic biology. The work in this chapter set out to develop a *C. elegans* host-microbe model, which could be used in future studies to rapidly explore host-microbe interactions and characterise the behaviour of live biotherapeutics and bacterial diagnostics *in vivo*. This process is outlined within Figure 4.1.

The work presented within this chapter contributed towards the following publication:

- **J. Rutter**, T. Ozdemir, E. Galimov, L. Quintaneiro, L. Rosa, G. Thomas, F. Cabreiro, C. Barnes. Detecting changes in the *Caenorhabditis elegans* intestinal environment using an engineered bacterial biosensor. *ACS Synthetic*

Biology (2019). DOI: 10.1021/acssynbio.9b00166.

4.2 Aims

The first aim of this chapter was to confirm that the *C. elegans* nematode could be colonised and survive on an engineered biosensor strain. Following this I wished to show that fluorescent reporters could be readily imaged in the *C. elegans* digestive tract. I then wanted to modify protocols for rapidly characterising biosenor induction *in vivo*, followed by recording environmental changes in the *C. elegans* digestive tract using an engineered biosensor. Finally, I wished to try and record the presence of a biologically relevant metabolite using a whole-cell biosensor.

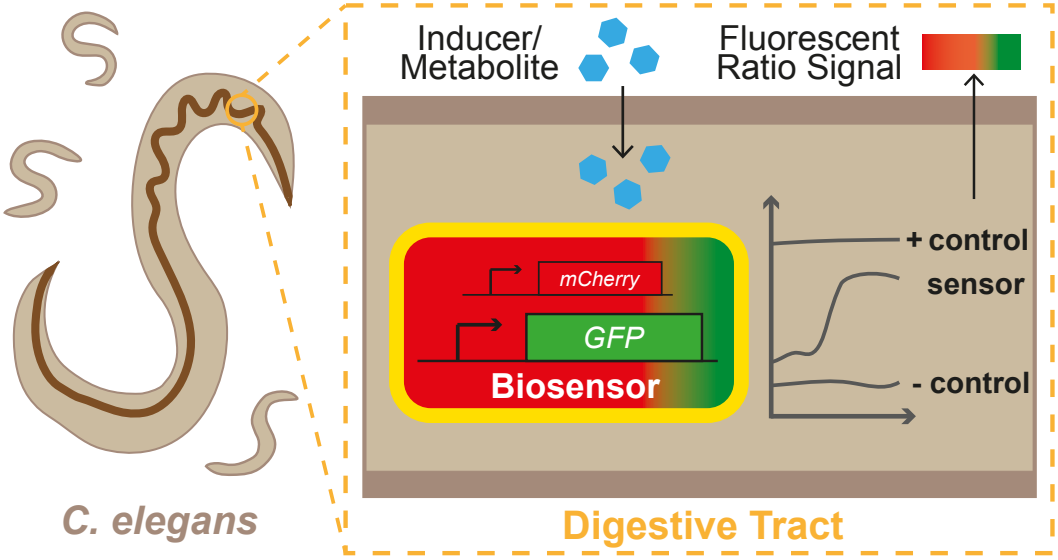

Figure 4.1: Schematic of how biosensors may be used to report on environmental changes within the *C. elegans* digestive tract. Bacterial biosensors reside within the digestive tract and report on inducer conditions within the immediate environment through a ratiometric, fluorescent signal. Providing insights into biosensor behaviour and host-microbe interactions.

4.3 Results

4.3.1 Confirmation of *C. elegans* Colonisation and Imaging Protocols

4.3.1.1 Colonisation of *C. elegans* nematodes

Hwang et al. (discussed in section 4.1.3) were able to use mRFP1 and GFP to report on the extent of *P. aureginosa* infection from inside the digestive tracts of *C. elegans* [159]. Initially a similar approach was adopted, using mCherry and GFP as reporters for an EcN colonisation protocol of the *C. elegans* digestive tract. Within the developed approach, immature worms were grown on the engineered EcN strains and fluorescence microscopy used to visualise EcN colonisation. The final colonisation protocol can be seen in Figure 4.2A. Two control strains were used to test the viability of mCherry and GFP as *in vivo* reporters in *C. elegans*. These were EcN_OG241 and EcN_OXB19, constitutively expressing mCherry and GFP + mCherry, respectively. From the images presented in Figure 4.2B and 4.2C it can be seen that both mCherry and GFP were readily visualised in the *C. elegans* digestive tract. In addition, for both EcN_OG241 and EcN_OXB19, the mCherry and GFP signals appeared to be strongly localised to the digestive tract of *C. elegans*. This gave confidence that the engineered EcN strains could be used to effectively report on environmental changes within the *C. elegans* intestines. It should be noted that not all worm images were found to be colonised through this protocol, this is discussed further within section 4.3.4.

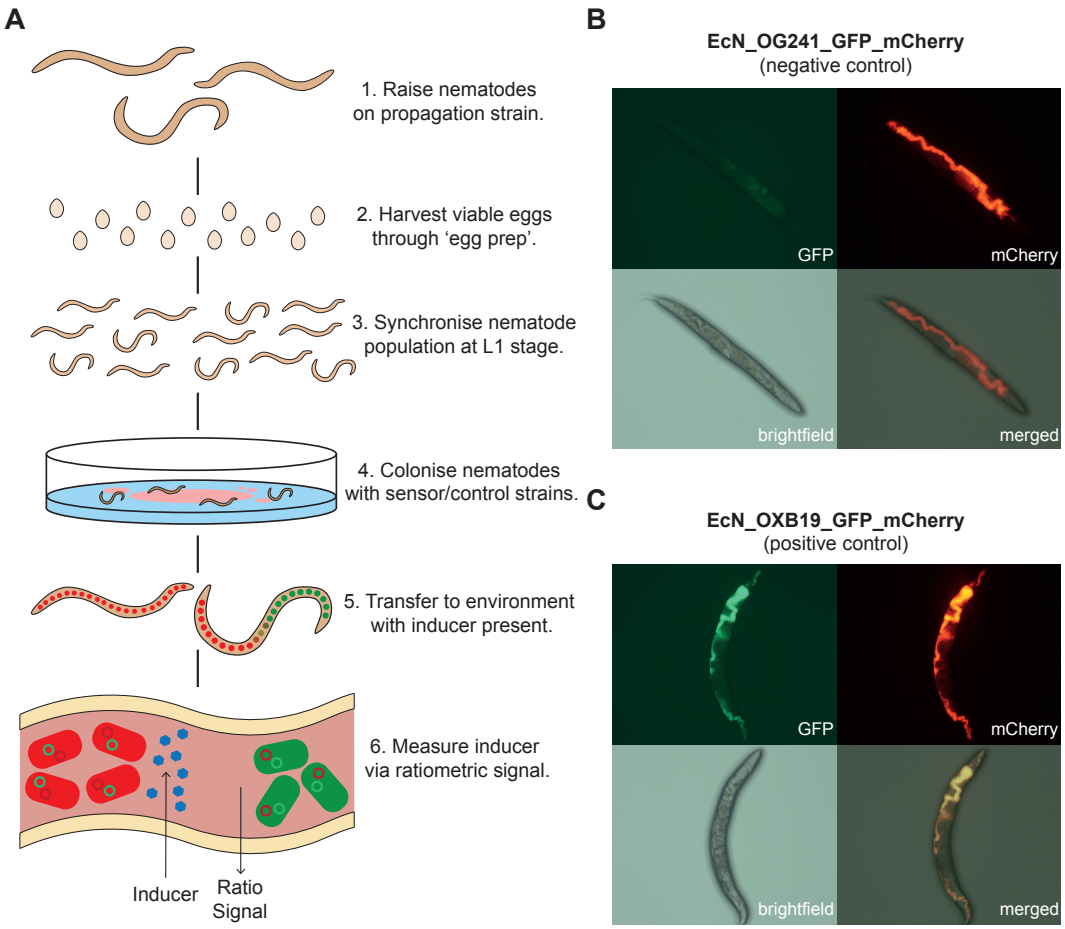

Figure 4.2: The experimental protocol developed for colonising *C. elegans* with engineered bacterial strains. (**A**) Colonisation protocol, microbe-free *C. elegans* are grown on the desired strain leading to colonisation of their digestive tracts. Representative images of *C. elegans* nematodes colonised with (**B**) the EcN_OG241 (negative control) strain, expressing mCherry and (**C**) the EcN_OXB19 (positive control) strain, expressing both GFP and mCherry. Panel labels refer to the imaging channel used.

4.3.2 Automating Image Analysis of *C. elegans*

After developing a robust colonisation protocol, an automated image pipeline was developed that could calculate the GFP:mCherry ratios of the *C. elegans* images rapidly, with minimal manual curation. This pipeline can be seen in Figure 4.3.

The pipeline included steps to compensate for GFP autofluorescence, a threshold to discard uncolonised worm images (this threshold was arbitrarily based on

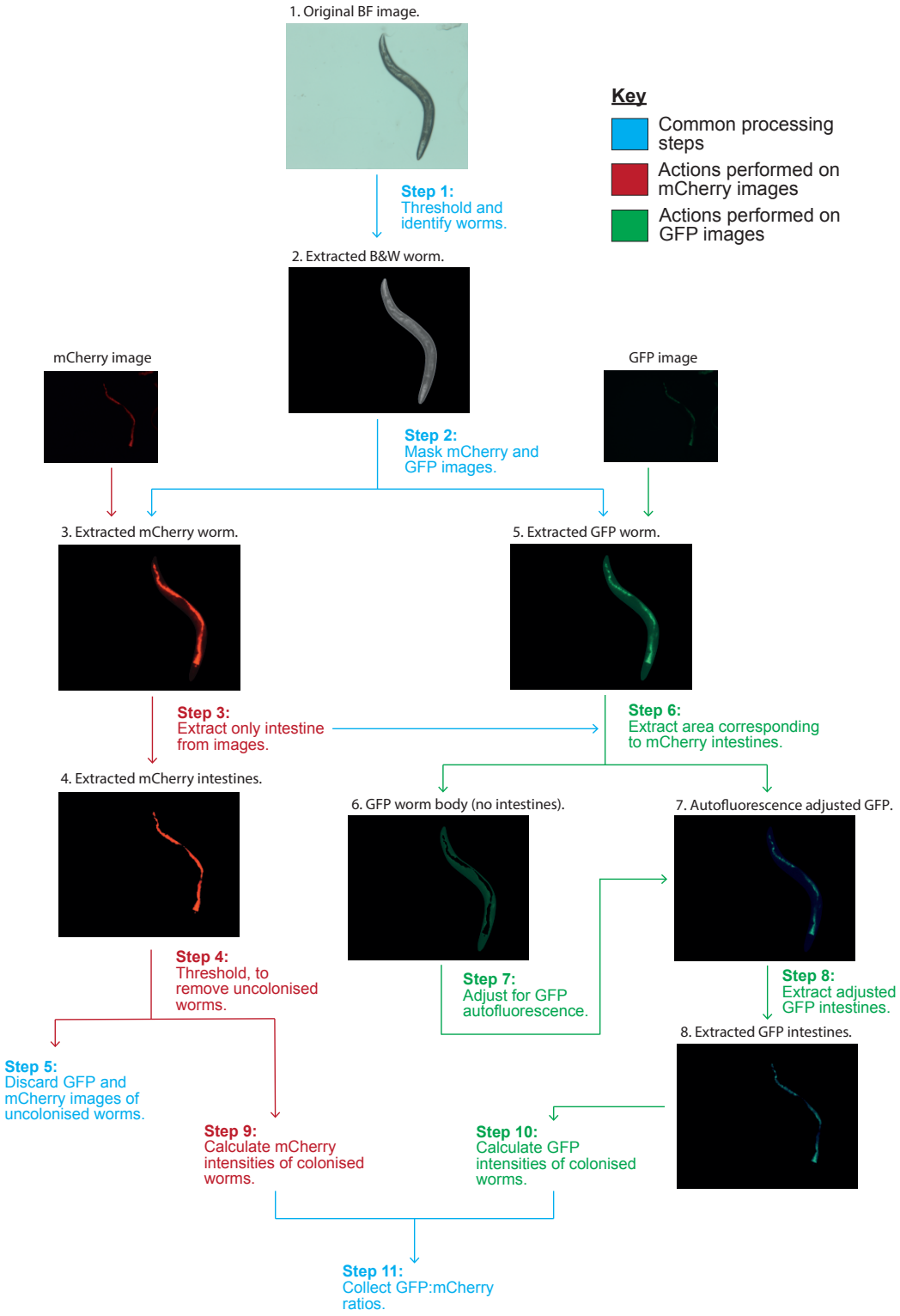

Figure 4.3: The automated pipeline developed for measuring ratiometric induction of the engineered bacterial biosensors, within the digestive tract of the *C. elegans* nematodes. The pipeline is able to extract the colonised worm body, discard uncolonised images and account for autofluorescence caused by the worm body. The final GFP:mCherry ratios for each image are then returned. BF = brightfield, B&W = black & white. (The brightness of these images has been adjusted to aid in viewing).

individual inspection of thresholded images) and background removal to prevent any external bacterial growth from influencing the final GFP:mCherry ratios. Further steps were added to exclude non-worm body objects from the masked images (for example, nematode eggs in the image). This protocol was originally tested on images collected by Tanel Ozdemir (Barnes Lab, UCL) the results of which can be seen in Figure 4.4. In addition, manual analysis of the EcN_pLac images seen in Figure 4.9 was also performed (ratios presented within Appendix A). From these comparisons it can be seen that the automated pipeline was able to measure GFP:mCherry ratios with performance equivalent to manual analysis, over a much shorter timeframe. As such, the protocol seen in Figure 4.3 was used to collect all subsequent *in vivo* GFP:mCherry ratios presented within this chapter.

4.3.3 *In vitro* Characterisation of an IPTG Inducible WCB

Following the development and validation of the *C. elegans* model protocols, attempts were made to use an engineered bacterial biosensor to capture changes in the *C. elegans* intestinal environment. As a proof of principle, the IPTG inducible EcN_pLac strain was chosen. Within this strain GFP expression was linked to IPTG exposure and constitutive mCherry expression used to calculate ratiometric induction. The circuit diagrams for this strain can be seen in Figure 4.5A.

In order to try and mimic the conditions of the *C. elegans* digestive tract, *in vitro* characterisation was performed at 20°C, alongside the standard 37°C (characterisation was also performed at 30°C to further explore the effect of temperature on the biosensor). From Figure 4.5 it can be seen that the EcN_pLac strain showed a ro-

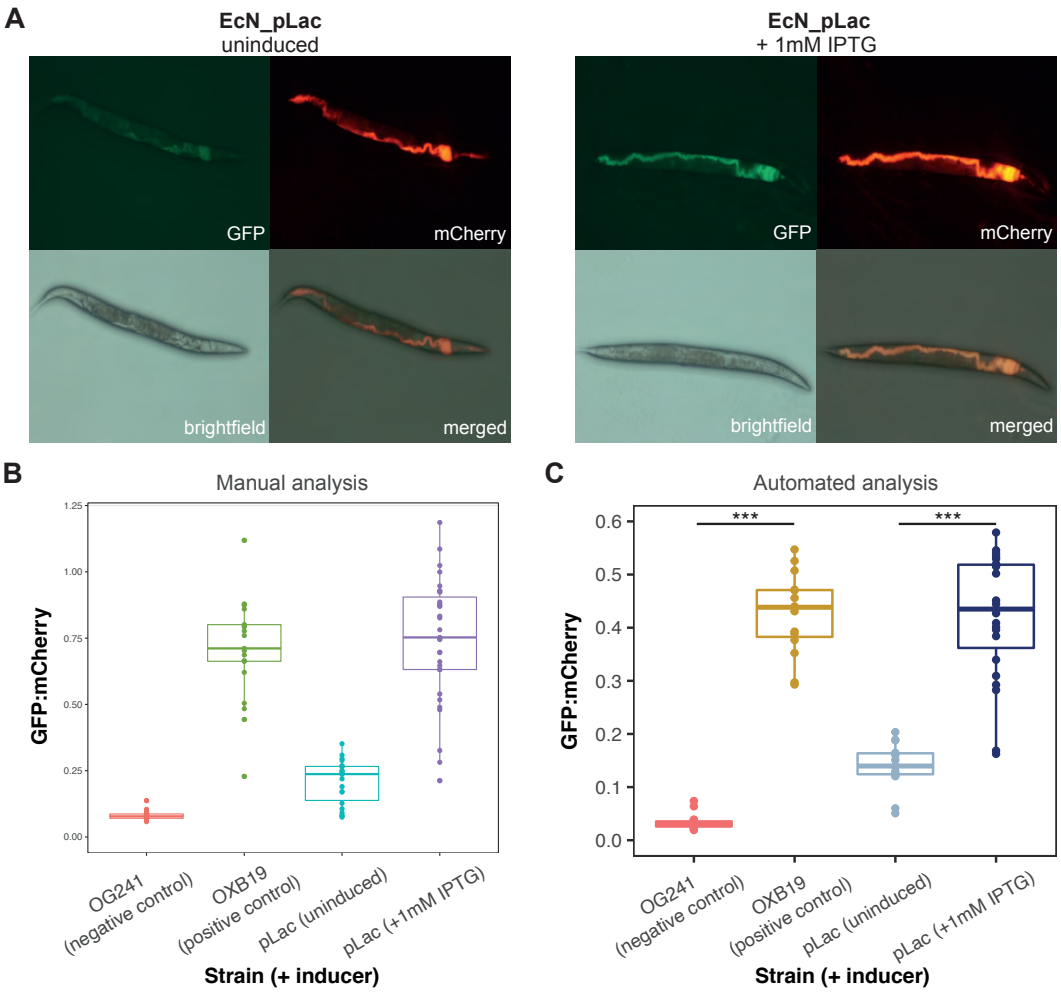

Figure 4.4: Comparison of the MATLAB pipeline ratios to ratios collected manually. (**A**) Example images (originally taken by Tanel Ozdemir of the Barnes lab) of colonised *C. elegans*, grown on strain and inducer together, used to test the automated image pipeline. (**B**) Ratios collected through manual analysis. (**C**) Ratios collected via the MATLAB pipeline. The manual and automated ratios collected from these images were found to display similar behaviours. ($n \geq 15$ images, p-value: *** < 0.05)

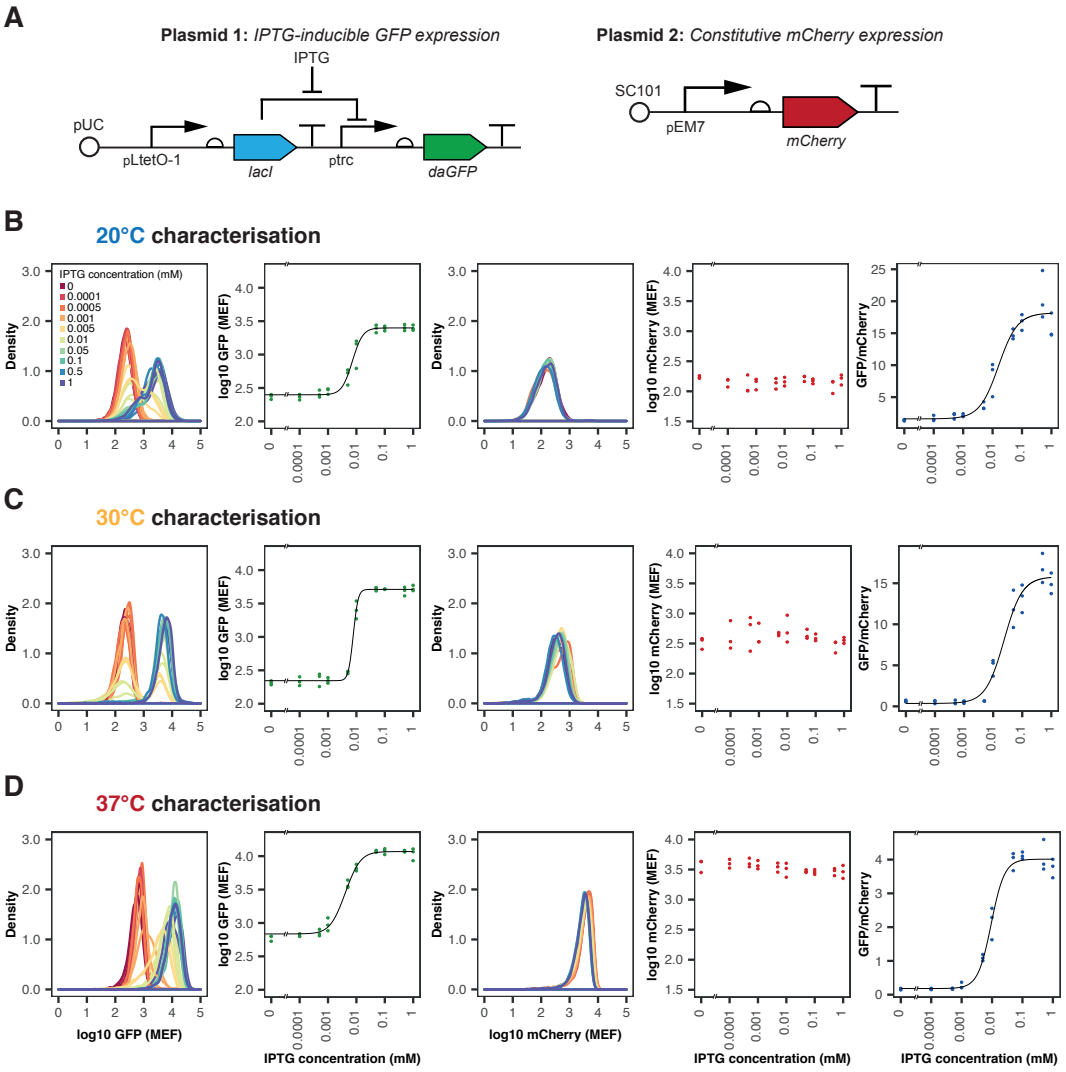

Figure 4.5: *In vitro* characterisation of the two plasmid EcN_pLac biosensor. (**A**) Circuit design of the two plasmids. (**B**) 20°C, (**C**) 30°C and (**D**) 37°C characterisation. From left to right: density plot of GFP induction, median GFP fluorescence, density plot of mCherry fluorescence, median mCherry fluorescence and GFP:mCherry ratios over all IPTG inducer concentrations. Flow cytometry data with 10 000 events. (n = 3 biological replicates)

bust increase in GFP:mCherry ratio upon induction of the dual-plasmid system at all three temperatures. Summaries of the fitted parameters are presented in Tables 4.1 and 4.2. This increase in the GFP:mCherry ratios was not seen in the EcN_OG241 or EcN_OXB19 control strains, at either temperature (Figure 4.6). Interestingly, it can be seen that both the $K_{1/2}$ and dynamic range were adversely affected at 20°C. This may be caused by slower growth and expression rates at 20°C. However, the linear range of the GFP:mCherry ratios was larger at 20°C than 37°C (Table 4.2). Overall these results showed that the EcN_pLac biosensor could be used to distinguish between a greater range of IPTG concentrations at 20°C.

Figure 4.7 provides *in vitro* timecourse data of the EcN_pLac biosensor. It should be noted that this data was collected by plate reader and could not be converted to MEF. As this data is presented as arbitrary units, it can not be quantitatively compared to the data in Figure 4.5. Furthermore, due to technical limitations of the plate reader 20°C could not be achieved, therefore the 'cold' timecourse was performed between 21-22°C. Firstly, it can be seen from Figure 4.7C that the addition of 1 mM IPTG did not significantly affect the growth rate of the EcN_pLac biosensor at either 20°C or 37°C. However, all samples grew more quickly at 37°C. In addition, during the initial hours of growth the GFP:mCherry ratios were heavily time dependent (Figure 4.7A). However, from around 8-9 hours post-induction the ratios remained fairly constant. This suggests that the biosensor requires a period of maturation before it can be used to reliably return a GFP:mCherry ratio. However, as the nematodes are colonised for 7 days before the biosensors are induced this should not be a problem *in vivo*.

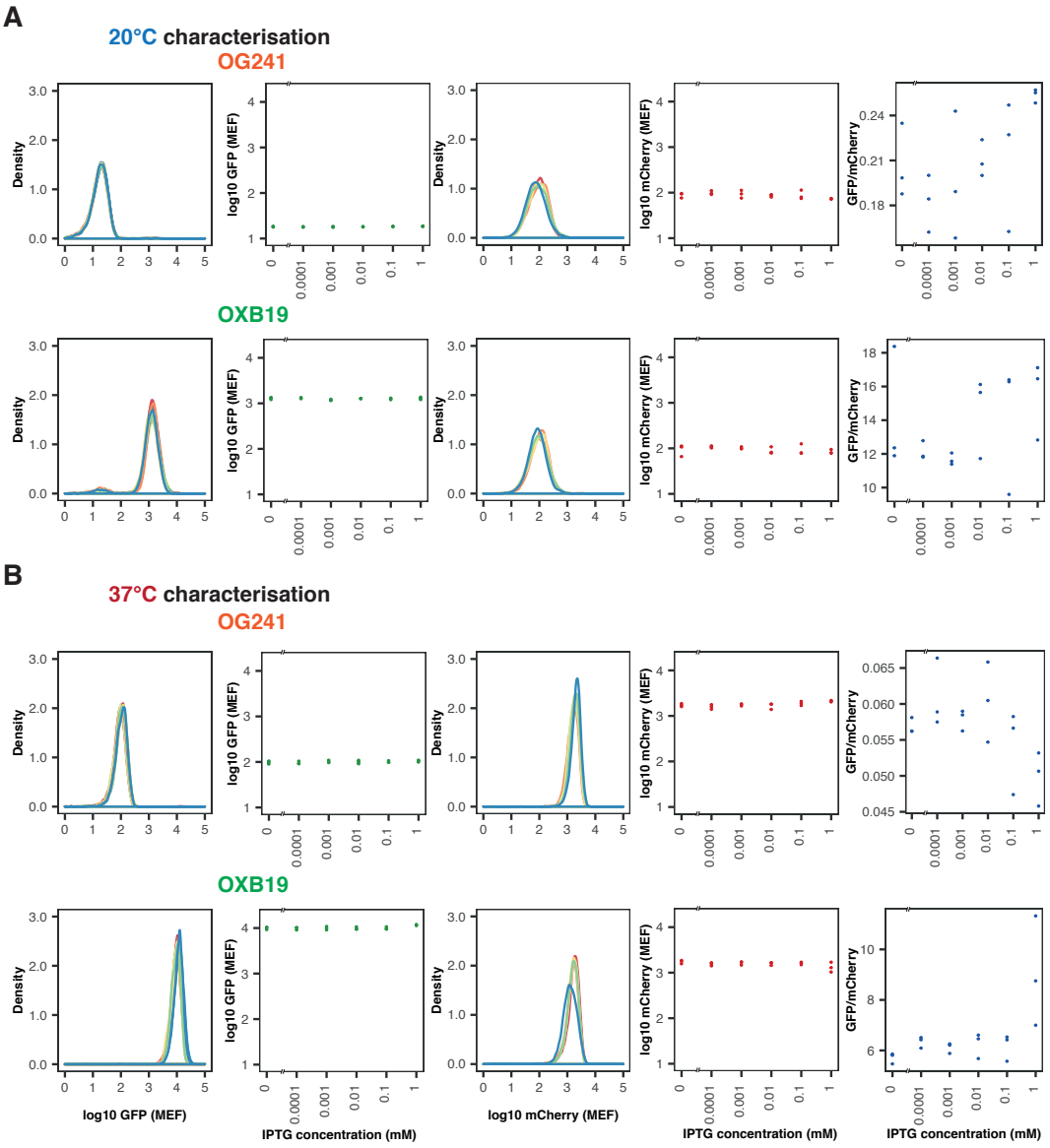

Figure 4.6: *In vitro* characterisation of the EcN_OG241 (promoterless GFP) and EcN_OXB19 (constitutive GFP) two plasmid, control strains. Characterisation at (**A**) 20°C and (**B**) 37°C. From left to right: density plot of GFP induction, median GFP fluorescence, density plot of mCherry fluorescence, median mCherry fluorescence and GFP:mCherry ratios over all IPTG inducer concentrations. Flow cytometry data with 10 000 events. (n = 3 biological replicates)

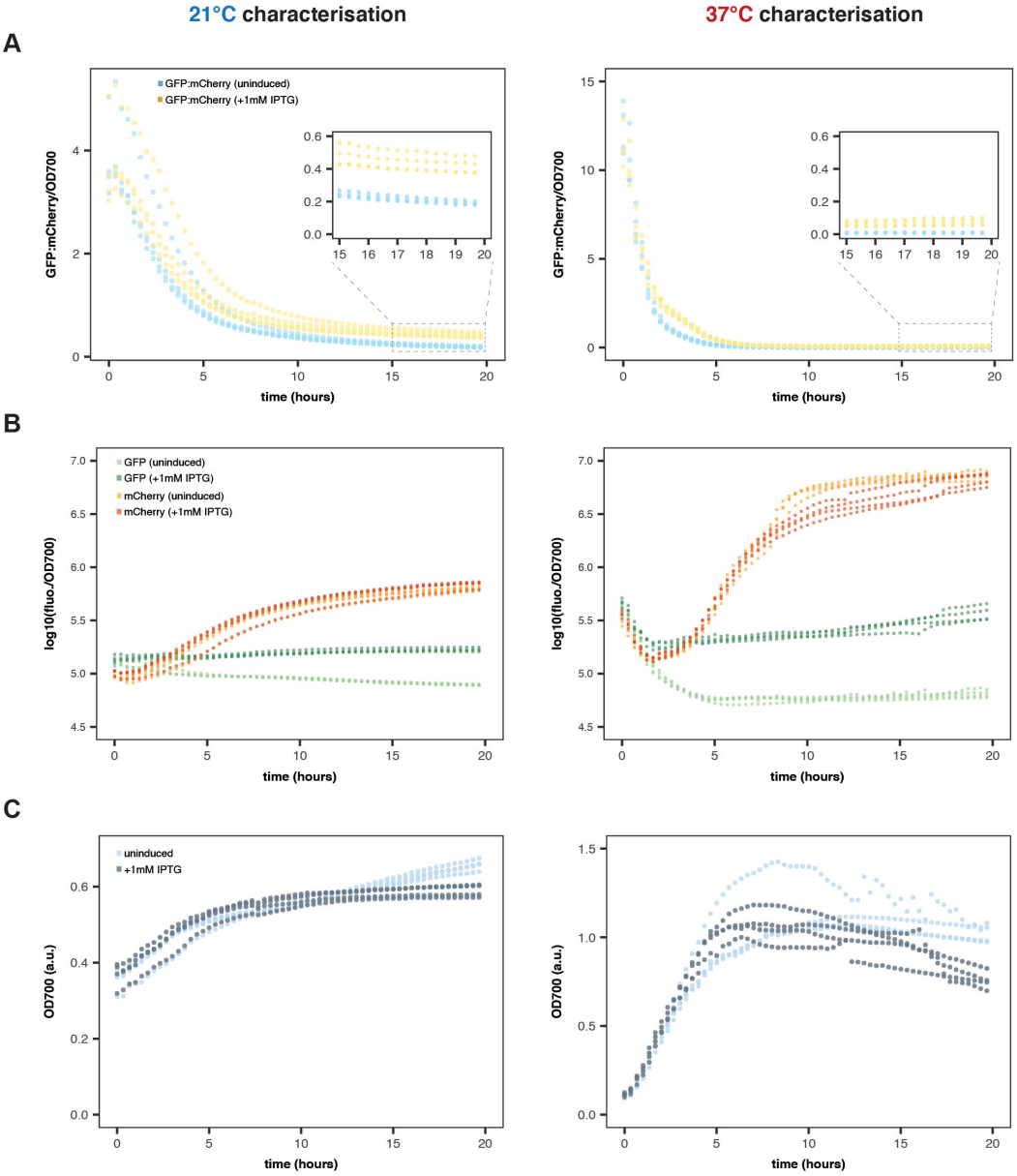

Figure 4.7: *In vitro* timecourse data of the two plasmid EcN_pLac biosensor. Left column: incubation at 21°C, right column: incubation at 37°C. (**A**) GFP:mCherry ratios of cells divided by measured cell OD, inlay shows close up of highlighted area. (**B**) GFP and mCherry fluorescence of cells and (**C**) OD_{700} of cells. (n = 3 biological replicates, circles give individual datapoints)

Table 4.1: Hill parameter fitting to flow cytometry data showing the GFP induction curves of the IPTG dual plasmid biosensor, for 20°C, 30°C and 37°C (fitted values ± SE, given to 3 s.f.).

Parameter	**20°C**	**30°C**	**37°C**
f^{min} (MEF)	250±60.9	221±104	685±254
f^{max} (MEF)	2510±64.6	5150±104	11700±269
$K_{1/2}$ (mM)	0.0112±0.00117	0.0101±0.000312	0.00868±0.000760
n	2.61±0.0828	5.94±4.55	1.88±0.379
dynamic range (MEF)	9.02	22.3	16.1
operating range (mM)	0.0347	0.0146	0.0341

Table 4.2: Hill parameter fitting to flow cytometry data showing the GFP:mCherry ratio curves of the IPTG dual plasmid biosensor, for 20°C, 30°C and 37°C (fitted values ± SE, given to 3 s.f.).

Parameter	**20°C**	**30°C**	**37°C**
f^{min}	1.60±0.603	0.353±0.392	0.182±0.0741
f^{max}	18.2±0.838	15.8±0.584	4.01±0.0794
$K_{1/2}$ (mM)	0.0159±0.00347	0.0237±0.00375	0.00939±0.000702
n	1.35±0.302	1.38±0.203	1.98±0.348
dynamic range	10.4	43.7	21.1
linear range (mM)	0.0729	0.107	0.0357

Furthermore, it can be seen that the timecourse data qualitatively reinforces the flow cytometry data. Both the final uninduced and induced ratios of the EcN_pLac biosensor were higher at 20°C than 37°C. This supports the fitted values for f^{min} and f^{max} provided in Table 4.2. Overall, this shows that the EcN_pLac biosensor was capable of reporting on environmental IPTG concentrations across a range of temperatures.

4.3.4 *In vivo* Characterisation of an IPTG Inducible WCB

Following *in vitro* characterisation, nematodes were colonised with EcN_pLac and exposed to environments containing various amounts of IPTG. The worms were then imaged to see if the GFP:mCherry ratiometric signal could be used to record

changes in the intestinal environment. As referred to in section 4.3.1, not all nematodes were found to be colonised upon imaging. Using the pipeline presented in Figure 4.3, around 17% of the nematode images from this experiment were discarded based on the mCherry threshold (Figure 4.8). However, the presented pipeline provides a method for easily identifying and removing these images without the need for extensive manual curation. An example of an uncolonised image is presented within Figure 4.8.

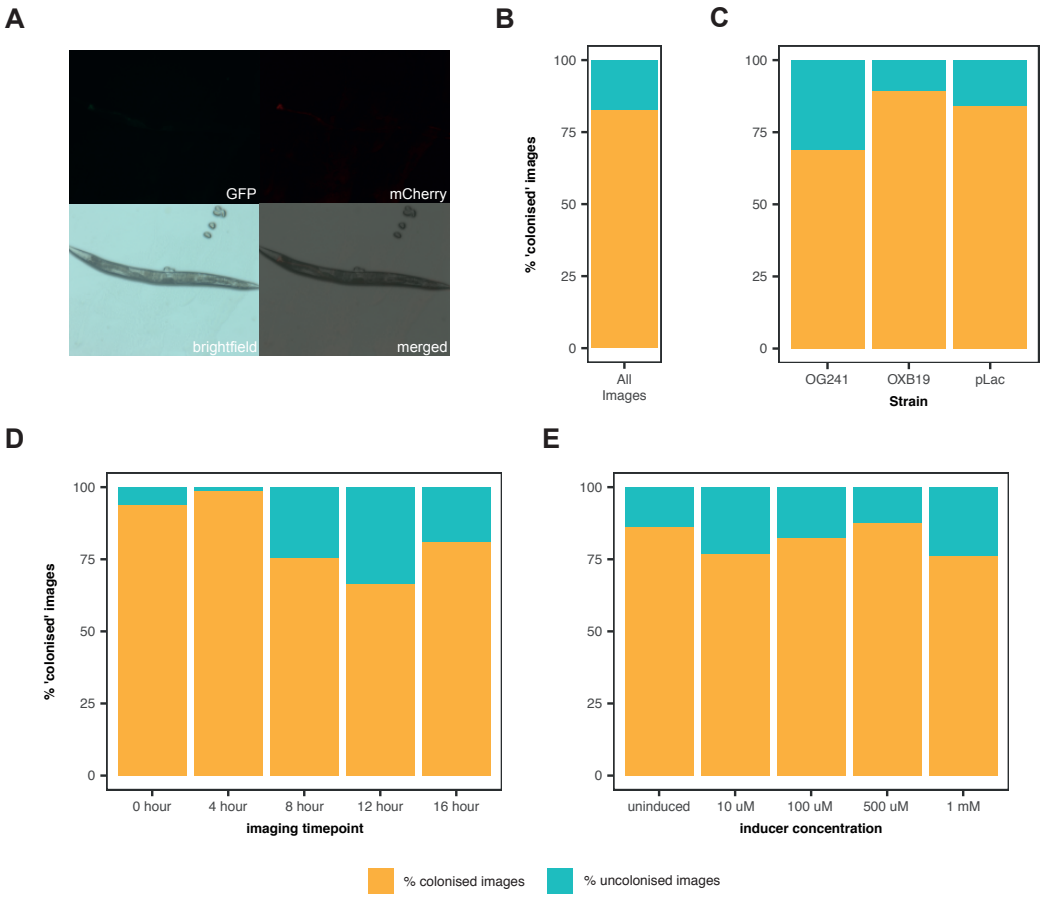

Figure 4.8: (**A**) Example image of a nematode which did not show mCherry fluorescence above the mCherry threshold and was therefore excluded during automated image analysis. Percentage of images which were kept ('colonised') or excluded ('uncolonised') during automated image analysis, for (**B**) all images, (**C**) images split by strain, (**D**) images split by timepoint, (**E**) images split by inducer concentration.

From Figure 4.9A it can be seen that the GFP:mCherry response of EcN_pLac increased in both a time and dose-dependent manner. An increase in GFP:mCherry was seen in as little as 4 hours, for only 10 μM IPTG. This was consistent with *in vitro* characterisation (see Figure 4.5B). No substantial changes in GFP:mCherry ratio were seen for the EcN_OG241 or EcN_OXB19 control strains, with or without IPTG inducer (Figure 4.10).

4.3.5 *In vitro* Characterisation of a Propionate Inducible WCB

The propionate inducible EcN_pProE strain was chosen as a promising candidate for exploring the capabilities of the *C. elegans* model. This is because propionate is a molecule that commands interest in both human health and nematode biology (as discussed in section 4.4.2). This biosensor was based on the *prp* operon shown in Figure 4.11; where propionate is converted to 2-methylcitrate (2-MC), which subsequently triggers transcription of the *prp* operon via the PrpR regulator.

As with the EcN_pLac biosensor (section 4.3.3), EcN_pProE was characterised *in vitro* at 20°C and 37°C. However, as the EcN_pProE biosensor had already been characterised within the Barnes lab this was performed after the *in vivo* characterisation [132]. The EcN_pProE strain showed an increase in GFP fluorescence with increasing propionate induction. Interestingly at 37°C, mCherry remained constant despite propionate induction, except for when exposed to very high concentrations of propionate (50 and 100mM), where mCherry fluorescence dropped. This may be due to the fact that propionate inhibits growth of the cells at higher concentrations. In addition, at 20°C mCherry was found to fluctuate with changing propionate lev-

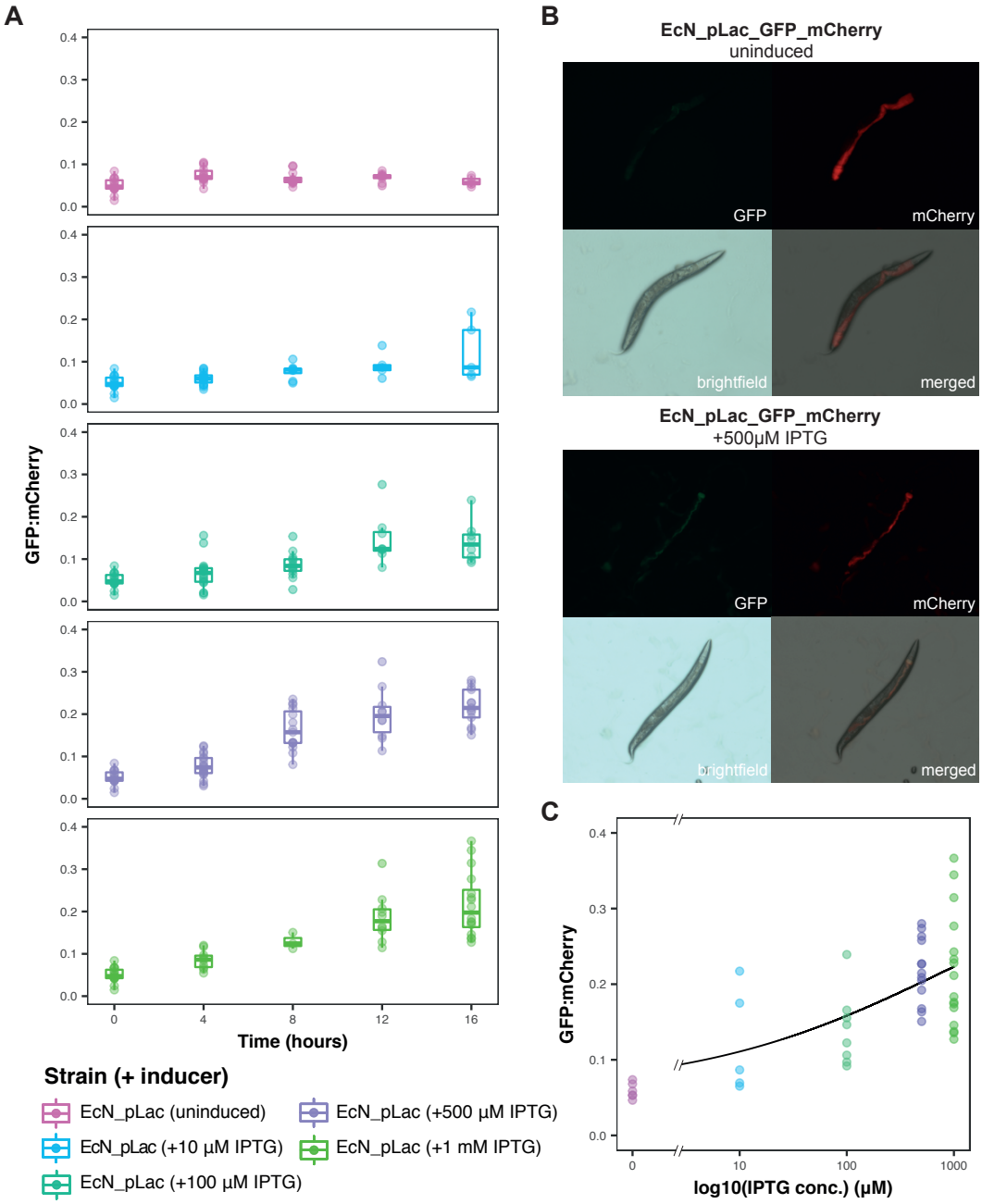

Figure 4.9: Full characterisation of the EcN_pLac biosensor *in vivo*. (**A**) Timecourse of GFP:mCherry ratios in individual 7 day old *C. elegans* worms, grown on EcN_pLac sensor strain and transferred to inducer plates supplemented with varying IPTG concentrations. (n $\geq$ 4 images). (**B**) Representative images of nematodes colonised with the EcN_pLac biosensor strain. The top panel shows an uninduced nematode and the bottom induction with 500μM IPTG. (**C**) Induction of the EcN_pLac biosensor with various IPTG concentrations at the 16 hour timepoint, the GFP:mCherry ratios have been fit with a Hill function.

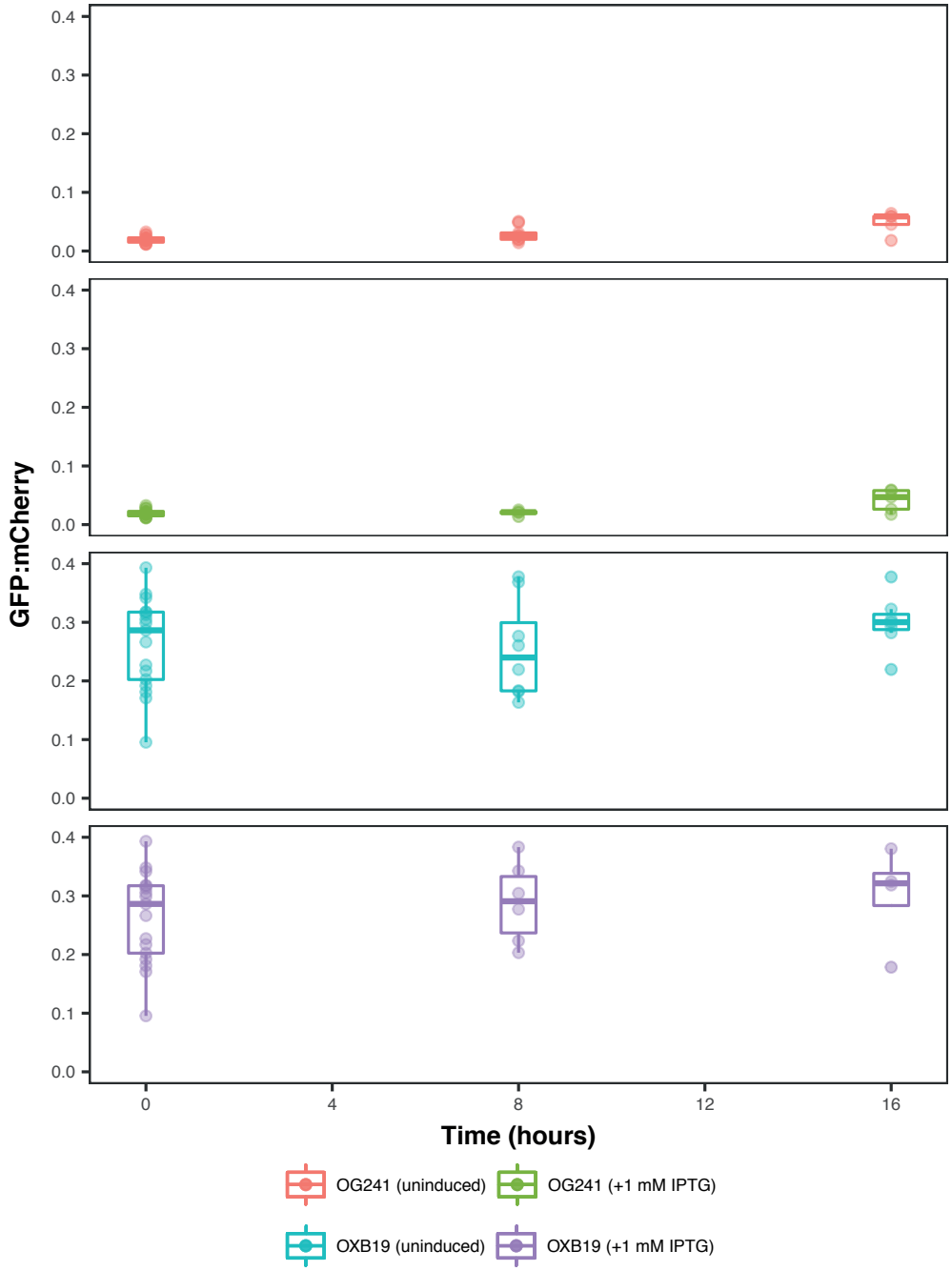

Figure 4.10: Characterisation of the EcN_OG241 (top) and EcN_OXB19 (bottom) control strains within the *C. elegans* digestive tract. Both with and without exposure to IPTG. (n $\geq$ 4 images).

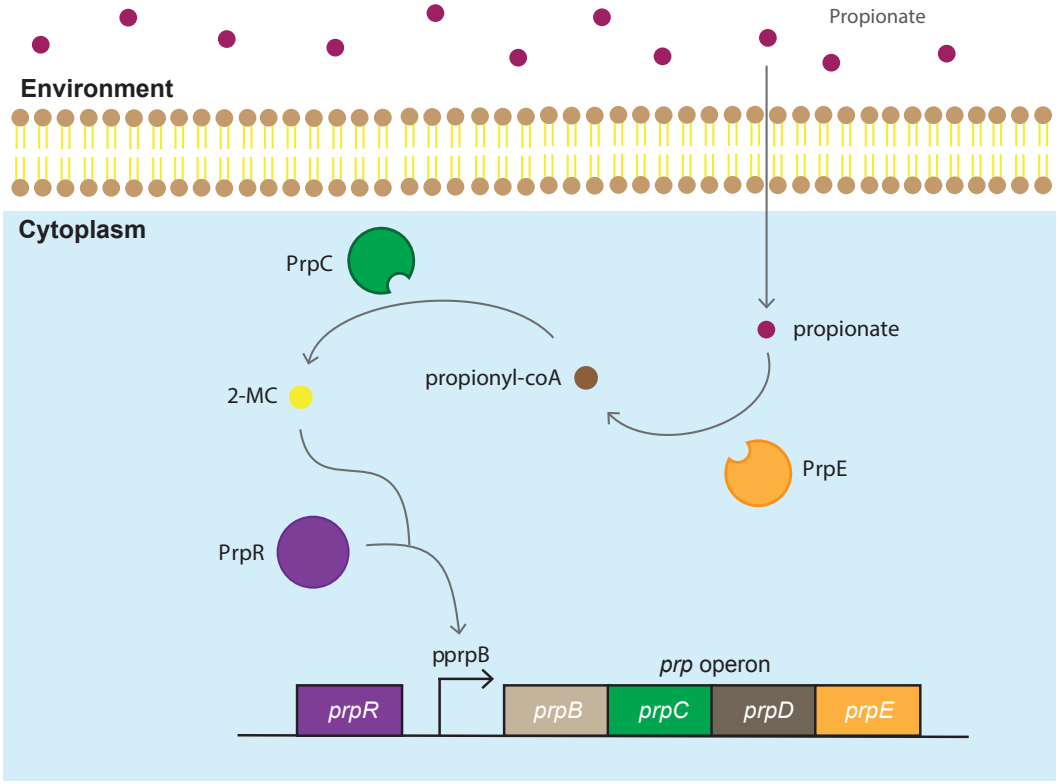

Figure 4.11: Layout of the *prp* operon, involved in propionate sensing. Propionate is converted to 2-methylcitrate (2-MC), via genes from the *prp* operon, which triggers expression from the pprpB promoter.

els.

Unfortunately, the data for this characterisation could not be converted to MEF. However, an increase in GFP production was seen with increasing levels of propionate, at 37°C, (Figure 4.12C). This increase in GFP production was also seen to a smaller extent at 20°C (Figure 4.12B). The fitted values for this induction are given in Table 4.3. However, it should be noted that the full induction curves could not be captured; as GFP induction continued beyond toxic levels of propionate. Despite some of the issues with the EcN_pProE performance, due to previous characterisation performed within the Barnes lab [132], attempts were made to try and stimulate expression from the biosensor within the *C. elegans* digestive tract.

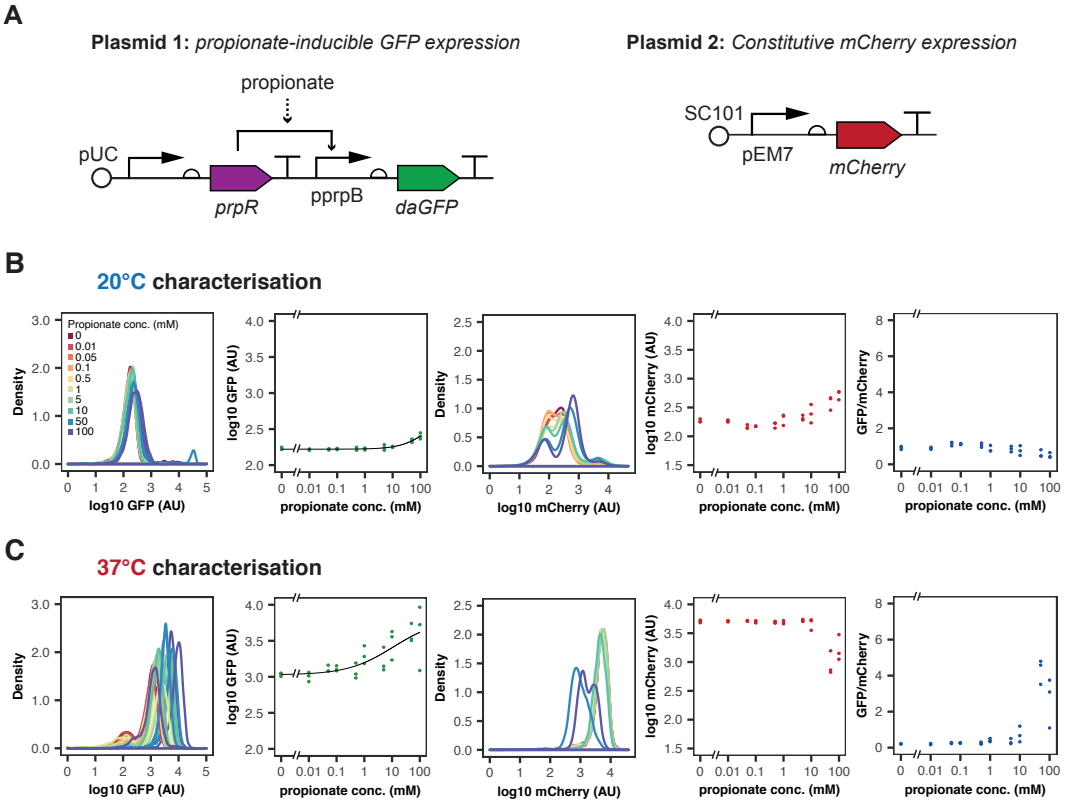

Figure 4.12: *In vitro* characterisation of the two plasmid EcN_pProE biosensor. (**A**) Circuit design of the two plasmids (the dashed arrow indicates intermediate steps have been omitted). (**B**) 20°C and (**C**) 37°C. From left to right: density plot of GFP induction, median GFP fluorescence, density plot of mCherry fluorescence, median mCherry fluorescence and GFP:mCherry ratios over all IPTG inducer concentrations. Flow cytometry data with 10 000 events. (n=3)

Table 4.3: Hill parameter fitting to flow cytometry data of the GFP induction curves for the propionate dual plasmid biosensor, at 20°C and 37°C (fitted values ± standard error, given to 3 s.f.).

Parameter	**20°C**	**37°C**
f^{min} (AU)	166±1.01	1060±1.21
f^{max} (AU)	552±5.95	6350±3.42
$K_{1/2}$ (mM)	200±558	11.2±32.8
n	0.893±0.381	0.527±0.448
dynamic range	0.235	4.97

4.3.6 *In vivo* Characterisation of a Propionate Inducible WCB

The EcN_pProE biosensor was characterised *in vivo* using the protocol presented in Figure 4.2 and exposing nematodes to propionate. During exposure the nematodes

were able to survive propionate concentrations up to 50 mM. However, the nematodes exposed to 100 mM propionate were found to be dead on imaging (Figure 4.13). This was consistent with previously reported toxicity levels, where the LD_{50} of propionate for *C. elegans* was found to be ∼80 mM [160]. Representative images of uninduced and induced nematodes, colonised with the EcN_pProE biosensor can be seen in Figure 4.14. The corresponding GFP:mCherry ratios are provided within Figure 4.15.

Significantly higher GFP:mCherry ratios were found for nematodes induced with 10 to 50 mM propionate, when compared to uninduced nematodes. This suggests that the EcN_pProE biosensor was capable of recording changes in propionate concentration within the *C. elegans* digestive tract. Images collected for nematodes exposed to 100 mM propionate were excluded from this analysis, as the majority of worms were found to be dead before imaging.

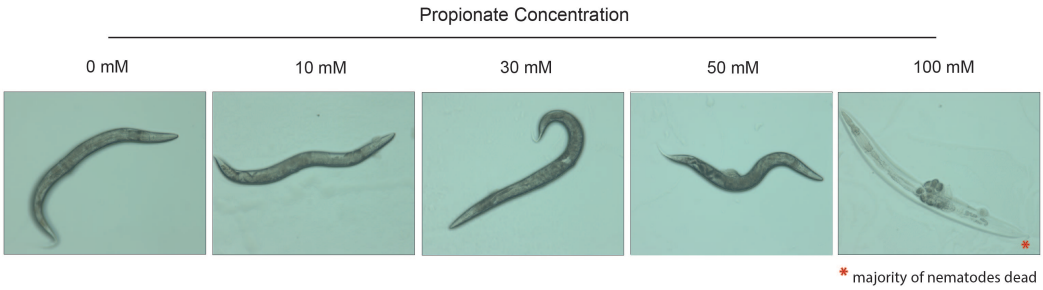

Figure 4.13: Representative nematode images, after induction on the propionate plates. The nematodes were able to survive propionate conditions up to 50 mM, but were dead on imaging when exposed to 100 mM propionate (red symbol indicates majority of nematodes were dead).

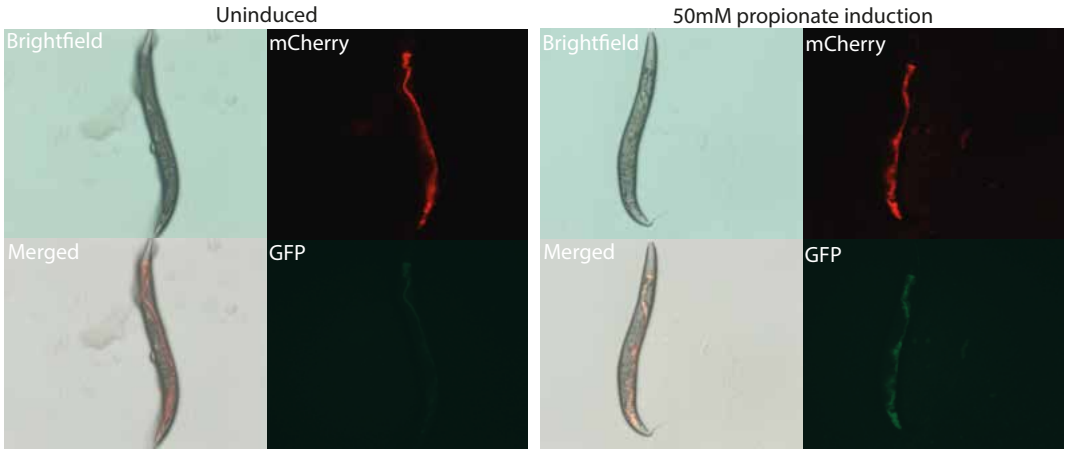

Figure 4.14: Example images of *C. elegans* colonised with the EcN_pProE biosensor strain, both uninduced (left) and induced (right). The images were taken after a 16 hour induction period, the panel labels refer to the imaging channel used to collect the images.

4.4 Discussion

4.4.1 A Promising Alternative Model to Mice in Synthetic Biology Studies

As discussed in section 4.1.1 the mouse is currently one of the most widely adopted models in microbiota and synthetic biology studies. Despite its widespread use, results obtained from this model are not always directly translatable to humans. One example is the *Lactobacillus rhamnosus* strain that has been shown to reduce stress-related behaviours in a mouse model. However, when tested in male humans no corresponding effects were observed [161]. Examples such as this highlight the requirement for further model systems that can supplement our understanding of host-microbe interactions. The *C. elegans* model is able to provide researchers with one such alternative to the standard mouse model.

It should be stressed that the intention of this *C. elegans* model is not to fully

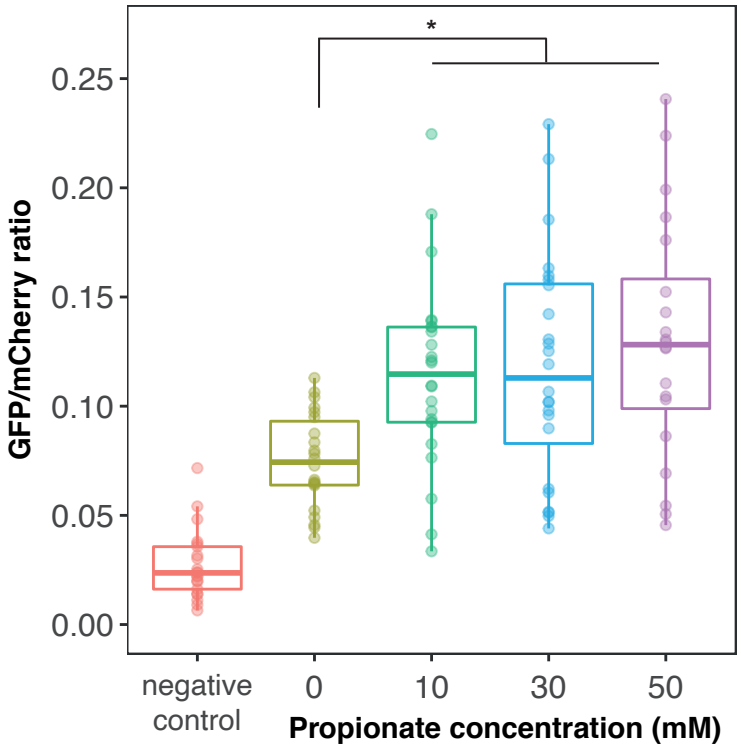

Figure 4.15: Characterisation of the EcN_pProE biosensor (propionate inducible) within the intestines of *C. elegans*. The boxplots show the EcN_OG241 (-ve control) strain, alongside the EcN_pProE strain induced with varying concentrations of propionate. (n $\geq$ 17 images, p-value: * $<$ 0.05).

replace current models within synthetic biology, but rather act in conjunction with them to further our ability to predict and characterise the behaviour of engineered bacterial strains. The model should facilitate a reduction in the number of vertebrate animals used during microbiome and synthetic biology studies; while also supporting the 'design-build-test-learn' cycle that is fundamental to synthetic biology. Subsequently, this should help to cut down on the amount of space, time and funding required to carry out complex microbiome engineering and synthetic biology studies.

4.4.2 Evaluating the *in vitro* and *in vivo* Performance of the Engineered WCBs

The results contained within this chapter provide a proof of principle that the developed protocols can be used to characterise the behaviour of a bacterial WCB *in vivo*. Protocols were developed that allow for the colonisation of *C. elegans* with specific EcN strains and subsequently an imaging pipeline, which was able to quickly measure GFP:mCherry fluorescence expressed within the *C. elegans* digestive tract. Furthermore, through automating the image processing workflow it was possible to minimise any operator variation. However, it should be noted that the image pipeline was not able to distinguish between multiple nematodes within a single image; instead returning a single ratio for the whole image. This may be improved in future, by adding steps that are able to threshold and isolate multiple worm bodies within a single image. A ratiometric reporter for the biosensor strains was chosen over absolute induction as this is considered more robust to changes in dynamic environments and allowed for measuring of *in vivo* biosensor induction, independent of differences in cell count [162]. Ratiometric analysis is also thought to help reduce variation in results collected across multiple experiments or between institutions [163].

Following the creation of these protocols, an IPTG inducible biosensor was used to show that the model allows for the detection and reporting of changes in the *C. elegans* intestinal environment. Although not clinically relevant, IPTG is commonly used as an inducer for synthetic biology circuits (discussed further within chapter 5). The *in vitro* characterisation presented in Figure 4.5 highlighted differ-

ences in biosensor performance across incubation temperatures. However, despite these differences, it was clear that the biosensor was capable of detecting changes in IPTG exposure at a temperature commensurate with that of the *C. elegans* digestive tract. Subsequent *in vivo* characterisation confirmed that changes in the intestinal environment could be reported on in both a time and dose-dependent manner. From the data presented in Figure 4.8 no clear correlation was found between the % of colonised images and either bacterial strain, imaging timepoint or inducer concentration. This suggests that the efficiency of colonisation is most likely determined by factors not involved in the induction process. One possible factor may be the length of the colonisation period prior to induction, which could be explored further in future by using alternatives to the 7 day colonisation period used here.

During the *in vivo* analysis, it was also observed that the uninduced ratios of EcN_pLac were higher than those of the EcN_OG241 control strain (Figures 4.9 and 4.10). This was also seen during *in vitro* characterisation (Figures 4.5 and 4.6). Therefore, it is likely that this 'leaky' expression is an intrinsic feature of the pLac plasmid; rather than caused by an environmental factor present in the *C. elegans* digestive tract. This is not a desirable trait for a biosensor and could be addressed in future attempts to improve EcN_pLac performance. Mannan et al. reported that increasing TF to operator affinity was able to suppress basal expression within TF biosensors with a repressed-repressor architecture, such as the pLac plasmid [122]. A similar approach could be employed here to try and reduce the observed levels of EcN_pLac basal expression.

The EcN_pLac biosensor could also be used in future studies to produce tar-

geted expression of specific compounds within the *C. elegans* digestive tract; similarly to how an aTc inducible system was used within a previous mouse study [164]. Another recent study showed that a *Providencia* species is able to modulate host *C. elegans* sensory behaviour [165]. The authors showed that this effect was conferred through bacterially produced tyramine within the *C. elegans* digestive tract [165]. Interesting future work could involve using the EcN_pLac biosensor to produce targeted expression of tyramine within the *C. elegans* gut. This would provide an insight into whether similar changes in host behaviour can be modulated through engineered *E. coli* strains.

After the IPTG-inducible biosensor, the developed protocols were repurposed to begin characterisation of a propionate-inducible biosensor. For humans, propionate is one of the major by-products of anaerobic fermentation in the gut [166]. It is also a SCFA, the importance of which is discussed further within chapter 2. Humans rely on a vitamin B12-dependent pathway for the breakdown of excess propionate. Mutations in the PCCA or PCCB genes of this pathway can lead to the on-set of propionic-acidemia [167]. A condition that can lead to vomiting, seizures, lethargy and pancreatitis [168]. The build up of excess propionate is also toxic to *C. elegans*, with the N2 strain displaying an LD_{50} of 80 mM [160]. Interestingly, deletion of the *pcca-1* gene in *C. elegans* leads to a phenotype similar to that seen with propionic-acidemia; with the Δ*pcca-1* strain showing an LD_{50} of 45 mM [160]. Subsequently, it has been suggested that this strain may be able to act as a disease model for propionic-acidemia [169]. Therefore, the propionate inducible EcN_pProE biosensor strain seemed a logical choice for further exploring the poten-

tial and limitations of the *C. elegans* host-microbe model. A propionate biosensor previously constructed within the Barnes lab was chosen for this [132]. The circuit diagrams for the EcN_pProE dual-plasmid strain can be seen in Figure 4.12. The results collected showed that an increase in GFP:mCherry ratios were found for *C. elegans* exposed to concentrations of propionate between 10-50 mM.

As with the EcN_pLac biosensor, the uninduced ratios of EcN_pProE were found to be higher than the ratios of the EcN_OG241 control (Figure 4.15). This suggests that this biosensor also has some basal level of leakiness, in a similar manner to the EcN_pLac strain, despite not sharing the repressed-repressor TF architecture. The addition of 10 mM propionate resulted in a significantly higher GFP:mCherry ratio than the uninduced nematodes (Figure 4.15). However, there was little difference in GFP:mCherry ratios between the 10, 30 and 50 mM inducer concentrations. This was in contrast to the behaviour of the EcN_pLac biosensor that exhibited a concentration dependent increase in GFP:mCherry ratio (see Figure 4.9C). One possible explanation for this is that the biosensor is already fully induced at a concentration of 10 mM; however, this was not supported by the *in vitro* characterisation. Therefore, it could be possible that the EcN_pProE biosensor may be recording the presence of propionate produced within the *C. elegans* host, which is raising propionate levels above the threshold needed for induction. As mentioned within the section 4.3.5, the EcN_pProE biosensor did not appear to work as anticipated at 20°C. Therefore, this will need to be addressed before any firm conclusions can be drawn from the *in vivo* characterisation of EcN_pProE. In future, the protocols presented here may be further adapted to gain insights into the

in vivo behaviour of other engineered biosensors.

4.4.3 The Potential to Gain Insights into Host-Microbe and Nematode Biology

Alongside, offering a model to characterise engineered microbial strains, the protocols developed here could be used to improve our knowledge of host-microbe interactions and nematode biology. Within the nematode field there is some debate over whether *E. coli* becomes dormant and acts purely as 'food' when ingested by *C. elegans* (insight from colleagues). The presented data, along with previously published data [159], provides evidence that this is not the case. Instead, the EcN strains remained active and were able to respond to environmental cues in a dynamic manner up to 7 days after colonisation. This paves the way for future studies that investigate the interactions between *C. elegans* and *E. coli* in greater detail.

Another study, published by Vega and Gore (2017), used fluorescently labelled bacteria to show the role that stochasticity plays in the formation of microbial communities within the *C. elegans* digestive tract [170]. Both the colonisation protocols and imaging pipeline reported here would readily lend themselves to similar studies, with relatively little modification. For example, the segmentation of additional fluorescent channels, alongside mCherry and GFP, could be included within the imaging pipeline to allow for rapid image processing in future experiments exploring the competition of bacterial strains within the *C. elegans* digestive tract.

4.5 Future Work

The results collated within this chapter open up a number of avenues for future exploration. Initially, it would be interesting to further investigate the effect that temperature has on the *in vitro* performance of the ratiometric EcN biosensors reported here. Alternatively, the efficiency of *C. elegans* colonisation (shown in Figure 4.8) could be investigated through using a range of colonisation periods. This could help to provide some insight into the initial formation and stability of microbial communities within the *C. elegans* digestive tract.

Another exciting direction for future work would be to attempt to use the EcN_pLac biosensor to produce targeted expression of a therapeutic or active molecule within the digestive tract. By replacing the current GFP output with a molecule such as tyramine (which has been shown to influence *C. elegans* sensory decisions) attempts could be made to modulate host nematode behaviour through the action of engineered bacterial strains [165].

Finally, as mentioned previously, this model could be used to characterise other bacterial biosensors. Possible candidates for this characterisation could be lactate or acetoacetate inducible biosensors. Another option would be to record the production of a host-derived metabolite within the digestive tract. This would involve developing a sensor for a metabolite that is known to be secreted into the *C. elegans* intestinal lumen. In addition, it should be noted that the characterisation reported here was performed under tightly-controlled conditions. It is possible that changes other than inducer concentration may impact on the GFP:mCherry ratios collected, within a less tightly controlled environment. Future work could explore the im-

pact of environmental conditions (for example media composition) on *in vivo* WCB behaviour in more detail.

4.6 Summary

The *C. elegans* nematode has not been widely used in synthetic biology studies. However, the results presented within this chapter highlight that it can be a simple, yet useful, model for characterising the performance of engineered bacterial strains. The protocols developed here have shown that WCBs can be used to report on changes *in vivo* within the *C. elegans* digestive tract. In future the *C. elegans* model may be used to further characterise other engineered bacterial strains. It is also possible that this work will further open up the possibility of using WCBs to explore the biology of nematode host-microbiota interactions (through both sensing and manipulation).

Chapter 5

Construction of a Whole-Cell Biosensor Platform for Improved Ratiometric Reporting and Plasmid Stability

Contents

5.1 Background

5.1.1 Plasmid Components

When designing plasmid-based circuits there are many components that can be tailored to engineer specific behaviour. These components include the selection mechanism, plasmid origin, promoters, sensing mechanism and output/reporter signals. All of these components can have an effect on biosensors, including parameters such as f^{min}, dynamic range and $K_{1/2}$ (discussed within section 2.4.3). For an in-depth review of these components and the other considerations that go into designing plasmid-based biosensors see Wen et al. (2019) [127].

5.1.2 Plasmid Stability

As mentioned previously, the genetic elements within this project are incorporated in strains on plasmids; this gives greater control over design aspects such as copy number. However, it is not a trivial task to ensure that plasmids remain within cells and over time plasmid bearing cells will become diluted and lost from the community [171]. This may be particularly problematic for strains that are designed to operate over prolonged periods, or for plasmids that place a high burden on the host cell. These include large plasmids, high-copy plasmids or plasmids that encode large amounts of constitutive expression [172, 173].

There are several methods that can be employed to help reduce plasmid loss. One of the most common methods is to use antibiotic selection; however, this is not suitable for use in a clinical setting- due to fears over the spread of antibiotic resistance and adversely disrupting the native microbiota [174–176]. Therefore,

during design of the new ratiometric plasmids in this chapter an additional post-segregational-killing (PSK) mechanism that may be used to help prevent plasmid loss was added.

This PSK mechanism was based on the Axe-Txe (AT) system, shown in Figure 5.1. The AT system was originally isolated from *Enterococcus faecium*, with the Txe protein shown to prevent cell growth via RNase activity, similar to the YoeB toxin [177]. The AT-bearing plasmid encodes both proteins of the AT system, the long-lived Txe toxin and short-lived Axe antitoxin (Figure 5.1B) [178]. Upon loss of the plasmid the antitoxin is no longer produced and the toxin is no longer neutralised, resulting in inhibited growth of the host cell [178]. This allows post-segregational killing of any non-plasmid bearing cells. In the study by Fedorec et al., the AT system was found to stabilise a plasmid bearing population over 30 passages; outperforming both the current standard Hok-Sok system and a microcin-V based stability system [171]. Therefore, this system was chosen as a promising candidate for stabilising the ratiometric biosensors constructed here.

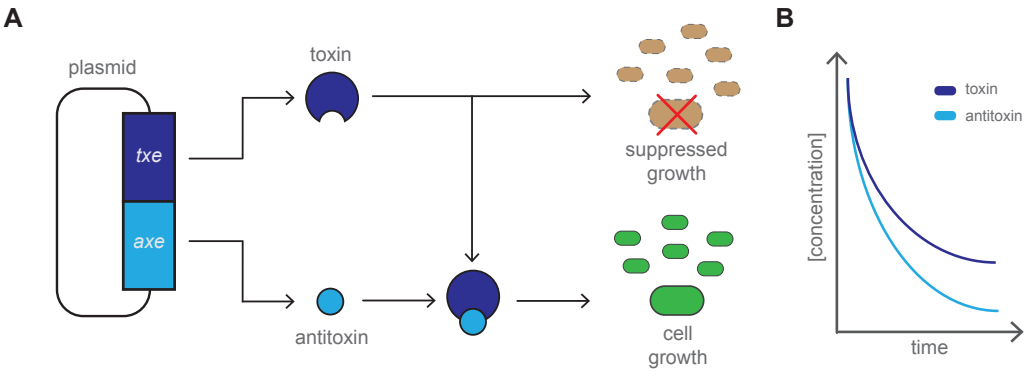

Figure 5.1: The Axe-Txe toxin-antitoxin system used to reduce plasmid loss. (**A**) The toxin (Txe) prevents cell growth; however, the antitoxin (Axe) is able to suppress the effects of Txe. (**B**) Txe has a longer lifetime than Axe, resulting in the suppressed growth of any cells that lose the AT-bearing plasmid.

5.1.3 Metabolite Biosensors

The new ratiometric plasmid system was intended to improve upon the system used in chapter 4. As such, an IPTG sensor circuit was incorporated onto the ratiometric plasmids of this chapter. The sensing mechanism that provided the basis of these sensor circuits is explained below. The majority of the biosensor characterisation was performed in the *E. coli* BW25113 strain. A derivative of the K-12 strain, BW25113 has been used widely in previous synthetic biology studies [179–181]. Also, it is the parent strain of the Keio knockout collection [182]. Therefore, a library of 3985 single-gene knockouts within this strain are available.

The *lac* Operon

IPTG-inducible biosensors were designed based on the *lac* operon, similar to the EcN_pLac biosensor described in chapter 4. The *lac* operon is responsible for lactose transport and metabolism within *E. coli* and is one of the most extensively studied genetic regulatory systems in molecular biology [183].

Within the natural system, the *lac* operon is repressed by a constitutively expressed regulatory protein, LacI (Figure 5.2). In the presence of allolactose, a product of lactose breakdown, the LacI protein undergoes an allosteric shift, which relieves repression of the *lac* operon [184]. Therefore, the *lac* system operates under a repressed-repressor architecture (see Figure 2.6). Allolactose is created from lactose by the product of the *lacZ* gene, an enzyme known as β-galactosidase. Interestingly, the *lacY* gene encodes the lactose permease transporter that is responsible for transporting lactose into the cell, therefore the *lac* system is responsible for transporting

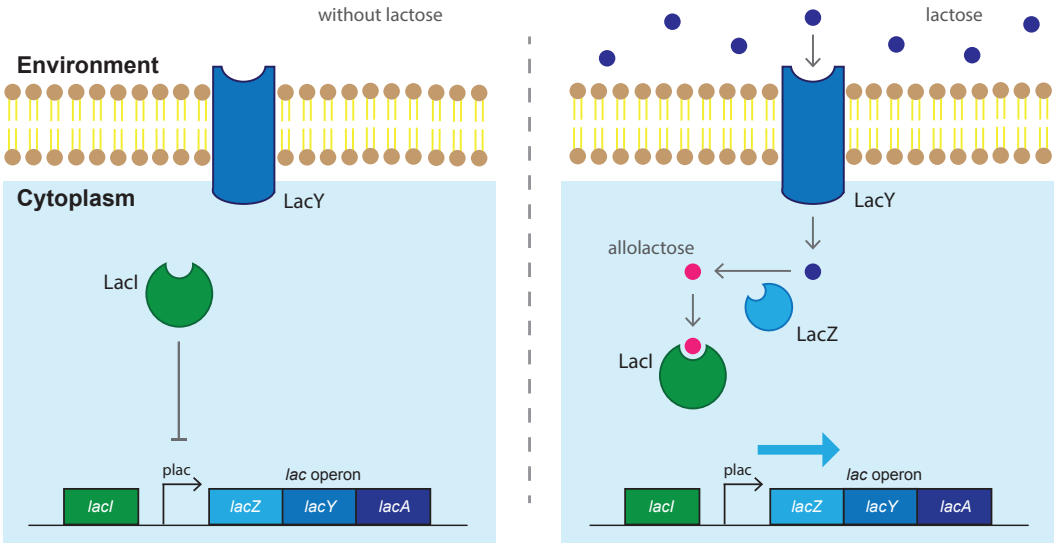

Figure 5.2: Layout of the *lac* operon, involved in lactose sensing. LacI acts as a repressor for the plac promoter, which is itself repressed in the presence of allolactose.

its own inducer- which can lead to a positive feedback effect when induced [185].

There are a number of different promoters that have been developed that can be integrated within the *lac* regulatory system. The natural system contains the plac promoter. Alternative promoters include placUV, ptrc and ptac. It has been previously reported that the ptac promoter has greater activity than the placUV, ptrc and plac promoters [184, 186]. Therefore, this promoter was incorporated into the ratiometric IPTG-biosensor plasmid design.

The molecule isopropyl β-D-1-thiogalactopyranoside (IPTG) is a structural analog of allolactose, which can act as a substitute to relieve repression of the *lac* operon. IPTG is also thought to be nonmetabolic, meaning that it does not get broken down within the cell. Although there is some evidence that *lacA* transacetylase can modify IPTG such that it can no longer act as an inducer [187]. Overall, these properties have led to the extensive use of IPTG as an inducer of recombinant

protein expression in biotechnology applications [187, 188]. Within this chapter a fragment containing the LacI repressor and ptac promoter were incorporated onto the pRBLac and pRBLac_AT plasmids to produce IPTG sensitive biosensors.

5.2 Aims

The primary aim of this chapter was to develop a new ratiometric plasmid system, that could be used to replace the dual-plasmid system used in chapter 4. This included the addition of an AT plasmid-stability system and attempts to introduce different sensor mechanisms onto the plasmid backbones. Finally, I wished to compare the performance of these new ratiometric WCBs against the performance of the previously constructed dual-plasmid IPTG WCB.

5.3 Results

5.3.1 WCB Circuits

The biosensors constructed within this chapter are given below (Figure 5.3). These include:

- Promoterless GFP 'negative' controls: pRB and pRB_AT, Figure 5.3A.
- Constitutive GFP 'positive' controls: pRBc and pRBc_AT, Figure 5.3B.
- IPTG-inducible GFP biosensors: pRBLac and pRBLac_AT, Figure 5.3C.

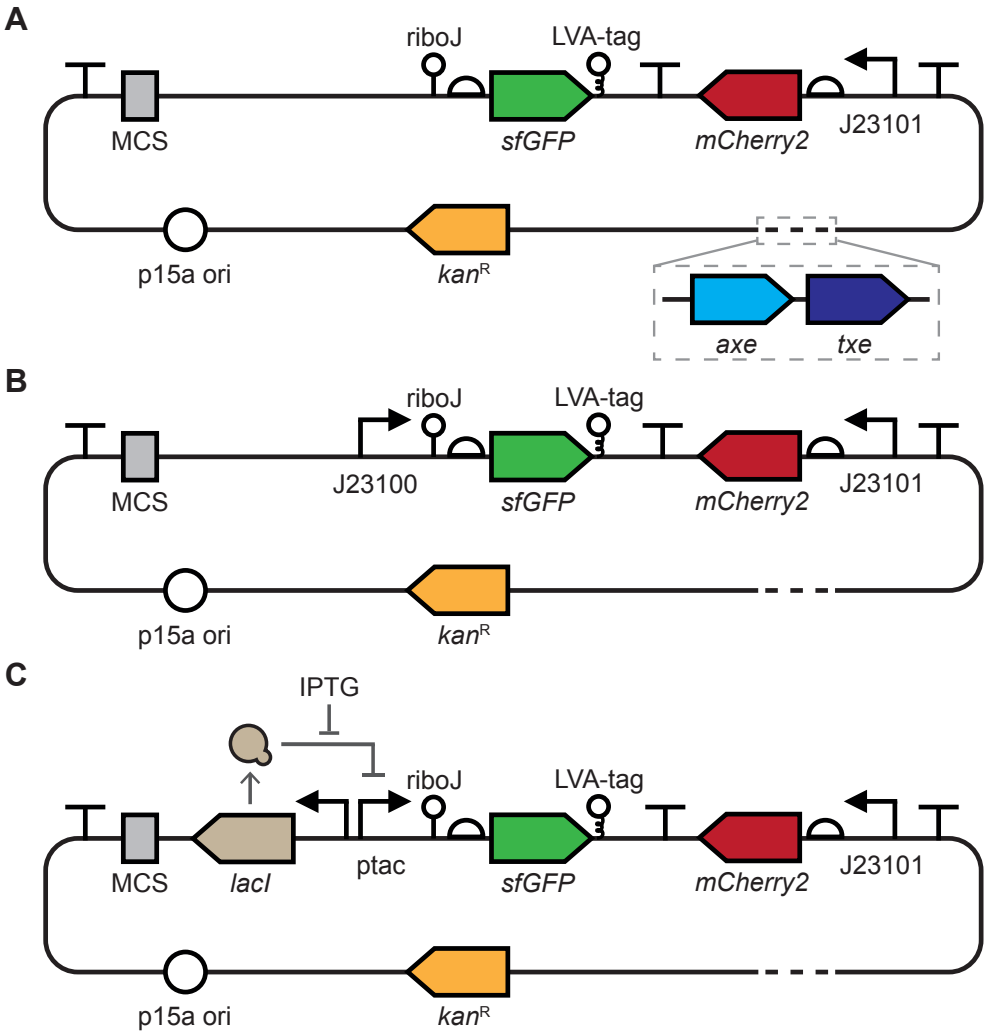

Figure 5.3: Plasmid maps of the ratiometric biosensors constructed within this chapter. (**A**) pRB- negative control, (**B**) pRBc- positive control, (**C**) pRBLac- IPTG inducible. A version of every plasmid containing the axe/txe system was also built, designated 'pRBxxx_AT'.

5.3.2 Constructing Ratiometric WCBs

Cloning of pRB and pRB_AT Backbone

The original GFP and constitutive mCherry fragment was ordered as a gBlock from Twist Bioscience (USA). The fragment contained promoterless sfGFP (with an LVA degradation tag), preceded by RiboJ, and mCherry2 (with an LVA degradation tag) under the control of the constitutive J23101 Anderson promoter. This was then transferred into the pSEVA_261 plasmid (provided by the SEVA collection) using the PacI and SpeI restriction sites, to produce the pSEVA_GFPmCherry plasmid. Initial testing of this plasmid showed that the constitutive mCherry signal could not be identified. Therefore, the LVA degradation tag on the mCherry2 protein was removed using the DegTag.F and DegTag.R primers. Blunt ligation was used to circularise the amplified product, resulting in the pRB plasmid.

The Axe-Txe fragment was amplified from the p246-AT plasmid (provided by Alex Fedorec, UCL), using the pJRBB_fragment.F and pJRBB_fragment.R primers. The pRB vector was amplified using the pJRBB_vector.F and pJRBB_vector.R primers. The fragment and vector were then ligated following the HiFi DNA assembly protocol (section 3.3.2), to produce the pRB_AT plasmid.

Cloning of pRBc and pRBc_AT

The high-strength constitutive J23100 promoter was amplified from the J23100_AB plasmid (provided from the CIDAR MoClo kit), using the pJRc_fragment.F and pJRc_fragment.R primers. A PCR reaction was then performed on the pRB and pRB_AT vectors, with the pJRc_vector.F and pJRc_vector.R primers. The J23100

fragment was then added to both vectors, using NEB HiFi assembly, to produce the pRBc and pRBc_AT plasmids.

Cloning of pRBLac and pRBLac_AT

Several attempts were made to clone the pRBLac and pRBLac_AT plasmids, through both NEB HiFi assembly and traditional restriction enzyme cloning. A successful method was found using NEB HiFi assembly. An IPTG-responsive fragment was amplified from the pRG-PhIF plasmid (containing the ptac promoter and *lacI* expression, provided by Zong et al.) [189], using the pJRLac_fragment.F and pJRLac_fragment.R primers. A PCR was then performed on the pRB and pRB_AT vectors, with the pJRLac_vector.F and pJRLac_vector.R primers. The fragment was then added to both vectors, using NEB HiFi assembly, to produce the pRBLac and pRBLac_AT plasmids.

5.3.2.1 Ratiometric Plasmid Design

Ratiometric biosensors are considered more robust than a single, absolute measurement. Also, as two-plasmid systems (such as those in chapter 4) are not convenient for engineering biological systems [190], due to factors such as incompatible origins and potential plasmid loss, both the mCherry and GFP sensor elements were incorporated onto a single plasmid. The original GFP:mCherry fluorescent plasmid was designed and ordered from Twist Bioscience. This was engineered such that constitutive mCherry2 expression provided a background signal and the sensor elements could be used to control GFP expression (similar to chapter 4). However, these new designs are different in several ways from the dual-plasmid biosensors reported

there. Firstly, the fluorescent reporters were replaced with sfGFP and mCherry2. These variants of GFP and mCherry have been reported to have improved folding times and higher stability [191]. In addition, mCherry2 has been reported to be less cytotoxic than the original mCherry protein [192]. An alternative design was also made that incorporated variants of cyan fluorescent protein (CFP) and yellow fluorescent protein (YFP), which have distinct excitation/emission spectra and faster folding times. However, Twist Bioscience were unable to successfully synthesise this fragment. Therefore, the CFP/YFP design was not taken further. In addition to the change in fluorescent reporters, LVA-ssrA degradation tags were added to both the sfGFP and mCherry2 proteins [193]. Degradation tags were added to achieve greater turnover in the reporter proteins. One of the drawbacks of using stable fluorescent proteins, is that they can persist within cells even after expression rates have dropped. This limits their use in monitoring transient gene expression [193]. Therefore, the degradation tags were added to provide more dynamic monitoring of the real-time expression of the reporter proteins. In addition, a RiboJ insulator was placed upstream of the *sfGFP* gene, in order to reduce context dependent variations introduced by the use of different input promoters [194].

It has been widely reported that the expression of non-native proteins can have an adverse effect on the growth of host cells [195]. This effect is often termed cost or 'burden'. It is thought that this burden is due (in part) to competition for finite resources within the host cell, for example polymerases or free ribosomes [196–198]. Therefore, for these backbones a p15a origin, which has a medium-low copy number, was chosen for two reasons. One, to try and help bal-

ance plasmid burden/expression and two, thanks to a study comparing the activity of a range of plasmid origins (from the SEVA collection) that found a p15a plasmid-harbouring strain produced a highly inducible and homogeneous population [199]. Across the literature there is some debate as to the exact copy number of different plasmid origins. For the p15a origin, reported values range from 8.6 copies [199], 12 copies [171], 14-16 copies [200], up to 20 copies [201]- depending on the study referenced. Both host strain and cultivation conditions are known to effect plasmid copy number, which likely accounts for some of this variability [199, 202]. However, there appears to be some agreement that the copy number of p15a is likely around 12-15 copies per cell. It should be noted that there is a wide range of other origins that are available and it has been shown that plasmid copy number can have a large influence on final plasmid behaviour. As the ratiometric plasmids were designed to follow the Standard European Vector Architecture (SEVA) format [203, 204], the p15a origin could be readily changed in future to further explore the effect of copy number if required. Finally, as discussed in section 5.1.2, the AT system was incorporated onto the plasmids to provide an alternative selection mechanism to antibiotic resistance.

Unfortunately, upon measuring the mCherry background signal it was found that the original G-Blocks received from Twist Bioscience did not produce a significantly higher mCherry signal than that of untransformed cells (Figure 5.4D). It was hypothesised that this may be due to the LVA-ssrA degradation tag attached to the mCherry protein, as the protein may be degraded before it had chance to mature into fluorescent mCherry. A recent study by Müller et al. (2019) used a similar degrada-

tion tag, LAA-ssrA, to rapidly degrade an mCherry signal within a circuit designed to compensate for genetic crosstalk [76]. This supported the hypothesis that the LVA-ssrA tag triggered degradation before a sufficient mCherry signal could be observed. Therefore, 'around the horn' PCR was used to remove the degradation tag. This resulted in a detectable constitutive mCherry signal. This new design with the mCherry degradation tag removed was used for future iterations of the ratiometric biosensor backbone. After a mCherry signal could be reliably observed, the fluorescent portion of the plasmid was transferred into a new vector, which conformed to the SEVA format- this backbone was termed 'pRB'. Finally, a subsequent version of pRB was made by incorporating the AT system, this final backbone was termed 'pRB_AT'. In addition to the clear mCherry signal, it was found that neither pRB or pRB_AT produced a higher GFP signal than untransformed cells (Figure 5.4C), suggesting that the ratiometric backbones have a low level of leakiness (f^{min}). This is desirable behaviour for many biosensor applications, as often no output is required in the presence of no input signal.

5.3.3 IPTG-inducible WCBs

Figure 5.5 shows that both pRBLac and pRBLac_AT displayed GFP induction with increasing concentrations of IPTG, in the BW25113 strain. The GFP response for pRBLac and pRBLac_AT showed similar levels of f^{min}, however the fitted $K_{1/2}$ decreased from pRBLac to pRBLac_AT (Table 5.1), showing that the pRBLac_AT WCB was more sensitive. An even more marked difference between pRBLac and pRBLac_AT was seen in the values of f^{max} and dynamic range. With the addition

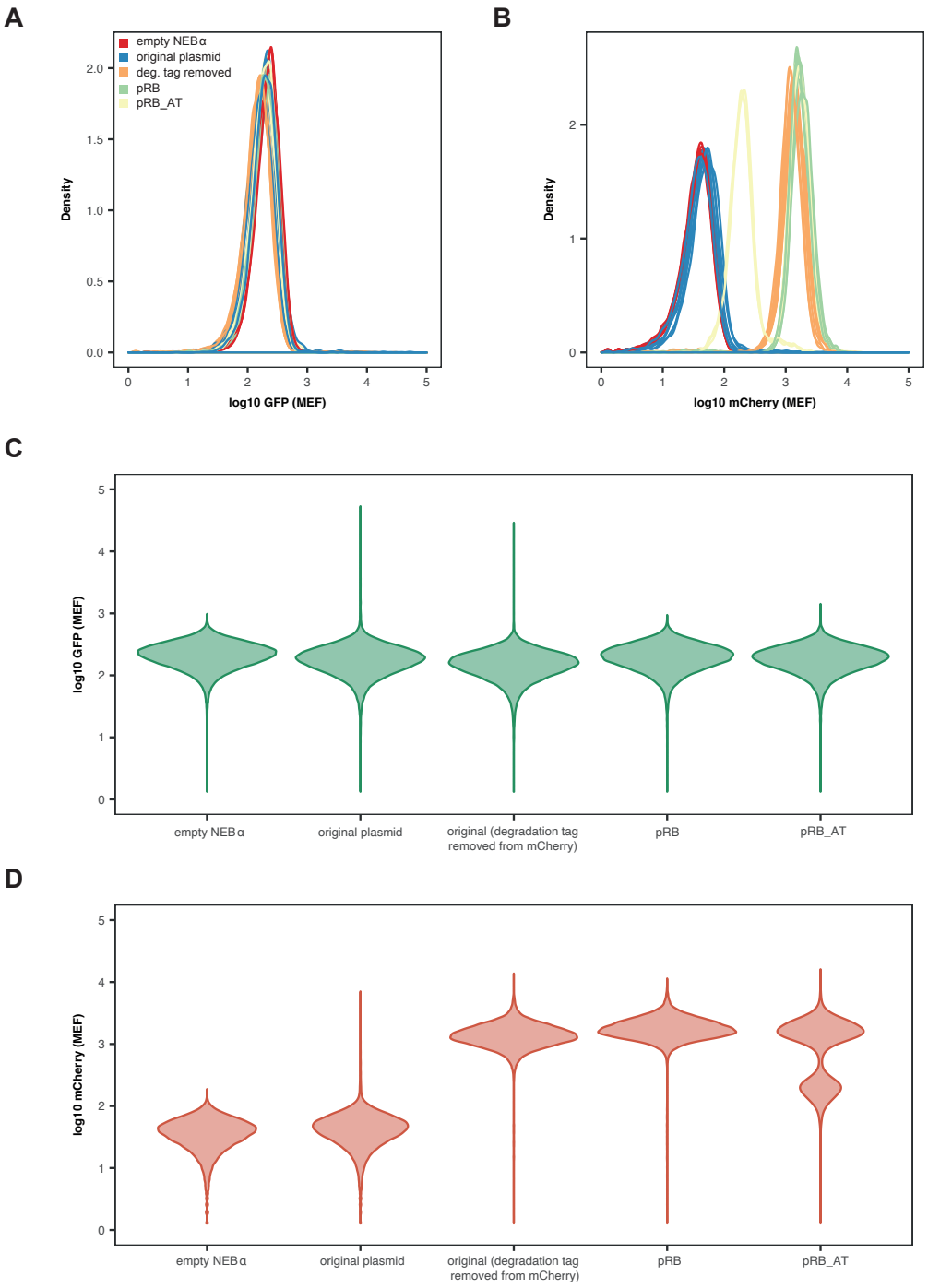

Figure 5.4: Comparisons of the GFP and mCherry levels for the various engineered ratiometric biosensor backbones, in the NEBα strain. Density plots of (**A**) GFP and (**B**) mCherry. Violin plots of (**C**) GFP and (**D**) mCherry fluorescence measured through flow cytometry. (n = 3 biological repeats x 3 technical replicates, 10 000 events each).

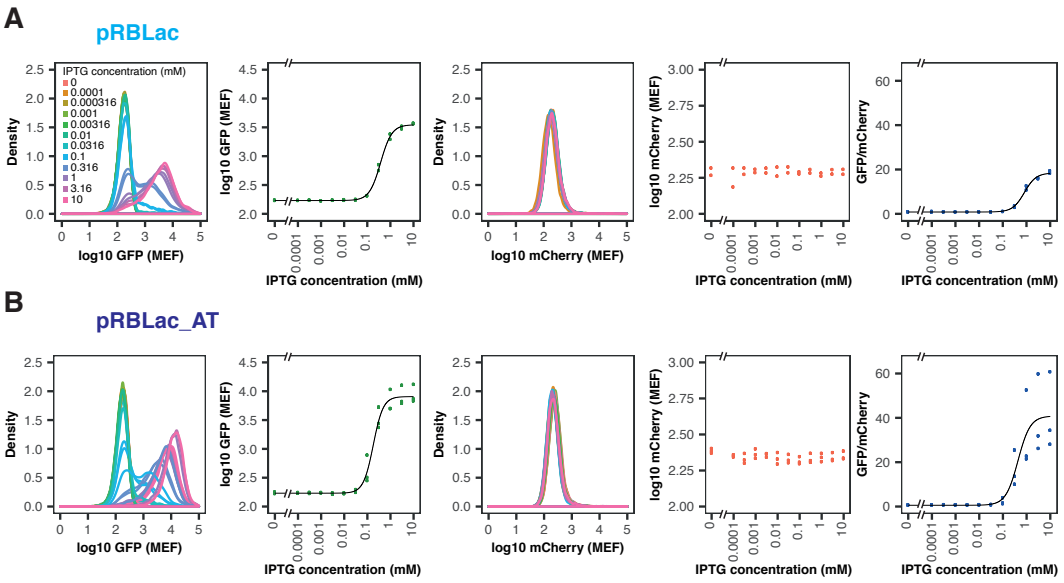

Figure 5.5: *In vitro* flow cytometry characterisation of the IPTG-inducible ratiometric biosensors in the BW25113 strain with LB media, 3 hours post induction. (**A**) pRBLac biosensor, (**B**) pRBLac_AT biosensor. From left to right: density plot of GFP induction, median GFP fluorescence, density plot of mCherry fluorescence, median mCherry fluorescence and GFP:mCherry ratios over all IPTG inducer concentrations. Flow cytometry data with 10 000 events. (n = 3 biological replicates)

of the AT system, both the f^{max} and dynamic range increased, for pRBLac_AT compared to pRBLac. These changes in behaviour were mirrored in the final GFP:mCherry ratio response, with the addition of AT leading to a lower $K_{1/2}$, higher f^{max} and improved dynamic range (Table 5.2). In addition, pRBLac appeared to show lower levels of constitutive mCherry fluorescence than pRBLac_AT (shown in Figure B.1). As the mCherry expression is constitutive, this may indicate a higher copy number of the plasmid within the pRBLac_AT transformed cells. Overall, this characterisation confirmed that both of the engineered IPTG-inducible biosensors were able to report on concentrations of IPTG in the micro-molar range, through both a GFP and GFP:mCherry ratio reporter.

Plate reader characterisation supported the data collected through flow cytometry, Figure 5.6. From the top panels, it can be seen that there appeared to be little difference in the growth rate between the biosensor with and without the AT system. Furthermore, increasing the concentration of IPTG did not appear to have any sizeable affect on the growth rate. Previous studies have shown that IPTG can have a negative effect on growth [205]; however, it has been reported that these effects may be dependent on the culture conditions used [206]. Therefore, it seems that the maximum inducer of 10 mM IPTG is not high enough to lead to toxic effects in this case.

The middle panels of Figure 5.6 show the GFP response of pRBLac and pRBLac_AT within BW25113. From this figure it can be seen that an increase in GFP fluorescence was seen rapidly after induction of the cells, with a robust increase

Table 5.1: Hill parameter fitting to GFP induction curves of IPTG ratiometric biosensors, in BW25113 (fitted values ± SE, given to 3 s.f.).

Biosensor	**pRBLac**	**pRBLac_AT**
f^{min} (MEF)	170 ± 1.02	170 ± 1.06
f^{max} (MEF)	3510 ± 1.04	8010 ± 1.10
$K_{1/2}$ (μM)	378 ± 13.8	181 ± 15.1
n	1.79 ± 0.106	2.03 ± 0.260
dynamic range	19.6	46.4

Table 5.2: Hill parameter fitting to ratio induction curves of IPTG ratiometric biosensors, in BW25113 (fitted values ± standard error, given to 3 s.f.).

Biosensor	**pRBLac**	**pRBLac_AT**
f^{min}	0.826 ± 0.143	0.568 ± 1.75
f^{max}	18.4 ± 0.394	40.8 ± 3.98
$K_{1/2}$ (μM)	817 ± 46.6	433 ± 129
n	1.77 ± 0.157	1.68 ± 0.720
dynamic range	21.3	70.9

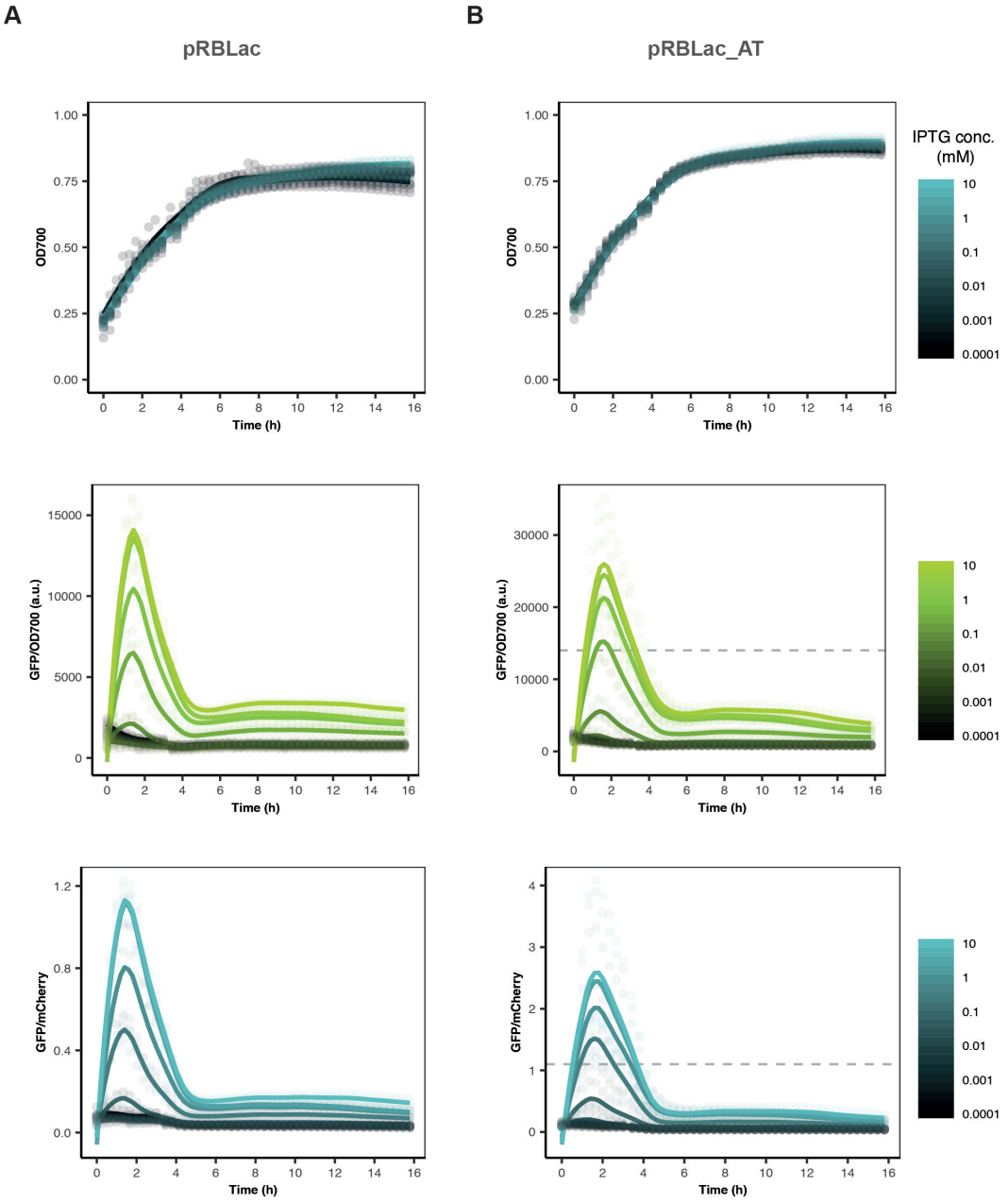

Figure 5.6: Platereader characterisation of (**A**) pRBLac and (**B**) pRBLac_AT, in BW25113. Top panels give the growth curves, centre panels give the GFP response with respect to optical density and the bottom panels give the GFP:mCherry ratios. Scales are not consistent between left and right columns. Grey dotted lines give the maximum recorded GFP and ratio response for the pRBLac biosensor. (n = 3 biological replicates, data normalised against empty LB media)

in GFP fluorescence seen in as little as 40 minutes post-induction (Figure 5.7). A peak in GFP fluorescence could be seen around the 1 hour 45 minute mark for all IPTG concentrations, which then fell away until levelling out after approximately 4 and a half hours. However, there was still a large response at 3 hours post-induction (the time point used for flow cytometry characterisation). This data suggests that these biosensors could be used for rapid detection of IPTG within samples. Similar behaviour was seen in the GFP:mCherry ratio responses for both biosensors (bottom panels of Figure 5.6). As with the flow cytometry data, pRBLac_AT showed a higher maximum GFP and GFP:mCherry response than the pRBLac biosensor highlighted by the grey dotted lines on Figure 5.6.

Figure 5.7 shows dose response curves collected from plate reader data at specific timepoints after induction. As mentioned previously, a robust GFP response was seen in both the pRBLac and pRBLac_AT sensors at 40 minutes post-induction (red data points). In addition, the data from 3 hours post-induction supports that shown in the flow cytometry characterisation, with higher GFP fluorescence seen for the induced pRBLac_AT biosensor. At 16 hours post-induction (yellow data points) the GFP and GFP:mCherry responses were much lower than those seen at earlier timepoints.

IPTG WCB Performance in *E. coli* Nissle

Following characterisation of pRBLac and pRBLac_AT in BW25113, the biosensors were transformed into EcN. Characterisation of the IPTG biosensors in the probiotic EcN strain is shown in Figure 5.8. This characterisation was performed at

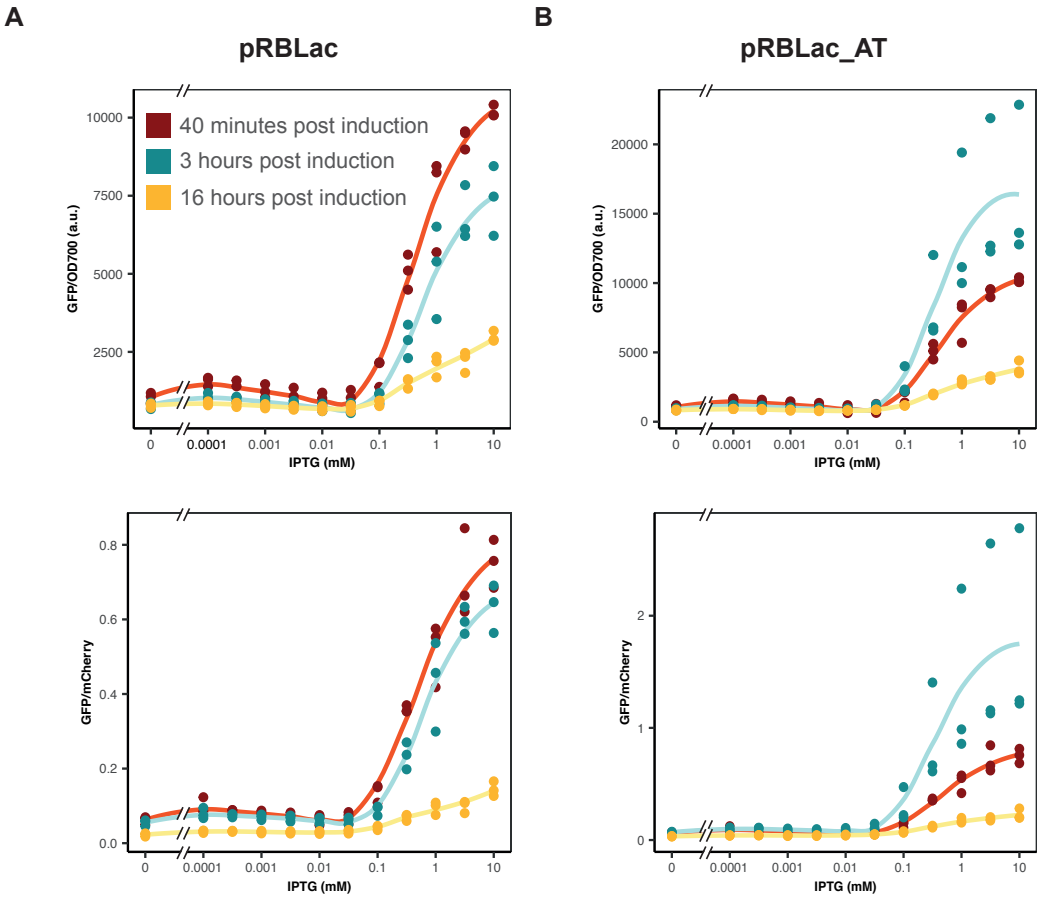

Figure 5.7: Plate reader GFP response curves of (**A**) pRBLac and (**B**) pRBLac_AT, at 40 minutes, 3 hours and 16 hours post induction. Top panels gives GFP response with respect to optical density. Bottom panels give the GFP:mCherry ratio response. The line fits are not Hill fits and are just for illustrative purposes. (n = 3 biological replicates, datapoints represent readings from a single culture)

3 hours post-induction, alongside the original dual-plasmid biosensor (EcN_pLac), used in chapter 4. EcN showed similar changes in GFP repsonse behaviour to BW25113. Between pRBLac and pRBLac_AT, the fitted values for $K_{1/2}$ decreased from 12.7 $\pm$ 1.15 to 5.06 $\pm$ 0.265 µM, whereas both the f^{max} and dynamic range increased (Table 5.3).

These changes were again mirrored in the ratio response, with a lower $K_{1/2}$, higher f^{max} and increased dynamic range seen with the addition of AT (Table

5.4). Furthermore, pRBLac_AT once again showed a higher level of constitutive mCherry fluorescence than pRBLac, as in BW25113. However, both pRBLac and pRBLac_AT showed significantly lower levels of mCherry fluorescence than EcN_pLac, despite the fact that mCherry is expressed from a plasmid with the SC101 origin (∼5 copies) in the two-plasmid system [201], which is a lower copy number than the p15a origin (∼12 copies) used in the pRBLac and pRBLac_AT biosensors [171]. This suggests that the J23101 promoter has much lower consti-

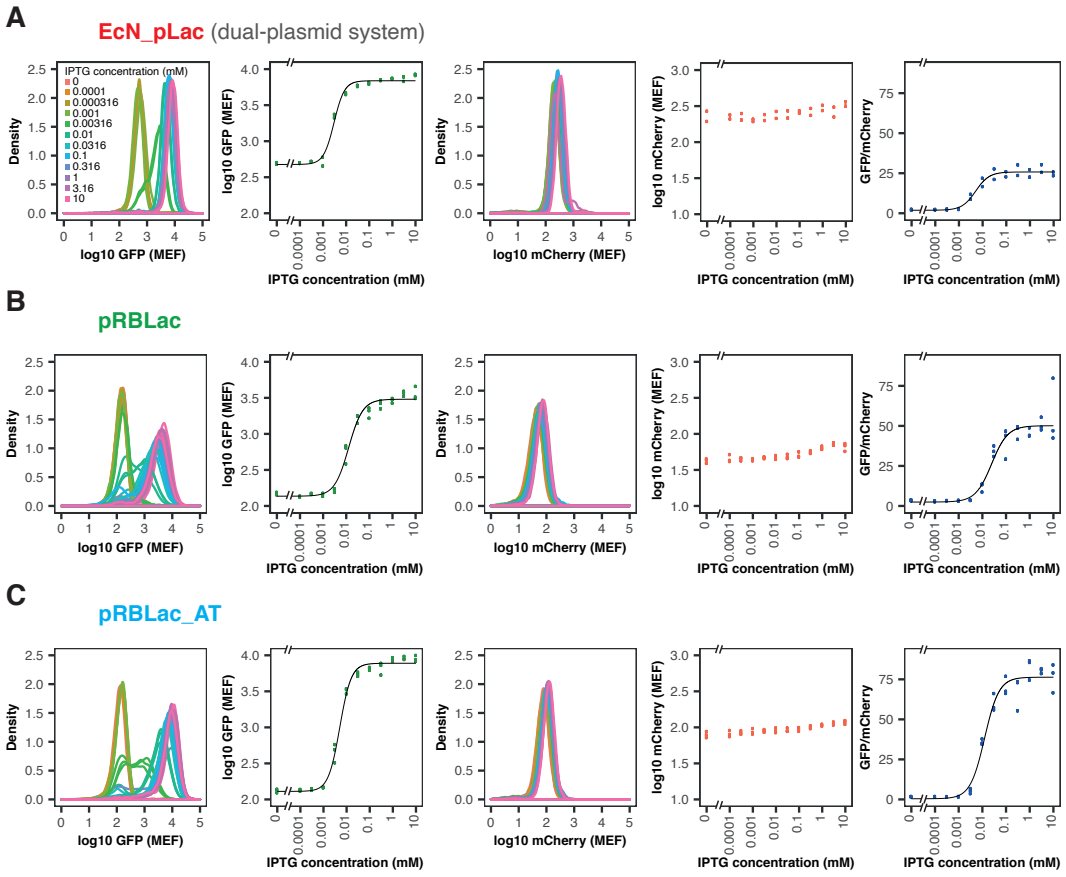

Figure 5.8: *In vitro* characterisation of the IPTG-inducible ratiometric biosensors, in *E. coli* Nissle with LB media, 3 hours post induction. (**A**) EcN_pLac biosensor, (**B**) pRBLac and (**C**) pRBLac_AT biosensor. From left to right: density plot of GFP induction, median GFP fluorescence, density plot of mCherry fluorescence, median mCherry fluorescence and GFP:mCherry ratios over all IPTG inducer concentrations. Flow cytometry data with 10 000 events. (n = 2 biological replicates for EcN_pLac, 3 for pRBLac and pRBLac_AT)

tutive expression than the pEM7 promoter used in EcN_pLac, despite the fact that J23101 is one of the strongest constitutive promoters in the Anderson collection (fourth strongest of the 20 promoters) [207].

Interestingly, as shown in Figure 5.9, pRBLac/pRBLac_AT displayed a much lower $K_{1/2}$ in EcN than BW25113. This was consistent between the GFP and ratio responses, with the WCBs displaying a $K_{1/2}$ over an order of magnitude lower in EcN. Furthermore, the WCBs in EcN showed a higher dynamic range in their ratio response. As can be clearly seen in Figure 5.9 both pRBLac and pRBLac_AT displayed far superior performance in EcN than BW25113. These differences in behaviour are summarised in Figures 5.10 and 5.11, which show the fitted Hill parameters for both the GFP and ratio responses. The differences in behaviour caused by addition of AT can also be seen more clearly within these figures. Across strains, the addition of AT led to a higher f^{max}, dynamic range and improved $K_{1/2}$.

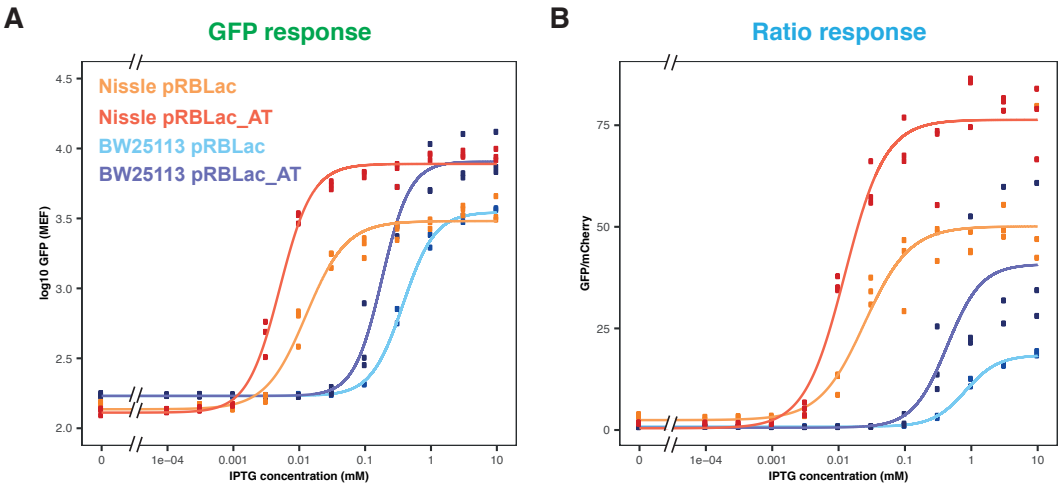

Figure 5.9: *In vitro* characterisation of the IPTG-inducible ratiometric biosensors, in the *E. coli* Nissle and BW25113 strains- 3 hours post-induction, LB media. Comparisons of the biosensors (**A**) GFP response and (**B**) ratio response. Measurements taken 3 hours after induction. Flow cytometry data with 10 000 events. (n = 3 biological replicates)

In comparison to the EcN_pLac system both pRBLac and pRBLac_AT displayed improved aspects of performance. For GFP response, Figure 5.12A shows that both pRBLac and pRBLac_AT had a significantly lower f^{min} than EcN_pLac. pRBLac showed a lower f^{max} than EcN_pLac, whereas pRBLac_AT showed a higher f^{max}. Both pRBLac and pRBLac_AT had a much greater dynamic range than EcN_pLac (owing mainly to the reduced levels of f^{min}). However, both pRBLac and pRBLac_AT displayed a higher $K_{1/2}$ than EcN_pLac. All three of the biosensors showed similar f^{min} values for the GFP:mCherry response. However, both pRBLac and pRBLac_AT had a much higher f^{max} and higher dynamic ranges. Overall, these changes in behaviour suggest that both pRBLac and pRBLac_AT outperform the original dual-plasmid EcN_pLac in terms of dynamic range and maximum outputs.

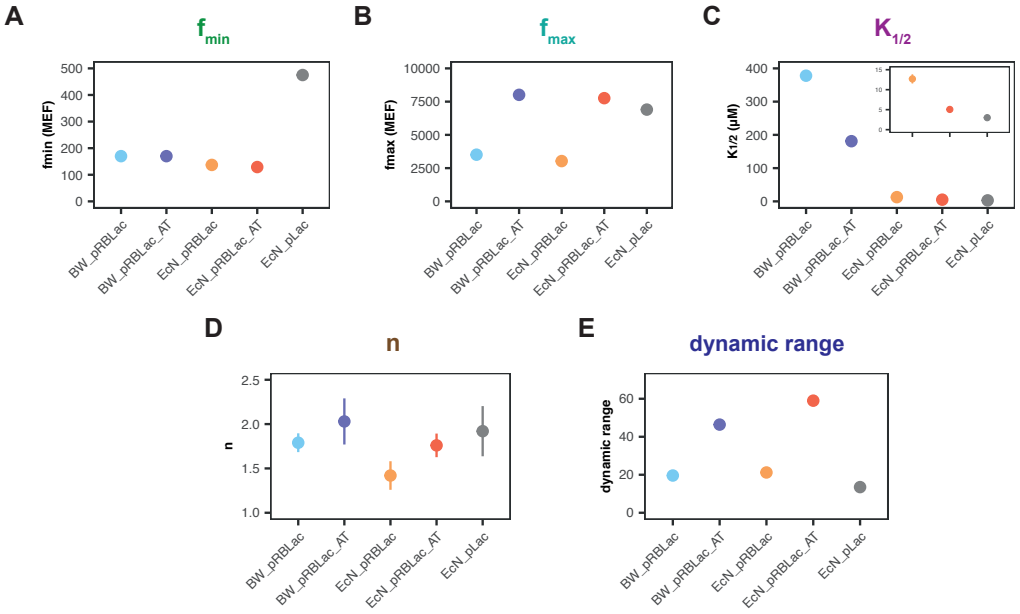

Figure 5.10: Fitted Hill function parameters, to the GFP response of pRBLac/pRBLac_AT: (**A**) f^{min}, (**B**) f^{max}, (**C**) $K_{1/2}$, (**D**) n and (**E**) dynamic range. 'BW_' refers to BW25113, 'EcN_' refers to *E. coli* Nissle. pLac is the IPTG WCB discussed in chapter 4 (grey). Inset in (**C**) shows a close up of the EcN transformed strains. (fitted parameter ± SE, except dynamic range)

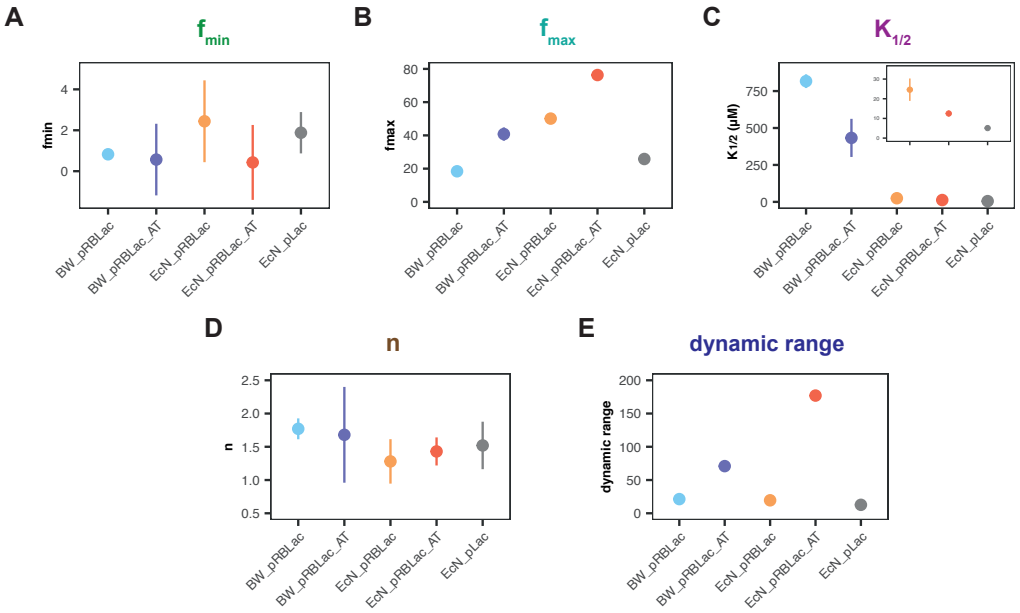

Figure 5.11: Fitted Hill function parameters, to the GFP:mCherry ratio response of pRBLac/pRBLac_AT: (**A**) f^{min}, (**B**) f^{max}, (**C**) $K_{1/2}$, (**D**) n and (**E**) dynamic range. 'BW_' refers to BW25113, 'EcN_' refers to *E. coli* Nissle. pLac is the IPTG WCB discussed in chapter 4 (grey). Inset in (**C**) shows a close up of the EcN transformed strains. (fitted parameter ± SE, except dynamic range)

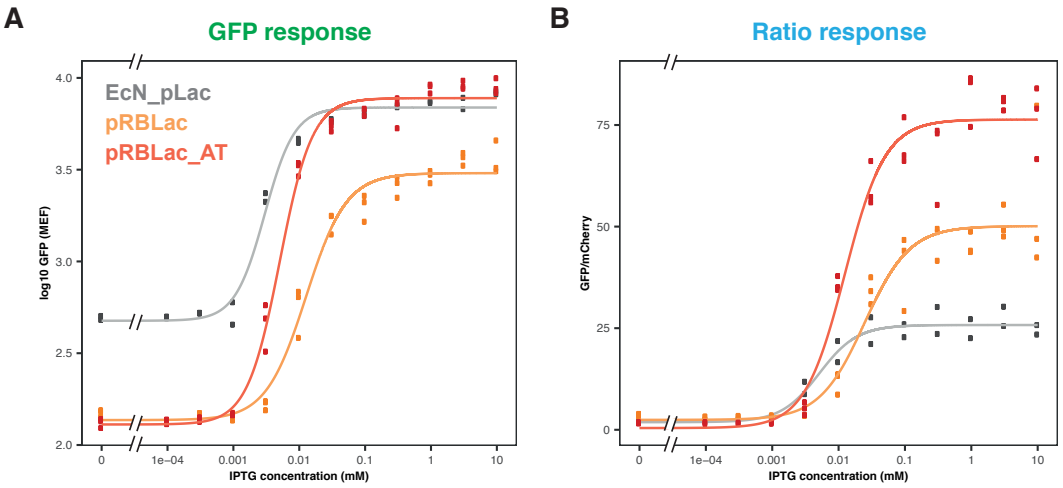

Figure 5.12: *In vitro* characterisation of the IPTG-inducible ratiometric biosensors, in *E. coli* Nissle with LB media. EcN_pLac is the original IPTG biosensor discussed in chapter 4. Comparisons of the biosensors (**A**) GFP response and (**B**) ratio response. Measurements taken 3 hours after induction. Flow cytometry data with 10 000 events. (n = 2 biological replicates for EcN_pLac, 3 for pRBLac and pRBLac_AT)

Table 5.3: Hill parameter fitting to GFP induction curves of IPTG ratiometric biosensors, in *E. coli* Nissle (fitted values ± SE, given to 3 s.f.).

Biosensor	**EcN_pLac**	**pRBLac**	**pRBLac_AT**
f^{min} (MEF)	475 ± 1.06	137 ± 1.06	129 ± 1.05
f^{max} (MEF)	6900 ± 1.04	3030 ± 1.05	7760 ± 1.04
$K_{1/2}$ (μM)	3.00 ± 0.237	12.7 ± 1.15	5.06 ± 0.265
n	1.92 ± 0.283	1.42 ± 0.161	1.76 ± 0.133
dynamic range	13.5	21.2	59.0

Table 5.4: Hill parameter fitting to ratio induction curves of IPTG ratiometric biosensors, in *E. coli* Nissle (fitted values ± SE, given to 3 s.f.).

Biosensor	**EcN_pLac**	**pRBLac**	**pRBLac_AT**
f^{min}	1.88 ± 1.01	2.44 ± 2.00	0.429 ± 1.83
f^{max}	25.8 ± 0.763	50.1 ± 2.16	76.3 ± 1.69
$K_{1/2}$ (μM)	5.09 ± 0.926	24.6 ± 5.70	12.5 ± 1.47
n	1.52 ± 0.357	1.28 ± 0.334	1.43 ± 0.211
dynamic range	12.7	19.5	177

5.4 Discussion

5.4.1 Evaluating pRBLac and pRBLac_AT Performance

From Figure 5.7, it can be seen that at 16 hours post induction the changes in GFP and GFP:mCherry responses with IPTG induction were nearly removed. I hypothesised that the low levels of GFP fluorescence seen at 16 hours post-induction were caused by the presence of the LVA-ssrA degradation tags on the sfGFP reporter. In their original report, Andersen et al. found that with the addition of the LVA-ssrA degradation tag GFPmut3 fluorescence was decreased by greater than 10-fold over 200 minutes, compared to the untagged GFPmut3 protein [193]. Therefore, the dramatic drop in GFP fluorescence seen between approximately 2 to 5 hours post-induction is likely caused by the action of the LVA-ssrA tag. This drop in GFP fluorescence would also account for the decrease seen in the GFP:mCherry ratios. As the drop coincides with the cells entering into stationary phase, it may be possible to investigate pRBLac and pRBLac_AT as sensors for exponential growth when grown in the presence of IPTG. Moreover, it would be interesting to see if spiking IPTG inducer into the cultures at later timepoints could produce subsequent peaks in the GFP fluorescence, or if exponential growth phase is required to produce the early peaks seen in Figure 5.6.

Following initial characterisation pRBLac and pRBLac_AT were characterised in EcN, alongside BW25113, to explore their performance within a commonly used microbiome engineering strain. The pRBLac and pRBLac_AT biosensors displayed a much lower fitted $K_{1/2}$ in the EcN host strain. As both EcN and BW25113 express

lacI from their genome, I hypothesised that the observed change in $K_{1/2}$ between strains may be caused by differences in this genomic expression. The BW25113 strain was originally reported to be $lacI^q$ [208, 209]. The $lacI^q$ strain designation signifies a mutant of the *lacI* repressor, which binds more tightly to the *lac* operator [210]. The study by Mannan et al. (2017), was able to elucidate a number of design principles for TF-based WCBs [122]. One of these predictions proposes that a higher TF-operator affinity (for a repressor-based TF) will result in an increased biosensor threshold. This may explain the higher observed $K_{1/2}$ within the BW25113 strain. If this is the case this suggests that knocking out *lacI* on the BW25113 genome may result in superior WCB performance within this strain. However, a recent report cast doubt on the assumption that the BW25113 strain is $lacI^q$, instead suggesting that the strain may instead be $lacI^+$ [211]. Therefore, it may be interesting in future to see if knocking out genomic expression of *lacI* in both the EcN and BW25113 host strains would subsequently result in similar fitted $K_{1/2}$ values.

IPTG does not hold any interest in terms of biomedical or clinical applications. However, the natural inducer of the *lac* system, lactose (Figure 5.2), plays a number of roles in human health. Approximately 75% of the world's population lose the ability to digest lactose at some point in their lives, leading to varying degrees of lactose intolerance [212]. Lactose intolerance can lead to a variety of symptoms including bloating, cramps and nausea [213]. There are also other conditions that can lead to the maldigestion of lactose; for example, celiac disease or Crohn's disease [214]. In addition, there is evidence that lactose plays a role in the

development and composition of the human microbiota [215]. This is thought to be through providing a growth benefit to bacterial taxa that are able to utilise lactose as a carbon substrate [18]. Alongside this, lactose is a component in a range of dairy and pharmaceutical products. Therefore, lactose WCBs may be useful for a range of microbiome or industrial applications. A previous study investigated the use of lactose as a cheap alternative to IPTG for protein expression using the *lac* system [216]. Their results showed that lactose was able to achieve comparable induction to IPTG, but that expression levels depended greatly on the time at which lactose was added to the growing cells [216]. As such, it would be interesting to investigate any differences in switching behaviour for both pRBLac and pRBLac_AT when exposed to the natural lactose inducer rather than IPTG.

5.4.2 Further Improving pRBLac and pRBLac_AT performance

The ratiometric WCBs designed in this chapter already display improved behaviour compared to the EcN_pLac biosensor used in chapter 4, through improved dynamic ranges. However, this coincided with higher $K_{1/2}$ values. Future work could attempt to further improve pRBLac/pRBLac_AT behaviour. As reported elsewhere, for TF biosensors with a repressor architecture, reducing the expression of the TF can result in a lowered $K_{1/2}$ (increased sensitivity) and higher max outputs; as the output promoter is not as tightly repressed [99, 217]. For the IPTG WCBs reported here the *lacI* repressor could be placed under the expression of a range of constitutive promoters (for example the Anderson promoter collection) and the construct

giving the best final behaviour selected, similar to the tuning performed by Wan et al. for arsenic and mercury biosensors [108], or Wang et al. for a TetR based biosensor [217]. Alternatively, genetic amplifiers (such as the LuxR amplifier reported by Nistala et al.) could be used to improve pRBLac and pRBLac_AT response [129].

5.4.3 The Effect of Axe-Txe on Biosensor Response

For the pRBLac and pRBLac_AT biosensors the addition of the AT fragment appeared to produce a small increase in the constitutive mCherry signal (Figure B.1). Furthermore, the addition of AT resulted in an increase in the max GFP expression and max GFP:mCherry ratio of the WCBs (Figures 5.10 and 5.11). For both pRBLac and pRBLac_AT this trend was consistent across the BW25113 and EcN host strains.

When cells undergo division, plasmids within the parent cell are split between two daughter cells. Within the AT system a minimum amount of antitoxin is required to neutralise the toxin in the daughter cells. Therefore, one hypothesis could be that the AT system drives up the copy number within cells; such that upon division both daughter cells receive enough copies to produce sufficient antitoxin to survive and those that do not are removed from the population. This higher copy number could explain the increase in mCherry fluorescence for cells carrying the AT versions of the biosensor plasmids. It also provides a possible explanation for the increases seen in the maximum GFP expression. To test this hypothesis quantitative real-time PCR (qPCR) could be used to measure the copy number within the biosensor strains and see if the AT fragment does indeed result in an increased

plasmid copy number [218].

5.5 Future Work

Despite the unanticipated benefits that addition of the AT fragment appeared to confer to the pRBLac_AT biosensors, the primary reason for adding AT to the biosensor design was to create plasmids that could be maintained within cells without the need for antibiotic selection. As such, plasmid loss experiments will need to be carried out to confirm that the AT fragment improves plasmid stability in the absence of antibiotics. Although the AT fragment seemed to result in improved biosensor performance, it should be noted that the plasmids reported all share the same origin of replication and similar plasmid architecture. Therefore, it would be interesting in future to see if the benefits of adding AT are maintained across different plasmids, for example differing copy numbers. This could be investigated by changing the origins of the plasmids created here, using the SEVA architecture. Finally, pRBLac/pRBLac_AT were designed as alternatives to the EcN_pLac WCB used in chapter 4; as such they could be tested in the *C. elegans* model to see if they are able to outperform the dual-plasmid biosensor *in vivo*.

5.6 Summary

The results presented within this chapter highlight a number of interesting findings. Firstly, the WCBs are constructed within a ratiometric format, as such they are amenable to the *in vivo C. elegans* characterisation reported in chapter 4. Additional sensing mechanisms may be incorporated into this ratiometric format in

future (preliminary attempts at propionate and acetoacetate-inducible WCBs have already been made, shown in Appendix B). In addition, characterisation of the IPTG-inducible WCBs has revealed the dramatic effect that using *E. coli* Nissle as a host can have on circuit behaviour. Within this work, the EcN host strain was able to improve IPTG biosensor performance in terms of $K_{1/2}$. However, the most interesting results came from the unexpected effect that the addition of AT had on WCB behaviour (which has not been explored previously). The addition of the AT fragment led to improved biosensor performance. Primarily, this involved increased f^{max} and dynamic ranges. These findings suggest, in this case, that the addition of AT may still be beneficial for WCB performance even if antibiotic selection is used.

Chapter 6

Engineering of Acetoacetate Whole-Cell Biosensors Based on the AtoSC Two-Component System

Contents

6.1 Background

6.1.1 Two Component Systems

As mentioned within section 2.4.2, TCSs are one of the most common bacterial sensing mechanisms [100], with hundreds of examples found within bacterial genomes [124, 219]. *E. coli* alone have 32 TCSs, although some of their functions remain to be determined [220]. TCSs consist of a histidine kinase (HK) sensor that detects a specific signal. This activates kinase activity and causes autophosphorylation of a conserved histidine residue [219]. This phosphoryl group then transfers to the response regulator (RR), through an aspartate residue [124]. Usually RRs are a transcription regulator capable of activating or repressing the expression of a specific gene. Thereby, they can control gene expression in response to an external input. TCSs respond to a huge range of input signals, including: quorum-sensing molecules [221], certain wavelengths of light [222], physical contact [223], oxidative stress [224] and human hormones [225].

Due to the ubiquitous nature of TCSs across a wide range of bacterial species and the fact that they have not yet been found within mammals [226], there is growing interest in their potential to act as targets for new antibiotics or therapeutics. As such, there are a range of reported TCSs that may be repurposed as biosensor circuits for biotechnology [219]. Daeffler et al. (2017) designed two biosensors to monitor thiosulfate and tetrathionate, molecules that are present in the gut during inflammation [141]. Both of these biosensors were created by repurposing TCSs found within marine *Shewanella* species and placing them within the probi-

otic EcN strain. Concurrently, Riglar et al. (2017) published the creation of another TCS tetrathionate biosensor incorporating a memory switch, which was designed to record the presence of tetrathionate long-term within the gut [118]. Landry et al. (2018) reported a nitrate biosensor within *Bacillus subtilis* and an aspartate biosensor within *E. coli* [219]. A further study created chimeric TCS biosensors, which were able to detect amino acids (in this case glutamate) [227]. Other chimeric TCS biosensors have been designed for the detection of malate [228] and fumarate [229]. Chimeric TCS biosensors are made by combining the sensor domain of one TCS with the histidine phosphotransfer region of another TCS. This allows for the detection of different input signals; while still using the RR and promoter of the original TCS. A review of the growing field of chimeric TCSs is given by Ganesh et al. (2019) [230].

Due to the wide range of TCSs that can be incorporated into biosensor designs, any techniques that can be found for predictably tuning TCS WCB performance may be extremely valuable. The work within this chapter focusses on the Ato TCS found within *E. coli* as a TCS for developing acetoacetate-inducible WCBs and exploring methods of modifying TCS WCB behaviour.

6.1.2 The Ato TCS

The Ato TCS is induced by acetoacetate and is responsible for salt sensitivity, SCFA metabolism, motility and poly-(R)-3-hydroxybutyrate (PHB) synthesis in *E. coli* [231–234]. PHB holds particular interest to industry, as it is one of the only 100% biodegradeable plastics [235]. Due to its unique properties PHB offers a

renewable, more environmentally friendly alternative to traditional petrochemical-derived plastics.

As shown in Figure 6.1, acetoacetate is detected by the AtoS histidine kinase (AtoS HK), resulting in a conformational change in the protein. This then goes on to phosphorylate the AtoC response regulator (AtoC RR). The phosphorylated AtoC then controls activity of the pato promoter, which is upstream of the *atoDAEB* operon. This operon is involved in acetoacetate and SCFA degradation [236]. Interestingly, the Ato system is not thought to respond to SCFAs. However, there is evidence that spermidine can affect PHB sysnthesis and also act as an inducer for the Ato TCS [237]. Currently the exact mechanism responsible for this induction is not known; although, Theodorou et al. proposed a number of viable mechanisms that could explain this observation [237].

6.1.3 Physiological Relevance of Acetoacetate

When glucose is not readily available within the body, the liver produces ketone bodies to act as an alternative energy source. For humans, the most prevalent ketone bodies are acetoacetate, 3-β-hydroxybutyrate (3HB) and acetone [238]. Ketone bodies are always found at some level within the blood (typically less than 0.5 mM) [239], their levels can become elevated during periods of prolonged fasting or intense exercise [240]. For tissues, such as the brain, that can not use fatty acids as an energy source, ketone bodies can provide up to two thirds of the tissue's energy requirements during fasting [241]. Ketone bodies have also been linked to protective effects on the neural system, which has led to the use of ketogenic diets

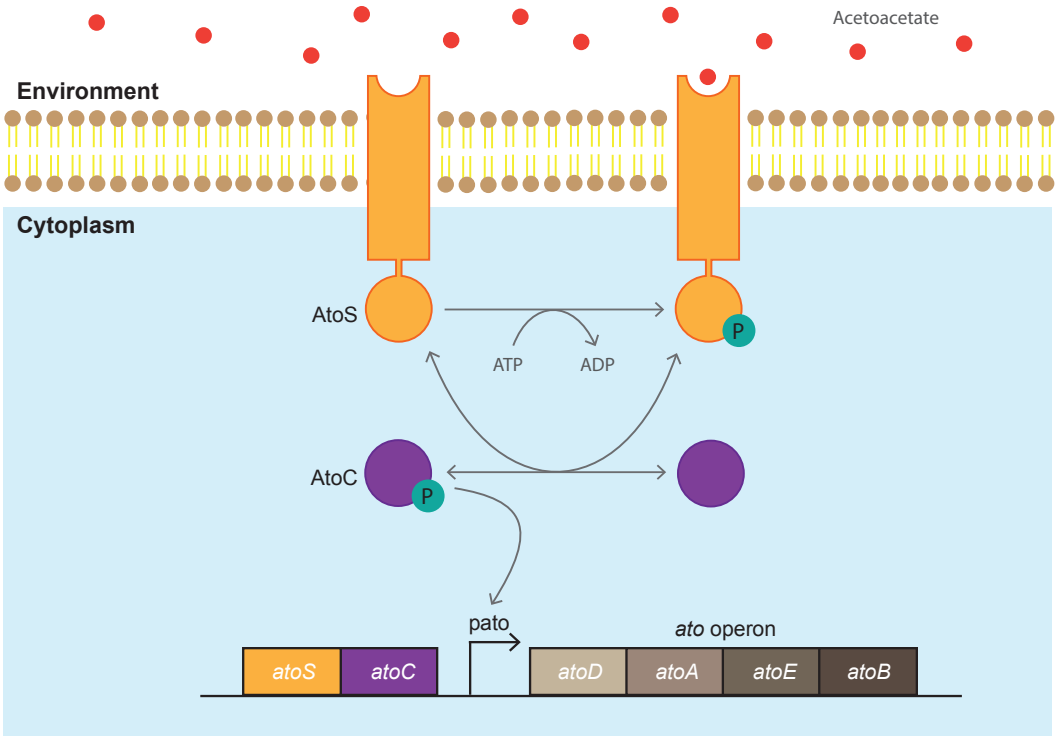

Figure 6.1: Layout of the *ato* operon, involved in acetoacetate sensing. Action of the AtoS histidine kinase and AtoC response regulator, control expression from the pato promoter.

as a method for preventing epileptic seizures [242]. Sustained periods of increased ketone body levels, particularly outside fasting or exercise, can also point towards a number of pathological states. These include alcoholic ketoacidosis, diabetic ketoacidosis or salicylate poisoning [238]. More specifically, acetoacetate has been shown to act as a signalling molecule for muscle regeneration and helped restore muscle function in a mouse model of muscular wasting [243]. Human mesenchymal stem cells (hMSCs) have also been shown to have a preference for acetoacetate as an energy-yielding substrate; leading to suggestions that acetoacetate could be added to hMSC culture medium [244].

6.1.4 Demand for an Acetoacetate WCB

There has not yet been any published examples of acetoacetate WCBs, despite their potential across a range of fields. As mentioned previously, acetoacetate plays a substantial role in human health. In addition, previous studies have looked at developing recombinant *E. coli* strains that are able to produce acetoacetate [245]. Elevated ketone levels in the blood and milk of cows are also linked to ketosis, a condition that adversely affects the health and milk production of cattle [246]. Therefore, acetoacetate WCBs could be useful for biomedical, bioproduction and agricultural applications. Currently, acetoacetate can be measured through a sodiumnitroprusside reaction, on coated strips such as 'Ketostix'. Ketostix are able to detect acetoacetate at concentrations of approximately 5 mg/dl ($\sim$500 μM) and above in urine samples [247]. However, Ato WCBs could offer a more sensitive alternative that may be used for complex *in vivo* monitoring of acetoacetate levels.

6.1.5 Modelling and Rational Design of WCBs

There are numerous examples of attempts to model and rationally engineer WCB behaviour. Mannan et al. were able to model transcription-factor (TF) based biosensors [122]. From their modelling results they were able to identify a number of design principles that could be used to tune TF biosensor behaviour. Berepiki et al. (2020) used a statistical modelling guided approach to rationally design the behaviour of both a TF based biosensor and a metabolic pathway linked biosensor [248]. Their method involved the use of Design of Experiments (DoE); using this approach the authors were able to create a map of potential biosensor behaviour

without the need for a classical iterative approach or the creation of a large library of biosensor constructs. Using this rational approach they were able to design improved biosensors for both protocatechuic and ferulic acid, reporting improvements in the maximum output (f^{max}), detection threshold $K_{1/2}$, sensitivity and operating ranges of the biosensors [248]. Chen et al. (2018) reported a method of effectively tuning the dynamic range of WCBs based on modifications made to the -10 and -35 sites of the output promoter [249]. Furthermore, Gonzalez-Flo et al. (2020) were able to modify the $K_{1/2}$ of AHL (quorum-sensing molecules) responsive biosensors through the modulation of receptor protein expression [250].

In a TCS focused report, Landry et al. (2018) modelled the phosphatase activity of a typical TCS [219]. They were able to show that decreasing phosphatase activity of the HK led to a corresponding decrease in the $K_{1/2}$ of the system. They went on to apply this design to a number of different TCS biosensors; in each case showing that modifying phosphatase activity was able to tune the $K_{1/2}$ of the biosensor. However, one caveat of this system, acknowledged by the authors, is that although increasing phosphatase activity would lead to an increase in $K_{1/2}$ they report very few viable mutations that led to an increase in phosphatase activity. Therefore, this method is only useful for applications where a lower $K_{1/2}$ is desired, which may not necessarily be the aim. Another recent work used a modelling approach to guide the design of a tetrathionate-responsive TCS, through varying RBS strength [251]; before going on to combine the sensor in an AND logic gate. In summary, these examples show that there are a growing number of examples where modelling techniques have been used to guide biosensor construction. These rational approaches

can help to cut down on lab costs and construction time; supporting the design-build-test-learn design cycle of synthetic biology. They have also been shown to apply for a selection of different WCB mechanisms.

6.1.6 Sensitivity Analysis

Sensitivity analysis (SA) allows investigation of how changes in a system from its 'natural' state affect final model output. In addition, SA can help identify which model parameters are particularly important in influencing specific aspects of a system's behaviour. There are several different methods that can be used to perform SA [252]. Within this chapter a modified version of Morris analysis was used. Morris analysis is a global method, which uses a one-at-a-time (OAT) approach to allow the exploration of large parameter spaces [253]. Within this method all parameters are initially set to a particular value. Parameters are then varied randomly, within pre-allocated bounds. This process is repeated until all parameters have been changed, creating a parameter trajectory, illustrated in Figure 6.2. The impact this trajectory has on model behaviour ('elementary effects') is then recorded. This process is repeated until the whole parameter space has been sampled. The impact each parameter has on model behaviour is then ranked through the mean value of the elementary effects, μ. Campolongo et al. (2007) suggested an updated version of this process, where the μ measure of impact is replaced by μ^* [254]. This updated version takes the mean of the absolute values of elementary effects, preventing the cancellation of opposing effects. The μ^* measure is employed within this chapter.

As stated here, SA can provide a useful starting point when proposing hypothe-

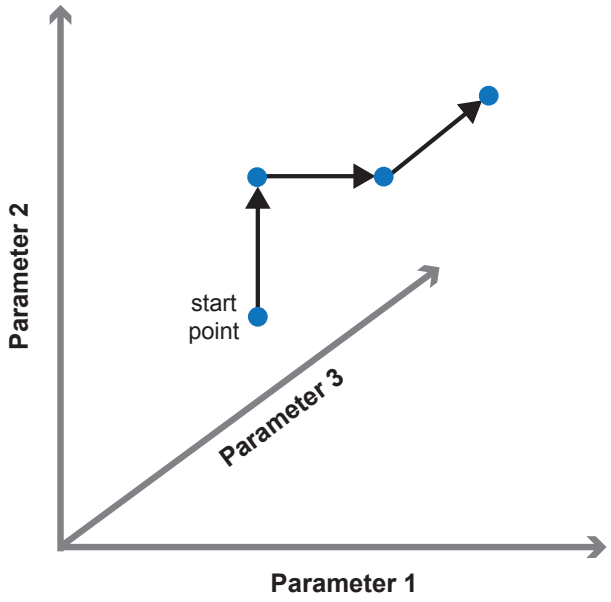

Figure 6.2: The one-at-a-time (OAT) sampling method used during Morris sensitivity analysis. Within this method each parameter is varied individually, until all parameters have been adjusted to create a parameter trajectory. This trajectory is then used to simulate changes in the final output of the model.

ses of how to redesign complex systems to produce a desired behaviour. Therefore, within this chapter SA was employed to model the parameters of the Ato TCS. To the best of our knowledge, Morris SA has not previously been used in the study of TCS response. SA may be able to identify promising areas for focusing effort during the design of new Ato WCBs.

6.2 Aims

Within this chapter, I wished to further develop an Ato ODE model describing the AtoSC TCS. Following this, I aimed to construct an acetoacetate-inducible biosensor, based on the AtoSC system. Subsequently, I aimed to create modified versions of the Ato biosensor, through varying plasmid expression of the AtoSC TCS

components- characterising any differences in their performance. Finally, I aimed to use the ODE model to explore possible future designs for the Ato WCBs; through evaluating the performance of the WCBs against their simulated model behaviour.

6.3 Results

6.3.1 Modelling the Ato TCS

As discussed previously, methods for rationally designing TCS biosensor behaviour could be an extremely valuable tool. In order to begin exploring methods of achieving this, an ODE model was constructed to try and model an Ato biosensor. This model was originally adapted from a previously published TCS model [255], through the addition of reactions describing the expression of GFP from the biosensor plasmid. This model described the well-characterised EnvZ/OmpR TCS; chosen as this TCS produces a graded response (similar to AtoSC) and is a prototypical TCS that does not require auxiliary proteins [255]. Figure 6.3 provides an overview of the model parameters and species that were used to describe the AtoSC TCS behaviour.

Firstly, AtoS can be autophosphorylated in the presence of acetoacetate, in the reverse of this reaction it can also be dephosphorylated:

$$S \underset{k_{ad}}{\overset{k_{ap}}{\rightleftharpoons}} S^*$$

Within this model the rate of k_{ap} is determined by the concentration of acetoacetate inducer; therefore, this rate was varied to simulate changing levels of acetoacetate inducer (as in the original study, from which this model was adapted) [255].

Following the autophosphorylation of AtoS, the phosphoryl group can be transferred between the AtoC response regulator. Firstly, AtoC binds to phosphorylated AtoS:

$$S^* + C \underset{k_{d1}}{\overset{k_{b1}}{\rightleftharpoons}} S^*C$$

The phosphoryl group is then transferred, followed by disassociation of the AtoS/AtoC complex:

$$S^*C \xrightarrow{k_{pt}} SC^*$$

$$SC^* \underset{k_{b2}}{\overset{k_{d2}}{\rightleftharpoons}} S + C^*$$

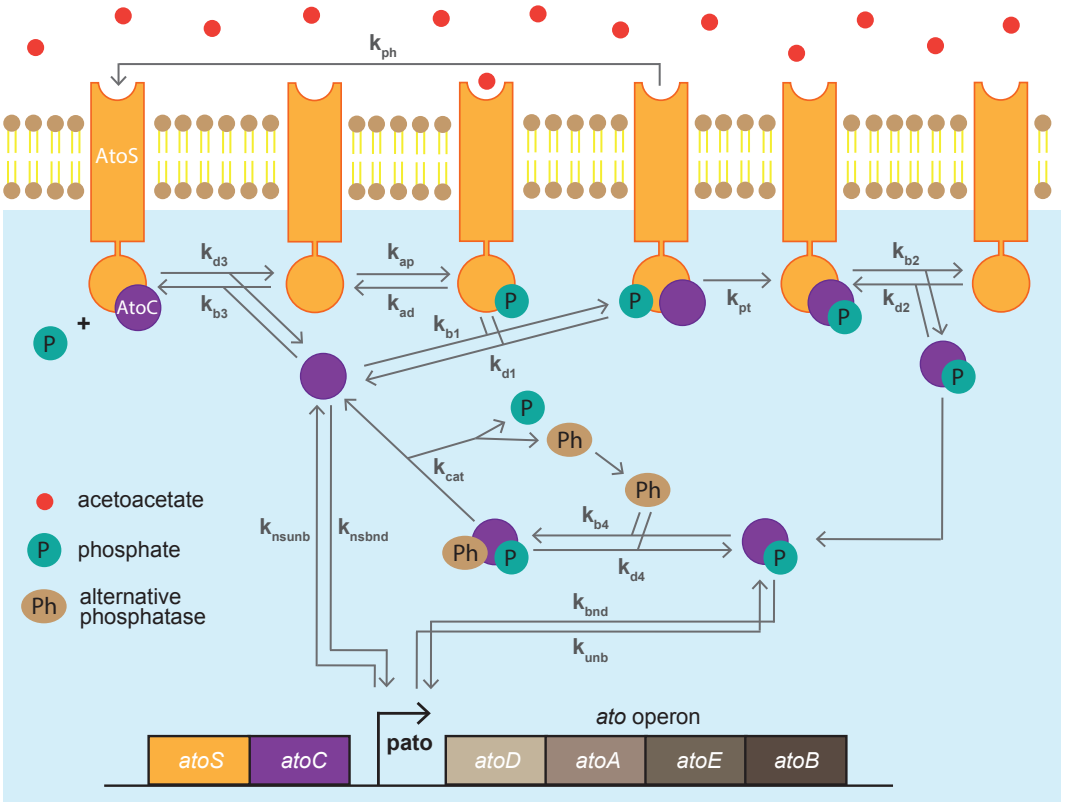

Figure 6.3: The major species and equations included within the developed Ato biosensor ODE model. The estimated values for each of these parameters are given in Table 6.1.

Alongside transferring the phosphoryl group to the RR, some HKs have been shown to dephosphorylate their cognate RR in the absence of their inducer. Therefore, an equation to describe this behaviour was added to the model. However, as this reaction has not yet been confirmed to take place in the Ato TCS it can effectively be ignored by setting the rate of k_{ph} to zero:

$$SC^* \xrightarrow{k_{ph}} SC + P$$

In addition, it has been shown that it is possible for HKs to bind to their RR even in the absence of a phosphoryl group. This leads to the formation of a 'deadend' complex, which effectively sequesters RR from the system:

$$S + C \underset{k_{d3}}{\overset{k_{b3}}{\rightleftharpoons}} SC$$

Previous reports have implied that the AtoC RR may interact with the HK of another TCS system *in vitro* [256]. Although a later study did not find evidence of this interaction *in vivo* [220]. Therefore, the possibility that AtoC may interact with and be dephosphorylated by an alternative HK within the cell was added to the model through the following reactions:

$$Ph + C^* \underset{k_{d4}}{\overset{k_{b4}}{\rightleftharpoons}} PhC^*$$

$$PhC^* \xrightarrow{k_{cat}} Ph + C$$

The phosphorylated AtoC interacts with the pato promoter to trigger expression of the *patoDAEB* operon. Within this model, binding of unphosphorylated AtoC to the pato promoter was also included as a source of leaky GFP expression:

$$C^* + p_{ato} \underset{k_{unb}}{\overset{k_{bnd}}{\rightleftharpoons}} C^* p_{ato}$$

$$C + p_{ato} \underset{k_{nsunb}}{\overset{k_{nsbnd}}{\rightleftharpoons}} Cp_{ato}$$

Finally, reactions which describe the production of GFP controlled by the pato promoter were added to the model:

$$C^* p_{ato} \overset{k_{pmgexp}}{\rightarrow} mGFP + C^* p_{ato}$$

$$Cp_{ato} \overset{k_{npmgexp}}{\rightarrow} mGFP + Cp_{ato}$$

$$mGFP + R \overset{k_{mgbnd}}{\rightarrow} mGFPR$$

$$mGFPR \overset{k_{gexp}}{\rightarrow} mGFP + uGFP + R$$

$$uGFP \overset{k_{mat}}{\rightarrow} GFP$$

$$mGFP \overset{k_{mgdeg}}{\rightarrow} \emptyset$$

$$GFP \overset{k_{gdeg}}{\rightarrow} \emptyset$$

All of the above reactions were then used to develop the differential equations for the Ato biosensor model. These can be split into two distinct groups:

1. Equations describing the Ato TCS:

$$\dot{S^*} = (k_{ap}S + k_{d1}SC^*) - S^*(k_{ad} + k_{b1}C)$$

$$\dot{C^*} = (k_{d2}SC^* + k_{d4}PhC^* + k_{unb}C^* p_{ato}) - C^*(k_{b2}S + k_{b4}Ph + k_{bnd}p_{ato})$$

$$\dot{SC} = (k_{b3}S.C + k_{ph}SC^*) - k_{d3}SC$$

$$\dot{S^*C} = k_{b1}S^*.C - S^*C(k_{d1} + k_{pt})$$

$$\dot{SC^*} = (k_{pt}S^*C + k_{b2}S.C^*) - SC^*(k_{d2} + k_{ph})$$

$$\dot{PhC^*} = (k_{b4}Ph.C^*) - PhC^*(k_{d4} + k_{cat})$$

$$\dot{C^*p_{ato}} = (k_{bnd}C^*.p_{ato}) - k_{unb}C^*p_{ato}$$

$$\dot{Cp_{ato}} = (k_{nsbnd}C.p_{ato}) - k_{nsunb}Cp_{ato}$$

2. Equations describing GFP biosensor elements:

$$\dot{mGFP} = (k_{pmgexp}C^*p_{ato} + k_{npmgexp}Cp_{ato} + k_{gexp}mGFPR)$$

$$- mGFP(k_{mgbnd}R + k_{mgdeg})$$

$$\dot{mGFPR} = (k_{mgbnd}mGFP.R) - k_{gexp}mGFPR$$

$$\dot{uGFP} = (k_{gexp}mGFPR) - k_{mat}uGFP$$

$$\dot{GFP} = (k_{mat}uGFP) - k_{gdeg}GFP$$

The conservation laws for the AtoSC model described above were as follows:

$$S_{tot} = S + S^* + S^*C + SC^* + SC$$

$$C_{tot} = C + C^* + S^*C + SC^* + SC + PhC^* + C^*p_{ato} + Cp_{ato}$$

$$Ph_{tot} = Ph + PhC^*$$

$$pato_{tot} = p_{ato} + C^*p_{ato} + Cp_{ato}$$

$$R_{tot} = R + mGFPR$$

Table 6.1: Ato biosensor model parameters. HK = histidine kinase (AtoS), RR = response regulator (AtoC), Ph = alternative phosphatase, * denotes phosphorylation. † Varied to simulate acetoacetate inducer concentrations. (Reasoning behind parameter guesses is given in Appendix C.2)

	Description	**Value**	**Ref.**
k_{ap}	HK autophosphorylation	0 - 10 s^{-1}	†
k_{ad}	HK* autodephosphorylation	0.001 s^{-1}	[255]
k_{pt}	Transfer of phosphoryl group to RR from HK*	1.5 s^{-1}	[255]
k_{ph}	Dephosphorylation of RR* by HK	0 s^{-1}	[255]
k_{b1}	Binding of HK* to RR	0.5 μM s^{-1}	[255]
k_{d1}	Dissociation of bound HK* and RR	0.5 s^{-1}	[255]
k_{b2}	Binding of HK and RR*	0.05 μM s^{-1}	[255]
k_{d2}	Dissociation of bound HK and RR*	0.5 s^{-1}	[255]
k_{b3}	Binding of HK and RR	0.5 μM s^{-1}	[255]
k_{d3}	Dissociation of HK and RR	0.5 s^{-1}	[255]
k_{b4}	Binding of Ph and RR	0.5 μM s^{-1}	[255]
k_{d4}	Dissociation of Ph and RR	0.5 s^{-1}	[255]
k_{cat}	Dephosphorylation of RR* via Ph	0.05 s^{-1}	[255]
k_{bnd}	Binding of RR* to pato promoter	0.5 s^{-1}	[255]
k_{unb}	Unbinding of RR* and pato promoter	0.05 s^{-1}	[255]
k_{nsbnd}	Binding of RR to pato promoter	1x10^{-5} s^{-1}	guess
k_{nsunb}	Unbinding of RR and pato promoter	0.001 s^{-1}	guess
	Biosensor element		
k_{pmgexp}	Trans. of GFPmRNA from RR* bound to pato	0.07 s^{-1}	guess
$k_{npmgexp}$	Trans. of GFPmRNA from RR bound to pato	0.007 s^{-1}	guess
k_{gexp}	Translation of unfolded GFP from mRNA	0.08 μM s^{-1}	guess
k_{mgdeg}	mGFP degradation	0.00223 s^{-1}	guess
k_{gdeg}	GFP degradation	0.00057 s^{-1}	guess
k_{mat}	maturation of mGFP from GFP	0.00042 s^{-1}	guess
	Species concentrations		
S_{tot}	*atoS* concentration	0.17 μM	[255]
C_{tot}	*atoC* concentration	6.0 μM	[255]
Ph_{tot}	Phosphate concentration	0.17 μM	[255]
$pato_{tot}$	Total pato promoter concentration	10.0 μM	[255]
R_{tot}	Ribosome concentration	10.0 μM	[255]

6.3.2 Developing an Acetoacetate WCB

As shown in Figure 6.1, the Ato sensing mechanism consists of three major components; the AtoS HK, the AtoC RR and the pato promoter. A basic Ato WCB was constructed by placing the pato promoter in front of a GFP output (Figure 6.6A). Subsequently, various iterations of this base biosensor were created and tested in several host strains. To help the reader distinguish between the different biosensors and host strains referred to within the subsequent sections of this chapter a naming convention for both the strains and plasmids is used. Host strains are represented by a symbol, which highlights whether the host has genomic expression of the AtoS HK (orange dot) or the AtoC RR (purple dot) proteins, this is shown in Figure 6.4. The plasmid biosensors are represented by a code name that identifies the components contained within the plasmid backbone. The biosensor names, alongside their plasmid layout, are given in Figure 6.5.

The ASAH0 biosensor is the most basic biosensor that can be constructed from the AtoSC TCS and incorporates only the pato promoter, relying on host expression of both the AtoS and AtoC proteins. As shown in Figure 6.6A, upon exposure to acetoacetate, the AtoS HK should phosphorylate the AtoC RR, which will then trigger expression of a GFP output from the pato promoter. The ASAH0 biosensor was characterised in three AtoSC^{+} strains. NEBα is a lab strain commonly used for cloning, BW25113 (as discussed in chapter 5) is the parent strain of the Keio knockout collection and *E. coli* Nissle was chosen as a probiotic strain (commonly used in microbiome engineering studies). As expected, ASAH0 produced a strong increase in GFP signal with increasing acetoacetate concentration in all three strains

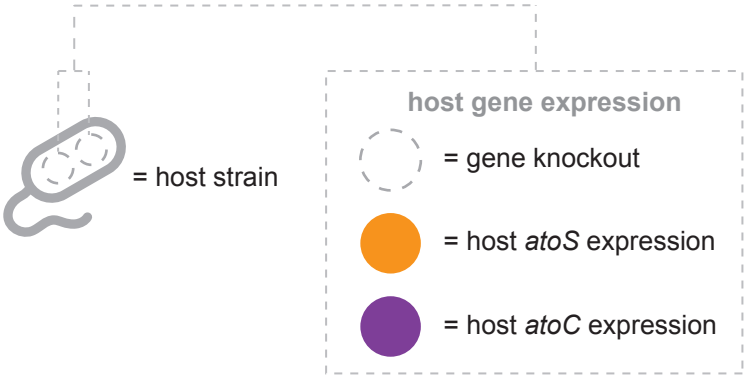

Symbol:	Strain:	*atoSC* expression:
	NEBα	both
	Nissle	both
	BW25113	both
	BW28878	Δ*atoS*, Δ*atoC*
	JW2213	Δ*atoS*
	JW2214	Δ*atoC*

Figure 6.4: A number of different strains are used within this chapter. In order to aid in understanding, a symbol designation was developed to highlight which strain is used to host each Ato biosensor. The two dots represent genomic expression of the AtoS (purple) and AtoC (orange) proteins. No dots represents a knockout of both genes within the strain.

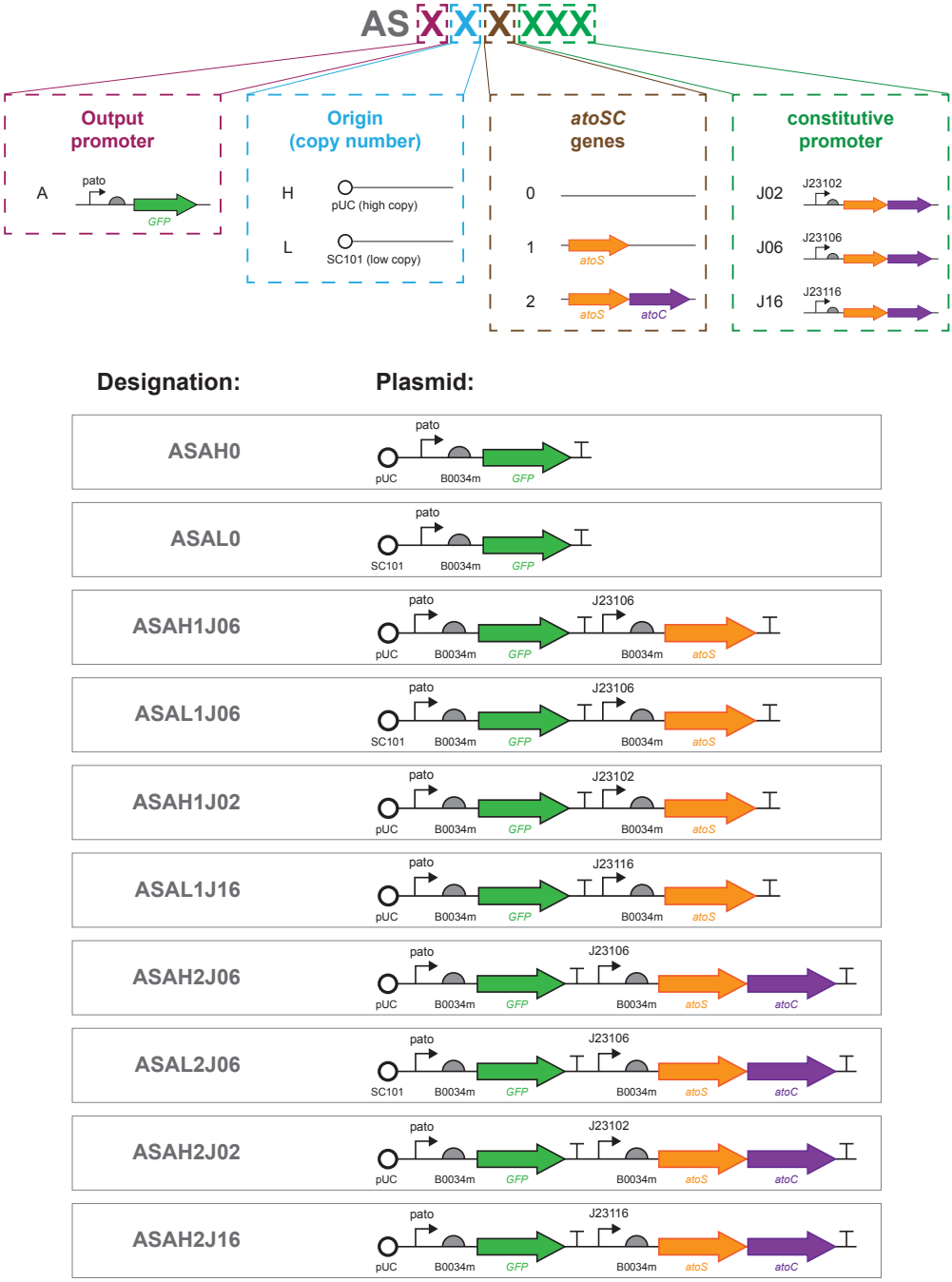

Figure 6.5: As with host strains, a number of different iterations of the acetoacetate biosensors were developed for this chapter. In order to help aid understanding, a naming convention was designed to describe the layout of each biosensor plasmid based on the code displayed here.

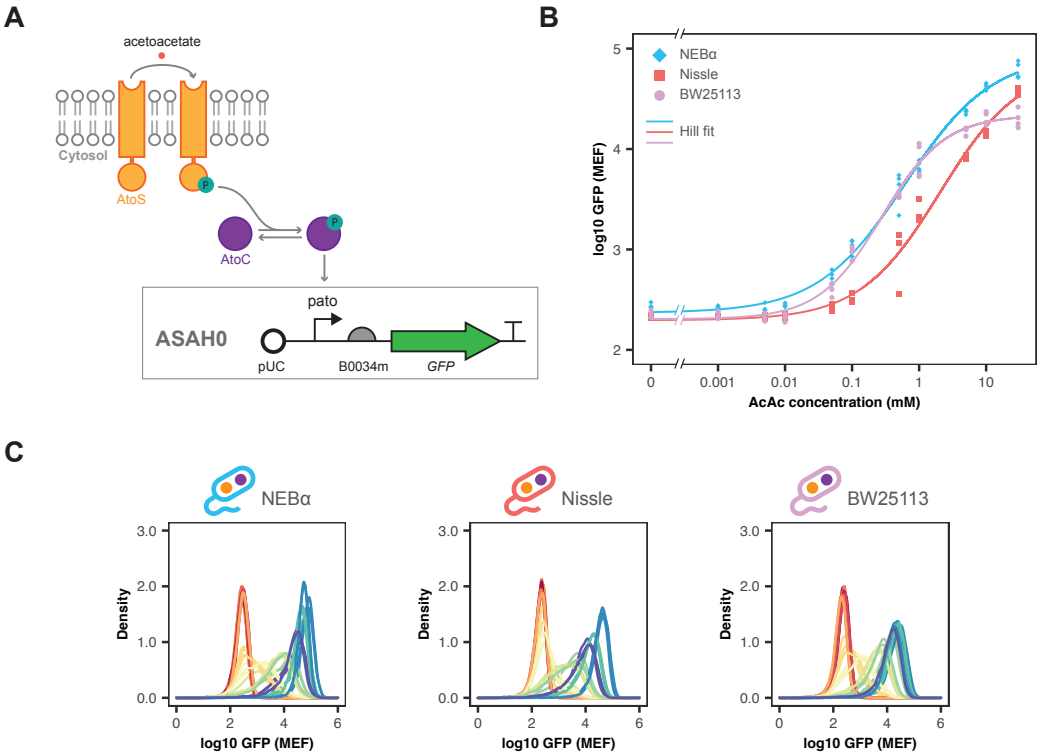

Figure 6.6: Performance of the ASAH0 version of the acetoacetate biosensors in 3 *E. coli* strains. (**A**) Plasmid design of the ASAH0 biosensor, relies on host expression of the *atoS* and *atoC* genes. (**B**) Medians plots of GFP fluorescence for varying acetoacetate concentrations in each of the three different host strains. (**C**) Density plots of GFP fluorescence of ASAH0 in the given host strain (n = 3 biological repeats for Nissle, 4 for NEBα and BW25113).

(Figure 6.6B and 6.6C). The fitted Hill parameters for this strain, and all subsequent strains of this chapter, are given in Table C.2 of Appendix C. The response was similar in all three strains, with BW25113 showing a slightly lower fitted $K_{1/2}$ value and NEBα showing the highest f^{max}.

From these results it was clear that the AtoSC TCS could be used to build an acetoacetate-inducible biosensor. Following testing of ASAH0 in AtoSC^{+} strains, the biosensor was tested in a number of knockout strains in order to further investigate biosensor behaviour in the presence of AtoS and AtoC. BW28878 is an AtoSC^{-} strain. JW2213 and JW2214 were obtained from the Keio knockout col-

lection and are Δ*atoS* and Δ*atoC* knockouts, respectively. In order to verify the correct knockout strains were received, PCR amplification was performed. This PCR confirmation required the design of primers that were able to bind within the regions of interest, these are given in Appendix C. The results of this confirmation can be seen in Figure 6.7E. Initial PCR reactions gave the expected pattern. However, attempts to repeat this for the JW2213 and JW2214 strains were inconclusive; therefore, the Δ*atoS* and Δ*atoC* strains were reordered before performing the rest of the characterisation shown in Figure 6.7.

As the Ato biosensors were going to be tested in different combinations of the 'Ato' strains (BW25113, BW28878, JW2213, JW2214) preliminary characterisation was performed to confirm that acetoacetate had no effect on the empty host strains. Addition of 20 mM acetoacetate produced very little increase in the GFP of any the four strains (Figure 6.7B and 6.7C). Also, neither the AtoSC knockouts nor addition of acetoacetate produced any substantial differences in growth between the four strains (6.7D). In order to further confirm that acetoacetate had no effect on any of these strains a full concentration assay was performed, spanning the concentration range over which the Ato biosensors were found to be responsive. As can be seen in Figure 6.8, no change in GFP fluorescence was seen in any of the four strains across this concentration range.

6.3.3 Genome vs Plasmid Expression of AtoSC

The ASAH0 biosensor was characterised in all four of the Ato strains. Before performing induction assays a growth assay was carried out to confirm that the addi-

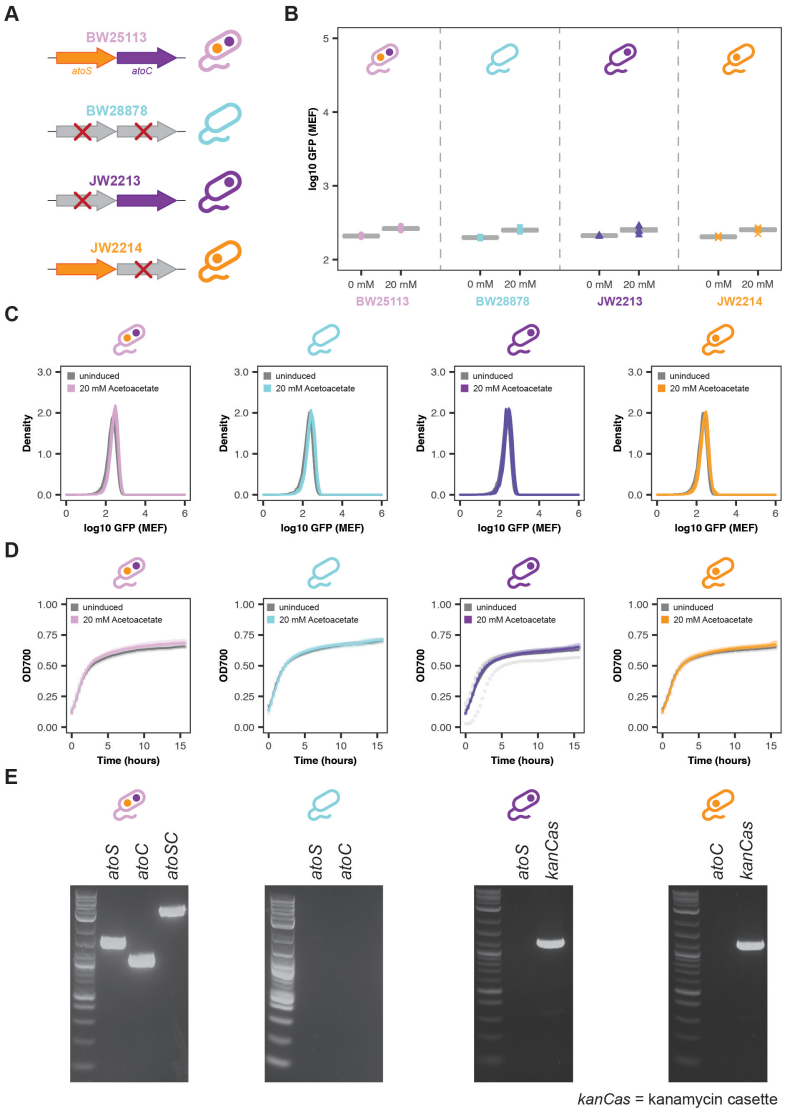

Figure 6.7: Characterisation of the Ato knockout strains. (**A**) Strain gene expression. (**B**) Induction of knockout strains with 20 mM acetoacetate (n = 4 biological repeats, points give medians and boxplot gives mean of medians). (**C**) Density plots of GFP fluorescence of strains exposed to 20 mM acetoacetate (n = 4 biological repeats). (**D**) Growth curves of strains exposed to 20 mM acetoacetate (n = 4 biological repeats). (**E**) PCR confirmation of strain knockouts.

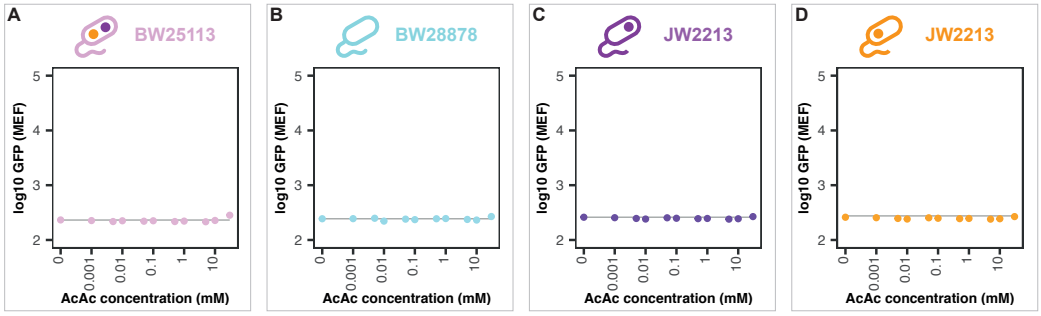

Figure 6.8: Concentration assays of the four empty 'Ato' knockout strains. Strains: (**A**) BW25113, (**B**) BW28878, (**C**) JW2213 and (**D**) JW2214. Points give medians, lines show median GFP fluorescence of uninduced cells (n = 1 biological repeat).

tion of acetoacetate would not adversely affect the growth of the BW25113 ASAH0 cells. As shown in Figure 6.9 no substantial changes in cell growth were seen up to an acetoacetate concentration of 31.6 mM. However, addition of acetoacetate produced a strong increase in GFP when ASAH0 was transformed into the BW25113 host (Figure 6.10B, as also seen in the characterisation in Figure 6.6B). In the BW28878, JW2213 and JW2214 hosts, no increase in GFP was seen.

ASAH2J06 was generated through addition of the *atoS*/*atoC* genes to ASAH0, under the control of a constitutive promoter; all of the other components of the plasmid were kept the same. The layout of this biosensor is given in Figure 6.11A. In contrast to ASAH0, the ASAH2J06 biosensor produced an acetoacetate-inducible change in GFP expression in all four Ato strains (Figure 6.11B).

In order to explore the effect of plasmid vs host gene expression in more detail the responses of ASAH0 in BW25113 (only host expression of AtoS/AtoC) and ASAH2J06 in BW28878 (only plasmid expression of AtoS/AtoC) were compared more closely in Figure 6.12. ASAH0 displayed a greater f^{max}, dynamic range and

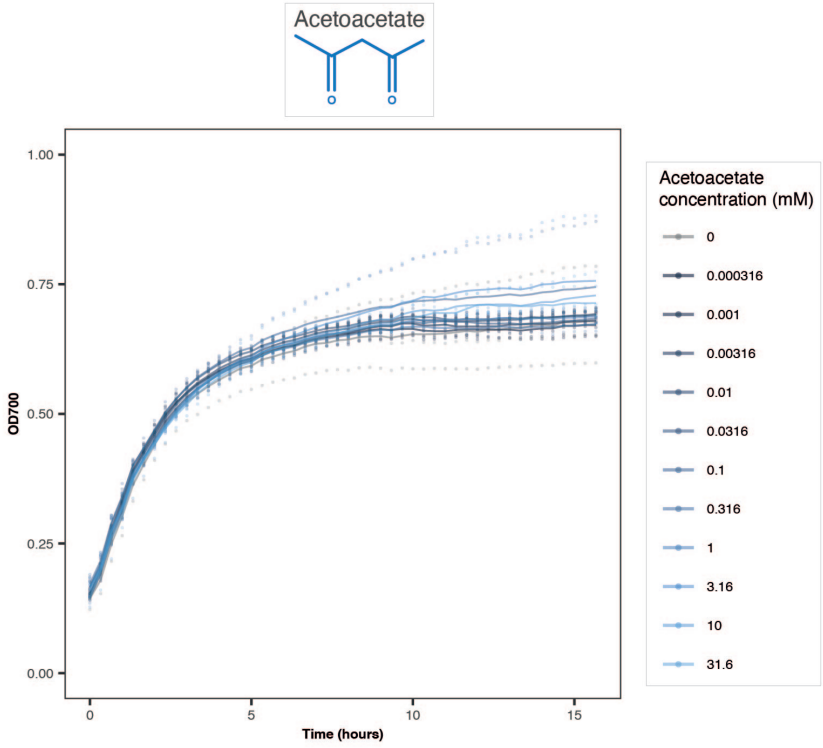

Figure 6.9: The effect of acetoacetate on the growth of the BW25113 strain hosting the ASAH0 biosensor plasmid. Points indicate individual repeats and solid lines mean values (n = 3 biological repeats).

lower f^{min} than ASAH2J06. However, ASAH2J06 showed a lower fitted $K_{1/2}$ (all Hill fit parameters given in Table C.2 of Appendix C). From the characterisation of ASAH0 and ASAH2J06 in all four strains, it can be seen that BW25113 ASAH0 produced the greatest dynamic range of all eight configurations. Interestingly, the higher f^{min} seen in ASAH2J06 was also present when the ASAH0 plasmid was transformed into the same host strain (BW28878, grey line Figure 6.12B), suggesting that the increase in basal expression was caused by the biosensor plasmid, rather than differences in the host strains (supported by the characterisation in Figure 6.8).

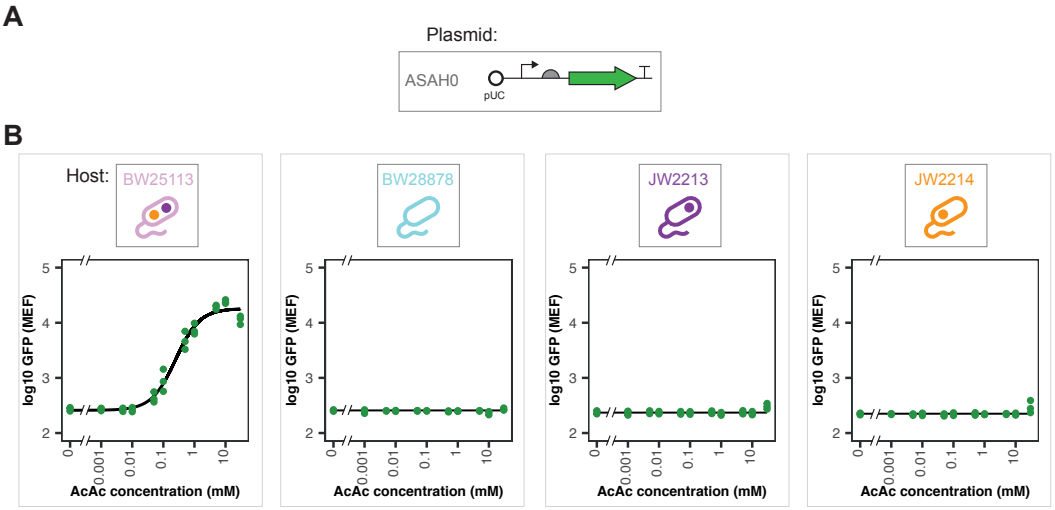

Figure 6.10: The performance of the ASAH0 biosensor plasmid in the four Ato knock-out strains. (**A**) Plasmid layout of ASAH0. (**B**) Median GFP fluorescence of ASAH0 biosensor in each of the given strains, at varying acetoacetate concentrations (n = 3 biological repeats, BW25113 host data fit with Hill function, other lines show median GFP of uninduced cells).

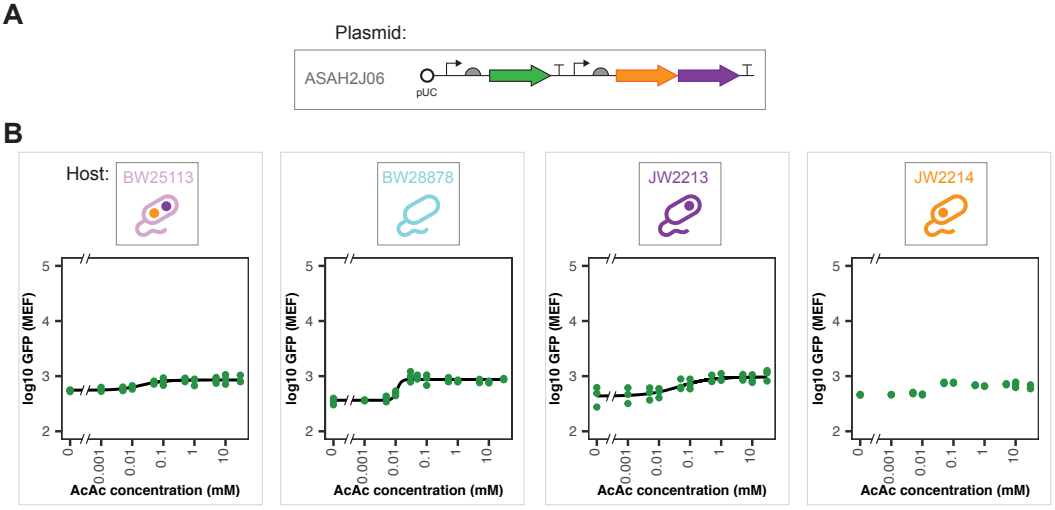

Figure 6.11: The performance of the ASAH2J06 biosensor plasmid in the four Ato knock-out strains. (**A**) Plasmid layout of ASAH2J06. (**B**) Median GFP fluorescence of ASAH2J06 biosensor in each of the given strains, at varying acetoacetate concentrations (n = 3 biological repeats, data fit with Hill function).

6.3.4 Specificity of the ASAH0 WCB

After demonstrating that the Ato TCS could be used to construct acetoacetate-inducible WCBs, alternative inducers were explored to check the specificity of the

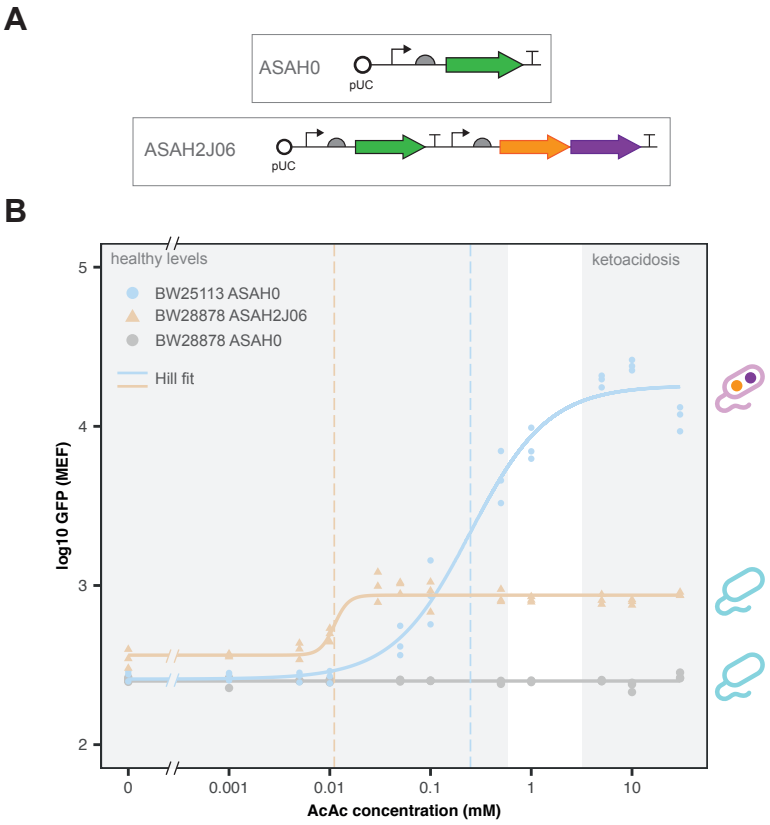

Figure 6.12: Response of the ASAH0 plasmid in both the BW25113 and BW28878 strains, compared to performance of the ASAH2J06 plasmid in the BW28878 strain. (**A**) Plasmid layouts of ASAH0 and ASAH2J06. (**B**) Median GFP fluorescence of the biosensors exposed to various concentrations of acetoacetate (n = 3 biological repeats, data fit with Hill function, dashed lines indicate the fitted $K_{1/2}$ values, grey areas indicate typical ketone body concentrations in a healthy state or ketoacidosis, cell symbols give the host chassis for each of the three WCB strains).

ASAH0 circuit. Six alternative inducers were tested, including SCFAs (acetate, propionate and butyrate), ketone bodies (acetone and hydroxybutyrate) and spermidine (a polyamine). All were tested at a concentration of 20 mM, a concentration above that shown to give maximum acetoacetate induction. When characterised in LB media acetoacetate produced the highest increase in GFP (Figures 6.13 and 6.14A), while the alternative inducers showed similar levels of GFP to the uninduced control. As 20 mM is a relatively high concentration, growth assays were measured to

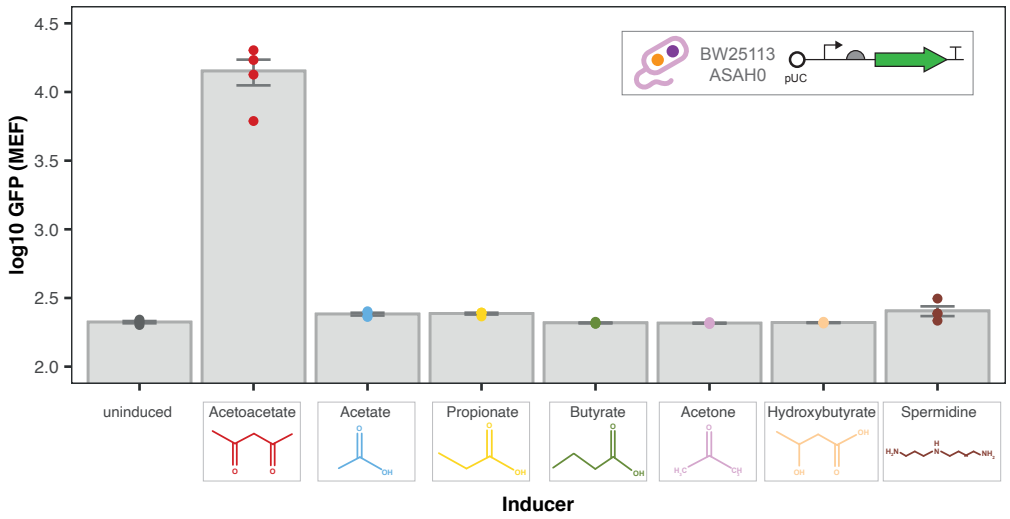

Figure 6.13: Median GFP fluorescence of BW25113 ASAH0 exposed to a range of alternative inducer molecules, all at 20 mM within LB media, compared to that of the biosensor exposed to acetoacetate. (n = 4 biological repeats, points give medians and bars mean of medians ± SE)

ensure the lack of GFP was not caused by toxicity of any of the inducers. All inducers produced no substantial changes in growth compared to the uninduced control, except for spermidine (Figure 6.15G), which was seen to prevent all cell growth.

As mentioned in section 6.1.2, a previous report provided strong evidence that spermidine can act as an alternative inducer for the Ato TCS [237]. However, the results collected in Figures 6.13 did not show an increase in GFP response to spermidine. From the subsequent growth curves it could be seen that spermidine was preventing cell growth at 20 mM (Figure 6.15). Therefore, in order to investigate whether the low GFP response when exposed to spermidine was caused purely by toxicity of the inducer, a full concentration assay was performed testing a range of lower spermidine concentrations (Figure 6.16). From these assays spermidine was found to produce little change in GFP response over concentrations commensurate with acetoacetate induction (Figure 6.16B).

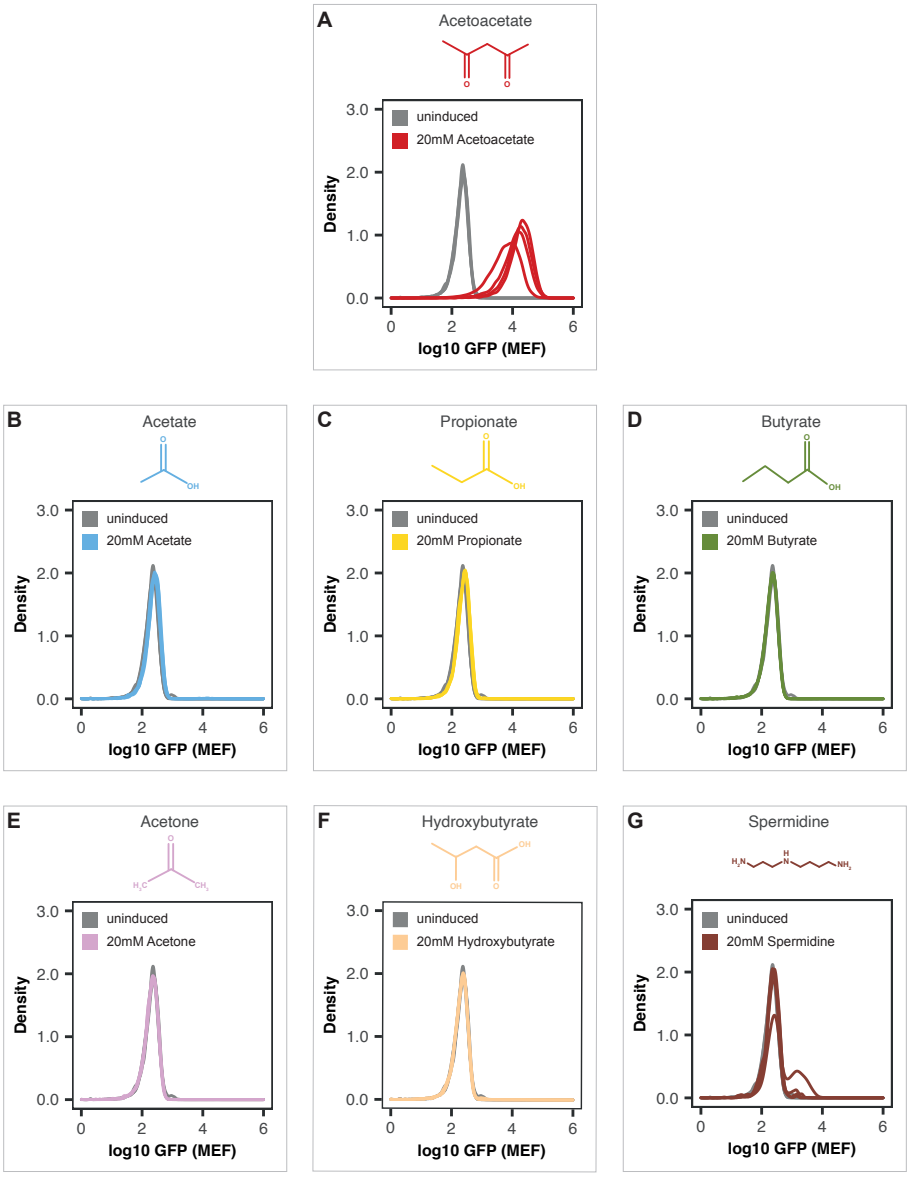

Figure 6.14: GFP fluorescence density plots of BW25113 ASAH0 exposed to a range of alternative inducer molecules, all at 20 mM within LB media, compared to that of the biosensor exposed to acetoacetate. Inducers: (**A**) uninduced, (**B**) acetoacetate, (**C**) acetate, (**D**) propionate, (**E**) butyrate, (**F**) acetone, (**G**) hydroxybutyrate and (**H**) spermidine (n = 4 biological repeats).

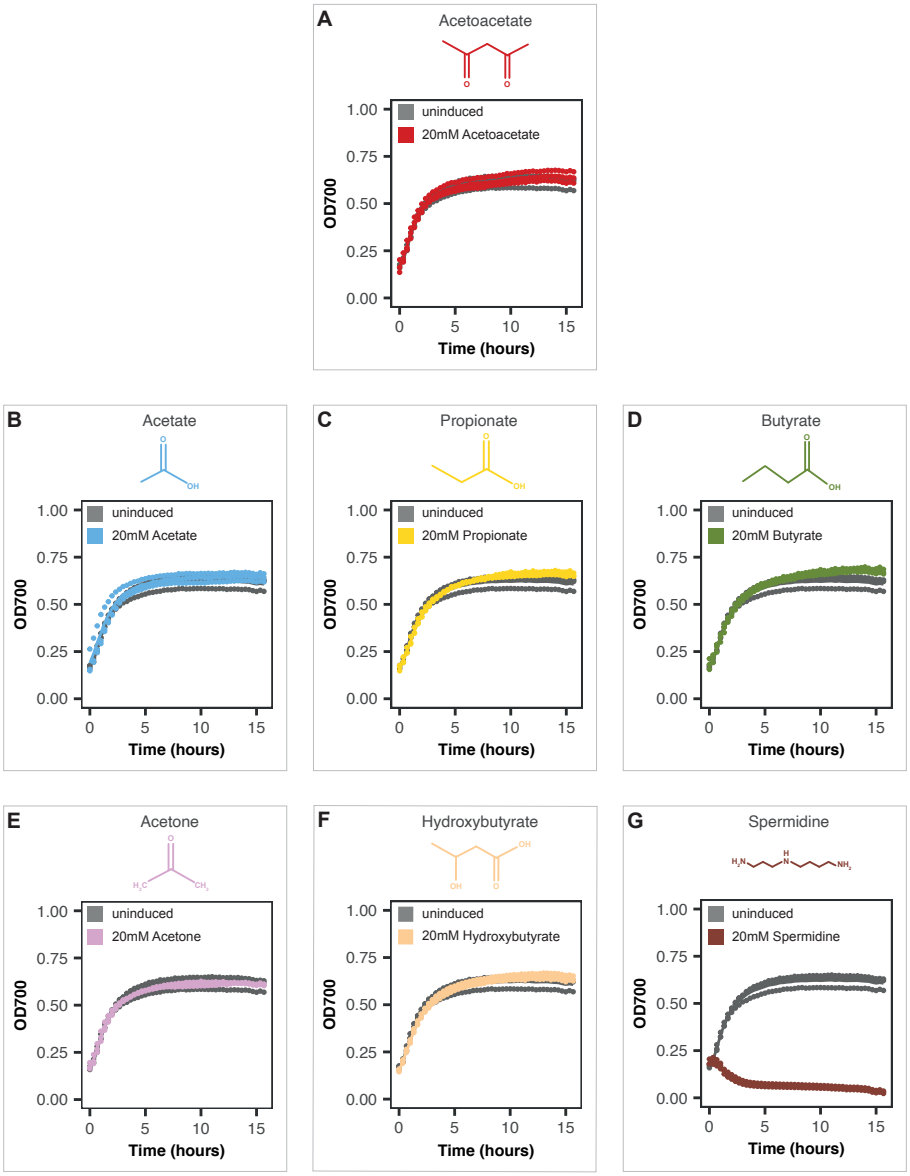

Figure 6.15: Growth curves of BW25113 ASAH0 exposed to a range of alternative inducer molecules, all at 20 mM within LB media, compared to that of the biosensor exposed to acetoacetate. Inducers: (**A**) uninduced, (**B**) acetoacetate, (**C**) acetate, (**D**) propionate, (**E**) butyrate, (**F**) acetone, (**G**) hydroxybutyrate and (**H**) spermidine (n = 4 biological repeats, solid lines give means and points individual repeats).

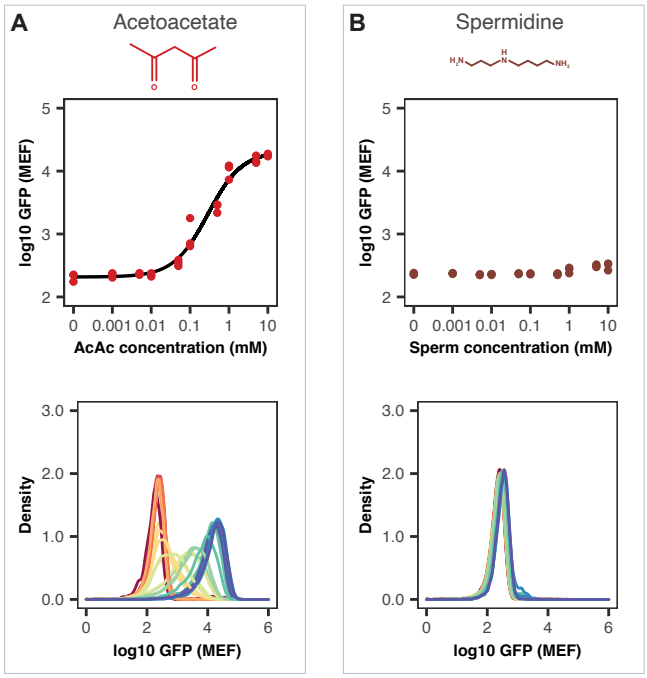

Figure 6.16: Concentration assays of BW25113 ASAH0 exposed to both (**A**) acetoacetate and (**B**) spermidine, within LB media. Top plots show median GFP fluorescence and bottom plots give density plots of GFP fluorescence (n = 3 biological repeats, line is data fit to Hill equation).

6.3.5 Model Guided Design of Ato WCBs

As mentioned in section 6.1.5, methods of tailoring biosensor response towards specific applications would be extremely useful. Therefore, the Ato model detailed in section 6.3 was explored further in order to try and identify alternative biosensors that may result in improved behaviour. As can be seen in the model schematic given in Figure 6.3, there is a large number of parameters and species that are involved in the Ato TCS. This presents a daunting task when trying to decide which parameters to change during circuit engineering. Due to this large number of parameters, Morris SA (discussed in section 6.1.6) was performed to try and identify the parameters that have the largest effect on biosensor behaviour. The results of

this attempt at Morris analysis are shown in Figure 6.18. For the $K_{1/2}$, parameter k_{b1} (the rate that AtoC binds to phosphorylated AtoS) was predicted to have the largest impact. This analysis was also performed for the other major components of biosensor behaviour (f^{min}, f^{max} etc.). Table 6.2 provides a summary of the mean effect that each parameter was predicted to have across all of the aspects of biosensor behaviour investigated. From this analysis AtoS, AtoC and pato concentration were all predicted to be in the top five most influential parameters. I wished to investigate whether I could tune biosensor performance purely through adjusting the expression levels of these three major TCS components within the biosensor plasmids. All three concentrations, AtoS HK, AtoC RR and the pato promoter, can be readily tuned experimentally through varying of plasmid copy number or strength of constitutive expression. In theory, this would require no need for modification of protein sequence/structure or binding affinities. In addition, it was hypothesised that any methods discovered may be portable to other TCS biosensors.

In order to investigate the effect of changing these concentrations multiple simulations were run, with AtoS, AtoC and pato concentrations varied over a wide range. These simulations are shown in Figure 6.17. Increasing AtoS concentration corresponded to a rapid decrease in the predicted $K_{1/2}$ of the biosensor (Figure 6.17A). In addition, at low concentrations f^{max} was predicted to increase and inversely, at high concentrations f^{min} was predicted to decrease. Varying AtoC concentration appeared to have no effect on the $K_{1/2}$ of the biosensor. However, increasing AtoC concentration led to an increase in both the f^{min} and f^{max} of the system, with a corresponding decrease in the dynamic range. Varying pato concen-

tration had a more complex effect on the predicted behaviour. Increasing pato led to an initial increase in both f^{min} and f^{max}. However, at high pato concentrations the levels of f^{min} dramatically increased, leading to an almost linear response (similar to the effect of increasing AtoC concentration).

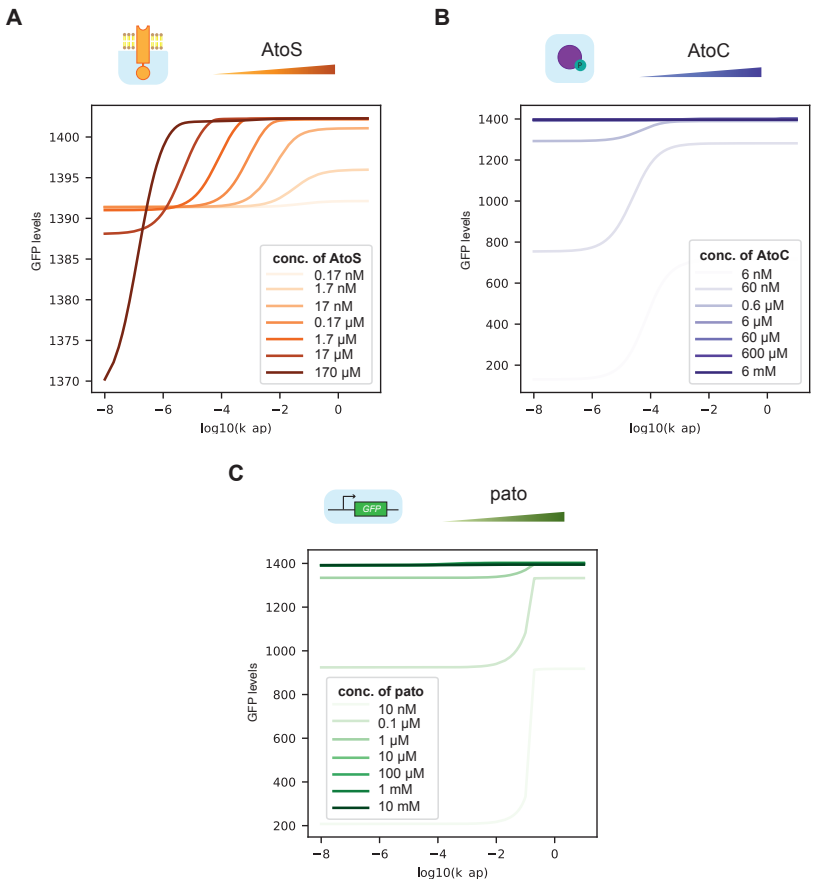

Figure 6.17: Simulated induction curves of the Ato WCBs, with the concentration of a central component varied in each panel: (**A**) the AtoS HK, (**B**) AtoC RR and (**C**) pato promoter. Concentrations were varied over a large range to try and capture the full behaviour of the system (all other values were kept constant, as given in Table 6.1).

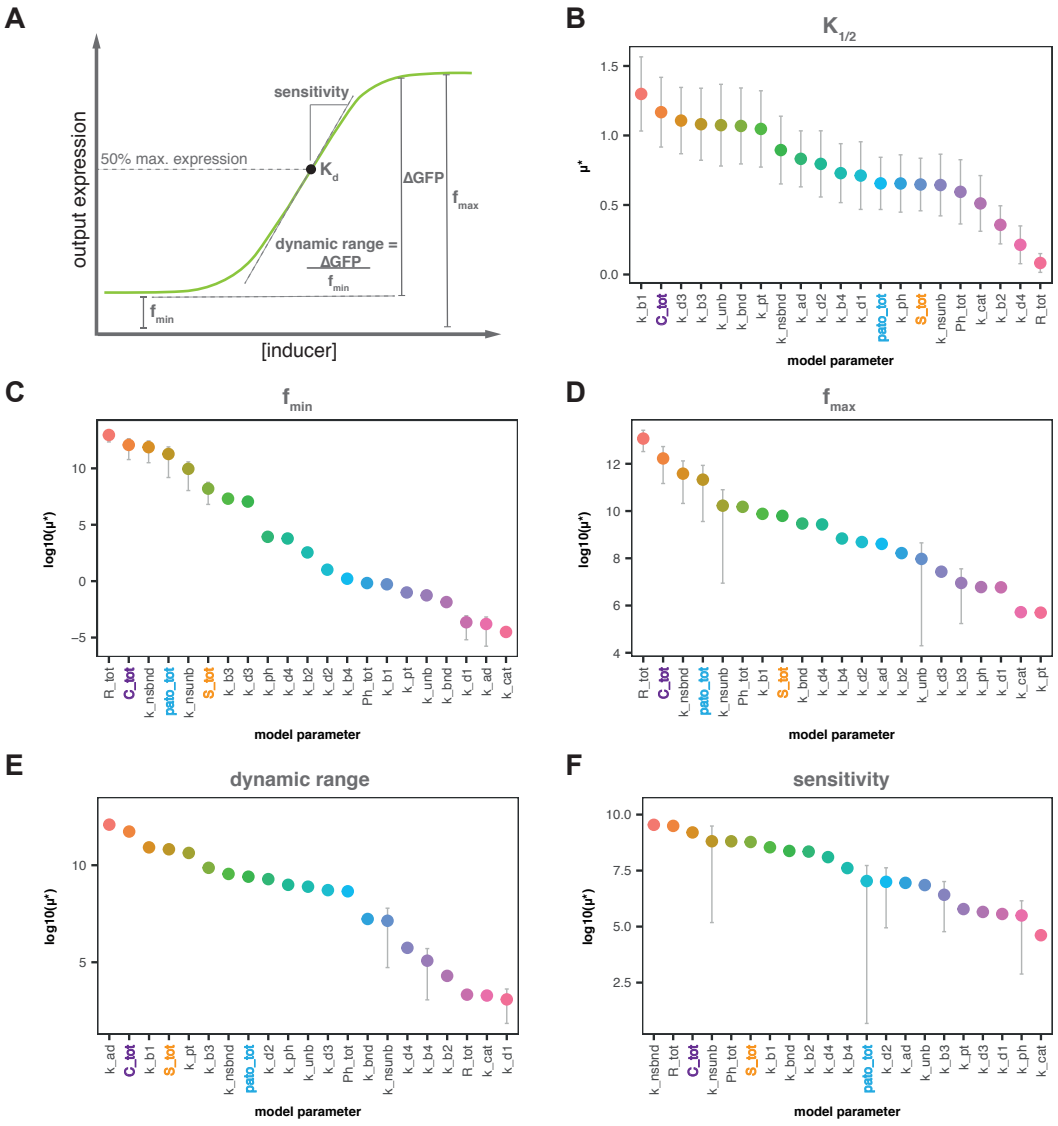

Figure 6.18: Results of the Morris sensitivity analysis conducted on the ato TCS. (**A**) Key aspects of biosensor behaviour screened during Morris sensitivity analysis. μ^* results for (**B**) $K_{1/2}$, (**C**) f^{min}, (**D**) f^{max}, (**E**) dynamic range and (**F**) sensitivity of the Ato TCS. The concentrations of AtoS, AtoC and the pato promoter have been highlighted. (Results from 300 samples, mean $\pm$ SE; points that do not show error bars had errors larger than the mean values)

Table 6.2: Rankings of the model parameter μ^* values, determining the importance of each parameter on biosensor behaviour, calculated through Morris sensitivity analysis.

Parameter	$K_{\frac{1}{2}}$	f_{min}	f_{max}	dynamic range	sensitivity	**mean rank**
$\mathbf{C}_{tot}$	2	2	2	2	3	**2.2**
k_{nsbnd}	8	3	2	7	1	**4.4**
k_{b1}	1	15	7	3	7	**6.6**
$\mathbf{S}_{tot}$	15	6	8	4	6	**7.8**
$\mathbf{pato}_{tot}$	13	4	4	8	12	**8.2**
R_{tot}	21	1	1	19	2	**8.8**
k_{nsunb}	16	5	5	15	4	**9**
k_{b3}	4	7	17	6	16	**10**
k_{bnd}	6	18	9	14	8	**11**
Ph_{tot}	17	14	6	13	5	**11**
k_{d2}	10	12	12	9	13	**11.2**
k_{d3}	3	8	16	12	18	**11.4**
k_{ad}	9	20	13	1	14	**11.4**
k_{b4}	11	13	11	17	11	**12.6**
k_{und}	5	17	15	11	15	**12.6**
k_{d4}	20	10	10	16	10	**13.2**
k_{pt}	7	16	21	5	17	**13.2**
k_{b2}	19	11	14	18	9	**14.2**
k_{ph}	14	9	18	10	20	**14.2**
k_{d1}	12	19	19	21	19	**18**
k_{cat}	18	21	20	20	21	**20**

Next, the effect of copy number was explored on four potential Ato WCB designs. These designs differed in the components that were expressed from the plasmid. Design A contained only the pato promoter (equivalent to the ASAH0 plasmid). Design B contained the AtoS HK and the pato promoter (equivalent to ASAH1J06). Design C contained the AtoC RR and pato promoter and finally design D contained all three components (the same as the ASAH2J06 plasmid). The simulated effect of copy number on these four different Ato WCB designs is shown in the plots of Figure 6.19. Changes in copy number were simulated by multiplying the estimated concentrations of each component contained on the plasmid by the simulated copy number (the concentrations of AtoS and AtoC were assumed to be the same, 0.17 μM, as they are expressed from the same promoter). All other parameter estimates were left as given in Table 6.1. Increasing the copy number of design A predicted a small increase in f^{min}, with a small fluctuation in $K_{1/2}$. Design B predicted a small change in f^{min} and decreasing $K_{1/2}$ with increasing plasmid copy number. Increasing the copy number of design C predicted a small increase in f^{max} alongside a larger increase in f^{min}. Finally the response curves for design D predicted similar changes to design C; with a decreasing $K_{1/2}$, increasing f^{max} and f^{min} seen with increasing plasmid copy number.

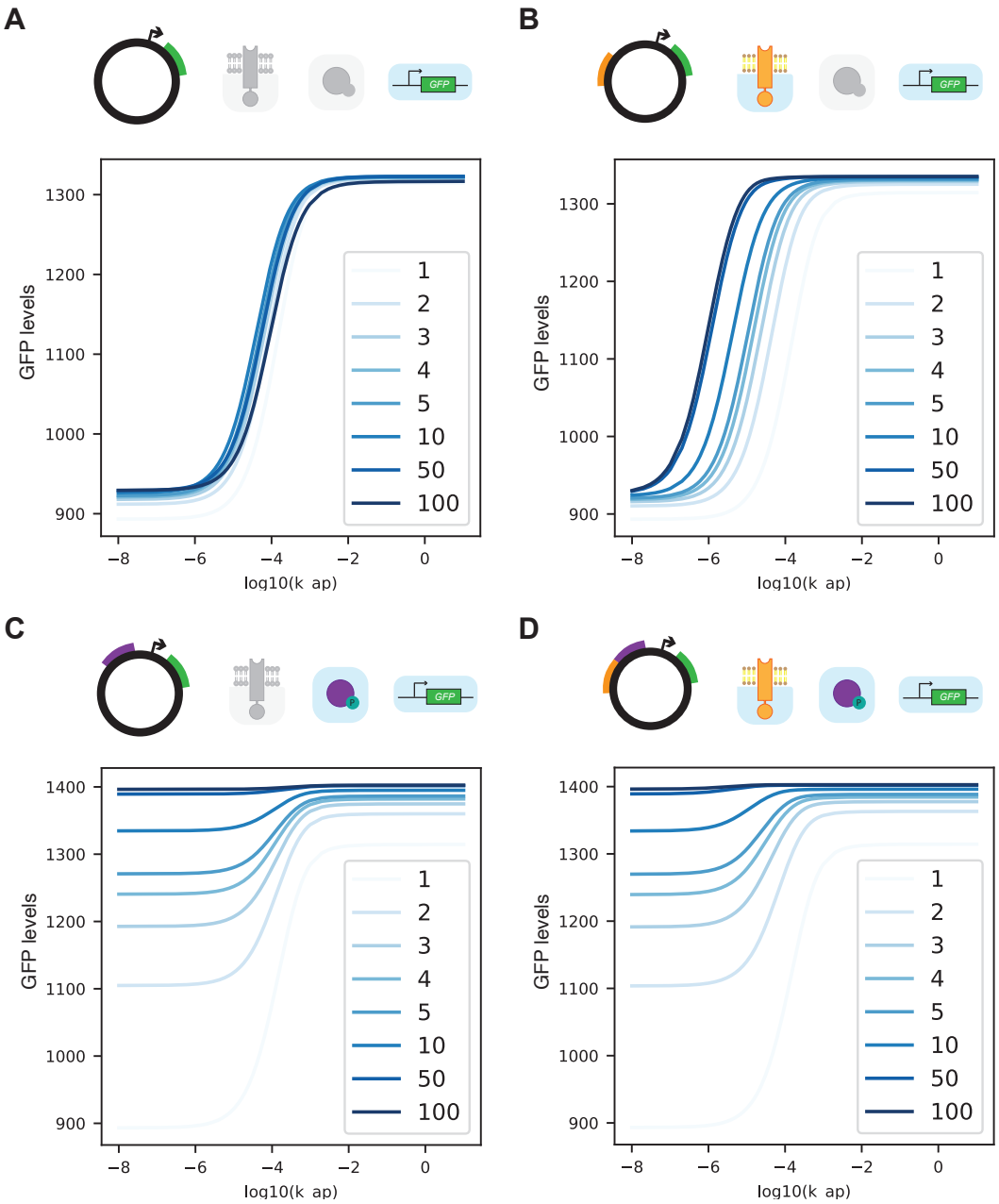

Figure 6.19: Potential plasmid designs for an engineered acetoacetate biosensor. Four different designs are shown, the top schematics show the components that are incorporated onto the plasmids, the bottom plots show the effect of increasing copy number (given by the legends) on the simulated biosensor response. (**A**) Design containing only the the pato promoter, (**B**) design containing the *atoS* gene and pato promoter, (**C**) design containing the *atoC* gene and pato promoter, and (**D**) design containing both the *atoS* and *atoC* genes alongside the pato promoter.

6.3.6 Engineered Ato Biosensors

Based on the designs shown in Figure 6.19 a range of Ato biosensor plasmids were created to try and produce different WCB behaviours. High and low copy versions of designs A, B and D were created. SC101 was chosen as a low copy origin and pUC as high copy; attempts to clone a medium copy version of these designs based on the p15a origin were unsuccessful.

Increasing the copy number of the plasmid containing only the pato promoter produced a large increase in the f^{max} of the final GFP response, while having no noticeable effect on f^{min} (Figure 6.20). Increasing the copy number of the plasmid containing both pato and the AtoS HK reversed this trend, with the lower copy number displaying a higher f^{max}. Again little difference was seen in f^{min} (Figure 6.21). Finally, increasing the copy number of the plasmid containing pato, AtoS and AtoC resulted in a vertical shift of the GFP response, increasing both f^{min} and f^{max} (Figure 6.22). All of these changes are summarised in Figure 6.23, which shows comparisons of the fitted Hill parameters for the high and low copy versions of the Ato biosensors. From this plot it is clear that the highest f^{min} was found with the BW28878 ASAH2J06 strain (Figure 6.23A). Furthermore, both BW28878 ASAH2J06 and ASAL2J06 displayed the lowest fitted $K_{1/2}$ values (Figure 6.23C).

Following characterisation of these plasmids two further designs were created. Both ASAH1J06 and ASAH2J06 were modified by varying the constitutive promoter responsible for AtoS and AtoS/AtoC expression. The responses of these WCBs can be seen in Figures 6.24 and 6.25, respectively. ASAH1J02 and ASAH2J02 did not produce an acetoacetate-inducible response, so these strains

were miniprepped and the plasmid sequences checked. In both cases the wrong sequence was found, so cloning for these WCB plasmids will need to be repeated again in future. However, from the remaining strains it could be seen that increasing AtoS expression produced a sharp decrease in f^{max} (Figure 6.24). Whereas, increasing both AtoS and AtoC together resulted in a reduced f^{max} and $K_{1/2}$.

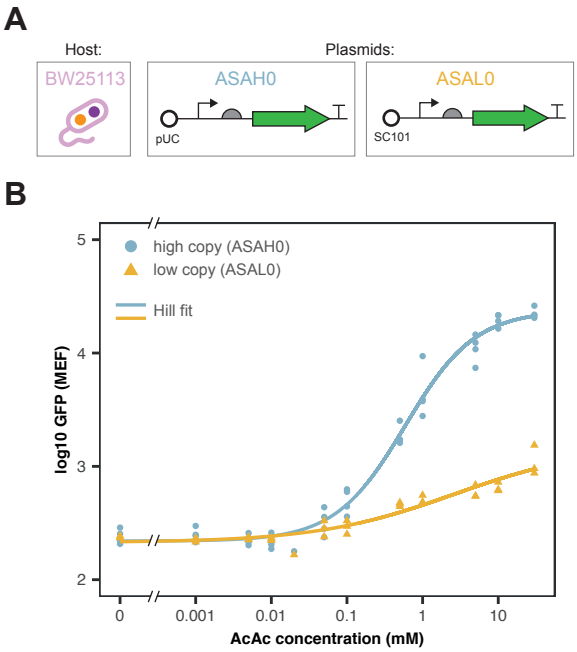

Figure 6.20: Performance of the ASAL0 and ASAH0 biosensors, both within the BW25113 host strain. (**A**) Plasmid layouts of the two biosensors. (**B**) Median GFP fluorescence of both biosensors at various acetoacetate concentrations (n = 3 biological repeats for ASAL0 and 4 for ASAH0, except for 0.2 mM datapoints, lines give data fits to Hill equation).

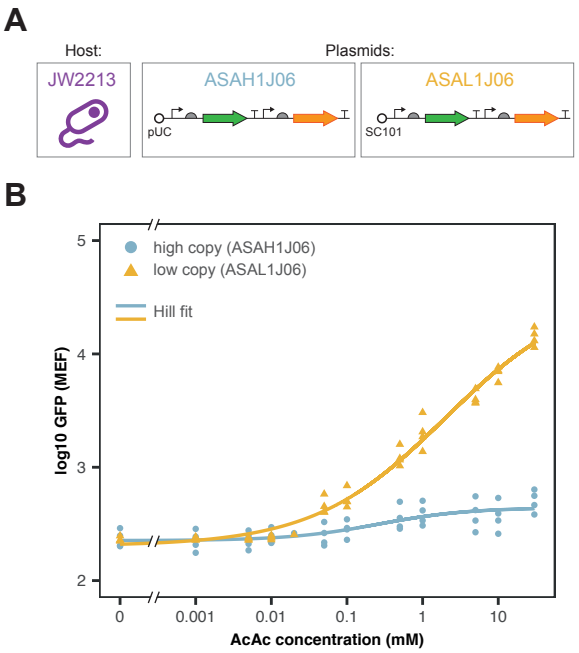

Figure 6.21: Performance of ASAL1J06 and ASAH1J06 WCBs, within the JW2213 host. (**A**) Plasmid layouts of the two biosensors. (**B**) Median GFP fluorescence at various acetoacetate concentrations (n = 4 biological repeats, except for 0.2 mM datapoints, lines give data fits to Hill equation).

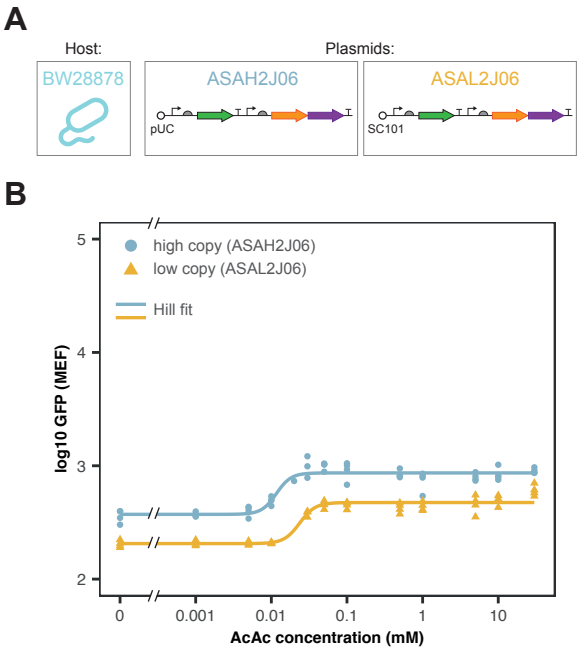

Figure 6.22: Performance of ASAL2J06 and ASAH2J06 WCBs, within the BW28878 host. (**A**) Plasmid layouts of the two biosensors. (**B**) Median GFP fluorescence at various acetoacetate concentrations (n = 4 biological repeats, except for 0.2 and 0.3 mM datapoints, lines give data fits to Hill equation).

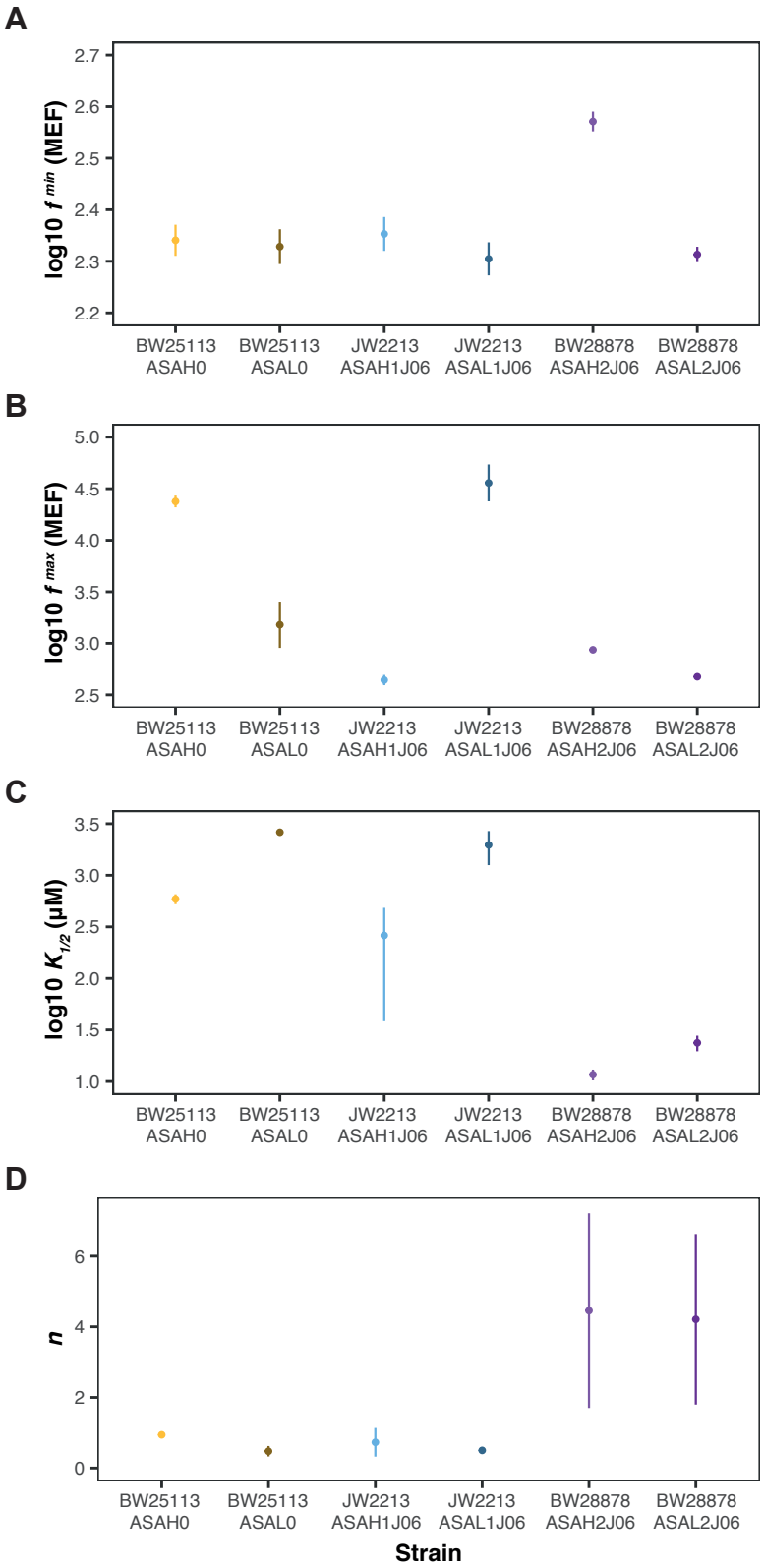

Figure 6.23: The fitted Hill parameters for the high and low copy Ato biosensor plasmids: (**A**) f^{min}, (**B**) f^{max}, (**c**) $K_{1/2}$, (**D**) n. (n = 4 except BW25113 ASAL0 where n = 3 biological repeats, fitted value $\pm$ standard error).

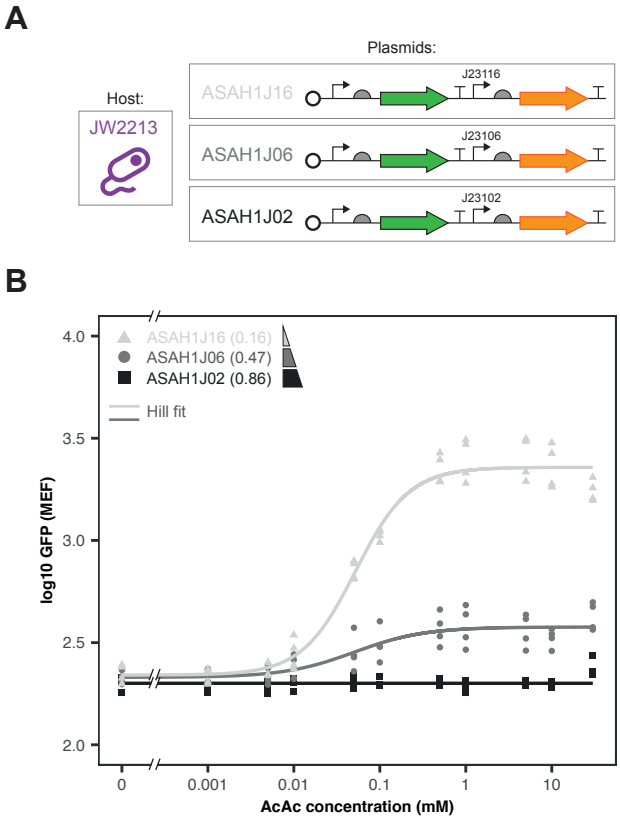

Figure 6.24: Performance of the ASAH1J02, ASAH1J06 and ASAH1J16 biosensors, all within the JW2213 host strain. (**A**) Plasmid layouts of the biosensors. (**B**) Median GFP fluorescence of both biosensors at various acetoacetate concentrations, numbers in brackets give the relative constitutive promoter strengths (n = 4 biological repeats, line for ASAH1J02 shows median GFP of uninduced cells, other lines give data fits to Hill equation).

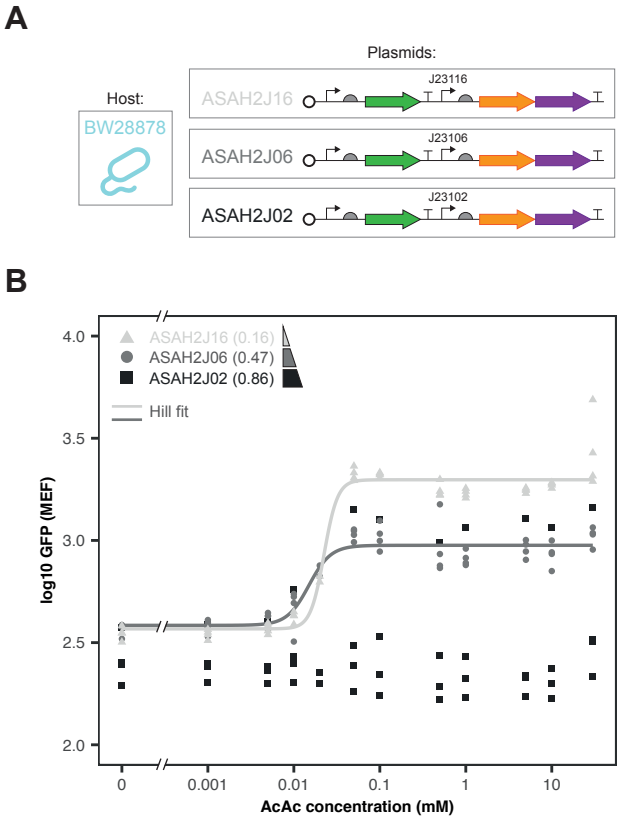

Figure 6.25: Performance of the ASAH2J02, ASAH2J06 and ASAH2J16 biosensors, all within the BW28878 host strain. (**A**) Plasmid layouts of the biosensors. (**B**) Median GFP fluorescence of both biosensors at various acetoacetate concentrations, numbers in brackets give the relative constitutive promoter strengths (n = 3 biological repeats for ASAH2J02 and 4 for ASAH2J06 and ASAH2J16, except for the 0.2 mM datapoints, lines give data fits to Hill equation).

6.4 Discussion

6.4.1 Using the Ato System to Create an Acetoacetate WCB

The ASAH0 plasmid is the simplest design for an acetoacetate sensitive biosensor that can be created from the Ato TCS, requiring host expression of AtoS and AtoC. Although this design is simple and in theory acetoacetate-inducible, it provides less components that can be modified to tune biosensor performance. The aim of the ASAH2J06 design was to provide a self contained plasmid that would (a), not rely on host expression of AtoS/AtoC, and (b), provide a greater potential design space from which to produce the desired biosensor behaviour. Both ASAH0 and ASAH2J06 were found to be acetoacetate-inducible.

As shown in Figure 6.12 the typical concentrations of ketone bodies within a healthy adult are $\leq$ 0.5 mM. It has been reported that these may increase to approximately 1.0 mM during hyperketonemia, or above 3.0 mM during ketoacidosis [238, 239]. A further review reported that ketone bodies may even reach levels in excess of 25 mM during cases of uncontrolled diabetes [257]. The original form of the WCB, BW25113 ASAH0, was able to sense and respond to acetoacetate concentrations within this physiologically relevant range, and displayed a $K_{1/2}$ lower than the detection limit of the commercially available Ketostix (249$\pm$32.8 μM vs $\sim$500 μM). These are desirable characteristics if the biosensor is to be used for diagnostic applications. However, it should be noted that the relative levels of the different ketone bodies may change across different diseased states. For example, in a healthy adult the ratio of 3HB to acetoacetate is 1:1, but in the case of acute

diabetic ketoacidosis this ratio may become as high as 10:1 [238]. Therefore, the actual levels of acetoactetate may not always fall within the grey highlighted area of Figure 6.12. This means that more sensitive biosensors (with a lower $K_{1/2}$) may be required for certain diagnostic applications. As can be seen from Figure 6.12, the modified BW28878 ASAH2J06 biosensor showed a substantially lower $K_{1/2}$ than the original BW25113 ASAH0 WCB. BW28878 ASAH0 showed no response to acetoacetate induction (Figures 6.10 and 6.12); this was as expected, as AtoS and AtoC are not expressed (either from the genome or plasmid) within this strain.

The BW25113 ASAH0 biosensor was found to be specific to acetoacetate when tested against a range of alternative inducers, a desirable trait for WCBs. As the Ato TCS is known to play a role in SCFA metabolism the SCFAs acetate, propionate and butyrate were tested as alternative inducers. The data collected here supports previous results that have reported SCFAs can not induce the Ato TCS [231, 258]. In addition, the two other ketone bodies, acetone and 3-β-hydroxybutyrate were tested for induction; neither were found to induce the BW25113 ASAH0 WCB. As discussed previously, spermidine has been reported elsewhere as an alternative inducer of the Ato TCS [237]. Characterisation of BW25113 ASAH0 did not show an increase in GFP response when exposed to spermidine (Figure 6.16). However, it is possible that the spermidine concentrations needed to trigger GFP production from this plasmid may be above those that become toxic to the cells. Therefore, the BW25113 ASAH0 strain may be killed before induction can be seen. It would be interesting in future to see if one of the WCB variants with a lower $K_{1/2}$ shows signs of spermidine induction at lower

concentrations.

6.4.2 Insights from Sensitivity Analysis

As demonstrated with the ODE model developed here, there are numerous factors that can affect biosensor behaviour. It is not an easy procedure to identify all of the factors that may impact on specific aspects of biosensor performance; nor will it be feasible in every case to tune all parameters within a system. Therefore, SA offers a viable route for trying to identify a subset of parameters that may be focused on when designing biosensor behaviour for specific applications.

When ranking the Morris SA all parameters involving the reporter elements (e.g. GFP maturation/degradation) were removed from the results. Biosensors can be built with a range of reporters [259]; therefore, I wished to focus on the parameters influencing the TCS, as these may be more applicable to other TCS based biosensors. In addition, it is important to remember that Morris analysis only provides a qualitative ranking of parameters, it does not provide any information on the quantitative differences between parameters. From the final rankings, given in Table 6.2, it can be seen that C_{tot} (AtoC RR concentration) was found to have the largest mean effect on WCB behaviour. The concentration of AtoS, S_{tot}, and pato promoter concentration, $pato_{tot}$, were ranked in fourth and fifth, respectively. These results provided some justification for the designs proposed in Figure 6.19, as changing the concentrations of the three main components was predicted to have a large effect on biosensor behaviour. Thereby, it should be possible to create a range of different behaviours from these designs. It should be noted that a previous study identified

theoretical mechanisms that could render the input-output response of some two-component systems robust to variations in the concentrations of the system proteins (such as the concentrations of the AtoS HK or AtoC RR) [260]. However, as noted by the authors not all bacterial sensing mechanisms show this robust response, for example systems involved in chemotaxis and sporulation. Similarly, the sensitivity analysis performed within this chapter suggests that the AtoSC TCS does not show this robust input-output relationship under the conditions explored here (as supported by the response curves reported in Figures 6.20, 6.21 and 6.22). This may be due to the inherent biology of the AtoSC TCS, or may indicate that some of the interactions involved in this system have not yet been fully identified. Therefore, it will be vital that the model described here is continuously modified in future as our understanding of the underlying biology of the AtoSC TCS continues to grow; in order to fully capture any interactions within this system and more accurately predict its behaviour.

Interestingly, S_{tot} ranked 15th for influence on $K_{1/2}$; this appeared to be in disagreement with the modelling results given in subsequent simulations that predict AtoS concentration may be able to tune $K_{1/2}$ (Figure 6.17A). This may be due to the bounds that were placed on parameter values during the Morris analysis. All parameter bounds were set to at least one order of magnitude above and below the values given in Table 6.1. It may be necessary to repeat this analysis in future with modified bounds. Furthermore, for all parameters (except $K_{1/2}$) Morris analysis was found to return large errors in the predicted μ^* values. The Morris analysis presented here was collected on 300 trajectories. The large recorded errors suggest

it may be necessary to repeat this analysis on a larger sample size in future. Alternatively some of the parameter values may be set at a fixed value, to help reduce the parameter space explored during the SA. These could be chosen based on the difficulty of modifying the parameters experimentally.

A preliminary attempt at Sobol analysis was also carried out. Although not discussed in detail here, Sobol analysis is a method that allows the quantitative ranking of model parameters. The Sobol method is computationally expensive. As such, it is not compatible with models that contain a large number of parameters. To avoid this drawback Sobol analysis is often performed as part of a two-part strategy with Morris analysis [261]. Within this two-part strategy Morris analysis is used to provide a qualitative ranking of all the parameters within a model. From this ranking the most relevant factors are selected and carried forward into the Sobol analysis. Pre-ranking the parameters in this way allows for the selection of a subset of important parameters, dramatically reducing the computational cost of performing Sobol analysis. Within this work a subset of five parameters (the highest ranked parameters from Table 6.2) were selected for Sobol analysis. However, even with this subset of parameters, Sobol analysis was found to be computationally unfeasible. Therefore, the attempts at Sobol analysis were not carried forward.

6.4.3 Modelling of the Ato System

The values (AtoS, AtoC, pato concentration) simulated in Figure 6.17 were varied across 7 orders of magnitude. This large range was chosen to try and capture all of the effects that varying each parameter may have on the final biosensor behaviour.

However, this range may not be experimentally viable in all cases. For example the concentration of pato is determined by the number of times it occurs within the cell; therefore, its concentration can be controlled through placing multiple copies within the genome or incorporating the promoter onto plasmids of differing copy number. The concentrations of AtoS and AtoC can be readily tuned within the host cells. As with the pato promoter, the concentrations of these proteins could be increased by placing the genes on higher copy plasmids or incorporating multiple copies of the gene in the genome. In addition, the genes could be placed under the control of stronger promoters. To reduce concentration the genes could be expressed from weak constitutive promoters, or from inducible-promoters that are only induced at extremely low levels.

However, it should be noted that although the concentration of all three components may be theoretically increased, extreme levels of expression will likely lead to burden on the host cells. Overexpressing components can lead to competition for resources that are required for essential processes performed by the host [262]. This competition can lead to burden and in turn, greatly impact the growth of the host cells. The current model setup does not take effects such as burden into account, this may limit its relevance to real-world situations [198]. Future work could aim to adapt this model by incorporating it within a whole-cell model. This would allow for effects such as burden or competition for cellular resources to be considered.

It was also noted that the simulation assays given in Figures 6.17A and 6.19 showed high basal levels of GFP expression, f^{min}. From the sensitivity analysis it could be seen that the concentration of AtoC was predicted to have one of the

greatest effects on f^{min} (Table 6.2). It was hypothesised that the estimate for the native concentration of AtoC within the cells may be too high, leading to the high simulated levels of uninduced GFP expression. In order to investigate the effect of this estimate on simulated biosensor behaviour, the assays presented in Figure 6.17 were repeated with three different estimates of AtoC concentration. These can be seen in Appendix Figure C.2. As expected decreasing the estimated concentration of native AtoC greatly reduced the levels of f^{min}. However, it did not affect the nature of the perturbations caused by the varying of other parameters. This suggests that the qualitative changes in biosensor behaviour reported in Figure 6.17 are likely to remain consistent regardless of the starting estimate used for AtoC concentration. For example, increasing AtoS was predicted to increase f^{max}, decrease f^{min} at high concentrations and decrease $K_{1/2}$. Increasing AtoC concentration was predicted to increase f^{max} and f^{min}, while having little effect on $K_{1/2}$. pato promoter concentration was predicted to increase f^{max}, f^{min}; with high concentrations leading to a linear response. Alternatively, the high basal levels may be caused by the inclusion of unphosphorylated AtoC binding to the pato promoter. As this has not been proven to occur experimentally, it would be a logical next step to remove this interaction from the model to see if lower levels of basal expression are predicted.

6.4.4 Comparison of *in silico* vs *in vitro* WCB Performance

A selection of the designs simulated in Figure 6.19 were created and characterised within the lab (Figures 6.20, 6.21 and 6.22). SA predicted that the total concentration of AtoS, AtoC and pato have a large effect on the output of the AtoSC TCS.

This was supported in the experimental results, which showed that varying the concentrations of these components resulted in a range of WCB behaviours (Figure 6.23). The responses of the ASAH2J06/ASAL2J06 plasmids qualitatively matched the simulated responses (Figure 6.19D vs Figure 6.22), with increasing copy number producing a vertical shift in GFP response. This agreement was achieved despite the complexity of the AtoSC TCS and lack of knowledge of its complete biology. The behaviour of ASAH0/ASAL0 and ASAH1J06/ASAL1J06 did not produce good agreement with the predicted response curves (Figures 6.19A vs 6.20 and 6.19B vs 6.21, respectively). One possible reason for this disagreement may be the estimates used for parameters such as AtoS HK, AtoC RR and pato concentrations. These estimates were taken from a model developed for the EnZ/OmpR TCS [255]. It could be possible in future to use experimental timecourse data to fit the Ato model, thereby obtaining better estimates of the initial parameters. This would offer a starting point for obtaining more reliable predictions of Ato WCB performance.

Interestingly, only the ASAH2J06 plasmid design appeared to produce substantial changes in the observed f^{min} values (Figure 6.23A). This suggests that varying the level of the AtoC RR, rather than those of the AtoS HK or pato promoter, has a large impact on basal expression of the AtoSC TCS. A similar phenomenon was observed in the light-inducible *ccaS-ccaR* TCS, where increasing expression of the CcaR RR resulted in an increase in expression from the system in the 'OFF' state [263]. The authors suggested this may be caused by autophosphorylation of the CcaR RR or DNA-binding in its nonphosphorylated form; therefore, it is possible a

similar mechanism is responsible for the increase in f^{min} seen with the ASAH2J06 biosensor. Furthermore, a previous study was able to optimise a nitrate-inducible TCS biosensor by varying constitutive expression of the NarX HK and NarL RR proteins, in a similar manner to the designs explored in Figure 6.25 [121]. For the NarXL biosensor a similar trend was observed to the AtoSC designs characterised here, where lower constitutive expression of the proteins resulted in a larger final dynamic range of the biosensor. The observation of similar trends in behaviour across different TCS-based biosensors suggest that the design rules explored here may be more widely-applicable to other TCS-based biosensors in future, where there is a mismatch between desired and observed behaviour.

6.5 Future Work

As discussed, the Ato model does not fully predict Ato WCB behaviour in its current form. Therefore, I would suggest this as the starting point for any future work. To improve the models predictive capabilities the initial parameter estimates (given in Table 6.1) could be replaced by values obtained through fitting of the model to experimental timecourse data. This would hopefully result in more realistic model predictions. Alternatively, future work could explore characterising the Ato WCBs in more complex culture conditions. This could include aerobic vs anaerobic environments and more complex media- to simulate the conditions that would be encountered within the body. This characterisation may also help to elucidate any further interactions or crosstalk that influences AtoSC TCS behaviour.

6.6 Summary

To date no examples of an acetoacetate-inducible WCB have been published. Within this chapter a range of WCBs were constructed, based on the AtoSC TCS. In addition, attempts to model this system have provided an insight into which parameters may be important in determining final WCB behaviour. Subsequent WCB designs, which varied these parameters, showed that they were able to produce dramatic changes in the final biosensor performance. In future it may be possible to apply a similar approach to the engineering of other TCS biosensors. Furthermore, the WCBs presented here may be used in studies that require monitoring of acetoacetate, for example during the bioproduction of ketone bodies.

Chapter 7

General Conclusions

Contents

7.1 Conclusions

The fields of synthetic biology and microbiome engineering are fascinating areas of scientific research, that hold the potential to improve our knowledge of human health and offer new therapeutic strategies to patients around the world. One aspect of this field is the creation of biosensors that can be incorporated into engineered biotherapeutics, to help produce targeted expression of therapeutic molecules or monitor for biomarkers of disease. However, for these concepts to be successful in future, new methods for modifying and characterising these strains *in vivo* are needed.

Within this project I have developed a *C. elegans* model that can be used to improve our understanding of WCBs, host-microbe interactions and general nematode health. The protocols presented here will hopefully encourage other researchers to adopt the *C. elegans* model for synthetic biology studies, helping to reduce the use of mice and other current vertebrate models. They may also be used to help expand our knowledge of microbial communities and how they develop and interact within nematode hosts. Alongside the *C. elegans* model a selection of ratiometric WCBs have been produced. These could be readily used in conjunction with the *C. elegans* model in future. Finally, I report a range of acetoacetate-inducible biosensors. The Ato WCBs created display a variety of responses and are sensitive to acetoacetate at physiologically relevant concentrations. These may be used in future experimental studies that require monitoring of acetoacetate.

In conclusion, the work within this thesis helps to build on our knowledge of WCBs and host-microbe interactions. It is hoped that this will help to inform future

attempts to construct WCBs and engineered biotherapeutic strains.

7.2 Future Perspectives

The systems used to build WCBs are often complex and troubleshooting inadequate biosensor responses can be a difficult task. The use of mathematical modelling to overcome these challenges, through identifying rational design strategies for improving WCB performance, is becoming increasingly commonplace. Over the coming years I expect this trend to continue, with techniques such as sensitivity analysis helping to further focus future engineering efforts.

Furthermore, it is likely that there will be growing interest in methods that are able to interface modern electronics with engineered synthetic biology strains. Although this may initially sound like the realms of science-fiction, progress has already been made in this area. One previous study was able to develop an ingestible micro-bio-electronic device, which combined an engineered bacterial biosensor with low-power microelectronics. The final device was able to detect and report on the presence of blood *in situ*, within the gastrointestinal tract of pigs [264]. As discussed by the authors, combining synthetic biology and microelectronic advances in this way will allow us to leverage the advantages inherent to each method. These devices may be an invaluable tool for *in vivo* biosensing in harsh conditions and could be used to probe the changing conditions within the digestive tract, in both a spatial and temporal manner; helping to improve the diagnosis and monitoring of health within patients. I suspect that these methods will be built upon in the coming decades.

Finally, I anticipate there will be an increase in the number of studies that attempt to replace the standard reporter proteins of WCBs with therapeutic payloads. This will allow us to transition from purely diagnostic applications, to using WCBs for combatting disease states *in vivo*. This is a vital next step that will be needed if WCBs and engineered biotherapeutics are to find success in clinical applications. As these technologies begin to move to real-world applications it will be crucial that health officials, regulators and scientists come together to regulate and classify this new branch of therapeutics. Ensuring that they are safe and effective for patients around the world. It will be exciting in future to see how these promising technologies are received by the general public and how many are successfully translated to the clinic.

Bibliography

[1] L.K. Urseull, J.L. Metcalf, L.W. Parfrey, and R. Knight. Defining the Human Microbiome. *NIH Manuscripts*, 70(Suppl 1):1–12, 2013.

[2] E. Thursby and N. Juge. Introduction to the human gut microbiota. *Biochemical Journal*, 474(11):1823–1836, jun 2017.

[3] R. Sender, S. Fuchs, and R. Milo. Revised Estimates for the Number of Human and Bacteria Cells in the Body. *PLOS Biology*, 14(8):e1002533, aug 2016.

[4] B. Wang, M. Yao, L. Lv, Z. Ling, and L. Li. The Human Microbiota in Health and Disease. *Engineering*, 3(1):71–82, feb 2017.

[5] J. Qin, R. Li, J Raes, M. Arumugam, K.S. Burgdorf, C. Manichanh, T. Nielsen, N. Pons, F. Levenez, T. Yamada, D.R. Mende, J. Li, J. Xu, S. Li, D. Li, J. Cao, B. Wang, H. Liang, H. Zheng, Y. Xie, J. Tap, P. Lepage, M. Bertalan, J.M. Batto, T. Hansen, D. Le Paslier, A. Linneberg, H.B. Nielsen, E. Pelletier, P. Renault, T. Sicheritz-Ponten, K. Turner, H. Zhu, C. Yu, S. Li, M. Jian, Y. Zhou, Y. Li, X. Zhang, S. Li, N. Qin, H. Yang, J. Wang, S. Brunak, J. Doré, F. Guarner, K. Kristiansen, O. Pedersen, J. Parkhill, J. Weissenbach, P. Bork, S.D. Ehrlich, and J. Wang. A human gut microbial gene catalogue established by metagenomic sequencing. *Nature*, 464(7285):59–65, mar 2010.

[6] F. Backhed. Host-Bacterial Mutualism in the Human Intestine. *Science*, 307(5717):1915–1920, 2005.

[7] T. Yatsunenko, F.E. Rey, M.J. Manary, I. Trehan, M.G. Dominguez-Bello, M. Contreras, M. Magris, G. Hidalgo, R.N. Baldassano, A.P. Anokhin, A.C. Heath, B. Warner, J. Reeder, J. Kuczynski, J.G. Caporaso, C.A. Lozupone, C. Lauber, J.C. Clemente, D. Knights, R. Knight, and J.I. Gordon. Human gut microbiome viewed across age and geography. *Nature*, 486(7402):222–227, jun 2012.

[8] P. Hugon, J.C. Dufour, P. Colson, P.E. Fournier, K. Sallah, and D. Raoult. A comprehensive repertoire of prokaryotic species identified in human beings. *The Lancet Infectious Diseases*, 15(10):1211–1219, oct 2015.

[9] L. Dethlefsen, M. McFall-Ngai, and D.A. Relman. An ecological and evolutionary perspective on human microbe mutualism and disease. *Nature*, 449(7164):811–818, 2007.

[10] A.D. Kostic, M.R. Howitt, and W.S. Garrett. Exploring host microbiota interactions in animal models and humans. *Genes & Development*, 27:701–718, 2013.

[11] A.M. O'Hara and F. Shanahan. The gut flora as a forgotten organ. *EMBO reports*, 7(7):688–693, jul 2006.

[12] B.D. Karkaria, N.J. Treloar, C.P. Barnes, and A.J.H. Fedorec. From Microbial Communities to Distributed Computing Systems. *Frontiers in Bioengineering and Biotechnology*, 8:834, jul 2020.

[13] K.Z. Coyte and S. Rakoff-Nahoum. Understanding Competition and Cooperation within the Mammalian Gut Microbiome. *Current Biology*, 29(11):R538–R544, jun 2019.

[14] P.J. Turnbaugh, R.E. Ley, M. Hamady, C.M. Fraser-Liggett, R. Knight, and J.I. Gordon. The Human Microbiome Project. *Nature*, 449(7164):804–810, oct 2007.

[15] E. Rinninella, P. Raoul, M. Cintoni, F. Franceschi, G. Miggiano, A. Gasbarrini, and M. Mele. What is the Healthy Gut Microbiota Composition? A Changing Ecosystem across Age, Environment, Diet, and Diseases. *Microorganisms*, 7(1):14, jan 2019.

[16] M.J. Gosalbes, A. Durbán, M. Pignatelli, J.J. Abellan, N. Jiménez-Hernández, A.E. Pérez-Cobas, A. Latorre, and A. Moya. Metatranscriptomic Approach to Analyze the Functional Human Gut Microbiota. *PLoS ONE*, 6(3):e17447, mar 2011.

[17] S. Arboleya, C. Watkins, C. Stanton, and R.P. Ross. Gut Bifidobacteria Populations in Human Health and Aging. *Frontiers in Microbiology*, 7:1204, aug 2016.

[18] O. Volokh, N. Klimenko, Y. Berezhnaya, A. Tyakht, P. Nesterova, A. Popenko, and D. Alexeev. Human Gut Microbiome Response Induced by Fermented Dairy Product Intake in Healthy Volunteers. *Nutrients*, 11(3):547, mar 2019.

[19] E. Le Chatelier, T. Nielsen, J. Qin, E. Prifti, F. Hildebrand, G. Falony, M. Almeida, M. Arumugam, J.M. Batto, S. Kennedy, P. Leonard, J. Li, K. Burgdorf, N. Grarup, T. Jørgensen, I. Brandslund, H.B. Nielsen, A.S. Juncker, M. Bertalan, F. Levenez, N. Pons, S. Rasmussen, S. Sunagawa, J. Tap, S. Tims, E.G. Zoetendal, S. Brunak, K. Clément, J. Doré, M. Kleerebezem, K. Kristiansen, P. Renault, T. Sicheritz-Ponten, W.M. de Vos, J.D. Zucker, J. Raes, T. Hansen, P. Bork, J. Wang, S.D. Ehrlich, O. Pedersen,

E. Guedon, C. Delorme, S. Layec, G. Khaci, M. van de Guchte, G. Vandemeulebrouck, A. Jamet, R. Dervyn, N. Sanchez, E. Maguin, F. Haimet, Y. Winogradski, A. Cultrone, M. Leclerc, C. Juste, H. Blottière, E. Pelletier, D. LePaslier, F. Artiguenave, T. Bruls, J. Weissenbach, K. Turner, J. Parkhill, M. Antolin, C. Manichanh, F. Casellas, N. Boruel, E. Varela, A. Torrejon, F. Guarner, G. Denariaz, M. Derrien, J.E.T. van Hylckama Vlieg, P. Veiga, R. Oozeer, J. Knol, M. Rescigno, C. Brechot, C. M'Rini, A. Mérieux, and T. Yamada. Richness of human gut microbiome correlates with metabolic markers. *Nature*, 500(7464):541–546, 2013.

[20] N. Kamada, S.U. Seo, G.Y. Chen, and G. Núñez. Role of the gut microbiota in immunity and inflammatory disease. *Nature Reviews Immunology*, 13(5):321–335, 2013.

[21] H.J. Flint, K.P. Scott, P. Louis, and S.H. Duncan. The role of the gut microbiota in nutrition and health. *Nature Reviews Gastroenterology & Hepatology*, 9(10):577–589, oct 2012.

[22] G. den Besten, K. van Eunen, A.K. Groen, K. Venema, D.J. Reijngoud, and B.M. Bakker. The role of short-chain fatty acids in the interplay between diet, gut microbiota, and host energy metabolism. *The Journal of Lipid Research*, 54(9):2325–2340, 2013.

[23] E.N. Bergman. Energy contributiuons of volatile fatty acids from the gastrointestinal tract in various species. *Physiological reviews*, 70(2):567–590, 1990.

[24] E.W. Pomare, W.J. Branch, and J.H. Cummings. Carbohydrate fermentation in the human colon and its relation to acetate concentrations in venous blood. *Journal of Clinical Investigation*, 75(5):1448–1454, may 1985.

[25] S. Tedelind, F. Westberg, M. Kjerrulf, and A. Vidal. Anti-inflammatory properties of the short-chain fatty acids acetate and propionate: a study with relevance to inflammatory bowel disease. *World journal of gastroenterology*, 13(20):2826–32, may 2007.

[26] P. Konturek, I. Harsch, K. Konturek, M. Schink, T. Konturek, M. Neurath, and Y. Zopf. Gut-Liver Axis: How Do Gut Bacteria Influence the Liver? *Medical Sciences*, 6(3):79, sep 2018.

[27] J.F. Cryan, K.J. O'Riordan, C.S.M. Cowan, K.V. Sandhu, T.F.S. Bastiaanssen, M. Boehme, M.G. Codagnone, S. Cussotto, C. Fulling, A.V. Golubeva, K.E. Guzzetta, M. Jaggar, C.M. Long-Smith, J.M. Lyte, J.A. Martin, A. Molinero-Perez, G. Moloney, E. Morelli, E. Morillas, R. O'Connor, J.S. Cruz-Pereira, V.L. Peterson, K. Rea, N.L. Ritz, E. Sherwin, S. Spichak, E.M. Teichman, M. van de Wouw, A.P. Ventura-Silva, S.E. Wallace-Fitzsimons, N. Hyland, G. Clarke, and T.G. Dinan. The Microbiota-Gut-Brain Axis. *Physiological Reviews*, 99(4):1877–2013, oct 2019.

[28] J.F. Cryan and S.M. O'Mahony. The microbiome-gut-brain axis: from bowel to behavior. *Neurogastroenterology & Motility*, 23(3):187–192, mar 2011.

[29] National academy of Sciences. Factors that Contribute to Variation in the Human Microbiome. In *Environmental Chemicals, the Human Microbiome, and Health Risk: A Research Strategy*. National Academies Press, Washington, 2017.

[30] C.A. Gaulke and T.J. Sharpton. The influence of ethnicity and geography on human gut microbiome composition. *Nature Medicine*, 24(10):1495–1496, oct 2018.

[31] M.J. Hopkins, R. Sharp, and G.T. Macfarlane. Variation in human intestinal microbiota with age. *Digestive and Liver Disease*, 34:S12–S18, sep 2002.

[32] V.K. Gupta, S. Paul, and C. Dutta. Geography, Ethnicity or Subsistence-Specific Variations in Human Microbiome Composition and Diversity. *Frontiers in Microbiology*, 8:1162, jun 2017.

[33] S. Zhang and DC. Chen. Facing a new challenge: the adverse effects of antibiotics on gut microbiota and host immunity. *Chinese Medical Journal*, 132(10):1135–1138, may 2019.

[34] S. Carding, K. Verbeke, D.T. Vipond, B.M. Corfe, and L.J. Owen. Dysbiosis of the gut microbiota in disease. *Microbial Ecology in Health & Disease*, 26(0):26191, feb 2015.

[35] T. Yang, M.M. Santisteban, V. Rodriguez, E. Li, N. Ahmari, J.M. Carvajal, M. Zadeh, M. Gong, Y. Qi, J. Zubcevic, B. Sahay, C.J. Pepine, M.K. Raizada, and M. Mohamadzadeh. Gut Dysbiosis Is Linked to Hypertension Novelty and Significance. *Hypertension*, 65(6):1331–1340, jun 2015.

[36] J. Shen, M.S. Obin, and L. Zhao. The gut microbiota, obesity and insulin resistance. *Molecular Aspects of Medicine*, 34(1):39–58, 2013.

[37] M. Million, J.C. Lagier, D. Yahav, and M. Paul. Gut bacterial microbiota and obesity. *Clinical Microbiology and Infection*, 19(4):305–313, 2013.

[38] K.H. Lee, Y. Song, W. Wu, K. Yu, and G. Zhang. The gut microbiota, environmental factors, and links to the development of food allergy. *Clinical and Molecular Allergy*, 18(1):5, dec 2020.

[39] M.J. Bull and N.T. Plummer. Part 1: The Human Gut Microbiome in Health and Disease. *Integrative medicine (Encinitas, Calif.)*, 13(6):17–22, 2014.

[40] T. Zuo and S.C. Ng. The Gut Microbiota in the Pathogenesis and Therapeutics of Inflammatory Bowel Disease. *Frontiers in Microbiology*, 9:2247, sep 2018.

[41] S.J.D. O'Keefe. Diet, microorganisms and their metabolites, and colon cancer. *Nature Reviews Gastroenterology & Hepatology*, 13(12):691–706, 2016.

[42] J. Dou and M.R. Bennett. Synthetic Biology and the Gut Microbiome. *Biotechnology Journal*, 13(5):1700159, may 2018.

[43] M.R. Charbonneau, V.M. Isabella, N. Li, and C.B. Kurtz. Developing a new class of engineered live bacterial therapeutics to treat human diseases. *Nature Communications*, 11(1):1738, dec 2020.

[44] J.R. Bober, C.L. Beisel, and N.U. Nair. Synthetic Biology Approaches to Engineer Probiotics and Members of the Human Microbiota for Biomedical Applications. *Annual Review of Biomedical Engineering*, 20(1):277–300, jun 2018.

[45] J. Ang, E. Harris, B.J. Hussey, R. Kil, and D.R. McMillen. Tuning Response Curves for Synthetic Biology. *ACS Synthetic Biology*, 2(10):547–567, oct 2013.

[46] D.E. Cameron, C.J. Bashor, and J.J. Collins. A brief history of synthetic biology. *Nature Reviews Microbiology*, 12(5):381–390, 2014.

[47] M. Heinemann and S. Panke. Synthetic Biology- putting engineering into biology. *Bioinformatics*, 22(22):2790–799, 2006.

[48] H.D. Goold, P. Wright, and D. Hailstones. Emerging Opportunities for Synthetic Biology in Agriculture. *Genes*, 9(341):1–17, 2018.

[49] W. Liu and C. N. Stewart Jr. Plant Synthetic Biology. *Trends in Plant Science*, 20(5):309–317, 2015.

[50] S. Jagadevan, A. Banerjee, C. Banerjee, C. Guria, R. Tiwari, B. Mehak, and P. Shukla. Recent developments in synthetic biology and metabolic engineering in microalgae towards biofuel production. *Biotechnology for biofuels*, 11(185), 2018.

[51] D.T. Riglar and P.A. Silver. Engineering bacteria for diagnostic and therapeutic applications. *Nature Reviews Microbiology*, 16:214, feb 2018.

[52] K.K. Jain. Synthetic Biology and Personalized Medicine. *Medical Principles and Practices*, 22:209–219, 2013.

[53] M.B. Elowitz and S. Leibler. A synthetic oscillatory network of transcriptional regulators. *Nature*, 403:335–338, 2000.

[54] J.J. Collins, T.S. Gardner, and C.R. Cantor. Construction of a genetic toggle switch in Escherichia coli. *Nature*, 403(6767):339–342, 2000.

[55] F. Meng and T. Ellis. The second decade of synthetic biology: 20102020. *Nature Communications*, 11(1):5174, dec 2020.

[56] A.A.K. Nielsen, B.S. Der, J. Shin, P. Vaidyanathan, V. Paralanov, E.A. Strychalski, D. Ross, D. Densmore, and C.A. Voigt. Genetic circuit design automation. *Science*, 352(6281):aac7341–aac7341, apr 2016.

[57] C.A. Hutchison, R.Y. Chuang, V.N. Noskov, N. Assad-Garcia, T.J. Deerinck, M.H. Ellisman, J. Gill, K. Kannan, B.J. Karas, L. Ma, J.F. Pelletier, Z.Q. Qi, R.A. Richter, E.A. Strychalski, L. Sun, Y. Suzuki, B. Tsvetanova, K.S. Wise, H.O. Smith, J.I. Glass, C. Merryman, D.G. Gibson, and J.C. Venter. Design and synthesis of a minimal bacterial genome. *Science*, 351(6280):aad6253–aad6253, mar 2016.

[58] S. Gleizer, R. Ben-Nissan, Y.M. Bar-On, N. Antonovsky, E. Noor, Y. Zohar, G. Jona, E. Krieger, M. Shamshoum, A. Bar-Even, and R. Milo. Conversion of Escherichia coli to Generate All Biomass Carbon from CO2. *Cell*, 179(6):1255–1263.e12, nov 2019.

[59] P. Opgenorth, Z. Costello, T. Okada, G. Goyal, Y. Chen, J. Gin, V. Benites, M. de Raad, T.R. Northen, K. Deng, S. Deutsch, E.E.K. Baidoo, C.J. Petzold, N.J. Hillson, H. Garcia Martin, and H.R. Beller. Lessons from Two Design-Build-Test-Learn Cycles of Dodecanol Production in Escherichia coli Aided by Machine Learning. *ACS Synthetic Biology*, 8(6):1337–1351, jun 2019.

[60] P.S. Freemont. Synthetic biology industry: data-driven design is creating new opportunities in biotechnology. *Emerging Topics in Life Sciences*, 3(5):651–657, nov 2019.

[61] E. Andrianantoandro, S. Basu, D.K. Karig, and R. Weiss. Synthetic biology: new engineering rules for an emerging discipline. *Molecular Systems Biology*, 2:1–14, 2006.

[62] M. Heinemann and S. Panke. Synthetic biology- putting engineering into biology. *Bioinformatics*, 22(22):2790–2799, nov 2006.

[63] J.C. Way, J.J. Collins, J.D. Keasling, and P.A. Silver. Integrating Biological Redesign: Where Synthetic Biology Came From and Where It Needs to Go. *Cell*, 157(1):151–161, mar 2014.

[64] K.M. Müller and K.M. Arndt. Standardization in Synthetic Biology. In *Synthetic Gene Networks*, pages 23–43. 2012.

[65] T. Knight. Idempotent Vector Design for Standard Assembly of BioBricks. *MIT Synthetic Biology Working Group*, 2005.

[66] M. Galdzicki, C. Rodriguez, D. Chandran, H.M. Sauro, and J.H. Gennari. Standard Biological Parts Knowledgebase. *PLoS ONE*, 6(2):e17005, feb 2011.

[67] Y.Y. Chen, K.E. Galloway, and C.D. Smolke. Synthetic biology: advancing biological frontiers by building synthetic systems. *Genome Biology*, 13(2):240, 2012.

[68] R. Kwok. Five hard truths for synthetic biology. *Nature*, 463(7279):288–290, jan 2010.

[69] V. Chubukov, A. Mukhopadhyay, C.J. Petzold, J.D. Keasling, and H.G. Martín. Synthetic and systems biology for microbial production of commodity chemicals. *npj Systems Biology and Applications*, 2(1):16009, dec 2016.

[70] J.W. Lee, D. Na, J.M. Park, J. Lee, S. Choi, and S.Y. Lee. Systems metabolic engineering of microorganisms for natural and non-natural chemicals. *Nature Chemical Biology*, 8(6):536–546, jun 2012.

[71] J. Chen, S. Sun, C.Z. Li, Y.G. Zhu, and B.P. Rosen. Biosensor for Organoarsenical Herbicides and Growth Promoters. *Environmental Science & Technology*, 48(2):1141–1147, jan 2014.

[72] S. Jaiswal and P. Shukla. Alternative Strategies for Microbial Remediation of Pollutants via Synthetic Biology. *Frontiers in Microbiology*, 11:808, may 2020.

[73] M.T.Q Duong, Y. Qin, S.H. You, and J.J. Min. Bacteria-cancer interactions: bacteria-based cancer therapy. *Experimental & Molecular Medicine*, 51(12):1–15, dec 2019.

[74] S. Zhou, C. Gravekamp, D. Bermudes, and K. Liu. Tumour-targeting bacteria engineered to fight cancer. *Nature Reviews Cancer*, 18(12):727–743, dec 2018.

[75] E. Yeung, A.J. Dy, K.B. Martin, A.H. Ng, D. Del Vecchio, J.L. Beck, J.J. Collins, and R.M. Murray. Biophysical Constraints Arising from Compositional Context in Synthetic Gene Networks. *Cell Systems*, 5(1):11–24.e12, jul 2017.

[76] I.E. Müller, J.R. Rubens, D. Jun, T.and Graham, R. Xavier, and T.K. Lu. Gene networks that compensate for crosstalk with crosstalk. *Nature Communications*, 10(1):4028, dec 2019.

[77] E.M. Nikolados, A.Y. Weiße, F. Ceroni, and D.A. Oyarzún. Growth Defects and Loss-of-Function in Synthetic Gene Circuits. *ACS Synthetic Biology*, 8(6):1231–1240, jun 2019.

[78] T. Ozdemir, A.J.H. Fedorec, T. Danino, and C.P. Barnes. Synthetic Biology and Engineered Live Biotherapeutics: Toward Increasing System Complexity. *Cell Systems*, 7(1):5–16, jul 2018.

[79] M.E. Inda, E. Broset, T.K. Lu, and C. de la Fuente-Nunez. Emerging Frontiers in Microbiome Engineering. *Trends in Immunology*, 40(10):952–973, oct 2019.

[80] M.C. Waller, J.R. Bober, N.U. Nair, and C.L. Beisel. Toward a genetic tool development pipeline for host-associated bacteria. *Current Opinion in Microbiology*, 38:156–164, aug 2017.

[81] U. Sonnenborn. Escherichia coli strain Nissle 1917-from bench to bedside and back: History of a special Escherichia coli strain with probiotic properties. *FEMS Microbiology Letters*, 363(19):1–6, 2016.

[82] F. Scaldaferri, V. Gerardi, F. Mangiola, L.R. Lopetuso, M. Pizzoferrato, V. Petito, A. Papa, J. Stojanovic, A. Poscia, G. Cammarota, and A. Gasbarrini. Role and mechanisms of action of Escherichia coli Nissle 1917 in the maintenance of remission in ulcerative colitis patients: An update. *World journal of gastroenterology*, 22(24):5505–11, jun 2016.

[83] M. Reister, K. Hoffmeier, N. Krezdorn, B. Rotter, C. Liang, S. Rund, T. Dandekar, U. Sonnenborn, and T.A. Oelschlaeger. Complete genome sequence of the Gram-negative probiotic Escherichia coli strain Nissle 1917. *Journal of Biotechnology*, 187:106–107, oct 2014.

[84] J.D. Palmer, E. Piattelli, B.A. McCormick, M.W. Silby, C.J. Brigham, and V. Bucci. Engineered Probiotic for the Inhibition of Salmonella via Tetrathionate-Induced Production of Microcin H47. *ACS Infectious Diseases*, 4(1):39–45, jan 2018.

[85] A. Rodríguez-Nogales, F. Algieri, J. Garrido-Mesa, T. Vezza, M.P. Utrilla, N. Chueca, J.A. Fernández-Caballero, F. García, M.E. Rodríguez-Cabezas, and J. Gálvez. The Administration of Escherichia coli Nissle 1917 Ameliorates Development of DSS-Induced Colitis in Mice. *Frontiers in Pharmacology*, 9, may 2018.

[86] C.A. Somabhai, R. Raghuvanshi, and G. Nareshkumar. Genetically Engineered Escherichia coli Nissle 1917 Synbiotics Reduce Metabolic Effects Induced by Chronic Consumption of Dietary Fructose. *PLOS ONE*, 11(10):e0164860, oct 2016.

[87] Z. Zhou, X. Chen, H. Sheng, X. Shen, X. Sun, Y. Yan, J. Wang, and Q. Yuan. Engineering probiotics as living diagnostics and therapeutics for improving human health. *Microbial Cell Factories*, 19(1):56, dec 2020.

[88] L.A. Lagenaur, B.E. Sanders-Beer, B. Brichacek, R. Pal, X. Liu, Y. Liu, R. Yu, D. Venzon, P.P. Lee, and D.H. Hamer. Prevention of vaginal SHIV transmission in macaques by a live recombinant Lactobacillus. *Mucosal Immunology*, 4:648, jul 2011.

[89] B. Álvarez and L.Á. Fernández. Sustainable therapies by engineered bacteria. *Microbial biotechnology*, 10(5):1057–1061, 2017.

[90] M. Sassone-Corsi, S.P. Nuccio, H. Liu, D. Hernandez, C.T. Vu, A.A. Takahashi, R.A. Edwards, and M. Raffatellu. Microcins mediate competition

among Enterobacteriaceae in the inflamed gut. *Nature*, 540(7632):280–283, dec 2016.

[91] N. Saeidi, C.K. Wong, T. Lo, H.X. Nguyen, H. Ling, S.S.J. Leong, C.L. Poh, and M.W. Chang. Engineering microbes to sense and eradicate Pseudomonas aeruginosa , a human pathogen. *Molecular Systems Biology*, 7(1):521, jan 2011.

[92] M. Mojibian, M.M. Glavas, and T.J. Kieffer. Engineering the gut for insulin replacement to treat diabetes. *Journal of diabetes investigation*, 7 Suppl 1:87–93, apr 2016.

[93] L. Putcha, P.W. Taylor, and J.L. Boyd. Biopharmaceutical challenges of therapeutics in space: formulation and packaging considerations. *Therapeutic Delivery*, 2(11):1373–1376, nov 2011.

[94] A.A. Voorhies and H.A. Lorenzi. The Challenge of Maintaining a Healthy Microbiome during Long-Duration Space Missions. *Frontiers in Astronomy and Space Sciences*, 3, jul 2016.

[95] L. Goers, C. Ainsworth, C.H. Goey, C. Kontoravdi, P.S. Freemont, and K.M. Polizzi. Whole-cell Escherichia coli lactate biosensor for monitoring mammalian cell cultures during biopharmaceutical production. *Biotechnology and Bioengineering*, 114(6):1290–1300, jun 2017.

[96] Q. Gui, T. Lawson, S. Shan, L. Yan, and Y. Liu. The Application of Whole Cell-Based Biosensors for Use in Environmental Analysis and in Medical Diagnostics. *Sensors (Basel, Switzerland)*, 17(7), jul 2017.

[97] H. Sun, H. Zhao, and E.L. Ang. A New Biosensor for Stilbenes and a Cannabinoid Enabled by Genome Mining of a Transcriptional Regulator. *ACS Synthetic Biology*, 9(4):698–705, apr 2020.

[98] N.I. Johns, A.L.C. Gomes, S.S. Yim, A. Yang, T. Blazejewski, C.S. Smillie, M.B. Smith, E.J. Alm, S. Kosuri, and H.H. Wang. Metagenomic mining of regulatory elements enables programmable species-selective gene expression. *Nature Methods*, 15(5):323–329, may 2018.

[99] M. Hicks, T.T. Bachmann, and B. Wang. Synthetic Biology Enables Programmable Cell-Based Biosensors. *ChemPhysChem*, 21(2):132–144, jan 2020.

[100] K. Jung, F. Fabiani, E. Hoyer, and J. Lassak. Bacterial transmembrane signalling systems and their engineering for biosensing. *Open Biology*, 8(4):180023, apr 2018.

[101] B. Wang, M. Hicks, and T.T. Bachmann. Synthetic Biology Enables Programmable Cell-Based Biosensors. *ChemPhysChem*, page cphc.201900739, oct 2019.

[102] A.A. Bulich and D.L. Isenberg. Use of the luminescent bacterial system for the rapid assessment of aquatic toxicity. *ISA transactions*, 20(1):29–33, 1981.

[103] P. Quillardet, O. Huisman, R. D'Ari, and M. Hofnung. SOS chromotest, a direct assay of induction of an SOS function in Escherichia coli K-12 to measure genotoxicity. *Proceedings of the National Academy of Sciences*, 79(19):5971–5975, oct 1982.

[104] J.M.H. King, P.M. DiGrazia, B. Applegate, R. Burlage, J. Sanseverino, P. Dunbar, F. Larimer, and G.S. Sayler. Rapid, Sensitive Bioluminescent Reporter Technology for Naphthalene Exposure and Biodegradation. *Science*, 249(4970):778–781, aug 1990.

[105] G.I. Paton, C.D. Campbell, L.A. Glover, and K. Killham. Assessment of bioavailability of heavy metals using lux modified constructs of Pseudomonas fluorescens. *Letters in Applied Microbiology*, 20(1):52–56, jan 1995.

[106] J. Stocker, D. Balluch, M. Gsell, H. Harms, J. Feliciano, S. Daunert, K.A. Malik, and J.R. van der Meer. Development of a Set of Simple Bacterial Biosensors for Quantitative and Rapid Measurements of Arsenite and Arsenate in Potable Water. *Environmental Science & Technology*, 37(20):4743–4750, oct 2003.

[107] Y. Berset, D. Merulla, A. Joublin, V. Hatzimanikatis, and J.R. van der Meer. Mechanistic Modeling of Genetic Circuits for ArsR Arsenic Regulation. *ACS Synthetic Biology*, 6(5):862–874, may 2017.

[108] X. Wan, F. Volpetti, E. Petrova, C. French, S.J. Maerkl, and B. Wang. Cascaded amplifying circuits enable ultrasensitive cellular sensors for toxic metals. *Nature Chemical Biology*, 15(5):540–548, may 2019.

[109] Y. Wu, C.W. Wang, D. Wang, and N. Wei. A Whole-Cell Biosensor for Point-of-Care Detection of Waterborne Bacterial Pathogens. *ACS Synthetic Biology*, page acssynbio.0c00491, jan 2021.

[110] C.M. Zammit, D. Quaranta, S. Gibson, A.J. Zaitouna, C. Ta, J. Brugger, R.Y. Lai, G. Grass, and F. Reith. A Whole-Cell Biosensor for the Detection of Gold. *PLoS ONE*, 8(8):e69292, aug 2013.

[111] L. Bereza-Malcolm, S. Aracic, and A. Franks. Development and Application of a Synthetically-Derived Lead Biosensor Construct for Use in Gram-Negative Bacteria. *Sensors*, 16(12):2174, dec 2016.

[112] L.D. Rasmussen, S.J. Sørensen, R.R. Turner, and T. Barkay. Application of a mer-lux biosensor for estimating bioavailable mercury in soil. *Soil Biology and Biochemistry*, 32(5):639–646, may 2000.

[113] B. Shemer, N. Palevsky, S. Yagur-Kroll, and S. Belkin. Genetically engineered microorganisms for the detection of explosives' residues. *Frontiers in Microbiology*, 6, oct 2015.

[114] H. Chong and C.B. Ching. Development of Colorimetric-Based Whole-Cell Biosensor for Organophosphorus Compounds by Engineering Transcription Regulator DmpR. *ACS Synthetic Biology*, 5(11):1290–1298, nov 2016.

[115] J.K. Rogers and G.M. Church. Genetically encoded sensors enable real-time observation of metabolite production. *Proceedings of the National Academy of Sciences*, 113(9):2388–2393, mar 2016.

[116] T. Danino, A. Prindle, G.A. Kwong, M. Skalak, H. Li, K. Allen, J. Hasty, and S.N. Bhatia. Programmable probiotics for detection of cancer in urine. *Science Translational Medicine*, 7(289):289ra84–289ra84, may 2015.

[117] A. Courbet, D. Endy, E. Renard, F. Molina, and J. Bonnet. Detection of pathological biomarkers in human clinical samples via amplifying genetic switches and logic gates. *Science Translational Medicine*, 7(289):289ra83–289ra83, may 2015.

[118] D.T. Riglar, T.W. Giessen, M. Baym, S.J. Kerns, M.J. Niederhuber, R.T. Bronson, J.W. Kotula, G.K. Gerber, J.C. Way, and P.A. Silver. Engineered bacteria can function in the mammalian gut long-term as live diagnostics of inflammation. *Nature Biotechnology*, 35(7):653–658, jul 2017.

[119] J.W. Kotula, S.J. Kerns, L.A. Shaket, L. Siraj, J.J. Collins, J.C. Way, and P.A. Silver. Programmable bacteria detect and record an environmental signal in the mammalian gut. *Proceedings of the National Academy of Sciences*, 111(13):4838–4843, apr 2014.

[120] N. Mao, A. Cubillos-Ruiz, D.E. Cameron, and J.J. Collins. Probiotic strains detect and suppress cholera in mice. *Science Translational Medicine*, 10(445):eaao2586, jun 2018.

[121] S.G. Woo, S.J. Moon, S.K. Kim, T.H. Kim, H.S. Lim, G.H Yeon, B.H. Sung, C.H. Lee, S.G. Lee, J.H. Hwang, and D.H. Lee. A designed whole-cell biosensor for live diagnosis of gut inflammation through nitrate sensing. *Biosensors and Bioelectronics*, 168:112523, nov 2020.

[122] A.A. Mannan, D. Liu, F. Zhang, and D.A. Oyarzún. Fundamental Design Principles for Transcription-Factor-Based Metabolite Biosensors. *ACS Synthetic Biology*, 6(10):1851–1859, oct 2017.

[123] S. Wang. Bacterial Two-Component Systems: Structures and Signaling Mechanisms. In *Protein Phosphorylation in Human Health*. InTech, sep 2012.

[124] A.M. Stock, V.L. Robinson, and P.N. Goudreau. Two-Component Signal Transduction. *Annual Review of Biochemistry*, 69(1):183–215, jun 2000.

[125] S. Tiwari, S.B. Jamal, S.S. Hassan, P.V.S.D. Carvalho, S. Almeida, D. Barh, P. Ghosh, A. Silva, T.L.P. Castro, and V. Azevedo. Two-Component Signal Transduction Systems of Pathogenic Bacteria As Targets for Antimicrobial Therapy: An Overview. *Frontiers in Microbiology*, 8, oct 2017.

[126] J. Hirakawa, H.and Kurushima, Y. Hashimoto, and H. Tomita. Progress Overview of Bacterial Two-Component Regulatory Systems as Potential Targets for Antimicrobial Chemotherapy. *Antibiotics*, 9(10):635, sep 2020.

[127] K.Y. Wen, J.W. Rutter, C.P. Barnes, and L. Dekker. Fundamental Building Blocks of Whole-Cell Biosensor Design. In *Handbook of Cell Biosensors*, pages 1–23. Springer International Publishing, Cham, 2020.

[128] X. Jia, T. Zhao, Y. Liu, R. Bu, and K. Wu. Gene circuit engineering to improve the performance of a whole-cell lead biosensor. *FEMS Microbiology Letters*, 365(16), aug 2018.

[129] G.J. Nistala, K. Wu, C.V. Rao, and K.D. Bhalerao. A modular positive feedback-based gene amplifier. *Journal of Biological Engineering*, 4(1):4, 2010.

[130] B. Wang, M. Barahona, and M. Buck. Engineering modular and tunable genetic amplifiers for scaling transcriptional signals in cascaded gene networks. *Nucleic Acids Research*, 42(14):9484–9492, aug 2014.

[131] A.J. Meyer, T.H. Segall-Shapiro, E. Glassey, J. Zhang, and C.A. Voigt. Escherichia coli Marionette strains with 12 highly optimized small-molecule sensors. *Nature Chemical Biology*, 15(2):196–204, feb 2019.

[132] T. Ozdemir. *Design and Construction of Therapeutic Bacterial Sensors in Escherichia coli Nissle 1917*. PhD thesis, University College London, 2017.

[133] S.M. Castillo-Hair, J.T. Sexton, B.P. Landry, E.J. Olson, O.A. Igoshin, and J.J. Tabor. FlowCal: A User-Friendly, Open Source Software Tool for Automatically Converting Flow Cytometry Data from Arbitrary to Calibrated Units. *ACS Synthetic Biology*, 5(7):774–780, jul 2016.

[134] S.V. Iverson, T.L. Haddock, J. Beal, and D.M. Densmore. CIDAR MoClo: Improved MoClo Assembly Standard and New E. coli Part Library Enable Rapid Combinatorial Design for Synthetic and Traditional Biology. *ACS Synthetic Biology*, 5(1):99–103, jan 2016.

[135] A.J.H. Fedorec, C.M. Robinson, K.Y. Wen, and C.P. Barnes. FlopR: An Open Source Software Package for Calibration and Normalization of Plate Reader and Flow Cytometry Data. *ACS Synthetic Biology*, 9(9):2258–2266, sep 2020.

[136] B. Goldstein and N. King. The Future of Cell Biology: Emerging Model Organisms. *Trends in Cell Biology*, 26(11):818–824, nov 2016.

[137] S.B. Hedges. The origin and evolution of model organisms. *Nature Reviews Genetics*, 3(11):838–849, nov 2002.

[138] A.D. Kostic, M.R. Howitt, and W.S. Garrett. Exploring host microbiota interactions in animal models and humans. *Genes & Development*, 27(7):701–718, apr 2013.

[139] A.E. Douglas. Which experimental systems should we use for human microbiome science? *PLOS Biology*, 16(3):e2005245, mar 2018.

[140] F. Hugenholtz and W.M. de Vos. Mouse models for human intestinal microbiota research: a critical evaluation. *Cellular and Molecular Life Sciences*, 75(1):149–160, jan 2018.

[141] Kr.N. Daeffler, J.D. Galley, R.U. Sheth, L.C. OrtizVelez, C.O. Bibb, N.F. Shroyer, R.A. Britton, and J.J. Tabor. Engineering bacterial thiosulfate and tetrathionate sensors for detecting gut inflammation. *Molecular Systems Biology*, 13(4):923, apr 2017.

[142] S. Chowdhury, S. Castro, C. Coker, T.E. Hinchliffe, N. Arpaia, and T. Danino. Programmable bacteria induce durable tumor regression and systemic antitumor immunity. *Nature Medicine*, 25(7):1057–1063, jul 2019.

[143] P. Praveschotinunt, A.M. Duraj-Thatte, I. Gelfat, F. Bahl, D.B. Chou, and N.S. Joshi. Engineered E. coli Nissle 1917 for the delivery of matrix-tethered therapeutic domains to the gut. *Nature Communications*, 10(1):5580, dec 2019.

[144] T.L.A. Nguyen, S. Vieira-Silva, A. Liston, and J. Raes. How informative is the mouse for human gut microbiota research? *Disease Models & Mechanisms*, 8(1):1–16, jan 2015.

[145] C.L. Franklin and A.C. Ericsson. Microbiota and reproducibility of rodent models. *Lab Animal*, 46(4):114–122, apr 2017.

[146] N. Fenwick, G. Griffin, and C. Gauthier. The welfare of animals used in science: how the "Three Rs" ethic guides improvements. *The Canadian veterinary journal = La revue veterinaire canadienne*, 50(5):523–30, may 2009.

[147] L. Frézal and M.A. Félix. The Natural History of Model Organisms: C. elegans outside the Petri dish. *eLife*, 4, mar 2015.

[148] The C. elegans Sequencing Consortium. Genome Sequence of the Nematode C. elegans: A Platform for Investigating Biology. *Science*, 282(5396):2012–2018, dec 1998.

[149] M.G. Sterken, L.B. Snoek, J.E. Kammenga, and E.C. Andersen. The laboratory domestication of Caenorhabditis elegans. *Trends in Genetics*, 31(5):224–231, may 2015.

[150] B.S. Samuel, H. Rowedder, C. Braendle, M.A. Félix, and G. Ruvkun. Caenorhabditis elegans responses to bacteria from its natural habitats. *Proceedings of the National Academy of Sciences*, 113(27):E3941–E3949, jul 2016.

[151] S. Brenner. The genetics of Caenorhabditis elegans. *Genetics*, 77(1):71–94, may 1974.

[152] H.A. Tissenbaum. Using C. elegans for aging research. *Invertebrate reproduction & development*, 59(sup1):59–63, jan 2015.

[153] F. Zhang, M. Berg, K. Dierking, M. Félix, M.A.and Shapira, B.S. Samuel, and H. Schulenburg. Caenorhabditis elegans as a Model for Microbiome Research. *Frontiers in microbiology*, 8:485, 2017.

[154] J. Zhang, A.D. Holdorf, and A.J.M. Walhout. C. elegans and its bacterial diet as a model for systems-level understanding of hostmicrobiota interactions. *Current Opinion in Biotechnology*, 46:74–80, aug 2017.

[155] M. Markaki and N. Tavernarakis. Modeling human diseases in Caenorhabditis elegans. *Biotechnology Journal*, 5(12):1261–1276, dec 2010.

[156] J.F. Cooper and J.M. Van Raamsdonk. Modeling Parkinson's Disease in C. elegans. *Journal of Parkinson's disease*, 8(1):17–32, 2018.

[157] M.C.K. Leung, P.L. Williams, A. Benedetto, C. Au, K.J. Helmcke, M. Aschner, and J.N. Meyer. Caenorhabditis elegans: an emerging model in biomedical and environmental toxicology. *Toxicological sciences : an official journal of the Society of Toxicology*, 106(1):5–28, nov 2008.

[158] O.R. Bracho, C. Manchery, E.C. Haskell, C.A. Blanar, and R.P. Smith. Circumvention of Learning Increases Intoxication Efficacy of Nematicidal Engineered Bacteria. *ACS Synthetic Biology*, 5(3):241–249, mar 2016.

[159] I.Y. Hwang, E. Koh, A. Wong, J.C. March, W.E. Bentley, Y.S. Lee, and M.W. Chang. Engineered probiotic Escherichia coli can eliminate and prevent Pseudomonas aeruginosa gut infection in animal models. *Nature communications*, 8:15028, apr 2017.

[160] E. Watson, V. Olin-Sandoval, M.J. Hoy, C.H. Li, T. Louisse, V. Yao, A. Mori, A.D. Holdorf, O.G. Troyanskaya, M. Ralser, and A.J.M. Walhout. Metabolic network rewiring of propionate flux compensates vitamin B12 deficiency in C. elegans. *eLife*, 5, jul 2016.

[161] S. Lebeer and I. Spacova. Exploring human hostmicrobiome interactions in health and diseasehow to not get lost in translation. *Genome Biology*, 20(1):56, dec 2019.

[162] J. Wang, S. Su, J. Wei, R. Bahgi, L. Hope-Weeks, J. Qiu, and S. Wang. Ratio-metric sensor to detect riboflavin via fluorescence resonance energy transfer with ultrahigh sensitivity. *Physica E: Low-dimensional Systems and Nanostructures*, 72:17–24, aug 2015.

[163] J.R. Kelly, A.J. Rubin, J.H. Davis, C.M. Ajo-Franklin, J. Cumbers, M.J. Czar, K. de Mora, A.L. Glieberman, D.D. Monie, and D. Endy. Measuring the activity of BioBrick promoters using an in vivo reference standard. *Journal of biological engineering*, 3:4, mar 2009.

[164] B. Lim, M. Zimmermann, N.A. Barry, and A.L. Goodman. Engineered Regulatory Systems Modulate Gene Expression of Human Commensals in the Gut. *Cell*, 169(3):547–558.e15, apr 2017.

[165] M.P. O'Donnell, B.W. Fox, P.H. Chao, F.C. Schroeder, and P. Sengupta. A neurotransmitter produced by gut bacteria modulates host sensory behaviour. *Nature*, jun 2020.

[166] M. Kasubuchi, S. Hasegawa, T. Hiramatsu, A. Ichimura, and I. Kimura. Dietary Gut Microbial Metabolites, Short-chain Fatty Acids, and Host Metabolic Regulation. *Nutrients*, 7(4):2839–2849, apr 2015.

[167] K.A. Chapman, J. Ostrovsky, M. Rao, S.D. Dingley, E. Polyak, M. Yudkoff, R. Xiao, M.J. Bennett, and M.J. Falk. Propionyl-CoA carboxylase pcca-1 and pccb-1 gene deletions in Caenorhabditis elegans globally impair mitochondrial energy metabolism. *Journal of Inherited Metabolic Disease*, 41(2):157–168, mar 2018.

[168] L. Pena, J. Franks, K.A. Chapman, A. Gropman, N. Ah Mew, A. Chakrapani, E. Island, E. MacLeod, D. Matern, B. Smith, K. Stagni, V.R. Sutton, K. Ueda, T. Urv, C. Venditti, G.M. Enns, and M.L. Summar. Natural history of propionic acidemia. *Molecular Genetics and Metabolism*, 105(1):5–9, jan 2012.

[169] E. Watson, L.T. MacNeil, H.E. Arda, L.J. Zhu, and A.J.M. Walhout. Integration of Metabolic and Gene Regulatory Networks Modulates the C. elegans Dietary Response. *Cell*, 153(1):253–266, mar 2013.

[170] N.M. Vega and J. Gore. Stochastic assembly produces heterogeneous communities in the Caenorhabditis elegans intestine. *PLOS Biology*, 15(3):e2000633, mar 2017.

[171] A.J.H. Fedorec, T. Ozdemir, A. Doshi, YK Ho, L. Rosa, J. Rutter, O. Velazquez, V.B. Pinheiro, T. Danino, and C.P. Barnes. Two New Plasmid Postsegregational Killing Mechanisms for the Implementation of Synthetic Gene Networks in Escherichia coli. *iScience*, 14:323–334, apr 2019.

[172] D. Summers. The kinetics of plasmid loss. *Trends in Biotechnology*, 9(1):273–278, jan 1991.

[173] F. Silva, J.A. Queiroz, and F.C. Domingues. Evaluating metabolic stress and plasmid stability in plasmid DNA production by Escherichia coli. *Biotechnology Advances*, 30(3):691–708, may 2012.

[174] B. Stecher, R. Denzler, L. Maier, F. Bernet, M. J. Sanders, D.J. Pickard, M. Barthel, A.M. Westendorf, K.A. Krogfelt, A.W. Walker, M. Ackermann, U. Dobrindt, N.R. Thomson, and W.D. Hardt. Gut inflammation can boost horizontal gene transfer between pathogenic and commensal Enterobacteriaceae. *Proceedings of the National Academy of Sciences*, 109(4):1269–1274, jan 2012.

[175] M.Y. Yoon and S.S. Yoon. Disruption of the Gut Ecosystem by Antibiotics. *Yonsei Medical Journal*, 59(1):4, 2018.

[176] M.P. Francino. Antibiotics and the Human Gut Microbiome: Dysbioses and Accumulation of Resistances. *Frontiers in Microbiology*, 6, jan 2016.

[177] E.M. Halvorsen, J.J. Williams, A.J. Bhimani, E.A. Billings, and P.J. Hergenrother. Txe, an endoribonuclease of the enterococcal Axe?Txe toxin?antitoxin system, cleaves mRNA and inhibits protein synthesis. *Microbiology*, 157(2):387–397, feb 2011.

[178] R. Grady and F. Hayes. Axe-Txe, a broad-spectrum proteic toxin-antitoxin system specified by a multidrug-resistant, clinical isolate of Enterococcus faecium. *Molecular Microbiology*, 47(5):1419–1432, feb 2003.

[179] V.K. Mutalik, J.C. Guimaraes, G. Cambray, C. Lam, M.J. Christoffersen, Q.A. Mai, A.B. Tran, M. Paull, J.D. Keasling, A.P. Arkin, and D. Endy. Precise and reliable gene expression via standard transcription and translation initiation elements. *Nature Methods*, 10(4):354–360, apr 2013.

[180] S. Cardinale, M.P. Joachimiak, and A.P. Arkin. Effects of Genetic Variation on the E. coli Host-Circuit Interface. *Cell Reports*, 4(2):231–237, jul 2013.

[181] P.F. Xia, Q. Li, L.R. Tan, M.M. Liu, Y.S. Jin, and S.G. Wang. Synthetic Whole-Cell Biodevices for Targeted Degradation of Antibiotics. *Scientific Reports*, 8(1):2906, dec 2018.

[182] T. Baba, T. Ara, M. Hasegawa, Y. Takai, Y. Okumura, M. Baba, K.A. Datsenko, M. Tomita, B.L. Wanner, and H. Mori. Construction of Escherichia coli K12 inframe, singlegene knockout mutants: the Keio collection. *Molecular Systems Biology*, 2(1), jan 2006.

[183] L.H. Hansen, S. Knudsen, and S.J. Sørensen. The Effect of the lacY Gene on the Induction of IPTG Inducible Promoters, Studied in Escherichia coli and Pseudomonas fluorescens. *Current Microbiology*, 36(6):341–347, jun 1998.

[184] D.F. Browning, R.E. Godfrey, K.L. Richards, C. Robinson, and S.J.W. Busby. Exploitation of the Escherichia coli lac operon promoter for controlled recombinant protein production. *Biochemical Society Transactions*, 47(2):755–763, apr 2019.

[185] A. Novick and M. Weiner. Enzyme induction as an all-or-none phenomenon. *Proceedings of the National Academy of Sciences*, 43(7):553–566, jul 1957.

[186] J. Brosius, M. Erfle, and J. Storella. Spacing of the -10 and -35 regions in the tac promoter effect on its in vivo activity. *The Journal of biological chemistry*, 260(6):3539–41, mar 1985.

[187] A. Marbach and K. Bettenbrock. lac operon induction in Escherichia coli: Systematic comparison of IPTG and TMG induction and influence of the transacetylase LacA. *Journal of Biotechnology*, 157(1):82–88, jan 2012.

[188] M. Kærn, W.J. Blake, and J.J. Collins. The Engineering of Gene Regulatory Networks. *Annual Review of Biomedical Engineering*, 5(1):179–206, aug 2003.

[189] Y. Zong, H.M. Zhang, C. Lyu, X. Ji, J. Hou, X. Guo, Q. Ouyang, and C. Lou. Insulated transcriptional elements enable precise design of genetic circuits. *Nature Communications*, 8(1):52, dec 2017.

[190] M.G. Thompson, A.N. Pearson, J.F. Barajas, P. Cruz-Morales, N. Sedaghatian, Z. Costello, M.E. Garber, M.R. Incha, L.E. Valencia, E.E.K. Baidoo, H.G. Martin, A. Mukhopadhyay, and J.D. Keasling. Identification, Characterization, and Application of a Highly Sensitive Lactam Biosensor from Pseudomonas putida. *ACS Synthetic Biology*, page acssynbio.9b00292, jan 2020.

[191] E. Balleza, J.M. Kim, and P. Cluzel. Systematic characterization of maturation time of fluorescent proteins in living cells. *Nature Methods*, 15(1):47–51, jan 2018.

[192] Y. Shen, Y. Chen, J. Wu, N.C. Shaner, and R.E. Campbell. Engineering of mCherry variants with long Stokes shift, red-shifted fluorescence, and low cytotoxicity. *PLOS ONE*, 12(2):e0171257, feb 2017.

[193] J.B. Andersen, C. Sternberg, L.K. Poulsen, S.P. Bjorn, M. Givskov, and S. Molin. New unstable variants of green fluorescent protein for studies of transient gene expression in bacteria. *Applied and environmental microbiology*, 64(6):2240–6, jun 1998.

[194] C. Lou, B. Stanton, Y.J. Chen, B. Munsky, and C.A. Voigt. Ribozyme-based insulator parts buffer synthetic circuits from genetic context. *Nature Biotechnology*, 30(11):1137–1142, nov 2012.

[195] P. Malakar and K.V. Venkatesh. Effect of substrate and IPTG concentrations on the burden to growth of Escherichia coli on glycerol due to the expression of Lac proteins. *Applied Microbiology and Biotechnology*, 93(6):2543–2549, mar 2012.

[196] F. Ceroni, R. Algar, G.B. Stan, and T. Ellis. Quantifying cellular capacity identifies gene expression designs with reduced burden. *Nature Methods*, 12(5):415–418, may 2015.

[197] Y. Qian, H.H. Huang, J.I. Jiménez, and D. Del Vecchio. Resource Competition Shapes the Response of Genetic Circuits. *ACS Synthetic Biology*, 6(7):1263–1272, jul 2017.

[198] A.Y. Weiße, D.A. Oyarzún, V. Danos, and P.S. Swain. Mechanistic links between cellular trade-offs, gene expression, and growth. *Proceedings of the National Academy of Sciences*, 112(9):E1038–E1047, mar 2015.

[199] M. Jahn, C. Vorpahl, T. Hübschmann, H. Harms, and S. Müller. Copy number variability of expression plasmids determined by cell sorting and Droplet Digital PCR. *Microbial Cell Factories*, 15(1):211, dec 2016.

[200] E. Hiszczyńska-Sawicka and J. Kur. Effect of Escherichia coli IHF Mutations on Plasmid p15A Copy Number. *Plasmid*, 38(3):174–179, nov 1997.

[201] M.G. Thompson, N. Sedaghatian, J.F. Barajas, M. Wehrs, C.B. Bailey, N. Kaplan, N.J. Hillson, A. Mukhopadhyay, and J.D. Keasling. Isolation and characterization of novel mutations in the pSC101 origin that increase copy number. *Scientific Reports*, 8(1):1590, dec 2018.

[202] K. Marisch, K. Bayer, M. Cserjan-Puschmann, M. Luchner, and G. Striedner. Evaluation of three industrial Escherichia coli strains in fed-batch cultivations during high-level SOD protein production. *Microbial Cell Factories*, 12(1):58, 2013.

[203] R. Silva-Rocha, E. Martínez-García, B. Calles, M. Chavarría, A. Arce-Rodríguez, A. de las Heras, A.D. Páez-Espino, G. Durante-Rodríguez, J. Kim, P.I. Nikel, R. Platero, and V. de Lorenzo. The Standard European Vector Architecture (SEVA): a coherent platform for the analysis and deployment of complex prokaryotic phenotypes. *Nucleic Acids Research*, 41(D1):D666–D675, jan 2013.

[204] E. Martínez-García, T. Aparicio, A. Goñi-Moreno, S. Fraile, and V. de Lorenzo. SEVA 2.0: an update of the Standard European Vector Architecture for de-/re-construction of bacterial functionalities. *Nucleic Acids Research*, 43(D1):D1183–D1189, jan 2015.

[205] P. Dvorak, L. Chrast, P.I. Nikel, R. Fedr, K. Soucek, M. Sedlackova, R. Chaloupkova, V. de Lorenzo, Z. Prokop, and J. Damborsky. Exacerbation of substrate toxicity by IPTG in Escherichia coli BL21(DE3) carrying a synthetic metabolic pathway. *Microbial Cell Factories*, 14(201), 2015.

[206] M.J. Kosinski, U. Rinas, and J.E. Bailey. Isopropyl-i-D-thiogalactopyranoside influences the metabolism of Escherichia coli. *Applied Microbiology and Biotechnology*, 36:782–784, 1992.

[207] Anderson promoter collection.

[208] K.A. Datsenko and B.L. Wanner. One-step inactivation of chromosomal genes in Escherichia coli K-12 using PCR products. *Proceedings of the National Academy of Sciences*, 97(12):6640–6645, jun 2000.

[209] I.A.D. Lessard, S.D. Pratt, D.G. McCafferty, D.E. Bussiere, C. Hutchins, B.L. Wanner, L. Katz, and C.T. Walsh. Homologs of the vancomycin resistance d-Ala-d-Ala dipeptidase VanX in Streptomyces toyocaensis, Escherichia coli and Synechocystis: attributes of catalytic efficiency, stereoselectivity and regulation with implications for function. *Chemistry & Biology*, 5(9):489–504, sep 1998.

[210] N. Casali and A. Preston. *E. coli plasmid vectors: methods and applications*. Humana, Totowa, 2003.

[211] F. Grenier, D. Matteau, V. Baby, and S. Rodrigue. Complete Genome Sequence of Escherichia coli BW25113. *Genome Announcements*, 2(5), oct 2014.

[212] R. Mattar, Mazo, and Carrilho. Lactose intolerance: diagnosis, genetic, and clinical factors. *Clinical and Experimental Gastroenterology*, page 113, jul 2012.

[213] S.J. Oak and R. Jha. The effects of probiotics in lactose intolerance: A systematic review. *Critical Reviews in Food Science and Nutrition*, 59(11):1675–1683, jun 2019.

[214] F. Fassio, M. Facioni, and F. Guagnini. Lactose Maldigestion, Malabsorption, and Intolerance: A Comprehensive Review with a Focus on Current Management and Future Perspectives. *Nutrients*, 10(11):1599, nov 2018.

[215] R.K. Singh, H.W. Chang, D. Yan, K.M. Lee, D. Ucmak, K. Wong, B. Abrouk, M.and Farahnik, M. Nakamura, T.H. Zhu, T. Bhutani, and W. Liao. Influence of diet on the gut microbiome and implications for human health. *Journal of Translational Medicine*, 15(1):73, dec 2017.

[216] P. Neubauer, K. Hofmann, O. Holst, B. Mattiasson, and P. Kruschke. Maximizing the expression of a recombinant gene in Escherichia coli by manipulation of induction time using lactose as inducer. *Applied Microbiology and Biotechnology*, 36(6), mar 1992.

[217] B. Wang, M. Barahona, and M. Buck. Amplification of small molecule-inducible gene expression via tuning of intracellular receptor densities. *Nucleic Acids Research*, 43(3):1955–1964, feb 2015.

[218] M. Skulj, V. Okrslar, S. Jalen, S. Jevsevar, P. Slanc, B. Strukelj, and V. Menart. Improved determination of plasmid copy number using quantitative real-time PCR for monitoring fermentation processes. *Microbial Cell Factories*, 7(1):6, 2008.

[219] B.P. Landry, R. Palanki, N. Dyulgyarov, L.A. Hartsough, and J.J. Tabor. Phosphatase activity tunes two-component system sensor detection threshold. *Nature Communications*, 9(1):1433, dec 2018.

[220] M.C. Theodorou, C.A. Panagiotidis, C.H. Panagiotidis, A.A. Pantazaki, and D.A. Kyriakidis. Involvement of the AtoS-AtoC signal transduction system in poly-(R)-3-hydroxybutyrate biosynthesis in Escherichia coli. *Biochimica et Biophysica Acta (BBA) - General Subjects*, 1760(6):896–906, jun 2006.

[221] K. Papenfort and B.L. Bassler. Quorum sensing signalresponse systems in Gram-negative bacteria. *Nature Reviews Microbiology*, 14(9):576–588, sep 2016.

[222] D. Duanmu, C. Bachy, S. Sudek, C.H. Wong, V. Jimenez, N.C. Rockwell, S.S. Martin, C.Y. Ngan, E.N. Reistetter, M.J. van Baren, D.C. Price, C.L. Wei, A. Reyes-Prieto, J.C. Lagarias, and A.Z. Worden. Marine algae and land plants share conserved phytochrome signaling systems. *Proceedings of the National Academy of Sciences*, 111(44):15827–15832, nov 2014.

[223] J.R. O'Connor, N.J. Kuwada, V. Huangyutitham, P.A. Wiggins, and C.S. Harwood. Surface sensing and lateral subcellular localization of WspA, the receptor in a chemosensory-like system leading to c-di-GMP production. *Molecular Microbiology*, 86(3):720–729, nov 2012.

[224] K.K. Singh. The Saccharomyces cerevisiae sln1p-ssk1p two-component system mediates response to oxidative stress and in an oxidant-specific fashion. *Free Radical Biology and Medicine*, 29(10):1043–1050, nov 2000.

[225] M.H. Karavolos, K. Winzer, P. Williams, and C.M.A. Khan. Pathogen espionage: multiple bacterial adrenergic sensors eavesdrop on host communication systems. *Molecular Microbiology*, 87(3):455–465, feb 2013.

[226] F. Padilla-Vaca, V. Mondragon-Jaimes, and B. Franco. General Aspects of Two-Component Regulatory Circuits in Bacteria: Domains, Signals and Roles. *Current Protein & Peptide Science*, 18(10), aug 2017.

[227] S. Ravikumar, Y. David, S.J. Park, and J. Choi. A Chimeric Two-Component Regulatory System-Based Escherichia coli Biosensor Engineered to Detect Glutamate. *Applied Biochemistry and Biotechnology*, 186(2):335–349, oct 2018.

[228] I. Ganesh, S. Ravikumar, I. Yoo, and S.H. Hong. Construction of malate-sensing Escherichia coli by introduction of a novel chimeric two-component system. *Bioprocess and Biosystems Engineering*, 38(4):797–804, apr 2015.

[229] I. Ganesh, S. Ravikumar, S.H. Lee, S.J. Park, and S.H. Hong. Engineered fumarate sensing Escherichia coli based on novel chimeric two-component system. *Journal of Biotechnology*, 168(4):560–566, dec 2013.

[230] I. Ganesh, T.W. Kim, J.G. Na, G.T. Eom, and S.H. Hong. Engineering Escherichia coli to Sense Non-native Environmental Stimuli: Synthetic Chimera Two-component Systems. *Biotechnology and Bioprocess Engineering*, 24(1):12–22, feb 2019.

[231] G. Pauli and P. Overath. ato Operon: a Highly Inducible System for Acetoacetate and Butyrate Degradation in Escherichia coli. *European Journal of Biochemistry*, 29(3):553–562, sep 1972.

[232] T. Oshima, H. Aiba, Y. Masuda, S. Kanaya, M. Sugiura, B.L. Wanner, H. Mori, and T. Mizuno. Transcriptome analysis of all two-component regulatory system mutants of Escherichia coli K-12. *Molecular Microbiology*, 46(1):281–291, oct 2002.

[233] E. Pilalis, A.A. Chatziioannou, A.I. Grigoroudis, C.A. Panagiotidis, F.N. Kolisis, and D.A. Kyriakidis. Escherichia coli genome-wide promoter analysis: Identification of additional AtoC binding target elements. *BMC Genomics*, 12(1):238, 2011.

[234] E.C. Theodorou, M.C. Theodorou, and D.A. Kyriakidis. Regulation of poly-(R)-(3-hydroxybutyrate-co-3-hydroxyvalerate) biosynthesis by the AtoSC-DAEB regulon in phaCAB + Escherichia coli. *Applied Microbiology and Biotechnology*, 97(12):5259–5274, jun 2013.

[235] A. Getachew and F. Woldesenbet. Production of biodegradable plastic by polyhydroxybutyrate (PHB) accumulating bacteria using low cost agricultural waste material. *BMC Research Notes*, 9(1):509, dec 2016.

[236] P.S. Filippou, E.E. Lioliou, C.A. Panagiotidis, C.M. Athanassopoulos, T. Garnelis, D. Papaioannou, and D.A. Kyriakidis. Effect of polyamines and synthetic polyamine-analogues on the expression of antizyme (AtoC) and its regulatory genes. *BMC biochemistry*, 8:1, jan 2007.

[237] M.C. Theodorou, E.C. Theodorou, C.A. Panagiotidis, and D.A. Kyriakidis. Spermidine triggering effect to the signal transduction through the AtoSAtoC/Az two-component system in Escherichia coli. *Biochimica et Biophysica Acta (BBA) - General Subjects*, 1770(8):1104–1114, aug 2007.

[238] L Laffel. Ketone bodies: a review of physiology, pathophysiology and application of monitoring to diabetes. *Diabetes/metabolism research and reviews*, 15(6):412–26.

[239] P. Kanikarla-Marie and S.K. Jain. Hyperketonemia and ketosis increase the risk of complications in type 1 diabetes. *Free Radical Biology and Medicine*, 95:268–277, jun 2016.

[240] M. Evans, K.E. Cogan, and B. Egan. Metabolism of ketone bodies during exercise and training: physiological basis for exogenous supplementation. *The Journal of Physiology*, 595(9):2857–2871, may 2017.

[241] J.O. Sass. Inborn errors of ketogenesis and ketone body utilization. *Journal of Inherited Metabolic Disease*, 35(1):23–28, jan 2012.

[242] E.G. Neal, H. Chaffe, R.H. Schwartz, M.S. Lawson, N. Edwards, G. Fitzsimmons, A. Whitney, and J.H. Cross. The ketogenic diet for the treatment of childhood epilepsy: a randomised controlled trial. *The Lancet Neurology*, 7(6):500–506, jun 2008.

[243] X. Zou, J. Meng, L. Li, W. Han, C. Li, R. Zhong, X. Miao, J. Cai, Y. Zhang, and D. Zhu. Acetoacetate Accelerates Muscle Regeneration and Ameliorates Muscular Dystrophy in Mice. *Journal of Biological Chemistry*, 291(5):2181–2195, jan 2016.

[244] M. Board, C. Lopez, C. van den Bos, R. Callaghan, K. Clarke, and C. Carr. Acetoacetate is a more efficient energy-yielding substrate for human mesenchymal stem cells than glucose and generates fewer reactive oxygen species. *The International Journal of Biochemistry & Cell Biology*, 88:75–83, jul 2017.

[245] D. Hu, Z. Shi, Q. Wu, and G.Q. Chen. Microbial production of acetoacetate by recombinant Escherichia coli. *Bioresource Technology*, 101(21):8477–8480, nov 2010.

[246] F. Enjalbert, M.C. Nicot, C. Bayourthe, and R. Moncoulon. Ketone Bodies in Milk and Blood of Dairy Cows: Relationship between Concentrations and Utilization for Detection of Subclinical Ketosis. *Journal of Dairy Science*, 84(3):583–589, mar 2001.

[247] J. Carrier, S. Stewart, S. Godden, J. Fetrow, and P. Rapnicki. Evaluation and Use of Three Cowside Tests for Detection of Subclinical Ketosis in Early Postpartum Cows. *Journal of Dairy Science*, 87(11):3725–3735, nov 2004.

[248] A. Berepiki, L.F.M. Kent, R.and Machado, and N. Dixon. Development of High-Performance Whole Cell Biosensors Aided by Statistical Modeling. *ACS Synthetic Biology*, 9(3):576–589, mar 2020.

[249] Y. Chen, J.M.L. Ho, D.L. Shis, C. Gupta, J. Long, D.S. Wagner, W. Ott, K. Josić, and M.R. Bennett. Tuning the dynamic range of bacterial promoters regulated by ligand-inducible transcription factors. *Nature Communications*, 9(1):64, dec 2018.

[250] E. Gonzalez-Flo, M.E. Alaball, and J. Macia. Two-Component Biosensors: Unveiling the Mechanisms of Predictable Tunability. *ACS Synthetic Biology*, 9(6):1328–1335, may 2020.

[251] L.N. Merk, A.S. Shur, A. Pandey, R.M. Murray, and L.N. Green. Engineering logical inflammation sensing circuit for gut modulation. *bioRxiv*, 2020.

[252] B. Iooss and P. Lemaître. A review on global sensitivity analysis methods. apr 2014.

[253] M.D. Morris. Factorial Sampling Plans for Preliminary Computational Experiments. *Technometrics*, 33(2):161–174, may 1991.

[254] F. Campolongo, J. Cariboni, and A. Saltelli. An effective screening design for sensitivity analysis of large models. *Environmental Modelling & Software*, 22(10):1509–1518, oct 2007.

[255] O.A. Igoshin, R. Alves, and M.A. Savageau. Hysteretic and graded responses in bacterial two-component signal transduction. *Molecular Microbiology*, 68(5):1196–1215, jun 2008.

[256] K. Yamamoto, K.and Hirao, T. Oshima, H. Aiba, R. Utsumi, and A. Ishihama. Functional Characterization in Vitro of All Two-component Signal Transduction Systems from Escherichia coli. *Journal of Biological Chemistry*, 280(2):1448–1456, jan 2005.

[257] T. Fukao, G.D. Lopaschuk, and G.A. Mitchell. Pathways and control of ketone body metabolism: on the fringe of lipid biochemistry. *Prostaglandins, Leukotrienes and Essential Fatty Acids*, 70(3):243–251, mar 2004.

[258] M.K. Matta, E.E. Lioliou, C.H. Panagiotidis, D.A. Kyriakidis, and C.A. Panagiotidis. Interactions of the Antizyme AtoC with Regulatory Elements of the Escherichia coli atoDAEB Operon. *Journal of Bacteriology*, 189(17):6324–6332, sep 2007.

[259] A. Lopreside, X. Wan, E. Michelini, A. Roda, and B. Wang. Comprehensive Profiling of Diverse Genetic Reporters with Application to Whole-Cell and Cell-Free Biosensors. *Analytical Chemistry*, 91(23):15284–15292, dec 2019.

[260] G. Shinar, R. Milo, M.R. Martinez, and U. Alon. Input output robustness in simple bacterial signaling systems. *Proceedings of the National Academy of Sciences*, 104(50):19931–19935, dec 2007.

[261] D.J. Morris, D.C. Speirs, A.I. Cameron, and M.R. Heath. Global sensitivity analysis of an end-to-end marine ecosystem model of the North Sea: Factors affecting the biomass of fish and benthos. *Ecological Modelling*, 273:251–263, feb 2014.

[262] H. Chen, S. Venkat, J. Wilson, P. McGuire, A. Chang, Q. Gan, and C. Fan. Genome-Wide Quantification of the Effect of Gene Overexpression on Escherichia coli Growth. *Genes*, 9(8):414, aug 2018.

[263] S.R. Schmidl, R.U. Sheth, A. Wu, and J.J. Tabor. Refactoring and Optimization of Light-Switchable Escherichia coli Two-Component Systems. *ACS Synthetic Biology*, 3(11):820–831, nov 2014.

[264] M. Mimee, P. Nadeau, A. Hayward, S. Carim, S. Flanagan, L. Jerger, J. Collins, S. McDonnell, R. Swartwout, R.J. Citorik, V. Bulović, R. Langer, G. Traverso, A.P. Chandrakasan, and T.K. Lu. An ingestible bacterial-electronic system to monitor gastrointestinal health. *Science*, 360(6391):915–918, may 2018.

Appendices

Appendix A

Additional *C. elegans* Model Characterisation

A.1 Image Pipeline Trial

The MATLAB image pipeline was trialled on images collected by Tanel Ozdemir (Barnes lab, UCL) and the automated ratios compared to the original, manually collected ratios (Figures 4.4 and A.1). It was found that the automated ratios showed strong qualitative agreement, with the original manual ratios in both cases. However, the ratios collected for all strains were lower than those collected manually; this is most likely caused by the auto-fluorescence removal step, which decreased the amount of background noise included within the ratios when collected through the pipeline. Overall, this early comparison gave us confidence that the automated pipeline was operating as intended.

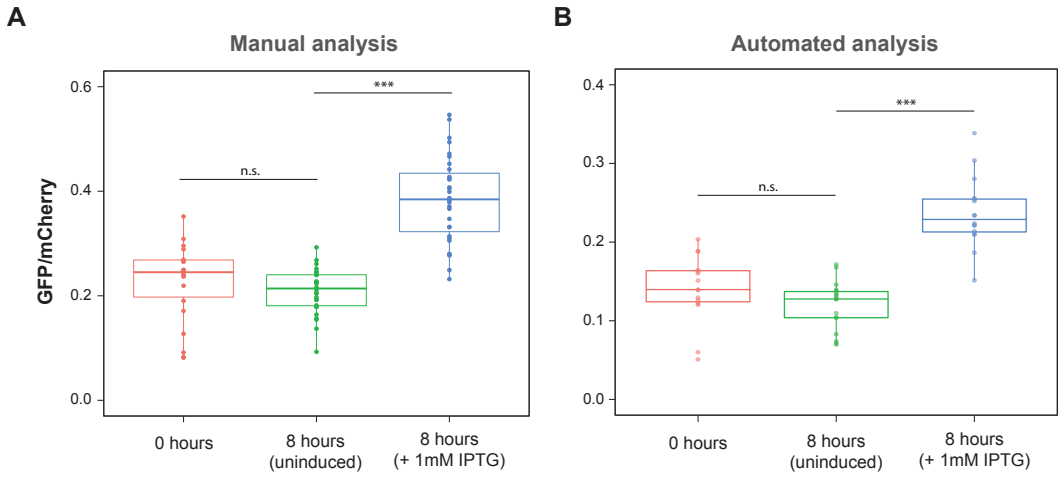

Figure A.1: Additional comparison of the automated analysis method, to manual ratios collected previously within the Barnes lab [132]. *C. elegans* colonised with EcN_pLac were placed on either NGM control plates or plates supplemented with 1 mM IPTG. Ratios were collected at either 0 or 8 hours: (**A**) manual ratios, (**B**) automated ratios. (n $>$ 27 images, p-values: ns $>$ 0.05, *** $<$ 0.05)

A.2 Manual *C. elegans* EcN_pLac image analysis

To further confirm the results gained from automated analysis of the *C. elegans* images were sensible, manual analysis was performed on the images gained during pLac biosensor characterisation. This analysis was performed using FIJI software. with the method given in chapter 3. The manual GFP:mCherry ratios were found to increase over time and with IPTG induction.

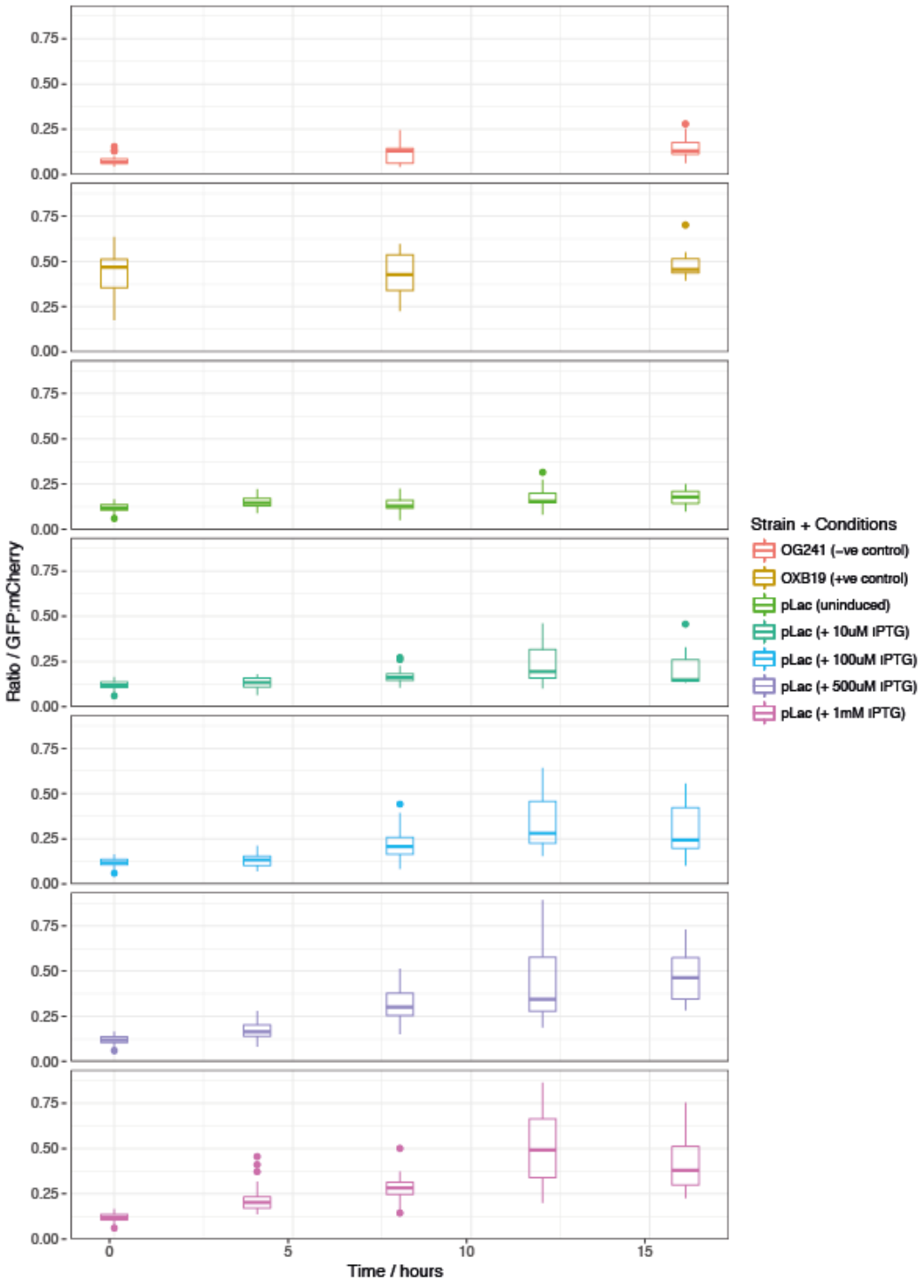

Figure A.2: Manually calculated ratios for induction of the EcN_pLac biosensor, within the *C. elegans* model system. Ratios were collected using the FIJI analysis method.

Appendix B

Additional Ratiometric Results

B.1 Axe-Txe Effect on WCB mCherry Fluorescence

The addition of the AT fragment to the pRBLac WCB produced a small increase in mCherry fluorescence, in both the BW25113 and EcN host chassis. This change in mCherry fluorescence is shown in Figure B.1.

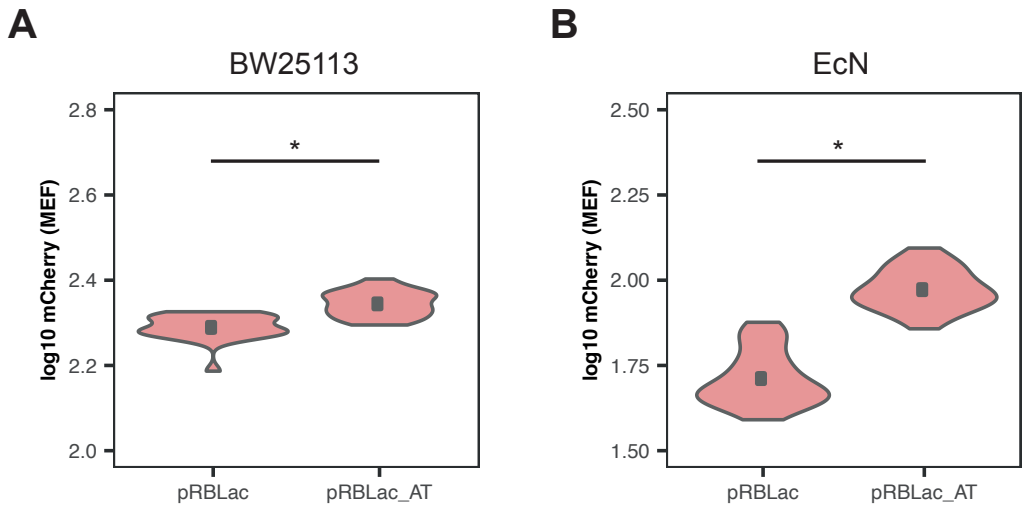

Figure B.1: Violin plots of the median mCherry signal measured from pRBLac and pRBLac_AT, in (**A**) BW25113 and (**B**) *E. coli* Nissle. In both chassis the addition of AT produced an increase in mCherry fluorescence. Flow cytometry data with 10 000 events. (n = 3 biological repeats, points give mean of medians $\pm$ SE, p-value: * < 0.05)

B.2 Construction of propionate and acetoacetate ratiometric WCBs

Cloning of pRBPro and pRBPro_AT

A fragment containing the *prpR* gene and pprp promoter was amplified from the pLD39 pAJM.223 mod + DE propionate_DF (J23016) plasmid (provided by Linda Dekker, UCL), using the pJRPro_fragment.F and pJRPro_fragment.R primers. A PCR was then performed on the pRB and pRB_AT vectors, with the pJRPro_vector.F and pJRPro_vector.R primers. The fragment was then added to both vectors, using NEB HiFi assembly, to produce the pRBPro and pRBPro_AT plasmids.

Cloning of pRBAto and pRBAto_AT

The pato promoter was cloned from the patoDAEB + GFP plasmid, using the pJRAto_fragment.F and pJRAto_fragment.R primers. A PCR was then performed on the pRB and pRB_AT vectors, with the pJRAto_vector.F and pJRAto_vector.R primers. The pJRAto fragment was then added to both vectors, using NEB HiFi assembly, to produce the pRBAto and pRBAto_AT plasmids.

Ratiometric biosensor performance

As described above, attempts were made to create propionate and acetoacetate-inducible WCBs based on the ratiometric platform; termed pRBPro/pRBPro_AT and pRBAto/pRBAto_AT, respectively (plasmid maps given in Figure B.2). These were based on the propionate sensing mechanism used in chapter 4 and the Ato system used in chapter 6. Induction assays of these constructs can be seen in Figures

B.3 and B.4. All four constructs showed some increase in GFP expression on induction; however, the GFP:mCherry ratios did not behave as expected in their current form.

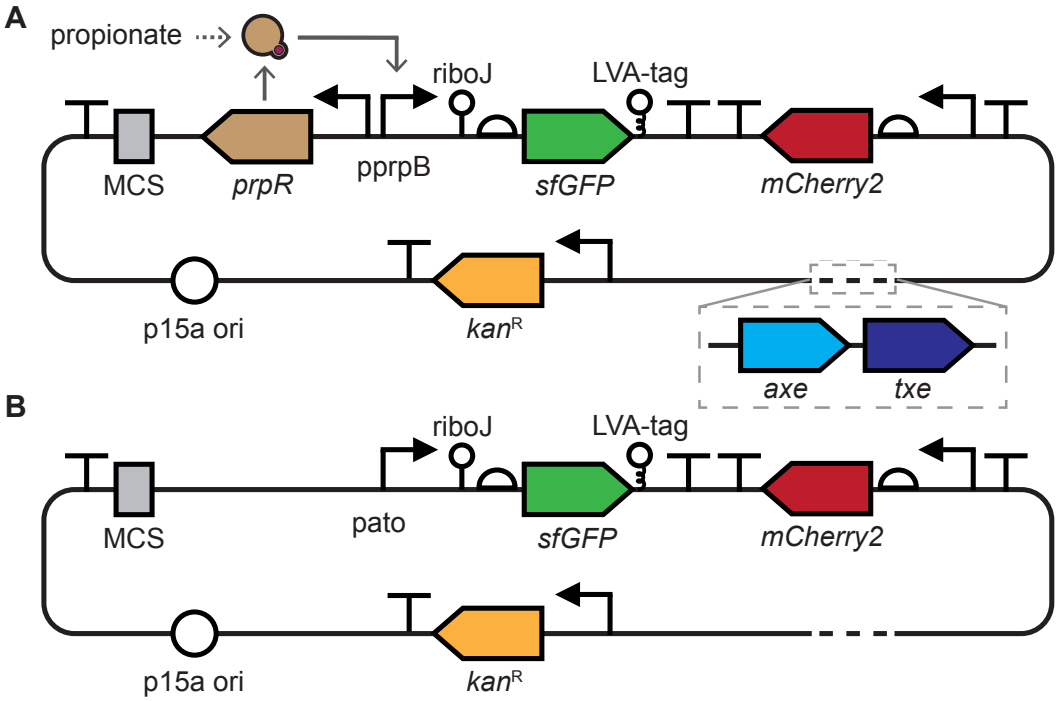

Figure B.2: Plasmid maps of the (**A**) propionate- and (**B**) acetoacetate-inducible ratiometric WCBs.

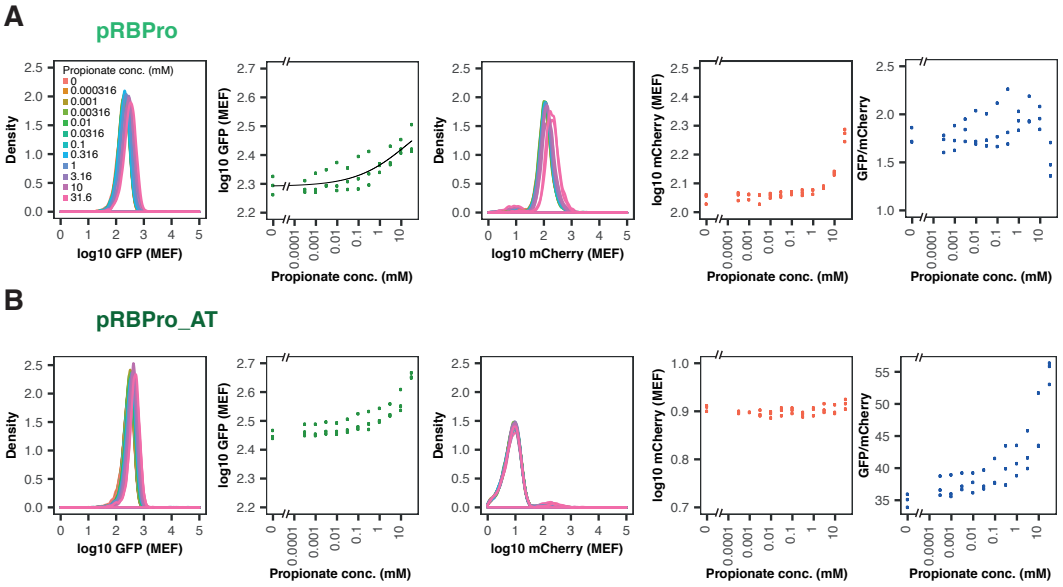

Figure B.3: *In vitro* characterisation of pRBPro/pRBPro_AT, in LB media 3 hours post-induction. (**A**) pRBPro, (**B**) pRBPro_AT WCB. From left to right: density plot of GFP induction, median GFP fluorescence, density plot of mCherry, median mCherry fluorescence and GFP:mCherry ratios. Flow cytometry data with 10 000 events. (n = 3 biological replicates)

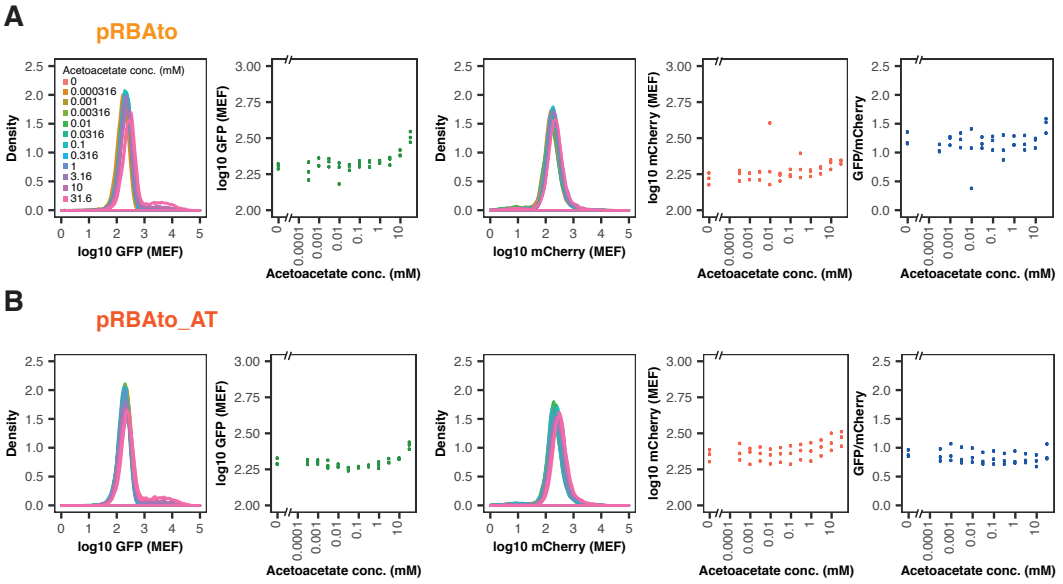

Figure B.4: *In vitro* characterisation of pRBAto/pRBAto_AT, in LB media 3 hours post-induction. (**A**) pRBAto, (**B**) pRBAto_AT WCB. From left to right: density plot of GFP induction, median GFP fluorescence, density plot of mCherry, median mCherry fluorescence and GFP:mCherry ratios. Flow cytometry data with 10 000 events. (n = 3 bioligical replicates)

Appendix C

Additional Ato WCB results

C.1 Confirmation of the Keio Collection Mutants

PCR amplification of the strain genomes (BW25113, BW28878, JW2213, JW2214) was performed, in order to confirm the gene knockouts, of strains received from the Kieo collection. Within the Keio knockout strains, the deleted genes are replaced with a kanamycin resistance cassette. Therefore, primers were created that could bind to both the original genes and the inserted kanamycin cassette. The primers designed for this are listed in Table C.1. These primers were designed to bind based on the schematic given in Figure C.1.

Table C.1: Primers used to confirm the knockout of the genes of interest within the Keio collection mutants (lowercase letters indicate the annealing sequence).

Primer Name	Sequence
p.AtoS.ext.F	caccgccgagaaatcatcac
p.AtoS.int.F	ctgatggcaatcctgatggt
p.AtoS.int.R	cctgtttgagcagttcacga
p.AtoC.ext.F	cagggtgatattcgcgtcgc
p.AtoC.ext.R	gcaaggggagtgccagaatg
p.AtoC.int.F	ccgtatgctgagcaccgctt
p.AtoC.int.R	aatatttcccggccatgaccag
p.KanCas.int.R	gaagcggtcagcccattc

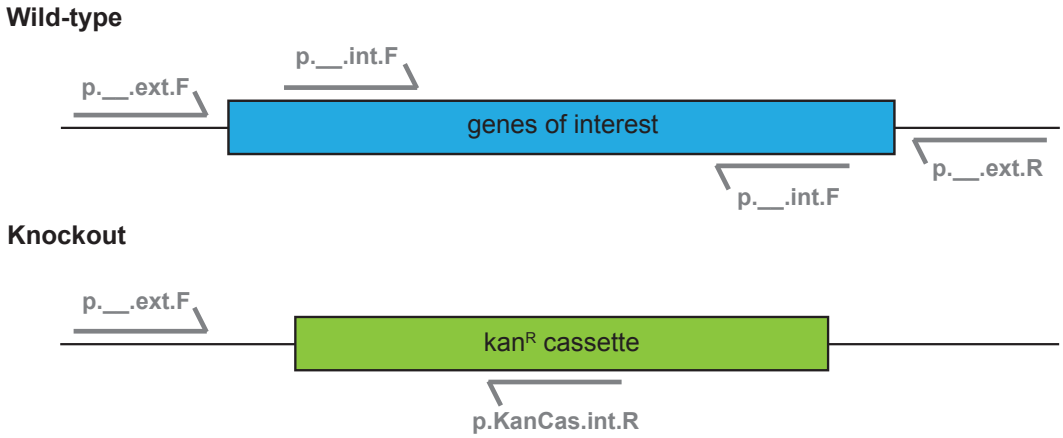

Figure C.1: Schematic illustrating where the designed primer sequences bind for each of the Keio knockout strains. Primers were designed so that PCRs could be used to confirm the presence of the gene (wild-type) or kan^R cassette (knockout).

C.2 AtoSC Model Parameter Estimates

The AtoSC model described in this thesis is complex and contains a number of reactions and parameters. AtoC is known to regulate the expression of the pato promoter; therefore, the binding of both phosphorylated and unphosphorylated AtoC to pato was included within this model. Unphosphorylated AtoC binding has not yet been proven to occur in the AtoSC TCS but was included as a source of GFP leakiness within the model; values of k_{nsbnd} and k_{nsunb} were estimated at values lower

than that of phosphorylated AtoC. The estimates of GFP production parameters in Table 6.1 were based on assumptions about general *E. coli* biology, using values from the 'bionumbers' database (https://bionumbers.hms.harvard.edu/search.aspx). The transcription rate of GFP mRNA was based on the length of the mRNA transcript (850 nucleotides) and the rate of transcription in *E. coli* (40-80 nucleotides/second). The translation rate of GFP was based on the length of the GFP protein (238 amino acids) and rate of translation (20 amino acids/second). The degradation rates for GFP mRNA and GFP protein were based on the half life of mRNA ($\sim$5 minutes) and doubling time of *E. coli* cells ($\sim$20 minutes), respectively. The ribosome concentration was estimated based on the estimated number of ribosomes per cell (6700-71000 ribosmoes, equating to $\sim$6-70 μM).

C.3 Additional Ato simulations

Additional simulations using the Ato model were performed by varying the predicted AtoC concentration. These are shown in Figure C.2.

C.4 Ato Biosensor Hill Fits

Hill functions were fit to the induction data of each Ato WCB. The fitted values for these induction curves are given in Table C.2.

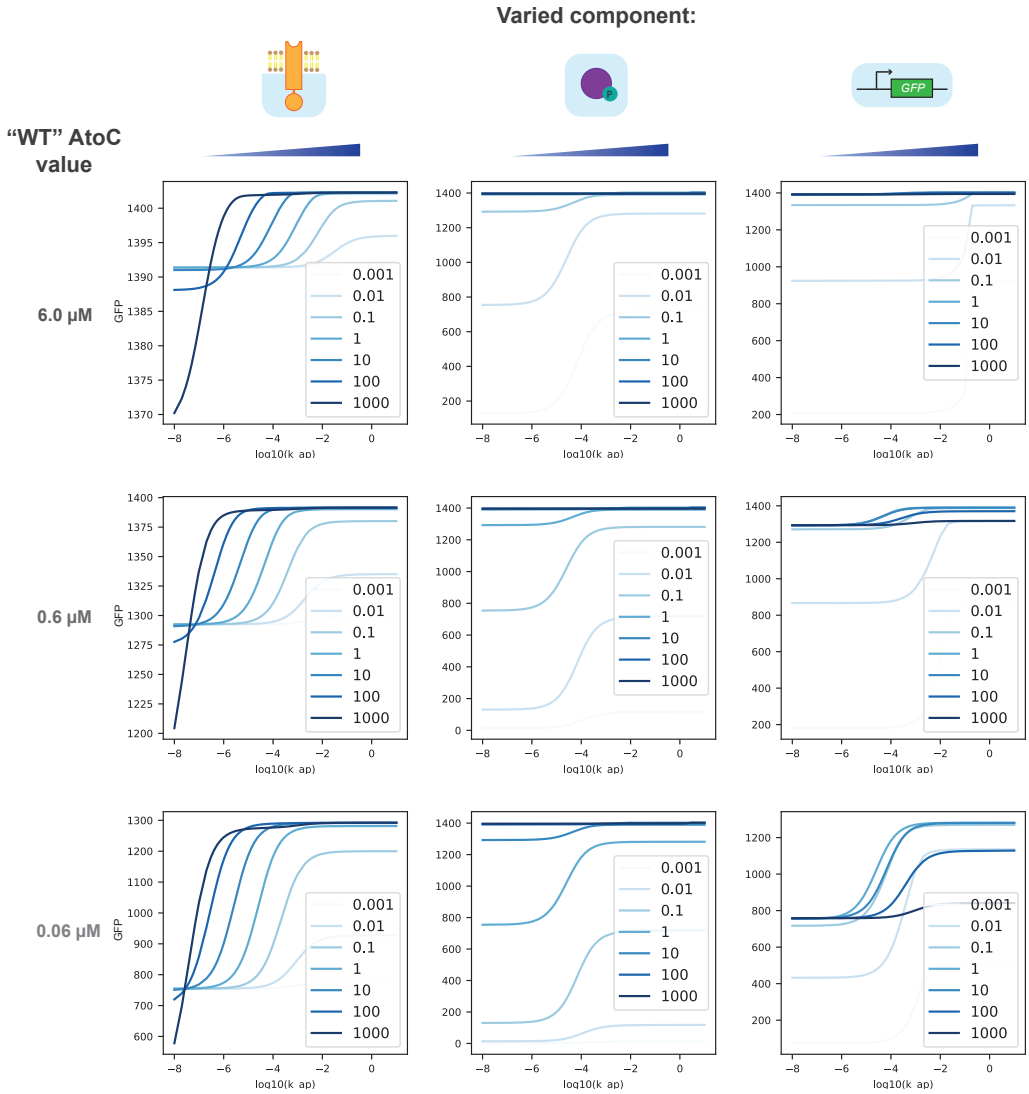

Figure C.2: Effect of 'wild-type' value of AtoC concentration on WCB behaviour. The simulations show the effect of varying AtoS, AtoC and pato concentration for three estimates of native AtoC concentration. The legends give the multiple of the wild-type value which was used for the simulation (i.e. $\times$ WT), columns give the varied parameters and rows give the AtoC concentration estimate used.

Table C.2: Hill parameter fitting to GFP induction curves of the Ato WCBs (fitted values ± SE, given to 3 s.f.).

Host	**Plasmid**	f^{min} (MEF)	f^{max} (MEF)	$K_{1/2}$ (μM)	n	dynamic range
NEBα	ASAH0	234±1.07	87200±1.18	615±72.6	0.670±0.0456	372
EcN	ASAH0	197±1.09	69700±1.49	2060±508	0.724±0.0861	352
BW25113	ASAH0	258±1.09	18100±1.12	249±32.8	1.13±0.130	69.0
BW25113	ASAL0	213±1.08	1510±1.05	2610±3210	0.476±0.148	6.10
BW28878	ASAH0			*linear response*		
JW2213	ASAH0			*linear response*		
JW2214	ASAH0			*linear response*		
JW2213	ASAH1J06	225±1.08	440±1.12	261±223	0.729±0.406	0.95
JW2213	ASAL1J06	202±1.08	36000±1.51	1970±715	0.500±0.0528	177
JW2213	ASAH1J16	219±1.06	2280±1.05	52.2±5.49	1.39±0.219	9.39
JW2213	ASAH1J02			*fit NA*		
BW25113	ASAH2J06	556±1.05	852±1.03	20.5±10.0	1.22±0.517	0.532
BW28878	ASAH2J06	373±1.05	865±1.03	11.7±1.40	4.46±2.76	1.32
BW28878	ASAL2J06	206±1.03	474±1.02	23.7±4.10	4.21±2.41	1.30
BW28878	ASAH2J16	369±1.05	1980±1.04	22.5±2.43	5.51±4.41	4.36
BW28878	ASAH2J02			*fit NA*		
JW2213	ASAH2J06	435±1.11	965±1.08	45.2±29.3	0.849±0.417	1.22
JW2214	ASAH2J06			*fit NA*		